Snapshot Reviews in Emerging Fields

Control of grain structure, phases, and defects in additive manufacturing of high-performance metallic components

T. Mukherjee [a], J.W. Elmer [b], H.L. Wei [c], T.J. Lienert [d], W. Zhang [e], S. Kou [f], T. DebRoy [a,*]

[a] Department of Materials Science and Engineering, Pennsylvania State University, University Park, PA 16802, USA
[b] Materials Engineering Division, Lawrence Livermore National Laboratory, Livermore, CA 94550, USA
[c] School of Mechanical Engineering, Nanjing University of Science and Technology, Nanjing, Jiangsu 210094, China
[d] Optomec, Inc. Albuquerque, NM 87109, USA
[e] Department of Materials Science and Engineering, Ohio State University, Columbus, OH 43210, USA
[f] Department of Materials Science and Engineering, University of Wisconsin-Madison, Madison, WI 53706, USA

ABSTRACT

The properties and serviceability of 3D-printed metal parts depend on a variety of attributes. These include the chemical composition, phases, morphology, spatial distributions of grain size and shape, crystallographic texture, and various defects. Control of these attributes remains an exciting opportunity and a major challenge because of the many process variants and parameters that need to be optimized. The desired attributes of industrially relevant common additive manufacturing alloys such as steels, nickel, titanium, aluminum, and copper alloys, and functionally graded materials vary widely and require alloy-specific strategies for their control. The recent reviews address the valuable processing-microstructure-property relations but do not focus on their control strategies. Here we seek to unify the disjointed literature and critically review recent advances in controlling grain structure, phases, and defects. The emerging use of digital tools such as mechanistic models and data-driven techniques such as machine learning, dimensional analysis, and statistical methods in controlling part attributes is emphasized. Finally, we identify opportunities for high-impact research in metal printing and present an outlook for the future based on existing evidence.

1. Introduction

Additive manufacturing (AM) is attractive because of its ability to produce unique components that cannot be made by more established conventional technologies [1–6]. Production of parts with intricate geometry such as components with internal cooling channels, the substitution of an assembly of many parts with one integrated design such as the fuel nozzle for jet engines, and the flexibility of a single machine to make a variety of parts are some of its attractions [7–15]. However, its market penetration has been tempered by quality consistency issues, specifically the inability to adequately control microstructural features that limit the performance of the parts without post-processing [2]. Its cost competitiveness and acceptability during the part qualification process are related to the chemical composition, phases, morphology, spatial distributions of grain size and shape, crystallographic texture, and

---

* Corresponding author.
  E-mail address: debroy@psu.edu (T. DebRoy).

various defects that define the microstructures, properties, and serviceability of additively manufactured metallic parts [1,3]. Since there are many process variants and process variables, control of these attributes remains a major challenge to optimize micro-structures and properties [1]. The desired grain structures, phases, and defects of industrially relevant common additive manufacturing alloys such as steels, nickel, titanium, aluminum, and copper alloys, and functionally graded materials are unique (Table 1.1) and require alloy-specific strategies for their control. Unlike in welding and casting, optimizing these attributes by trial and error is not a viable path because of the high cost of equipment and feedstock, and the need to cover the large process parameter space for metal printing [3].

An increasing number of publications and several reviews [16–23] on the microstructure and defect control of AM parts are available in the literature. Since AM is rapidly evolving and innovations are constantly developed, a periodic critical assessment of our understanding is necessary and this review seeks to fulfill this need. What is needed and not currently available are the specific roadmaps for the control of the most important microstructural features of the widely used alloy systems for metal printing to make parts with minimum defects and optimum microstructures. The large volume of individual papers and recent reviews address the valuable processing-microstructure-property relations qualitatively but do not focus on the control strategies of the important microstructural attributes. This is an area where the synthesis of emerging digital tools [1,4] and the available information on the characterization of additively manufactured materials can provide a useful pathway for engineers to adopt an expeditious route for

Table 1.1

Important features of grain structures, phases, and defects in additively manufactured parts of industrially important alloys [7–15].

Alloys	Grain structures	Phases	Defects
Austenitic stainless steels	• Solidification mode depends on the Ni and Cr equivalents • Solidifies primarily in either ferrite–austenite or austenite mode • The microstructure can be columnar or equiaxed or a mixture of both	• Microsegregation in the intercellular regions results in Cr and Mo enrichment which stabilize ferrite • Generally, no martensite formation • Nanoscale oxide inclusions are often observed	• Lack of fusion and porosity are often observed • Mn and Cr are susceptible to vaporization • Stress corrosion cracking is observed
Martensitic steels	• Primarily exhibit cellular or dendritic grain structure • Grains grow primarily along the preferential ⟨001⟩ solidification direction • Grain size varies widely depending on the cooling rates	• Tool steels, low alloy steels, and ferritic-martensitic steels form martensite and Cr, V, W, and Mo rich carbides • Maraging steels form Ni_3Mo and $Ni_3(Ti, Al)$ precipitates along with martensite.Cr • in maraging steels does not precipitate but raises the martensite start temperature	• Lack of fusion, gas porosity, and keyhole porosity are common • Mn and Cr are the most susceptible element to the vaporization • Solidification cracking is often observed
Duplex steels	• A high concentration of Cr stabilizes the primary δ-ferrite and austenite forms from ferrite • Grain boundary austenite, Widmanstatten austenite, intragranular austenite, and secondary austenite morphologies	• Brittle sigma phases are often observed • Nitride inclusions form at the grain boundaries depending on the nitrogen content • Fe and Cr rich carbides affect the mechanical properties	• Lack of fusion, gas porosity, keyhole porosity, and composition change are often observed • Less susceptible to cracking than other steels
Aluminum alloys	• Long columnar grains often cause anisotropic tensile properties • Grain refiners and inoculants are often added to achieve equiaxed grains • Dendritic arm spacing vary significantly depending on the cooling rates	• Si and Fe rich precipitates are often found within the primary α grains • Precipitation-strengthened alloys are often heat treated to achieve desired phases and properties	• Solidification cracking and liquation cracking are major issues • Mg and Zn may selectively vaporize • Lack of fusion and gas porosities are also observed
Nickel alloys	• Generally, columnar dendrites with a strong texture along the ⟨001⟩ direction aligned with the build direction are formed • Single crystals with no grain boundaries are also printed • Grain refiners are often added to form small equiaxed grains to improve mechanical properties • The formation of stray grains often affects single crystallinity	• Segregation of Nb, Mo, Al, Ta, and C in the inter-dendritic region forms carbides and laves phases-Strengthening precipitates (γ' and γ") • are formed in as-deposited as well as heat-treated samples and affect properties	• Solidification cracking, liquation cracking, ductility dip cracking, and strain age cracking are common • Susceptible to Cr vaporization loss • Lack of fusion, gas porosities, and keyhole porosities are often found
Titanium alloys	• β grains (BCC) form after solidification followed by α grains (HCP) within the prior β grains below the β transus temperature • β grains are long and columnar and α grains are small with dispersed and basketweave structure • Single phase β-grain structure is observed for metastable β alloys	• The volume fraction of α phases depends on α stabilizing elements such as Al, N, C, and O • α' martensite (HCP) is often formed at high cooling ratesAn orthorhombic α'' structure is observed depending on the amount of V, Cr, and Nb • (β stabilizer)	• Very sensitive to the pickup of C, N, O, and H from the atmosphere • Lack of fusion, gas porosity, keyhole porosity, and composition change are often found • Generally do not crack
Copper alloys	• Columnar and equiaxed dendrites are observed depending on process parameters and composition • Printed bronze parts show long grains aligned along the build direction	• Form grain boundary precipitates rich with Cr, Zr, Ti, and Ni • The shape and size of precipitates affect the toughness of parts	• Alloying element segregation causes cracking • Lack of fusion and gas porosities are common

advancing additive manufacturing by improving part quality based on scientific principles.

Control of solidification structure, grain structure, phase composition, and defects for each commonly used alloy system aided by the valuable and growing characterization literature and synthesized with powerful physics-based and data-driven techniques can impact all steps of AM technology [1]. There is a growing consensus that the technology of AM will not mature following the same path followed by the traditional established manufacturing technology such as welding and casting [1,3]. The advantages achievable by using emerging powerful digital tools such as mechanistic modeling, machine learning, and digital twins provide a more scientific and expeditious route for the development of AM than that achieved before for the other manufacturing technologies [4]. While there is growing literature on the characterization of metallic components, the papers focus on various alloys, AM processes, and process variables. The results show that there is no definitive single pathway for the control of grain structure, phases, and defects. Encompassing all aspects of AM including product design, process planning, production monitoring and control, control of microstructural features and defects, inspection, and qualification, digital tools can significantly reduce trial and error testing and part rejection, improve quality and reduce cost [1]. We seek to synthesize existing literature to provide a roadmap for each commonly used AM alloy
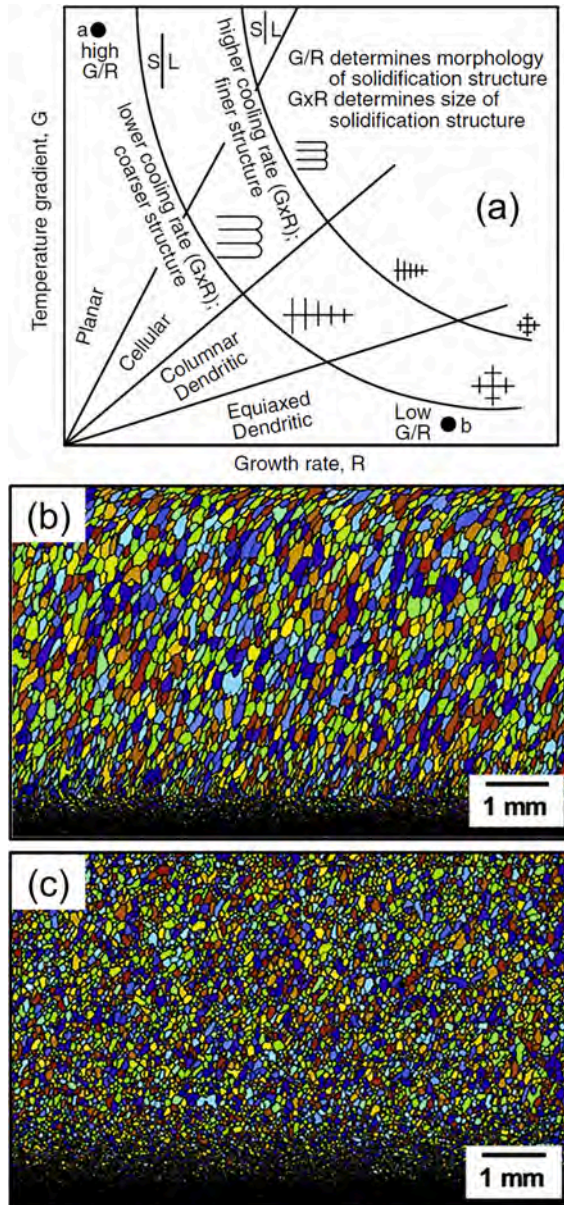
Fig. 2.1. (a) A schematic diagram of a solidification map showing grain morphology variation for different values of temperature gradient and solidification growth rate [32]. (b-c) Computed grain structures at two longitudinal vertical planes during DED-L of Inconel 718 showing smaller grain size away from the mid-section [36], (b) 240 μm from the central plane and (c) 840 μm from the mid-plane.

system for engineers to use as a practical guide based on scientific principles.

Here we critically review recent advances for controlling grain structure, phases, and defects based on experiments, mechanistic modeling, machine learning, and other data-driven techniques. We uncover the alloy-specific control strategies to achieve the desired microstructure**s** in various types of steels, aluminum, nickel, titanium, and copper alloys, and functionally graded materials produced by powder bed fusion with laser (PBF-L) and electron beam (PBF-EB) as well as directed energy deposition with laser (DED-L), electron beam (DED-EB), gas metal arc (DED-GMA), and plasma arc (DED-PA). These alloys are selected based on their importance in additively manufactured parts. We review the scientific foundation for the manufacture and repair of single crystal parts that are potentially attractive to aerospace and other industries. We also address the important need for the control strategies of common defects and review the emerging use of mechanistic models and data-driven techniques in controlling part attributes. Finally, we identify opportunities for high-impact research and present an outlook for the future based on evidence.

2. Theories of grain structures, phases, and defects formation

2.1. Grain structure

Solidification morphology and grain size are the two most important attributes of grain structure [24–29] because they affect the properties and serviceability of additively manufactured metallic parts. Theories of the evolution of grain morphology and size distribution in additive manufacturing have benefited from the rich knowledge base of metallurgy and fusion welding where the scientific principles of grain growth have been a subject of considerable interest for many decades.

2.1.1. Grain morphology
The liquid needs to be cooled below the liquidus temperature for the growth of a solid. The extent of undercooling [30], defined as the difference between the liquidus temperature and the liquid's local temperature, is the sum of contributions from solute undercooling (ΔT_C), curvature undercooling (ΔT_R), thermal undercooling (ΔT_T), and kinetic undercooling (ΔT_K):

$$\Delta T = \Delta T_C + \Delta T_R + \Delta T_T + \Delta T_K \tag{1}$$

The undercooling affects the evolution of microstructure, particularly the morphology of the solidification front and the phase selection. For example, Hunt [31] suggested that equiaxed growth would occur when the temperature gradient, G, is less than that given by the following expression:

$$G < 0.617 \, N_0^{1/3} \, \Delta T_C \, (1 - \Delta T_n^3 / \Delta T_C^3) \tag{2}$$

where N_0 is nucleant density (1/m^3), ΔT_C represents solute undercooling of dendrite tip (K) and ΔT_n represents undercooling for heterogeneous nucleation which is typically small. While the morphology has been correlated with the undercooling using elegant theories, the applications of these theories require values of parameters such as N_0 which cannot be accurately prescribed based on theory. Therefore, a usable framework that connects quantifiable parameters with morphology such as planar, cellular, or dendritic, is needed.

A commonly used methodology for estimating the morphology of a solidifying alloy is a plot of temperature gradient (G) versus solidification growth rate (R) [32] shown in Fig. 2.1 (a). The increase of G/R results in morphology change from equiaxed, to dendritic to cellular to planar. During additive manufacturing, the ratio of G/R is much lower than that required for planar solidification. In contrast, columnar dendritic morphology which is susceptible to cracking is often observed. Processing conditions and alloy composition determine the temperature field and the local solidification growth rate at various locations. The parameters, G and R are often controlled to achieve solidification conditions favorable for equiaxed grain formation. A low value for the temperature gradient to solidification rate ratio (G/R ratio) at the liquid/solid interface needs to be achieved to obtain equiaxed microstructure [25].

Heat source power, scanning speed, scanning pattern, beam radius, power distribution, preheating temperature, and other variables may be adjusted to achieve favorable G and R. A well-tested heat transfer and fluid flow model can provide reliable values of temperature field and solidification growth rates at various locations in the three-dimensional space. In addition, grain refiners and inoculants are often added to promote heterogeneous nucleation within the liquid to achieve equiaxed grains [26]. External agitations such as ultrasonic vibrations have also been used to break the long columnar grain during AM [27]. These techniques of controlling the morphologies are reviewed for different alloy systems in Section 3 of this review.

2.1.2. Grain size
Grain size controls the mechanical properties of parts such as hardness, yield strength, and creep life. Since grain growth depends on time–temperature history, the grain size can vary spatially depending on the local variation in temperature with time [29]. As a result, theories of grain size evolution have been of much interest in metallurgy. One of the first theories of grain growth was proposed by Burke and Turnbull [33] who assumed that the grain boundary velocity was inversely proportional to its radius of curvature, and showed the following parabolic kinetics for grain growth.

$$R_t^2 - R_0^2 = K \, t \tag{3}$$

where R_0 and R_t are the average radii of grains at times zero and t, and K is a constant. Since the diffusion of atoms across a grain boundary is considered to be an activated process, it can be shown that the constant K can be replaced by the following expression:

$$K = K_0\,e^{-Q/RT} \tag{4}$$

where K_0 is a constant, Q is the activation energy for diffusion and T is temperature. Thus, equation (4) indicates faster grain growth at higher temperatures. However, since grains are surrounded by other grains, they cannot be treated as isolated entities. Both the driving forces for the migration of boundaries and the topological considerations need to be considered for grain growth. Since the parabolic grain growth model, several other analytical models have been proposed to overcome its deficiencies [34]. However, the complexity of grain size variations in three dimensions in non-isothermal systems has not been modeled by analytical models. In addition, the spatial gradient of temperatures also imposes "thermal pinning" [35] which cannot be predicted by analytical calculations. Therefore, numerical models such as Monte Carlo simulations have been proposed considering grains as a topologically connected network in a three-dimensional space where significant variations of temperature exist [36].

Rapid cooling at low heat input results in smaller grains. Since different AM processes use significantly diverse heat inputs (Table 2.1), they exhibit a striking difference in grain size. For example, AlSi10Mg parts printed using PBF-L [37] using 0.28 to 0.41 J/ mm heat input exhibit significantly finer grain size (0.53 to 0.93 μm) than those produced using DED-L (48 μm) [38] where the heat input is 100 J/mm (Table 2.1). Schneider et al. [28] compared the grain size of Inconel 718 parts printed using DED-L, DED-GMA, and PBF-L. The lowest heat input in PBF-L resulted in rapid cooling and fine grains [28]. For the same heat input, Fig. 2.1 (b) and (c) compare grain growth during DED-L of Inconel 718 in two vertical longitudinal planes. The plane considered in (b) was 240 μm from the central vertical plane and the plane (c) was 840 μm from the central vertical plane. Temperatures are lower further away from the middle planes and as a result, the grain size in plane (c) was much smaller than the average grain size in the plane (b).

Table 2.1 provides several examples [36–52] of the variations in solidification morphologies and grain size in different alloy parts printed using various AM processes. Grain size can be controlled by adjusting the cooling rates by varying the processing conditions and by employing post-process heat treatment as explained in Section 3 of the review.

2.2. Phases

The evolution of grain structure, as discussed in the previous section, is a critical step in the formation of the microstructure of a metal AM part. However, after the metal has solidified and cooled below its solidus temperature, it must still cool to room temperature and can go through phase transformations along the way [53–56]. These transformations result in a wide variety of primary and secondary phases with diverse crystal structures and chemical compositions as summarized in Table 2.2. These phases significantly affect the microstructure and mechanical properties of parts [16,57]. The theories behind the formation of these phases are reviewed below.

2.2.1. Phase diagrams and constitution diagrams

Phase diagrams [58,59] are widely used for understanding the phase composition of an alloy of known chemical composition at a given temperature under equilibrium. For many systems, the phase transformations are time-dependent, and phase diagrams provide

Table 2.1

Selected examples [36–52] of the variations in solidification morphologies and grain size in different alloy parts printed using various AM processes.

Alloys	AM process	Heat input (J/mm)	Morphology	Grain size	References
Stainless steel SS 441	PBF-L	0.2	A mixture of cellular and columnar dendrites	Average grain size 1.61 to 1.76 μm	[39]
Stainless steel SS 304	DED-L	156.25 – 625	Columnar dendrites	Average grain size 9.2 to 13.3 μm	[40]
Low-carbon high-strength steel	DED-GMA	536.25	A mixture of columnar and equiaxed dendrites	Spatial variation of average grain size 9.94 to 12.76 μm	[41]
High-strength low alloy steel	DED-GMA	334.3 – 350	Columnar dendrites	Average grain size 20 to 75 μm	[42]
16.5 Cr, 1.7 Ni, 1 Mo steel	PBF-L	0.08 – 0.12	Cellular structure	Average grain size 0.467 to 0.481 μm	[43]
Ferritic /martensitic HT9 steel	DED-L	Not provided	Equiaxed dendrites	The average grain size of the as-built part is 3.2 μm	[44]
AlSi10Mg	PBF-L	0.35	A mixture of columnar and equiaxed dendrites	The columnar grains have a mean width of 20 μm and equiaxed grains have a diameter ranging from 5 to 20 μm.	[45]
AlSi10Mg	PBF-L	0.28 – 0.41	Ultrafine cellular	Average grain size 0.53 to 0.93 μm	[37]
AlSi10Mg	DED-L	100	Columnar dendrites	Average grain size 48 μm	[38]
Inconel 718	PBF-L	0.29	A mixture of columnar and equiaxed dendrites	Average grain size 14.5 to 19.1 μm	[46]
Inconel 718	DED-L	84	Columnar dendrites	The average grain size is around 90 μm	[36]
Inconel 625	PBF-L	0.29 – 0.46	Fine cellular and columnar dendrites	Average grain size 26.2 μm	[47]
Inconel 625	PBF-L	0.29	Equiaxed dendrites	Average grain size 27 μm	[48]
Inconel 939	PBF-L	0.19 – 0.20	A mixture of columnar and equiaxed dendrites	Average grain size 9 to 11 μm	[49]
Ti-6Al-4 V	PBF-EB	Not provided	Columnar prior β grains	The width of prior β grains varies from 20 to 180 μm	[50]
Ti-6Al-4 V	PBF-L	0.23	Columnar prior β grains	The average width of prior β grains is 33.6 μm	[51]
Ti-45Al-2Cr-5Nb	PBF-L	0.25 – 0.40	Columnar	Average grain size 6.52 to 10.87 μm	[52]

Table 2.2

A wide variety of phases with diverse crystal structures and chemical compositions formed in steels and alloys of aluminum, nickel, and titanium.

Phase	Symbol	Crystal Structure	Comment
Phases in C-Mn Steels			
Alpha Ferrite	α	BCC	Equilibrium phase
Austenite	γ	FCC	Equilibrium phase
Delta Ferrite	δ	BCC	Equilibrium phase
Cementite	θ (Fe_3C)	Orthorhombic	Iron carbide
Epsilon Carbide	ε ($Fe_{2.4}C$)	Hexagonal	Transition Carbide
Eta Carbide	η (Fe_2C)	Orthorhombic	Transition Carbide
Martensite	α'	Tetragonal	Non-Equilibrium phase
Bainite	α_{lb}, α_b	BCC + Carbides	Non-Equilibrium phase
Phases in Alloys Steels			
Alpha Ferrite	α	BCC	Equilibrium phase
Austenite	γ	FCC	Equilibrium phase
Delta Ferrite	δ	BCC	Equilibrium phase
Alloy Carbide	MC	FCC	M = Ti, Nb, V, Ta, W
Alloy Carbide	$M_{23}C_6$	FCC	M = Cr, Mo, Fe
Alloy Carbide	M_7C_3	Hexagonal	M: multiple elements
Alloy Carbide	M_6C	FCC	M: multiple elements
Martensite	α'	Tetragonal	Non-Equilibrium phase
Pearlite	P	BCC + Carbides	Ferrite + Carbide Constituents
Bainite	α_{lb}, α_b	BCC + Carbides	Ferrite + Carbide Constituents
Phases in Al Alloys			
Primary alpha	α_p	FCC	Equilibrium phase
Secondary alpha	α_s	FCC	Equilibrium phase
Primary beta	β_p	BCC	Equilibrium phase
Secondary beta	β_s	BCC	Equilibrium phase
Phases in Ni Alloys			
Gamma	γ	FCC	Equilibrium phase
Gamma prime	γ'	L12	Equilibrium phase
Delta	δ	FCC	Equilibrium phase
Sigma	σ	Orthorhombic	Non-Equilibrium
Laves phases	Ni_aX_b	L12	X = Cr, Mo, Fe
Phases in Ti Alloys			
Alpha	α	Hexagonal	Equilibrium phase
Beta	β	BCC	Equilibrium phase
Alpha Prime	α'	HCP	Martensitic phase
Alpha Double Prime	α''	Orthorhombic	Martensitic phase
Omega	ω	Hexagonal	Metastable phase

the state of the system after a long time when equilibrium is attained. A phase diagram is a graphical representation of the relationships between the various phases of a material at different temperatures, pressures, and compositions. It shows the conditions under which different phases exist and their stability ranges. By using phase diagrams, scientists and engineers can predict which phases will form during the additive manufacturing process [58,59]. Apart from the primary phases such as austenite and ferrite in steels, phase diagrams can include secondary phases such as carbides, nitrides, oxides, intermetallic compounds, and martensite [16,57]. Table 2.3 provides several examples [60–91] of such phases in different alloy parts printed using various AM processes. These phases significantly affect the mechanical properties of parts [16,57]. For example, Laves phases are intermetallic compounds formed during AM of nickel-base superalloys and are known to degrade the toughness of parts [57].

Constitution diagrams such as the Schaeffler diagram (Fig. 2.2 (a)) for stainless steels are useful tools for understanding the phase formation during additive manufacturing [92,93]. It is a graphical representation of the chemical composition of stainless steel, which helps to predict the austenitic, ferritic, or martensitic phase formation [92,93]. The diagram considers the effects of both alloying elements and thermal history on the formation of the phases. During additive manufacturing, stainless steel undergoes rapid heating and cooling, leading to complex phase transformations. By using the Schaeffler diagram, it is possible to predict the final microstructure of the material based on the initial chemical composition, processing conditions, and cooling rates [92,93].

2.2.2. Johnson–Mehl–Avrami–Kolmogorov equation

The Johnson–Mehl–Avrami–Kolmogorov (JMAK) equation [52,94,95] is a mathematical model used to describe the kinetics of phase transformations in materials. The JMAK equation relates the volume fraction of transformed material to time and temperature, taking into account the nucleation and growth of new phases. The JMAK equation is given by [52,95]:

$$V = 1 - \exp[-(k\,t)^n] \tag{5}$$

where V is the volume fraction of the new phase, k is the rate constant, t is time, and n is the Avrami exponent, which is related to the dimensionality of the growth process. The JMAK equation assumes that the phase transformation proceeds by nucleation and growth and that the growth rate is proportional to the volume fraction of the new phase. The Avrami exponent can take values between 1 and 4, depending on the geometry of the growing phase and the reaction mechanism [52,95]. By fitting experimental data to the

Table 2.3
Selected examples [60–91] of phases formed in different alloy parts printed using various AM processes.

Phases	Alloys	AM process	Description	References
Carbides	Stainless steel 316	PBF-L	Nano-scale carbides such as Mn_7C_3 are formed	[60]
	15–5 PH stainless steel	PBF-L	Fine, nano-scale carbide precipitates	[61]
	9Cr-1Mo steel	PBF-L	Precipitation of $M_{23}C_6$ carbide	[62]
	Inconel 718	PBF-L	Primarily (Nb, Ti)C carbides are observed	[63]
	Inconel 625	DED-L	$Cr_{23}C_6$ and NbC are formed	[64]
	Inconel 718	DED-GMA	Carbides precipitate in the heat-affected zone	[65]
	Alloy 800H	PBF-L	$Cr_{23}C_6$ and Cr_6C are formed	[66]
	Haynes 282 superalloy	DED-L	Globular, nano-sized Ti and Mo-rich carbides of MC and M_6C structure are observed	[67]
	Haynes 282 superalloy	DED-GMA	(Ti, Mo)C and $(Cr,Mn,Mo)_{23}C_6$ precipitate	[68]
	Ti-3Al-8 V-6Cr-4Mo-4Zr alloy	DED-L	Ti and Zr-rich carbides are formed	[69]
Nitrides	Inconel 718	PBF-L	Micro-sized, irregular-shaped, Ti-rich nitrides	[70]
	Duplex steel 2507	DED-GMA	Cr-rich nitrides precipitate in the heat-affected zone	[71]
	2205 duplex stainless steel	DED-GMA	Mainly Cr-rich nitrides form near the fusion boundary	[72]
	2205 duplex stainless steel	PBF-L	Nano-sized Cr-rich nitrides	[73]
Oxides	Stainless steel 316	PBF-L	Oxides of Cr and Mn	[74]
	Stainless steel 316	DED-L	Oxides of Cr and Mn	[74]
	Stainless steel 316	PBF-L	Depending on the oxygen concentration (Mn, $Cr)Cr_2O_4$, SiO_2, and Cr_2O_3 are formed	[75]
	17–4 PH steel	DED-PA	Micron-scale layers of Cr_2O_3 are formed	[76]
	Maraging Steel M789	PBF-L	TiO_2 and Al_2O_3 are formed	[77]
	Commercially pure Cu	PBF-L	Cu_2O and CuO oxide precipitates of 2 to 30 nm size are formed	[78]
	Stainless steel 316	DED-L	Nano-sized $MnSiO_3$ is formed	[79]
Intermetallic compounds	Stainless steel 316	DED-L	Cr, Mo, and Mn-rich intermetallic precipitates are formed	[79]
	Inconel 738LC	DED-GMA	$Ni_3(Al,Ti)$ intermetallic compounds are formed	[80]
	Al-Si alloy	DED-GMA	A short rod-like Fe-intermetallic compound was observed at the grain boundaries	[81]
	Inconel 718	DED-L	Laves phases are observed	[82]
	Inconel 718	PBF-L	Discrete nano-scale Laves phase particles are formed	[83]
	Inconel 718	DED-L	Laves phases significantly degrade the tensile properties	[84]
	Inconel 718	DED-L	Laves phases of different sizes and morphologies are obtained	[84]
Martensite	18Ni maraging steel	PBF-L	Low carbon BCC martensite and FCC retained austenite crystal structures	[86]
	Ti6242S alloy	PBF-L	Soft, orthorhombic martensite	[87]
	Ti-6Al-4 V	PBF-L	Long laths of martensite	[88]
	H13 tool steel	DED-GMA	Formation of martensite increased hardness	[89]
	Fe-0.45C steel	PBF-L	Martensites are partially tempered due to repeated thermal cycles	[90]
	Grade 91 ferritic steel	DED-L	The amount of martensite and tempered martensite affects the hardness variation	[91]

JMAK equation, researchers can extract the rate constant and the Avrami exponent, which provide insights into the kinetics of phase formation during additive manufacturing processes [52,94]. Transformations typically exhibit an s-shaped, or sigmoidal profile where transformation rates are slow at the start and end of the process, but rapid in the middle (Fig. 2.2 (b)). The slow rate at the beginning is due to the time it takes for a significant number of nuclei to form and grow. In the intermediate period, transformation is fast as the nuclei develop into particles and consume the old phase while new nuclei continue to form in the remaining parent phase. As the transformation approaches completion, there is minimal untransformed material for nucleation, resulting in a slowdown in the production of new particles. It is often applied to understand the phase formation that occurs during the additive manufacturing of metallic materials [52,94].

2.2.3. TTT curves and CCT curves

At a given temperature, the extent of a given diffusion-controlled transformation depends on the time of transformation. Time-temperature-transformation (TTT) diagrams or isothermal transformation diagrams show percentage transformation versus time at a constant temperature. Plots of temperature versus time (latter in a logarithmic scale) show percentage completion curves for a certain phase transformation (or reaction), in many cases the shape of these curves resembles that of "C" and is sometimes referred to as C-curves. Although they are most commonly used for austenite decomposition during cooling in steels, they can also be used to describe any phase transformations. For example, time–temperature-transformations diagrams are available for the growth and dissolution of various types of inclusions such as oxide and nitride inclusions in steels. [96,97]. Most standard textbooks provide many examples of TTT diagrams, most commonly for steels. For example, TTT diagrams for eutectoid steels show the transformations of austenite to coarse pearlite and fine pearlite or bainite. They also show the occurrence of a diffusionless process that results in the formation of martensite below the martensite start temperature when the specimens are cooled rapidly. Martensitic transformations are displacive transformations that involve the displacement of a large number of atoms by a small distance such as a small fraction of the interatomic spacing. For example, a face-centered cubic structure can be transformed into a hexagonal close-packed structure by the Martensitic transformation by sliding of {1 1 1} planes over one another of FCC structure.
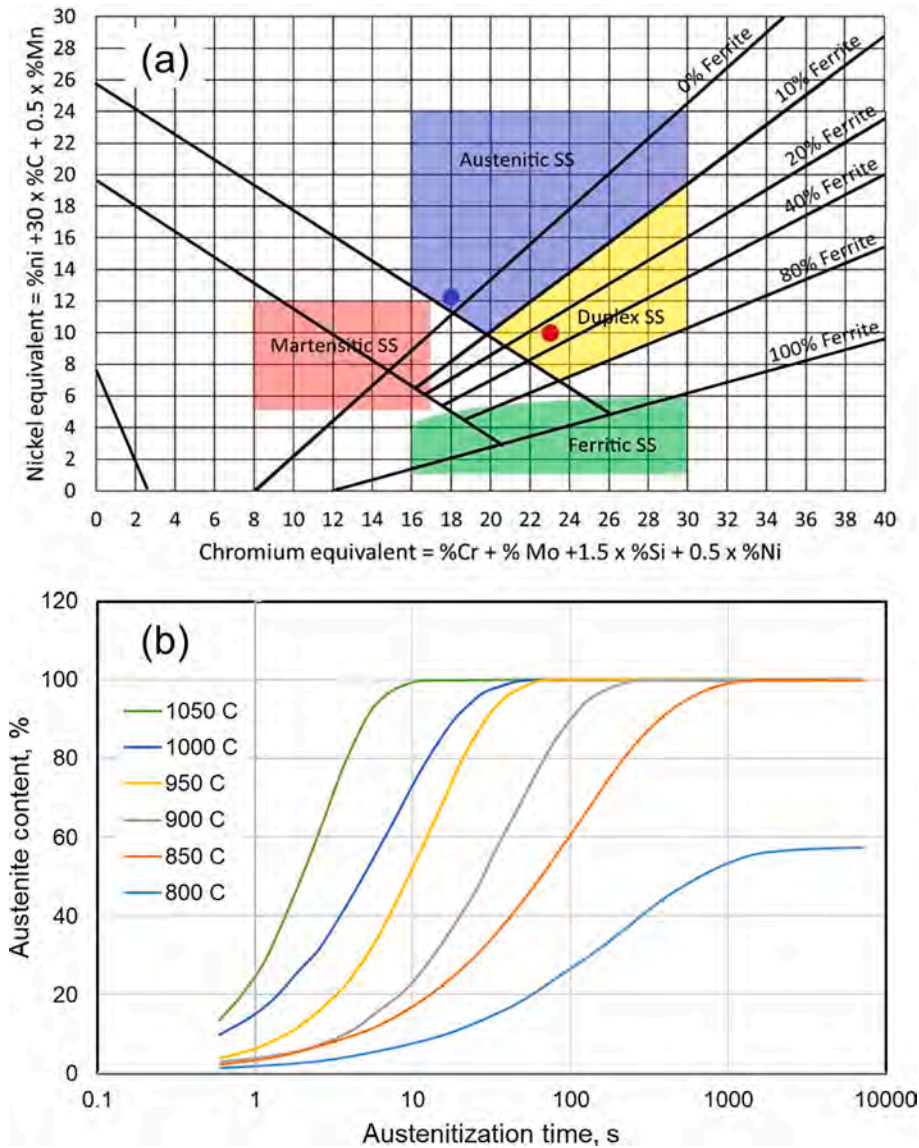
Fig. 2.2. (a) Schaeffler diagram of stainless steels [93]. (b) The relative content of newly formed austenite as functions of temperature and austenitization time. The plot is made using the data reported in [95].

In additive manufacturing, phase transformations do not occur under isothermal conditions because of repetitious heating and cooling. TTT diagrams can be transformed to include continuous temperature changes, particularly cooling, and the modified diagrams that take this into account are called continuous cooling transformation diagrams or CCT diagrams. Depending on how the temperature changes with time, the time necessary to attain a certain transformation changes. During continuous cooling, the transformation resulting from the cooling shifts the constant % transformation curves downwards and to the right of the TTT curves for isothermal transformation.

2.3. Defects

Mechanical properties, quality, reliability, and serviceability of parts are often affected by common defects such as cracking, loss of alloying elements, lack of fusion, porosity due to gas bubbles, and keyhole instability-induced porosity (Table 2.4). The theories of the evolution of these defects are discussed below.

2.3.1. Solidification cracking
Solidification cracking [98–102] is common in additively manufactured parts of aluminum and nickel alloys and austenitic stainless steels. Since an alloy melts and solidifies over a range of temperatures, a mushy zone forms behind the molten pool, and a

Table 2.4
Formation of common defects in additive manufacturing of alloys.

Defects	Alloys	Descriptions	References
Solidification cracking	Al alloys, Ni alloys, austenitic stainless steels	• Solidification cracking occurs when the tensile stress due to solidification shrinkage exceeds the yield strength and there is insufficient liquid metal to fill the crack. • Solidification cracking is affected by tensile stress due to shrinkage, solidification temperature range, temperature-solid fraction relation, and solidification morphology. • Long columnar grains can result in solidification cracking. • Alloys with a high slope of temperature versus solid fraction plot are more susceptible to solidification cracking.	[98–102]
Liquation cracking	Al alloys, Ni alloys, austenitic stainless steels	• Liquation cracking is caused by localized melting of low melting regions at a grain boundary under the influence of thermal strains.It is affected by the chemical compositions, the solidification range, solidification shrinkage, thermal contraction, and the presence of intermetallic compounds and precipitates. • It occurs adjacent to the fusion zone or in previously deposited layers where the temperature is below the solidus temperature.	[106–110]
Composition changes due to selective vaporization	All alloys	• Alloying elements vaporize from the molten pool at different rates. • Selective vaporization of alloying elements results in composition change. • Composition change affects the microstructure, corrosion resistance, and mechanical properties of parts. • Vapor pressure of elements over the liquid alloy, local temperature, alloy composition, and pool surface area to volume ratio affect composition change. • Magnesium and zinc in aluminum alloys, chromium and manganese in steels, chromium in nickel alloys, and aluminum in titanium alloys are the most susceptible elements.	[113–117]
Lack of fusion	All alloys	• Insufficient fusional bonding between adjacent tracks or successive layers may result in the lack of fusion voids. • Lack of fusion significantly degrades the tensile properties of parts.	[119–123]
Porosity	All alloys	• Hydrogen, oxygen, and nitrogen in the atmosphere and shielding gas used during additive manufacturing can be entrapped inside the molten pool and result in gas porosities. • Gas entrapped inside powders made by gas atomization can also cause gas porosities. • If vapors from the collapsed keyhole fail to escape the molten pool before it solidifies, keyhole porosities form.	[125–136]

partially melted zone exists in the region of the workpiece around the molten pool (Fig. 2.3 (a)). In the mushy zone, grains are typically columnar with intergranular liquid films (Fig. 2.3 (a)). This region has limited ductility and is unable to accommodate significant tensile deformation without cracking. Some areas adjacent to the fusion zone may also have limited ductility (Fig. 2.3 (a)) because for some alloys a significant ductility drop can occur in an intermediate temperature range below the solidus temperature (T_S), often between 0.6 and $0.9T_S$. The two-phase mushy zone tends to shrink because of the solidification shrinkage and thermal contraction but cannot shrink freely because its shrinkage is constrained by the much cooler bulk workpiece (Fig. 2.3 (a)). Thus, multi-axial tensile stresses are induced in the mushy zone that can separate growing dendritic grains from each other and cause cracking along the grain boundaries [98–102]. Cracks are often visible in the fusion zone, along grain boundaries, and the fracture surfaces show dendrites or cells [98–102]. Grain structure is a significant factor in cracking susceptibility. Long columnar grains can separate from each other under high tensile stress during solidification and result in solidification cracking.

Solidification cracking has been related to the nature of the temperature versus solid fraction curves. A simple index $|dT/d(f_S)^{1/2}|$ was used to evaluate the susceptibility to solidification cracking of different alloys, where T is temperature and f_S is the fraction of solid [103]. It was suggested that the maximum $|dT/d(f_S)^{1/2}|$ up to $(f_S)^{1/2} = 0.99$ (i.e., $f_S = 0.98$) is a convenient value for the index. This is because the maximum $|dT/d(f_S)^{1/2}|$ usually occurs near $(f_S)^{1/2} = 1$ and because beyond $f_S = 0.98$, the grains can bond to each other extensively to resist cracking. A steep variation in the temperature versus solid fraction plot means a very low liquid fraction near complete solidification over a relatively large temperature range. This depletion of the available liquid to heal the cracks over a large temperature range makes alloys susceptible to cracking. Fig. 2.3 (b) shows the variation of temperature with solid fraction for Al7075 and AlSi10Mg alloys [104]. It is observed that the change in temperature with the solid fraction is much steeper for Al7075 than AlSi10Mg, making Al7075 more susceptible to solidification cracking than AlSi10Mg.

This criterion for solidification cracking is useful to compare the susceptibilities of different alloys to solidification cracking. However, this criterion is devoid of any consideration of the specific additive manufacturing process or process variables. Comprehensive models for solidification cracking considering process variables are emerging [105].

2.3.2. Liquation cracking

Liquation cracking can occur during additive manufacturing of aluminum alloys, nickel-based alloys, and austenitic stainless steels [106–110]. It is caused by localized melting of low melting regions at grain boundaries under the influence of thermal strains. It generally occurs outside and adjacent to the fusion zone or in previously deposited layers where the temperature is below the solidus
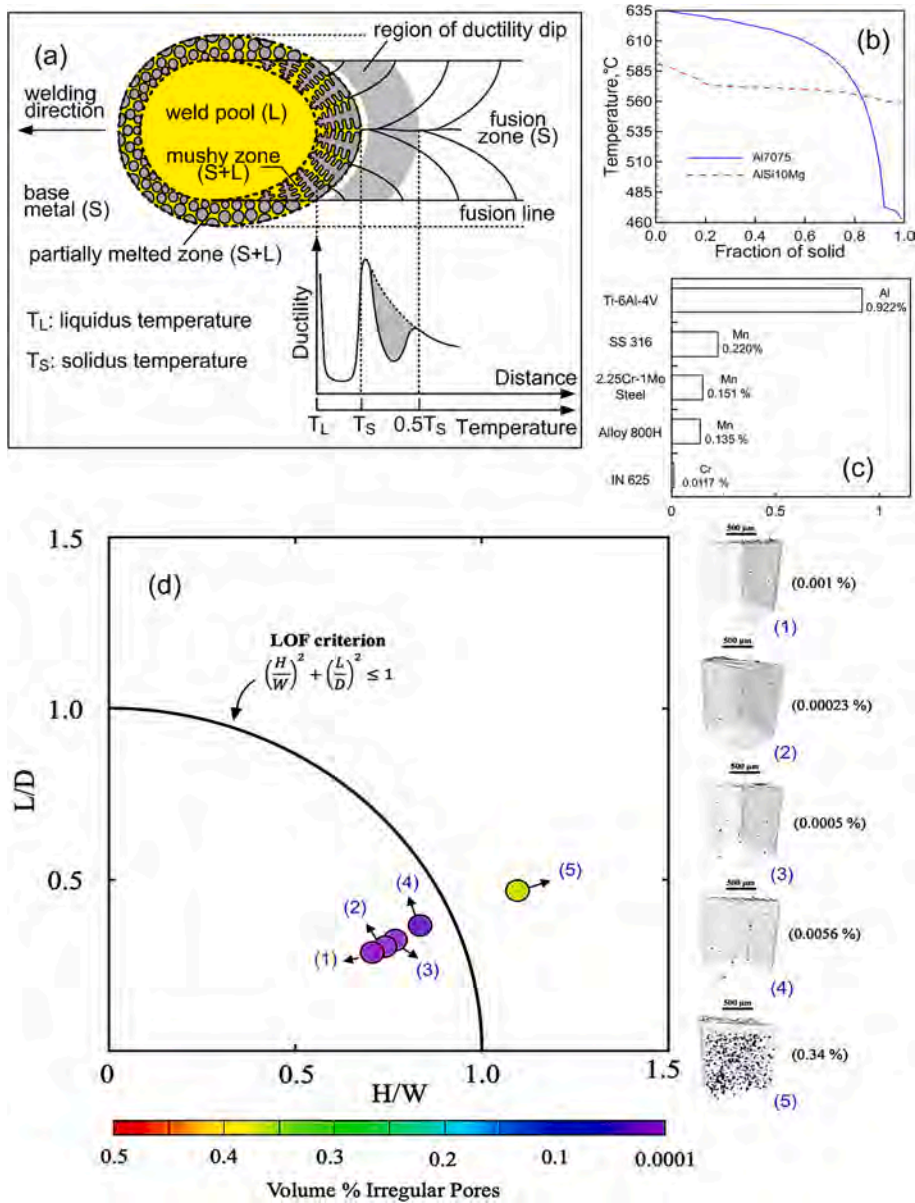
Fig. 2.3. (a) Schematic representation of the formation mechanism of solidification cracking [103]. (b) Temperature versus solid fraction curves for two aluminum alloys [104]. (c) Composition change of the most susceptible elements for different alloys during DED-L [118]. (d) Lack of fusion (LOF) pore criterion [124] boundary is plotted along with corresponding defect densities during PBF-L of Ti-6Al-4 V.

temperature of the alloy [106–110]. Liquation cracking depends on the alloy composition, the temperature range of solidification, solidification shrinkage, thermal contraction during cooling, and the presence of intermetallic compounds and precipitates [106–110].

Liquation cracking involves localized liquid formation (i.e., liquation) along grain boundaries as well as at isolated spots within grains. Liquation cracking can occur under significant tension induced by the solidifying/contracting mushy zone nearby. Alloys with a wide freezing temperature range are more susceptible. In arc welding, a suitably designed filler metal can be used to eliminate liquation cracking. A simple criterion was proposed by Kou and coworkers and verified experimentally [111]. It states that cracks occur if the fraction solid in the weld-metal is higher than that in the base-metal after the fraction solid reaches about 0.3. This criterion has been verified for Al and Mg alloys [111,112].

2.3.3. Composition change

Volatile alloying elements may selectively vaporize from the molten pool during additive manufacturing [113–117]. Different alloying elements vaporize at different rates at a given temperature. As a result, the chemical composition of the part can differ from that of the feedstock [113–117]. The rate of vaporization of an alloying element is affected by its vapor pressure above the liquid alloy,

which depends on the local temperature and the composition of the alloy. Loss of alloying elements and the composition change affect the microstructure, corrosion resistance, and mechanical properties of parts. Magnesium and zinc in aluminum alloys, chromium and manganese in steels, chromium in nickel alloys, and aluminum in titanium alloys are known to suffer from a significant change in composition (Fig. 2.3 (c)) during additive manufacturing [118].

The observed composition change [118] of alloying element i, Δ%i, can be related to its rate of evaporation through the following mass balance.

$$\Delta\%i = 100\, J_i\, A/(\rho v) \tag{6}$$

where J_i is the vaporization rate of an element i per unit surface area, A is the surface area, ρ is the density of the weld metal, and v is the volume of the alloy melted per unit time. The vaporization rate (J_i) is given by the Langmuir equation [118]:

$$J_i = \lambda\, P_i/\sqrt{2\pi\, M_i\, R\, T} \tag{7}$$

where λ is a positive fraction that is related to the recondensation of the vaporized species that depends on the total pressure, P_i is the equilibrium vapor pressure of i, M_i is the molecular weight of i, R is the gas constant, and T is the temperature. The value of λ is close to 1 at very low ambient pressures used typically when an electron beam is used as a heat source. When a laser beam is used and the ambient pressure is 1 atmosphere, a value of much lower than 1 is appropriate. The rate of evaporation per unit area depends on local temperature and varies spatially.

2.3.4. Lack of fusion voids

Lack of fusion voids [119–123] significantly degrade the tensile properties of parts and often lead to part rejection. Insufficient fusional bonding between adjacent tracks or successive layers may result in gaps between deposits known as the lack of fusion voids [119–123]. The undesirable space between adjacent tracks and successive layers is commonly attributed to insufficient feedstock melting as a result of incorrect process variable-alloy combinations. A heat source with low heat input, inappropriately fast scanning speed, thick layers, or high hatch spacing can result in such defects. Assuming that the lack of fusion is caused solely by a lack of overlap of fusion zones in adjacent tracks and layers, the geometric criteria (Fig. 2.3 (d)) for the lack of fusion have been proposed as follows [124]:

$$(H/W)^2 + (L/D)^2 \le 1 \tag{8}$$

where H is the hatch spacing, W is melt-pool width, L is layer thickness, and D is melt-pool depth. The above equation indicates that if the width and the depth of the fusion zone are both 41.4% larger than the hatch spacing and layer thickness, respectively, the lack of fusion defects do not form.

2.3.5. Porosity

Hydrogen, oxygen, and nitrogen are frequently present in trace amounts in the environment, and they are soluble in the alloys to varying degrees. Molten aluminum alloys, for example, absorb varying amounts of all of these gases from the atmosphere. Hydrogen is more soluble in liquid aluminum and magnesium than in solid phases. Hydrogen and nitrogen also dissolve in steels and can be trapped as porosity in solid alloys. In addition, shielding gas can be entrapped inside the molten pool and result in gas porosity [125–129]. Gas entrapped inside powders made by gas atomization can also cause gas porosity [125–129]. During the additive manufacturing processes, ambient gases may also dissolve in the part. For example, hydrogen, nitrogen, and oxygen, present at low concentrations in the environment may dissolve [130] in the fusion zone:

$$\frac{1}{2}\, G_2 = \underline{G} \tag{9}$$

$$a_G = K_{eq}\, (p_{G_2})^{1/2} \tag{10}$$

where G_2 is a diatomic gas such as hydrogen, nitrogen, and oxygen, p_{G2} is the partial pressure of the gas, a_G is the activity of the dissolved species in the alloy. The local concentration of dissolved gas can be found from the activity versus composition relation. When the ambient environment contains a plasma consisting of diatomic gases, dissociated monatomic species in their ionic, excited, and ground states, and electrons, the extent of dissolution of the gases [131] is significantly higher than that predicted by equation (10). The theory and the calculation procedure are available in the literature on fusion welding [131].

If the gas bubbles can escape from the molten pool before its solidification, gas porosities do not form. The escape of the bubbles depends on the size of the fusion zone, the thermophysical properties of the alloy, and process parameters. Bubbles can move within the fusion zone at the prevailing velocity of the liquid metal. Furthermore, the buoyancy force causes the bubbles to rise. The rising velocity (u) of spherical bubbles can be estimated roughly using the Stokes law, which is valid for low Reynolds numbers (<2) and is given by:

$$u = 2\, r^2\, \Delta\rho\, g/(9\mu) \tag{11}$$

where r is the radius of the bubble, Δρ is the density difference between the liquid and the gas bubble, g is the acceleration due to gravity, and μ is the viscosity of the liquid. The size of the bubble, as well as the time available for bubble growth and escape, are important factors in the formation of porosity. Low liquid viscosity and large bubble radius increase the likelihood of bubbles escaping

from the fusion zone. Rapid cooling, on the other hand, gives bubbles less time to escape.

Alloys can vaporize during additive manufacturing with a high-power density laser or electron beam. The recoil pressure produced by the vapors displaces the liquid metal and forms a vapor cavity, called a keyhole [132–136]. Keyholes are often unstable and the lower portion of the keyhole may collapse [134]. A portion of the vapors from the collapsed keyhole is trapped within the liquid pool. If the vapor packet fails to escape the molten pool before it solidifies, keyhole porosities form [132–136].

3. Control of grain structure, phases, and defects in steels

Printed parts of austenitic stainless steels, martensitic steels, duplex stainless steels, and other steels often exhibit long columnar grains that result in poor tensile properties. In addition, they form various phases that affect the mechanical properties. Cracking, lack of fusion, porosity, and composition change due to selective vaporization of the alloying elements are also common in printed steel parts. Table 3.1 provides a selected examples of controlling grain structure, phases, and defects in additively manufactured steel parts. The control strategies for each type of steels are reviewed in this section.

3.1. Austenitic stainless steels

Austenitic stainless steels contain high concentrations of chromium (>17 wt%) and appreciable amounts of nickel (typically 8%) and/or manganese to stabilize austenite. They are widely used in chemical, nuclear, and oil and gas industries for their excellent

Table 3.1
Selected examples of controlling grain structure, phases, and defects in additively manufactured steel parts.

Objective	Alloy	AM process	Description of control strategy	References
Control of grain structure	SS 316	PBF-L	Grain orientation was changed from the usual ⟨0 0 1⟩ to ⟨1 1 0⟩ using small hatch spacings and high laser power	[155]
	H13 tool steel	PBF-L	Low heat input attained by reducing the heat source power and rapid scanning increased the cooling rates and decreased the grain size and dendritic arm spacing	[171,177]
	CrNiMo low alloy steel	PBF-L	Grain size of the cellular solidification structure was reduced using faster scanning	[192]
	Reduced activation ferritic-martensitic steel	PBF-L	Grain structure was controlled by adjusting the local temperature gradient by implementing different scanning strategies	[193]
	High-strength low alloy steel	DED-GMA	SiC particles were added as grain refiners to refine the grains	[188]
	18-Ni 300 Maraging steel	PBF-L	Coarsening of grains was observed at higher heat treatment times and temperatures	[204]
	15–5PH stainless steel	PBF-L	Different scanning strategies were used to control the temperature gradient and cooling rates to refine grains	[218]
	Duplex DSS 2507	PBF-L	Rapid scanning reduced the grain size	[229]
	22Cr duplex steel	PBF-L	Low heat input resulted in high cooling rates and small grains	[221]
	ODS steel	PBF-L	An addition of 5 wt% yttria significantly refined the grain	[251]
	ODS steel	PBF-L	High melting point tellurium nanoparticles were used to refine the grains since they promoted heterogeneous nucleation	[252]
Control of phases	SS 316	DED-L	The microsegregation in the intercellular regions resulted in the enrichment of chromium and molybdenum both of which stabilized ferrite	[139,143]
	SS 316	PBF-L	High cooling rates resulted in a very fine microstructure that was claimed to hinder martensite formation	[147]
	H13 tool steel	DED-L	Post-process heat treatment was used to temper the martensite and improve the toughness	[178]
	18-Ni 300 Maraging steel	PBF-L	The size, amount, and distribution of the intermetallic compounds were controlled by adjusting the heat treatment temperatures and times	[199,202]
	15–5PH stainless steel	PBF-L	Post-process heat treatment was used in adjusting the shape, size, and quantity of the precipitates	[219]
	SHER120-G Maraging steel	DED-GMA	An addition of 0.39 wt% of copper significantly refined the martensitic lath size	[212,213]
	ODS steel	PBF-L	Amount of dispersed oxides were controlled by adjusting the heat input, adding oxide-forming elements, and changing the chemical composition	[250]
Control of defects	H13 tool steel	PBF-L	Solidification cracking was minimized by adjusting the laser power, scanning speed, layer thickness, and hatch spacing	[174]
	Duplex stainless steel	PBF-L	The lack of fusion defects were mitigated using higher power	[223]
	Fe-14Cr stainless steel	PBF-L	The lack of fusion was controlled by increasing the heat input at a higher laser power	[259]
	TRIP steel	PBF-L	The lack of fusion was minimized by increasing the heat input	[272]
	H13 tool steel	PBF-L	The lack of fusion defects were minimized by increasing the energy density of the laser beam	[174]
	Maraging steel	PBF-L	Scanning with a shorter track length reduced the lack of fusion	[210]
	2205 duplex steel	DED-GMA	Gas porosity was reduced at high interlayer temperature	[233]
	CrNiMo low alloy steel	PBF-L	The higher energy density of the laser beam reduced gas porosity	[187]
	H13 tool steel	DED-L	Mn loss decreased with a reduction in laser energy input	[176]

corrosion and oxidation resistance, fabricability, and good mechanical properties. Their high thermal expansion coefficient precludes their use in some power plants and other applications.

3.1.1. Microstructure control

Additively manufactured austenitic stainless steels such as 316 L and 304 contain mainly austenite [137] with or without a small amount of retained δ ferrite [138,139] and/or martensite [140]. For the solidification of austenitic stainless steels, the solidification mode depends on the nickel and chromium equivalents of the alloys and solidifies primarily in either ferrite–austenite or austenite mode [141,142]. Typical microstructures of austenitic stainless steels in powder bed fusion and directed energy deposition are somewhat different from each other. In the directed energy deposition of 316L stainless steel, the microsegregation in the intercellular regions results in the enrichment of chromium and molybdenum both of which stabilize ferrite, and between 8 and 10% ferrite has been observed in the microstructure [139,143]. Segregation of ferrite stabilizers also occurs in powder bed fusion. However, the cooling rates are high in the powder bed fusion process and the extent of segregation is insufficient to stabilize ferrite [144,145], and ferrite is not commonly observed in the microstructure. Typical microstructures of austenitic stainless steel components made by additive manufacturing are compared with the microstructural features of other steels in Fig. 3.1.1. Because of the high cooling rates encountered in powder bed fusion, the microstructures are typically quite fine [146]. PBF-L produced 316L has a very fine microstructure that is claimed to hinder martensite formation [147]. SS 316L components produced by powder bed fusion show high elongation at fracture because of twinning-induced plasticity [148]. The typical microstructure exhibits several important features in different length scales. The solidification microstructure can be columnar or equiaxed or a mixture of both at the submillimeter scale.
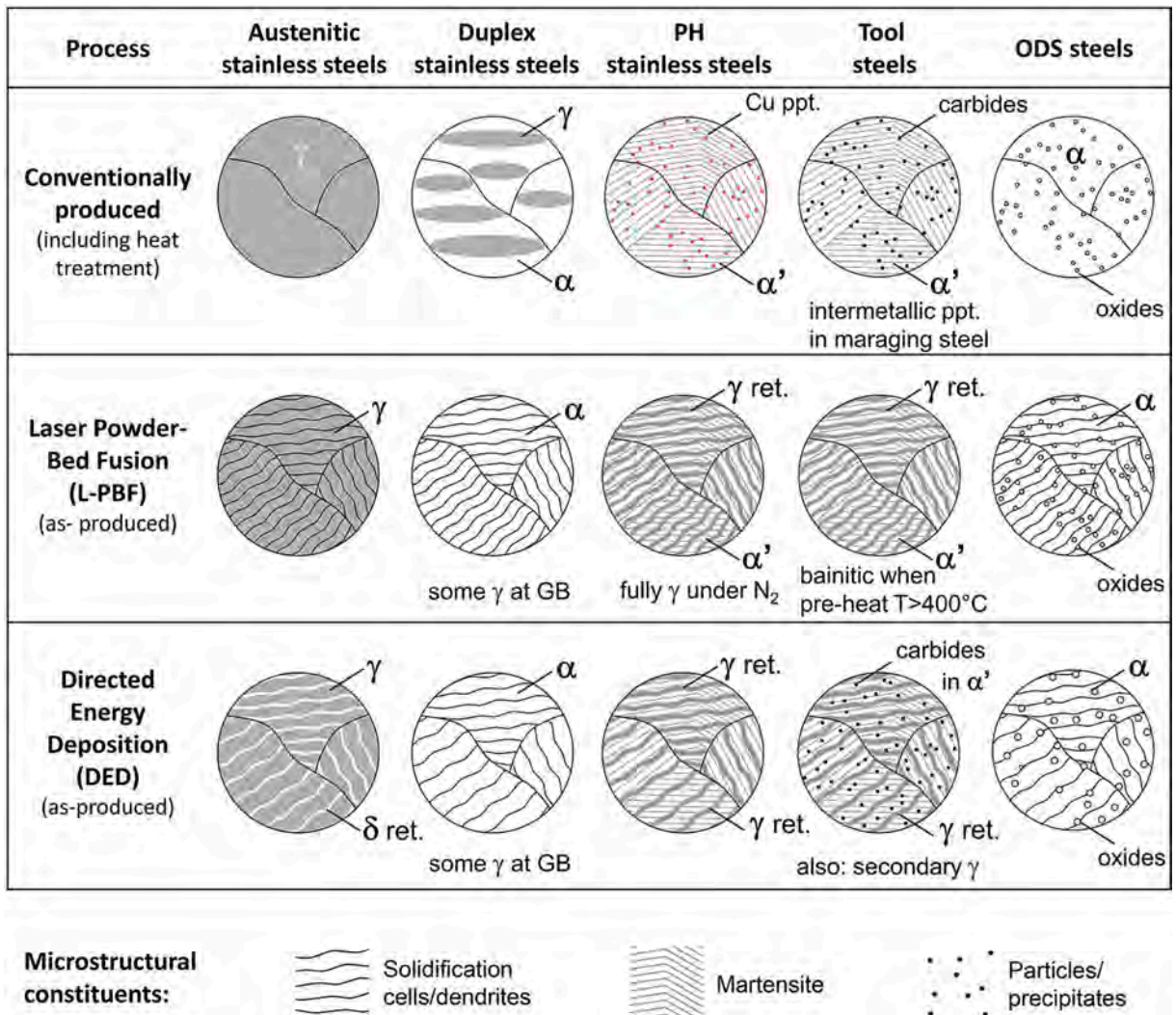
Fig. 3.1.1. Typical microstructures [137] of the different steels produced conventionally and after additive manufacturing. Depending on processing conditions, different microstructures may be observed after AM. ppt.: precipitates, ret.: retained, α: ferrite, bcc, α': martensite bcc/bct, γ: austenite, fcc.

The subgrain features include numerous very fine cells, of dimensions typically smaller than a micrometer [145] and cell boundaries of the order of about 100 nm with the boundaries lined with networks of dislocations. The size of the oxide inclusions is typically 50 nm but can vary significantly in the range between 5 nm to micrometers and chemical composition vary from spinels to many other complex compositions depending on the alloy composition and processing conditions. Fig. 3.1.2 shows important features of additively manufactured 316L stainless steel at different length scales [145].

Although the microstructures of these additively manufactured steels are dominated by austenite, it is the hierarchical microstructure [145,146] that has attracted much attention because the microstructure is thought to be the underlying source of the unique combination of outstanding properties not achieved in conventionally made parts. In most alloys, the improvements in the strength of an alloy resulting from heat treatment are accompanied by a decrease in ductility. The additive manufacturing of austenitic stainless steel is an exception because a higher strength is achieved without sacrificing ductility [145]. These favorable properties can further be improved through metallurgical post-processing of DED-wire 304L SS for increased ductility and reduced AM texture [149,150]. Optimizing the features of the hierarchical microstructure is an important goal to achieve superior properties in austenitic stainless steels.

Wang et al. suggested that the microstructural features can be controlled by adjusting process parameters [145]. Control of cooling rates and temperature gradients is possible by adjusting power, scanning speed, and scanning pattern. Although simultaneous improvements in both strength and ductility not achievable in conventional processing is an exciting possibility, more work is needed to correlate process variables with the many features of the hierarchical microstructure excluding the parameter space where common defects compromise properties.

3.1.2. Grain structure control

Elongated columnar grains [151,152] in the building direction are common in the powder bed fusion of austenitic stainless steels such as SS304. High volumetric energy density was found to be responsible for strong texture in [100] direction in parts made with SS316 austenitic stainless steel [153]. However, at lower volumetric energy densities, a multicomponent texture was obtained which was attributed to the high nucleation rate and the deviation of grain orientation from the [100] easy growth direction [153]. Some austenitic stainless steels such as 304L often form annealing twins during additive manufacturing because of their low stacking fault energy [153].

During solidification of cubic materials, the dendrites grow along the dominant heat flow direction perpendicular to the local fusion zone curvature along the $\langle 001 \rangle$ direction which is the fastest growth direction. As a result, a crystallographic texture with the $\langle 001 \rangle$ direction along the build direction is commonly observed [154]. The heat flow direction varies locally depending on the shape of the fusion zone although most heat is extracted to the base plate for small components. Since the shape of the fusion zone can be controlled by adjusting process parameters, particularly scan parameters and alloy composition including the concentrations of the surface-active elements, the texture can be controlled. It has been shown [155] that the crystallographic texture can be changed from the usual $\langle 001 \rangle$ to $\langle 110 \rangle$ using small hatch spacings and high laser power. It has also been shown that texture can be controlled by scanning strategy in cubic alloys [156]. Scanning strategy can also avoid anisotropy of most mechanical properties. Grain size and topology also depend on the process variables and alloy properties and affect both strength and ductility. Although control of grain structure and topology can be implemented by controlling process parameters, care must be taken to avoid defects that are common in additively manufactured parts.
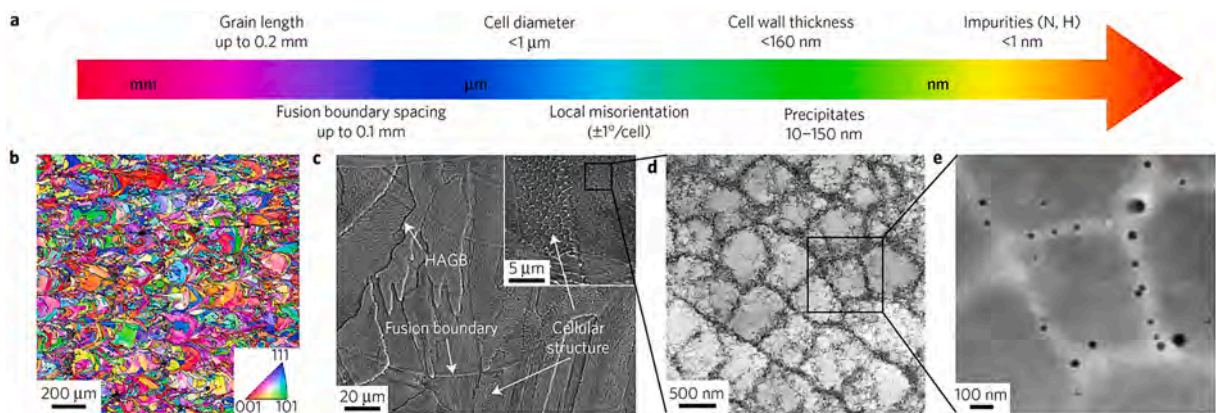
Fig. 3.1.2. Microstructural features of a 316L austenitic stainless steel part at various length scales. a) Various length scales of the microstructural features. b) EBSD inverse pole figure mapping showing the grain orientations. C) SEM image of the cross-section showing high-angle grain boundaries, fusion boundaries, and the cellular solidification structure. d) Bright-field TEM image of the cellular structure showing dislocation networks in the cell boundaries. e) high-angle annular dark-field scanning TEM image of the solidification cells showing oxide particles [145]. The figure is adapted from reference [137].

3.1.3. Control of defects

Common defects in parts made using austenitic stainless steel parts include porosity and lack of fusion, residual stress and distortion, and anisotropy [2]. Pores in the components often originate from dissolved oxygen and nitrogen in the powder and wire feedstocks [153]. These pores are typically round in shape and small, of the order of a few tens of micrometers in diameter and can be controlled by the way the feedstocks are made. Also, some alloys are more susceptible to gas porosity because of their high solubility of common impurities such as oxygen, nitrogen, and hydrogen in the feedstock. Larger voids typically deviate from the spherical shape and may appear from a lack of fusion [118,157] or instability of a keyhole [158]. They affect fatigue property [159,160], corrosion resistance [161,162], and other mechanical properties such as wear resistance [163,164]. Residual stresses arise in additively manufactured parts because of substantial temperature gradients and repeated heating and cooling that varies with location within the part. Both process variables and alloy properties affect residual stresses and distortion. While preventing these defects during the manufacturing of parts is desirable, often post-processing is a practical way to alleviate these defects. Hot isostatic pressing is effective in removing small gas porosities to a large extent.

Appropriate standards for the feedstock, particularly the powder manufacturing method, and limits on concentrations of oxygen, nitrogen, and hydrogen would be beneficial in preventing small gas-induced pores in parts. Lack of fusion defects are prevented by large fusion zone sizes, smaller hatch spacing, and thinner layer thickness, all of which promote sufficient overlap of the fusion zone between different tracks in a layer and between different layers [157]. However, the build time increases when tracks are closely spaced and when thinner layers are used. So, increasing heat source power and reducing scanning speed can also increase the overlap of the fusion zone between adjacent tracks and layers and increase part density. If large pores are found to originate from the keyhole instability, process variables have to be adjusted to enhance the stability of the keyhole. Vigorous recirculation of large melt pools owing to Marangoni convection has been suggested as a mechanism for the removal of porosities in austenitic steel processed using high volumetric energy density [153]. Although there is no definitive protocol for reducing keyhole instability in austenitic stainless steels, previous work in other alloy systems indicates that increasing power density may result in increased stability of the keyhole and reduce keyhole-induced porosity [158]. It was found that the density of the additively manufactured parts was higher when a higher volumetric energy density was used [153]. Previous works on the mitigation of residual stresses and strains in additive manufacturing show significant benefits from preheating. A scanning strategy is also used to reduce residual stresses and distortion as well as to control grain structure [3]. In addition, heat treatment after the component is made is also used to reduce residual stresses and distortion and reduce property anisotropy [3]. Although post-processing is widely used to improve the microstructure and properties of additively manufactured austenitic stainless steel components, optimization of heat treatment parameters is still undertaken by trial and error guided by the previous work on the heat treatment of the conventionally manufactured cast and wrought materials.

3.2. Martensitic steels

This section reviews two categories of martensitic steels (1) steels that utilize the martensitic transformation as the dominant strengthening mechanism and (2) steels that develop low carbon, soft martensite structure but are mainly strengthened via subsequent aging reactions by forming intermetallic precipitates [165]. The first category includes tool steels, low alloy steels, and ferritic-martensitic steels, while those in the second group are maraging steels and precipitation hardening (PH) steels [165]. These steels are introduced below.

- Tool steels [56,166–186] are high carbon steels containing carbide-forming elements such as Cr, V, Mo, Nb, and W. These steels are used to make tools such as drills, punches, dies, and other cutting tools. These steels generally exhibit a hard martensite matrix with dispersed carbides that provide excellent wear resistance and hardness. Although several tool steels are used, H13 tool steel is the most common in additive manufacturing. We have focused on H13 tool steel in this review.
- Low alloy steels [42,187–191] typically contain Ni, Cr, and Mo and carbon content between 0.3 and 0.4 wt%. Commonly used low alloy steels are 4140, 4340, and HSLA 100. They are used for machine parts, connecting rods, and crankshafts. Rapid cooling during AM forms martensite and carbides of Ni, Cr, and Mo that provide high hardness.
- Steels with ferritic-martensitic [44,192–197] crystal structures have low thermal expansion coefficients, high thermal conductivity, and high resistance to void swelling which make these steels popular in both fossil fuel and nuclear power industries. These steels contain from 2% to 12 % Cr and are tempered to transform the martensite into tempered martensite and ferrite. Grade 91 (9% Cr) and HT-9 (12% Cr) are the most common ferritic-martensitic steels for AM.
- Maraging steels [198–213] are strengthened by the precipitation of one or more nano-scale intermetallic compounds in a soft Fe-Ni martensite matrix. These steels have excellent toughness where the soft martensite matrix provides the ductility and the high strength originates because of the presence of the intermetallic compounds. In addition, they have good weldability and printability without hydrogen-induced cracking issues. These properties make maraging steels suitable for airframe structural applications (landing gear) and various dies and molds for metal forming. The 18 Ni-300 maraging steel is the most commonly used and discussed in this review.
- Precipitation hardened (PH) steels [214–220] form a soft martensitic structure that allows components to be easily formed or machined and provides good ductility. Their strength is developed via precipitation hardening of fine intermetallic phases during aging treatments after deposition. The 17–4 PH, 15–5 PH, and 13–8 PH are the most commonly used PH stainless steel.

For these martensitic steels, the mechanical properties are largely contributed by the formation of martensitic phases and secondary phases such as intermetallic compounds. Therefore, most of the research has been performed to control these phases by adjusting the

processing conditions and performing post-process heat treatment at different aging times and temperatures. A relatively lower volume of literature is available on controlling grain structures of these steels by adjusting process variables such as heat input. Primarily, these steels are susceptible to lack of fusion, porosity, and cracking and several attempts have been made to control these defects. This section reviews the common strategies to control grain structure, phases, and defects in martensitic steels.

3.2.1. Control of grain structure

Martensitic steels primarily exhibit cellular or dendritic grain structure. The size of cellular grains and the arm spacings of dendrites are controlled by adjusting the processing conditions. Laser power, scanning speed, preheating temperature, layer thickness, and hatch spacing are adjusted to alter the temperature gradient, solidification growth rates, and cooling rates to control the solidification morphologies and grain structure. For H13 tool steels, the grain structure consists of a cellular solidification microstructure with intercellular carbides or dendritic morphology [175]. The size of grains with cellular morphology and the arm spacing of dendritic structures can be controlled by adjusting the process variables [171,176,177]. For example, low heat input attained by reducing the heat source power and rapid scanning increases the cooling rates and decreases the grain size and dendritic arm spacing [171,176,177]. The grain size of the cellular solidification structure during PBF-L of H13 tool steel can be significantly reduced by printing the parts using faster scanning speeds [171]. Finer grains improve the mechanical properties of parts. A similar approach was also used to control grain structure for other alloys such as PBF-L of CrNiMo low alloy steel and PBF-L of a reduced activation ferritic-martensitic steel [192]. Fig. 3.2.1 shows the grain structures [192] determined using EBSD for a reduced activation ferritic-martensitic steel component made using two energy densities of the laser beam during PBF-L. Components were produced using a zig-zag scanning pattern and a 90° rotation of the scan direction between layers [192]. The sample produced with a lower energy density displayed a "checkerboard" pattern when viewed from above (Fig. 3.2.1 (a)) and stacked rows of melt pool regions of high-aspect-ratio in the front view (Fig. 3.2.1 (b)). In contrast, the sample produced using high energy density was characterized by a more random and equiaxed microstructure in the top view (Fig. 3.2.1 (c)) with a stack of melt pools of lower aspect ratios (Fig. 3.2.1 (d)). Both samples revealed a microstructure consisting of two different grain sizes [192]. The same group of authors also showed that grain structure during PBF-L of a reduced activation ferritic-martensitic steel can be controlled by adjusting the local temperature gradient by implementing different scanning strategies [193].

Apart from the adjustment of processing conditions to refine grains, a few attempts have been made to add inoculants to refine grains during AM of martensitic steels. For example, SiC particles were added during DED-GMA of high-strength low alloy steel to refine the grains [188]. However, the size and amount of the particles were determined by trials. A comprehensive theoretical and experimental investigation is needed to make this method commercially viable.

During the solidification of maraging steels, the primary solid γ phase forms at the interface between the solid and liquid phases along the preferential ⟨001⟩ solidification direction [210]. During further cooling, at temperatures lower than the martensite start temperature (approximately 200 °C), α phase martensite starts forming within the prior γ phase grain boundaries. The prior γ phase grain morphology [204,207] is either cellular (Fig. 3.2.2 (a)) or a mixture of cellular and dendritic structures (Fig. 3.2.2 (b)). For maraging steels, the mechanical properties are largely affected by the martensite and precipitates of intermetallic compounds formed during aging. Therefore, more research has been done to control the phases (see Section 3.2.2) compared to that for controlling the
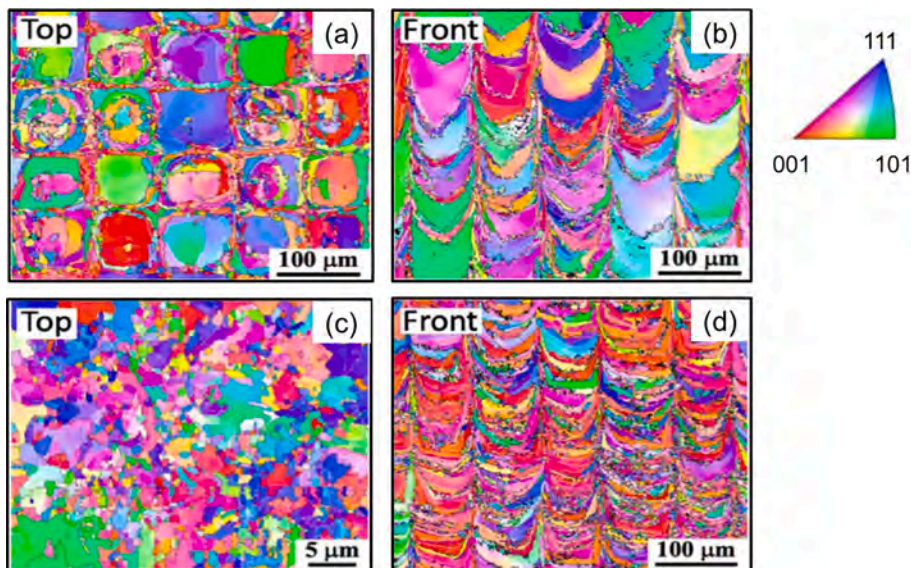
Fig. 3.2.1. Grain structures characterized by EBSD for a reduced activation ferritic-martensitic steel made by PBF-L [192]. Grain structures are shown at (a) top and (b) front views for the sample made using 98 J/mm³ energy density and at (c) top and (d) front views for the sample made using 209 J/mm³ energy density.
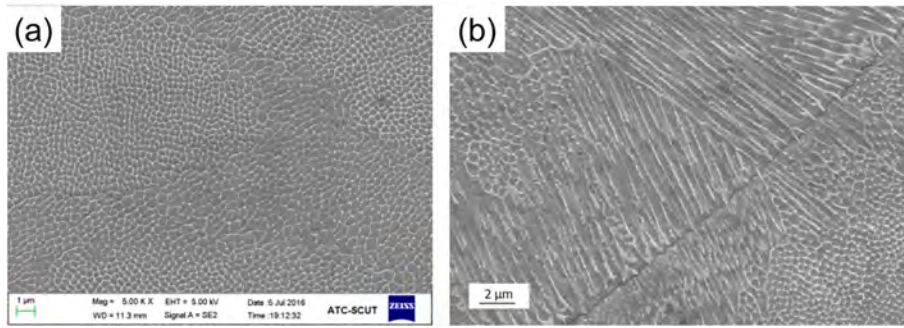
Fig. 3.2.2. SEM images showing the (a) cellular [207] and (b) cellular and dendritic [204] microstructure in 18Ni-300 maraging steel parts made by PBF-L.

grain structure. A few examples of controlling grain structure in maraging steels include the application of post-process heat treatment [204]. In this study, different combinations of heat treatment temperatures and times were used to control the size of the cellular grains. Coarsening of grains was observed at higher heat treatment times and temperatures [204]. High flow rates of the shielding gas during additive manufacturing of maraging steel resulted in rapid cooling and refined grains [209].

Similar to the maraging steels, post-process heat treatment is also used to control the grain structure of additively manufactured PH steels. For example, Fig. 3.2.3 shows that the post-process heat treatment of 15–5PH stainless steel parts fabricated by DED-L [217] homogenized the grain structure and improved the mechanical properties. Grain structure during PBF-L of 15–5PH stainless steel parts can be controlled by adjusting the local temperature gradient by implementing different scanning strategies [218]. In this study, four different scanning strategies were used (Fig. 3.2.4). The island scanning strategy with the small hatch length was the most effective in refining the grains. However, more work is needed to find a quantitative basis for selecting an appropriate scanning strategy and processing conditions to achieve the desired grain structure.
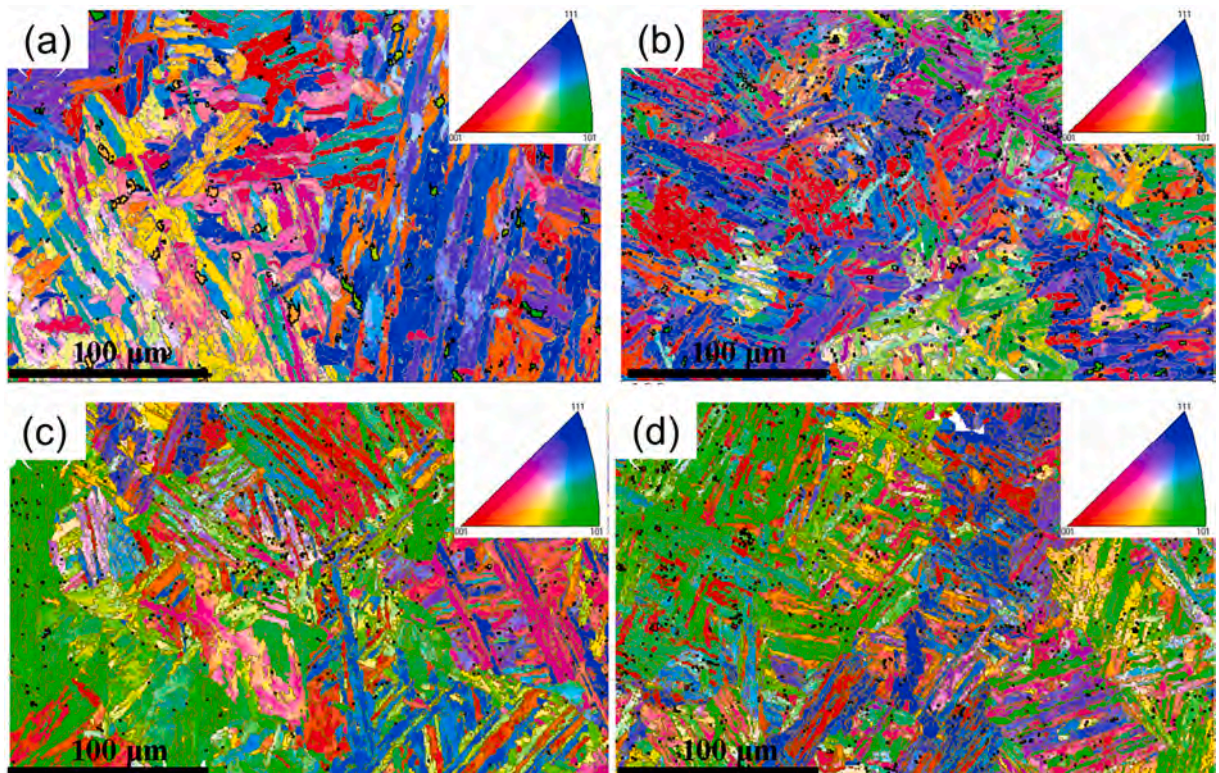
Fig. 3.2.3. EBSD orientation maps showing grains structures of 15–5PH stainless steel parts fabricated by DED-L [217]. Grain structures are shown for the as-fabricated part on (a) horizontal plane and (b) transverse plane and for the heat-treated part on (a) horizontal plane and (b) transverse plane.
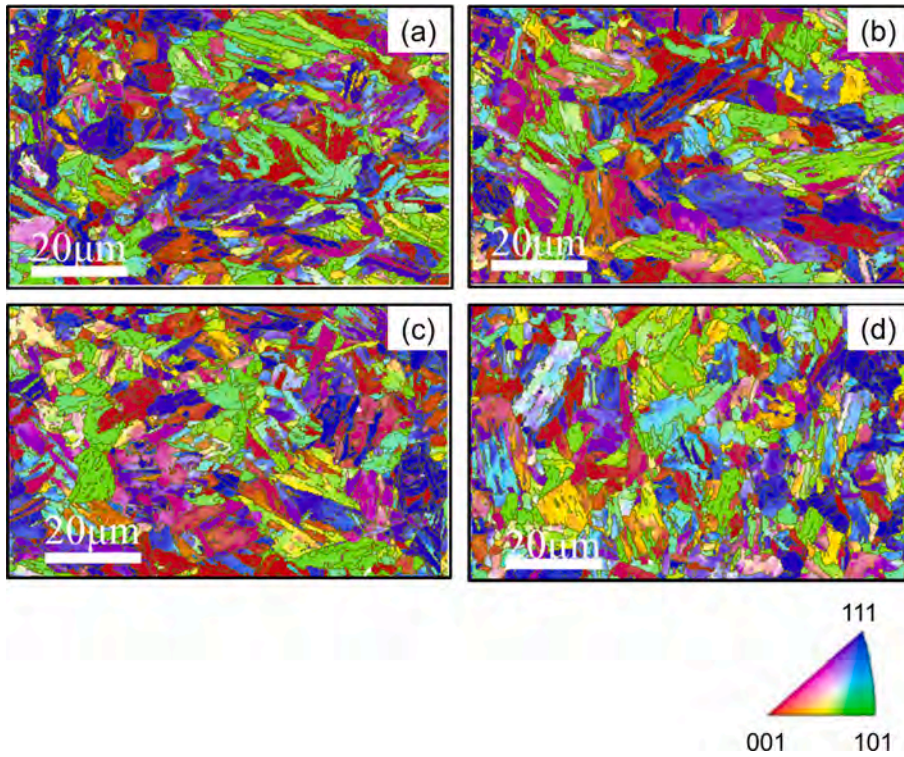
Fig. 3.2.4. EBSD orientation maps showing grains structures of 15–5PH stainless steel parts fabricated by PBF-L [218] with (a) unidirectional, (b) bidirectional, (c) cross-directional, and (d) island scanning strategies.

3.2.2. Control of phases

Tool steels, low alloy steels, and ferritic-martensitic steels form hard martensite due to the rapid cooling rates during AM. The martensite increases the strength and hardness but significantly reduces the ductility and toughness. Post-process heat treatment is often employed to temper the martensite and improve the toughness [173,178]. For example, Fig. 3.2.5 shows the change in the microstructure of the H13 part made by PBF-L at different heat treatment temperatures [173]. When the temperature is between 350
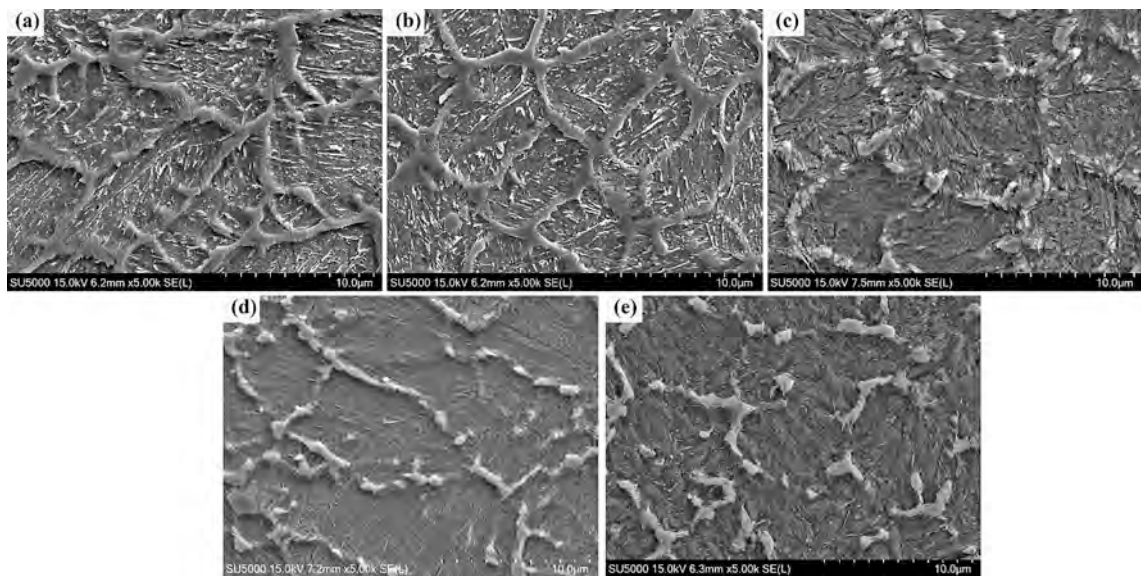
Fig. 3.2.5. Microstructure of H13 tool steel parts produced by DED-L and heat-treated at different temperatures: (a) 350C, (b) 450C, (c) 550C, (d) 600C, and (e) 650C. Figure courtesy: Professor Min Zhang from Soochow University, China.

and 450 °C, there was no big difference between the heat-treated samples. Only a small fraction of martensite was transformed into tempered martensite and formed Cr and V-rich carbides. However, when the tempering temperature increased, more carbon precipitated and reacted with Cr and V forming alloy carbides (Mo_2C, VC, Cr_7C_3, and $Cr_{23}C_6$). These carbides significantly improve toughness [173]. Post-process heat treatment is used to temper martensite and improve the toughness of martensitic steels. However, post-process heat treatment adds an extra cost and is thus often not desirable.

Tempering of martensite also occurs because of multiple heating and cooling cycles during the deposition of many layers and hatches during AM. This process is often called in-situ heat treatment. The martensite formed in a deposited layer may be transformed partially or fully to tempered martensite during the deposition of subsequent layers. This phenomenon has been reported for DED-L of H13 tool steels [179–182], DED-GMA of a high strength low alloy steel [42], and DED-L of grade 91 steel [194]. It is evident that the extent of transformation of martensite into tempered martensite is affected by the local thermal cycles [179,180] and thus can be controlled by adjusting the heat input, layer thickness, and scanning strategies.

For maraging and precipitation-hardened steels the mechanical properties of the parts are affected by the size, amount, and distributions of the secondary phases such as micro and nanoscale intermetallic compounds. As-deposited maraging steel contains a soft, heavily dislocated iron-nickel lath (untwinned) martensite. Subsequent aging produces a fine dispersion of intermetallic phases (Fig. 3.2.6) along dislocations left by the martensitic transformation [201,205]. Additional alloying agents include Mo, which forms a Ni_3Mo intermetallic phase, and Al and Ti, which are incorporated into a $Ni_3(Ti, Al)$ intermetallic precipitate (Fig. 3.2.6). Co does not form precipitates but raises the martensite start temperature and promotes the formation of Ni_3Mo by lowering the solubility of Mo in the matrix [201,205]. Fig. 3.2.7 (a) and (b) show that the Ti and Ni enriched precipitates are spherical but both spherical and irregular shapes are observed for Mo enriched precipitates [202]. The size, amount, and distribution of the intermetallic compounds are controlled by adjusting the heat treatment temperatures and times [199,202,208,211]. For example, an increase in the heat treatment temperature supports the precipitation process and increases the size of the precipitates (Fig. 3.2.7 (c)) which significantly affects the
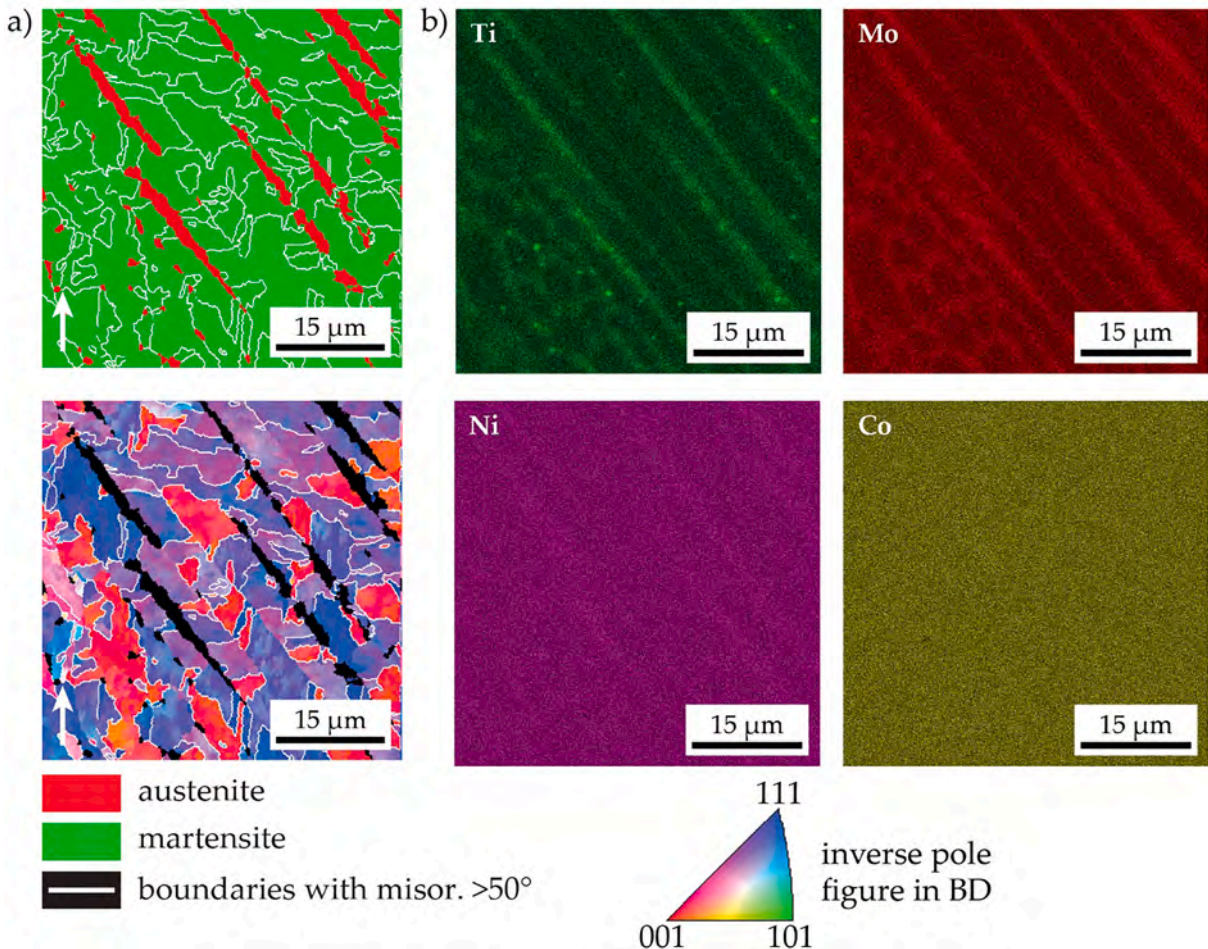
Fig. 3.2.6. A high-magnification EBSD and corresponding EDS element maps of various elements for an 18Ni-300 maraging steel part made by DED-L. The phase map in figure (a) indicates the location of the retained austenite in the interdendritic areas. Figure (b) shows the enrichment of Ti, Mo, and Ni in these regions of retained austenite. Co does not generally form intermetallic compounds but alters the martensitic start temperature [205].
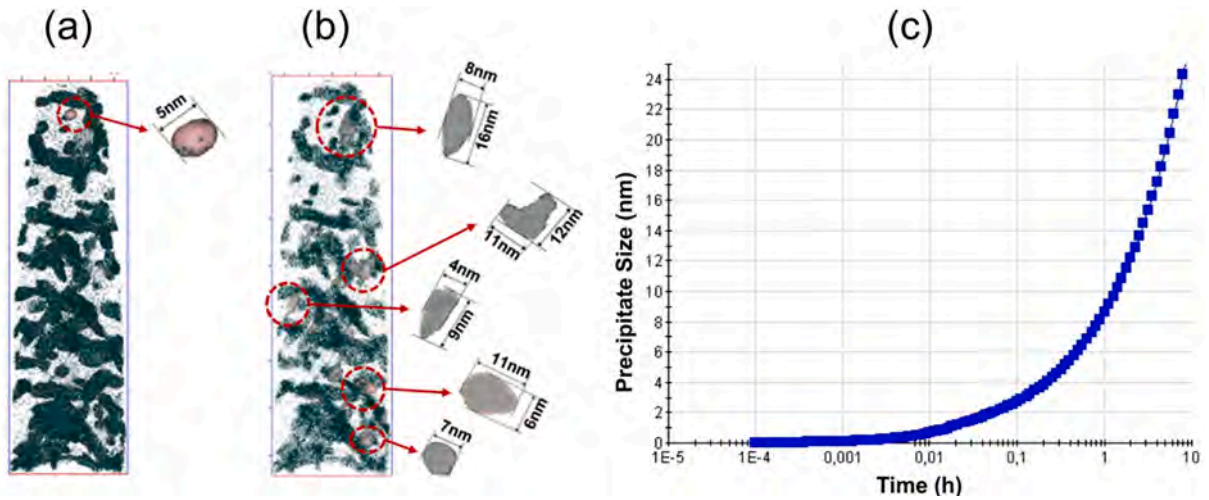
Fig. 3.2.7. Size of (a) spherical Ti and Ni enriched precipitates and (b) spherical and irregular-shaped Mo enriched precipitates. (c) An increase in the average size of the precipitates with the aging time at 510 °C aging temperature. All figures are for 18Ni-300 maraging steel parts made by PBF-L [202].

mechanical properties [202]. Controlling the time and temperature of the post-process heat treatment was also helpful in adjusting the shape, size, and quantity of the precipitates and thus achieving the desired properties of 15–5 PH steel parts made by powder bed fusion [219]. However, care should be taken in selecting the range of heat treatment temperatures and times because excessive heat treatment is known to cause the decomposition of the martensite and reversion to austenite for maraging steels [206].
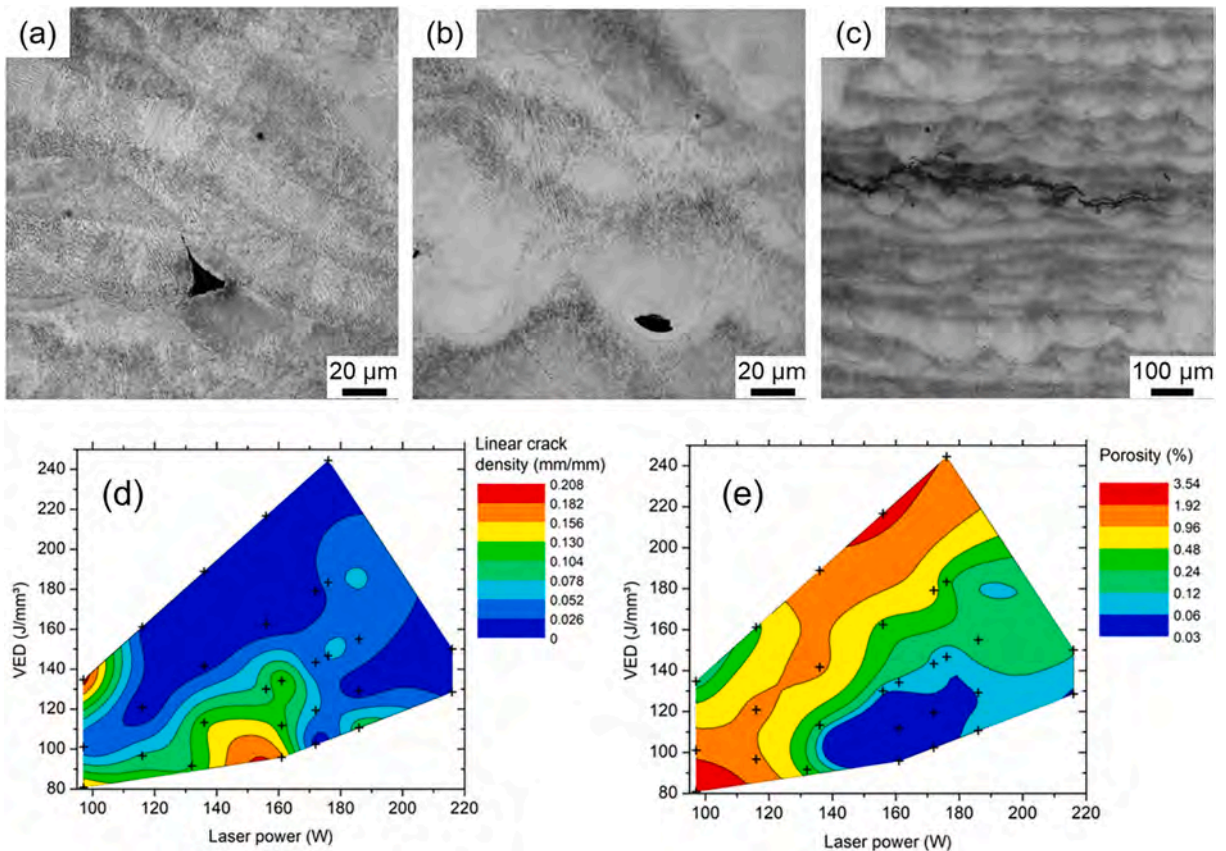
Fig. 3.2.8. Defects in H13 tool steel parts made by PBF-L (a) lack of fusion between melt pools, (b) gas pores within melt pool, and (c) crack along deposition planes [174]. Process maps show how to control (d) cracking and (e) porosity by adjusting the process parameters [174].

Recently, it has been reported [212,213] that the addition of just 0.39 wt% of copper can significantly refine the martensitic lath size during DED-GMA of maraging steels and affect the mechanical properties. However, the detailed mechanism of refining the martensitic lath is not known and needs further research.

3.2.3. Control of defects

Martensitic steels are susceptible to composition change, lack of fusion, porosity, and cracking. Composition change occurs due to the loss of alloying elements due to their selective vaporization during AM. For example, Mn loss [176] was observed during DED-L of H13 tool steel which was shown to decrease with a reduction in laser energy input. Solidification cracking or hot tearing is possible during AM of martensitic steels. Hydrogen-induced cracking of martensitic steels, similar to that encountered in welding processes using flux coatings contaminated by moisture and exacerbated by residual tensile stress, is possible for AM of martensitic steels owing to the presence of hard "susceptible" microstructures and residual stress. Reheat cracking, involving precipitation of carbides in grain interiors causing wedge cracking due to grain boundary sliding is also found during AM of martensitic steels. Cracking is observed in PBF-L of H13 tool steel [174], PBF-L of high-speed tool steels [184], and PBF-L of maraging steels [202]. For example, Fig. 3.2.8 shows various types of defects in PBF-L of H13 tool steel where Fig. 3.2.8 (c) shows long cracks in the printed part [174]. Such cracks were shown to be minimized [174] by adjusting the laser power, scanning speed, layer thickness, and hatch spacing (Fig. 3.2.8 (d)). Voids generated due to the lack of fusion and gas porosities degrade the mechanical properties of parts. Such defects are observed in PBF-L of H13 tool steel [174,183], maraging steels [199,200,202], 15-5PH steel [218], and 17-4PH steel [220]. For example, Fig. 3.2.8 (a) and (b) show the lack of fusion voids and gas pores, respectively, in H13 tool steel parts made by PBF-L [174]. Such voids were minimized by increasing the energy density of the laser beam (Fig. 3.2.8 (e)). The higher energy density of the laser beam also reduced porosity during PBF-L of CrNiMo low alloy steel [187]. Several attempts have also been made to minimize these defects by adjusting the process variables [200,206,209,210] for AM of maraging steels. For example, the lack of fusion voids was minimized [200] by increasing the energy density during PBF-L of 18Ni-300 maraging steel which significantly improved the density of the part (Fig. 3.2.9). The number of voids was also reduced by adjusting the scanning pattern [210]. Scanning with a shorter track length resulted in the return of the heat source to its initial position quickly, thus enhancing heat accumulation, a larger pool, and reduced lack of fusion voids.

3.3. Duplex stainless steels

Duplex stainless steels have higher concentrations of chromium (>19.5 wt%) and typically lower concentrations of nickel (3 to 8.5%) than those in austenitic stainless steels. A high concentration of chromium stabilizes the primary δ-ferrite that forms during solidification and austenite forms subsequently from ferrite during cooling. Nearly equal amounts of δ-ferrite and austenite in the microstructure of duplex stainless steels provide excellent combinations of strength and ductility. The tendency to form austenite in duplex steels is influenced by the ratio of the chromium equivalent, Cr_{eq}, and nickel equivalent, Ni_{eq}. Cr_{eq} depends on the concentration of the ferrite stabilizing elements such as Cr and Mo, and Ni_{eq} is computed from the concentrations of austenite stabilizing elements such as Ni and N. A low value of Cr_{eq}/Ni_{eq} facilitates the formation of austenite [18].

In addition to the formation of ferrite and austenite, the alloying elements also contribute to solid solution strengthening. A high concentration of nitrogen in these steels increases the tendency to both form austenite and nitride precipitates. Properties of the duplex steel parts also depend on the amount and size distribution of carbide precipitates, M_7C_3 and $M_{23}C_6$ where M is Fe or Cr. The microstructure also contains brittle intermetallic phases of Fe and Cr, such as the sigma phase (s) which is rich in iron, chromium, and molybdenum and has a tetragonal crystal structure. Duplex steels are relatively more affordable than austenitic stainless steels because of their lower nickel concentrations and they provide excellent resistance to pitting and crevice corrosion at relatively low-temperature applications in oil and gas, shipbuilding, petrochemical, and other industries.
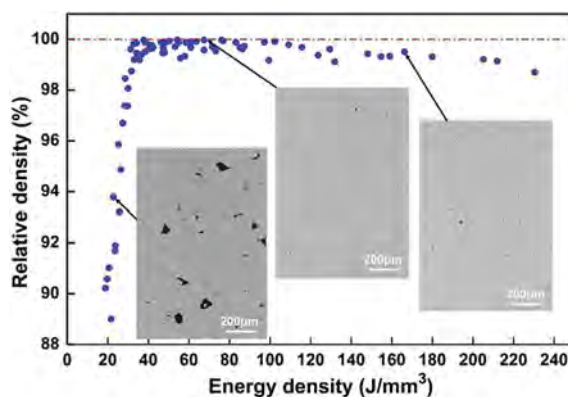
Fig. 3.2.9. Control of part density by controlling the void formation by adjusting the energy density during PBF-L of 18Ni-300 maraging steel [200]. Here energy density is represented by power/(speed × layer thickness × hatch spacing).

3.3.1. Microstructure control

During the additive manufacturing processes, the time–temperature history affects the kinetics of the transformation of δ-ferrite to austenite and therefore the proportion of the ferrite and austenite, and the resulting properties of the part. The optimum amount of austenite, about 50% in the final microstructure, requires slow cooling to provide enough time for the solid-state transformation of ferrite to austenite. During additive manufacturing, particularly powder bed fusion, the cooling rate in the 1200 to 800 °C range is too rapid to transform ferrite to the optimum amount of austenite. For example, Jiang et al. [221] studied the PBF-L of two duplex steels 22.5Cr-5.5Ni-3.5Mo-0.21 N and 25.7Cr-7.3Ni-4.4Mo-0.3 N and found nearly 100% ferrite in the microstructure. In the powder bed fusion process, the time for the transformation of δ-ferrite to austenite is insufficient to achieve 50% austenite, and the microstructure of the as-built part is composed mainly of ferrite. Fig. 3.3.1 shows the ferrite microstructure of PBF-L 2507 duplex stainless steel [222] and the EBSD shows the single-phase ferritic structure with a mosaic-type macrostructure [222]. If the steel contains significant amounts of nitrogen, nitride inclusions are also observed at the grain boundaries [223]. Post-built heat treatment is necessary at temperatures above 900 °C to achieve the necessary amount of austenite. Care must be taken to select the temperature and duration of the heat treatment to prevent significant amounts of brittle phases such as the sigma phase while forming the necessary amount of austenite. For example, Iams et al. [224] increased austenite percentage from 38.5% to 57.6% by hot isostatic pressing at 1170 ∘C and 145 MPa for 3 h after the DED of duplex 2205.

In the DED-GMA process, the heat input per unit length is higher than those of laser and electron beam based PBF and DED processes. As a result, the cooling rates of the DED-GMA process are lower than those in the PBF and DED processes. So in DED-GMA, δ-ferrite has more time to transform to austenite and higher austenite content is observed in the microstructure. Also, the brittle intermetallic phases such as the sigma phase can form during the slow cooling and the microstructure can contain coarse grains. Control of heat input is useful for achieving the desired grain structure [18] and to increase the ferrite concentration in additively manufactured duplex steel parts [225]. Eriksson et al. [226] found that the ferrite content in wire-arc duplex steel 2760 ranged between 15% and 27%, depending on the heat input. The ferrite content tended to decrease with increasing arc energy [227]. At high heat inputs, there is more time for the ferrite to transform to Widmanstatten type austenite at ferrite grain boundaries at elevated temperatures and as a result, the austenite fraction in the microstructure is high at high heat inputs. The σ phase can be prevented in the as-produced state [227] by controlling heat input. For the 2507 alloy, the predominantly ferritic microstructure in the as-produced state has good yield strength [228] and UTS of PBF-L produced part. The fracture occurs in a ductile mode and the elongation at fracture is 8%. Heat treatment at elevated temperatures such as 1200˚C leads to some σ phase precipitates [228] which makes the parts quite brittle at room temperature with only 1.8% elongation at fracture and relatively low strength which is attributed to the presence of austenite. It is possible to reach 55% austenite and 45% ferrite and > 99.5% relative density with heat treatment of the parts [137].

Where possible, adjustment of heat input may affect the proportion of ferrite and austenite in the microstructure. However, duplex steel parts produced by AM do not reach the right balance between the ferrite and austenite phases and post-process heat treatment is needed to achieve the optimum microstructure. The time and temperature of heat treatment are determined by experimental trials.

3.3.2. Grain structure control

Among the three commonly used AM processes, PBF, DED-L, and DED-GMA, the cooling rate between the liquidus and the solidus temperatures is highest in the PBF and lowest in DED-GMA. As a result, the grain sizes are the largest in DED-GMA and the smallest in PBF. The typical grain size of parts made by PBF is smaller than 10 μm which results in good strength and ductility of the parts. Also, for a given AM process, the process variables such as heat input per unit length determine the cooling rate and the average grain size. For example, Murkute et al. [229] found that during the PBF-L of DSS 2507 an increase in the scanning speed from 100 to 1000 mm/s resulted in the decrease of the average grain size from 108 to 19 μm^2. During the AM of duplex steels, ferrite forms from the liquid, and its morphology depends on the ratio of the temperature gradient (G) to the solidification growth rate (R). Small values of G/R favor the formation of equiaxed grains and large values point to the formation of columnar grains. This ratio is highest in PBF and lowest in DED-GMA. Thus, the primary ferrite in duplex steels shows columnar grains in PBF and equiaxed grains in parts of duplex steels made by DED-GMA. The austenite that forms from the ferrite by solid-state phase transformation shows different morphologies depending on alloy composition and processing conditions [18] ranging from grain boundary austenite (GBA), Widmanstatten austenite (WA),
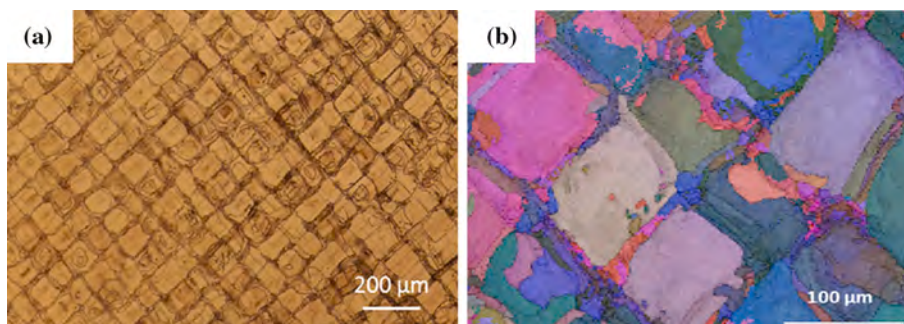
Fig. 3.3.1. (a) Microstructure of PBF-L 2507 Duplex stainless steel [222] and (b) EBSD of the microstructure showing the single-phase ferritic structure with a mosaic-type macrostructure [222].

intragranular austenite (IGA), and secondary austenite. GBA forms below 1350 ∘C and WA with lath morphology grows from GBA at temperatures below 800 ∘C. Also, IGA precipitates in the ferrite matrix when sufficient time is available [18]. The secondary austenite forms by the reheating process.

The primary ferrite grows along the building direction because the temperature gradient is maximum along this direction. The width of the ferrite grains depends on the time at high temperatures, narrow when the cooling rate is fast, and wide for slow cooling. For example, in PBF-L the width of ferrite grains is small because of the rapid cooling of 22Cr duplex stainless steel [221]. DED-GMA of a superduplex steel showed columnar ferrite with a strong [0 0 1] texture in the build direction, while the austenite had [1,101] orientations [230]. Zhang et al. reported the anisotropy of tensile properties with lower tensile strength along the vertical build direction than in the horizontal direction in ER2594 samples [230]. The anisotropy in mechanical properties due to the texture formation can be minimized by using an appropriate scanning strategy [231].

3.3.3. Control of defects

The main issues in making sound parts involve controlling the lack of fusion defects, gas and keyhole collapse porosity, residual stress and distortion, and avoiding significant changes in chemical composition. These defects have been reported in the additive manufacturing of duplex stainless steels in addition to the common issue of the need to balance the proportion of ferrite and austenite fractions mentioned in the previous section.

The lack of fusion defects is common in metallic parts made by AM. For the AM of duplex steels, the lack of fusion defects have been mitigated using higher power [223]. This experience could be anticipated since achieving an appropriate fusion zone geometry is important in ensuring adequate bonding between different layers and tacks. Previous work shows [157,232] that larger penetration compared with the layer thickness and larger fusion zone width compared with the hatch spacing are beneficial in avoiding the void space between successive layers and adjacent tracks (hatches). These geometric requirements can be achieved by enhancing heat input which is the ratio of the heat source power and scanning speed. Avoiding the lack of fusion defects improves the density of parts and in many cases avoids the expensive and time-consuming post-build hot isostatic pressing.

Gas porosity is much smaller than the lack of fusion voids and is nearly spherical being a few tens of micrometers in diameter. Their presence has been reported [223,233] during the AM of duplex stainless steels. The gas porosity results from the oxygen, nitrogen, and hydrogen dissolved in the powder and wire feedstock during their manufacture and storage, and their presence in the shielding gas during AM. Contamination of these species from the AM environment is less pronounced in PBF because of its use of a chamber where the deposition environment can be more effectively controlled than in DED-L and DED-GMA processes. The difference in the solubilities of oxygen, nitrogen, and hydrogen between the liquid and the solid alloys often results in the rejection of gases during solidification. Since the bubbles are very small and the solidification of the moving fusion zone is fairly rapid, there is commonly an insufficient time for the gas bubbles to escape from the solidifying parts. Knezovic et al. found that the porosity increased with a decrease in the interlayer temperature during the deposition of a 2205 duplex steel part [233]. Careful control of the feedstock and the part environment during AM is the most effective way of controlling the gas porosity in the part and can avoid the post-processing step.

When a high power density heat source such as a laser or electron beam interacts with an alloy, significant vaporization of alloying elements often results in a deep and narrow cavity filled with metal vapors known as a keyhole [234]. Depending on the process parameters and materials properties, the shape and size of the keyhole may change with time and the lower portion of the keyhole may collapse forming a cavity. This cavity, resulting from the instability of the keyhole, is common [235] in the PBF of alloys such as the 2205 duplex stainless steel. It is known from the literature on fusion welding that the keyhole-induced pores can be reduced by lowering the total pressure of the system [236] and by adjusting the process variables such as power and scanning speed. No systematic study has been undertaken to investigate the effects of total pressure and other process variables during additive manufacturing of duplex stainless steels.
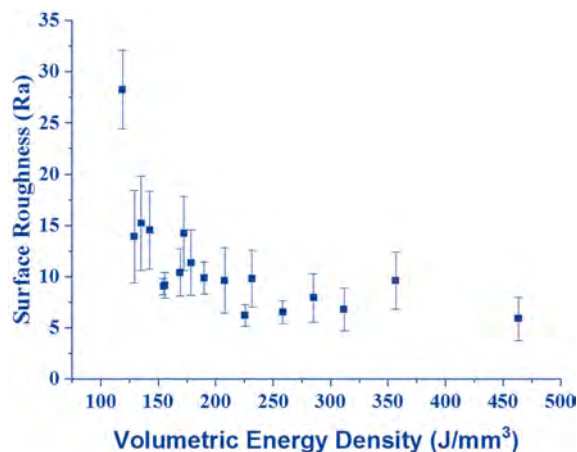
Fig. 3.3.2. Surface roughness of a 2205 duplex steel part deposited by PBF-L as a function of volumetric energy density [235].

Residual stress and distortion are major concerns for large parts made using high heat input. Among the common AM processes, the problem is most pronounced in DED-GMA and least prominent for PBF-L. The maximum residual tensile [230] stress was reported to be 800 MPa for PBF-L of duplex steel 2205. However, the stress was reduced significantly after a heat treatment at 1000 ∘C for 5 min. Distortion is often controlled using reinforced supports [237] and heat treatment is commonly used to mitigate the residual stresses [18]. Since the literature on residual stress and distortion is scarce, and the thermophysical properties of the duplex steels are somewhat similar to the austenitic stainless steels, the existing studies on similar alloys may serve as a good starting point.

Surface roughness influences fatigue and corrosion properties and depend on process variables such as the heat source power, scanning speed, and alloy properties. For powder bed fusion, the surface roughness is relatively less pronounced and can be controlled by adjusting process variables. Fig. 3.3.2 shows [235] the surface roughness of 2205 duplex steel parts made by PBF-L as a function of the volumetric energy density. The roughness decreases with higher energy and the results show that a relatively smooth surface may be obtained by adjusting volumetric energy density. Fast scanning contributes to the roughness by forming lines of balls [238] rather than a continuous stream of thin molten metal layers. Thus for parts made by PBF-L, apart from high energy density, relatively low scanning speed to avoid balling would result in surfaces smooth enough to avoid post-processing. Parts made by DED-GMA and DED-L need post-processing such as machining, sand-blasting, or etching.

3.4. Other steels

This section reviews the strategies to control grain structures, phases, and defects in additive manufacturing of plain carbon steels, oxide dispersion strengthened (ODS) steels, and transformation induced plasticity (TRIP) steels [239]. These steels are introduced below.

- Plain carbon steels [90,240–248] are iron-carbon alloys with a small amount of Mn, Si, Cu, P, and S. These steels are further categorized based on the carbon content such as low carbon steels (<0.3 wt% C) medium-carbon steels (0.3–0.6 wt% C), and high-carbon steels (0.6–1.0 wt% C). Plain carbon steels are very popular for making structural components. However, their usage in additive manufacturing is limited because of cost considerations and the cracking susceptibility of medium and high carbon steels. A few attempts have been made to print parts of plain carbon steels using wire arc-based processes using the wires available for fusion welding [242–245] and using PBF-L [90,240,241,247].
- Oxide dispersion strengthened (ODS) steels [249–270] contain nano-sized oxides with excellent thermal stability that are uniformly dispersed in the iron-based alloy matrix. For example, Fig. 3.4.1 shows the presence of fine oxides of Al and Y in a part made by PBF-L [250]. Oxides of Ti, Fe, and Cr are also common. These steels have excellent strength and high-temperature creep strength owing to the dispersion strengthening of the oxide particles as well as the solid solution strengthening of the iron-based alloy matrix. ODS steel parts are printed generally using PBF-L and DED-L methods [250–270].
- Transformation induced plasticity (TRIP) steels [271,272] are high-strength steels used in the marine and automotive industries because of their excellent combination of strength and toughness. These steels contain retained austenite within a ferrite matrix that transforms into martensite when stress is applied. This unique behavior results in both high strength and toughness.

High cooling rates during AM result in very fine cellular or dendritic solidification structures in plain carbon steel parts [240]. The size and morphology are controlled by altering the temperature gradients and cooling rates by adjusting the process parameters [240]. Apart from adjusting the processing conditions, yttria (Y_2O_3) [251,253–255] and Tellurium (Te) [252] nanoparticles have been added to refine the grain structure during AM of ODS steels. For example, Fig. 3.4.2 (a) and (b) show that an addition of 5 wt% yttria significantly refines the grain during PBF-L [251]. The average size of the grains is reduced from 7 ± 6 μm (Fig. 3.4.2 (a)) to 3.7 ± 3 μm (Fig. 3.4.2 (b)). Yttria nanoparticles act as potential inoculants and facilitate heterogeneous nucleation to refine the grains. High melting point tellurium nanoparticles are also used to refine the grains since they promote heterogeneous nucleation [252]. The addition of Te narrows the grain size distribution. The range of the grain size changes from 2.5 to 25 μm to 1.5–10.5 μm. Often, Y in ODS steels forms Y_2O_3 which acts as a grain refiner [250,256]. In addition, grain structures in additively manufactured ODS steel parts
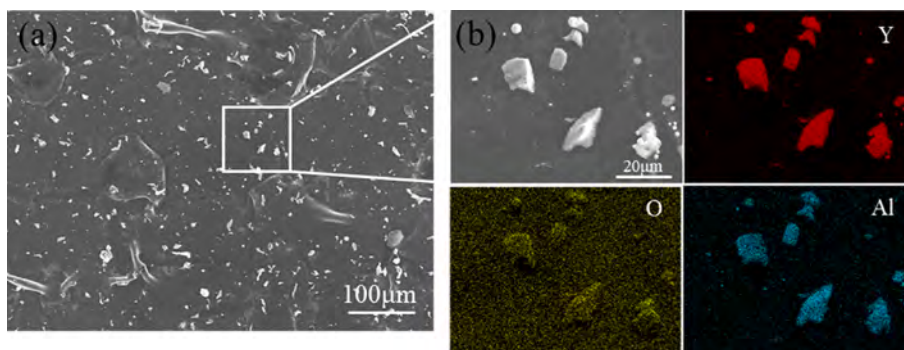
Fig. 3.4.1. Nano-sized oxides formed during PBF-L of pre-alloyed ODS steel [250].
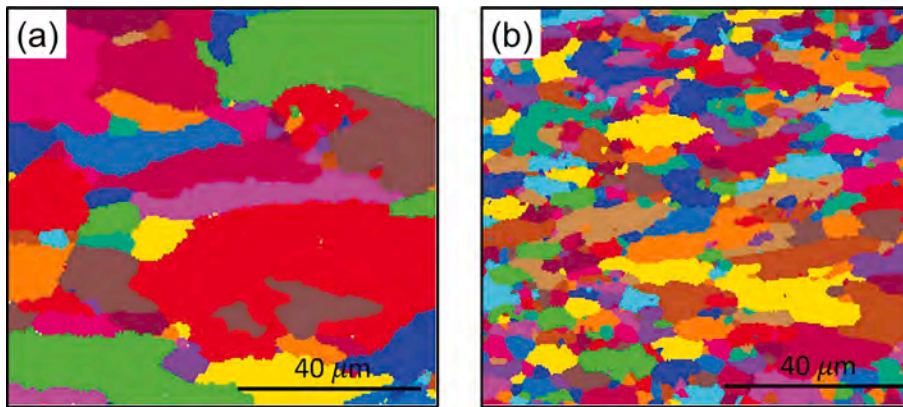
Fig. 3.4.2. EBSD grain map micrograph of PBF-L parts of (a) SS 304L and (b) SS 304L + 5 wt% yttria [251]. The reprint permission is obtained from Dr. Joseph Beaman.

are often controlled by post-process heat treatment [257,258] which adds an extra cost.

Rapid cooling during AM of plain carbon steels results in the formation of martensite. The amount of martensite is controlled by tempering the martensite using post-process heat treatment [240]. Tempering of martensite also occurs because of multiple heating and cooling cycles during the deposition of multiple layers during AM [90]. This process is often called in-situ heat treatment. The martensite formed in a deposited layer is often transformed partially or fully to tempered martensite during the deposition of subsequent layers. Tempered martensite is formed by the precipitation of nano-sized Fe_3C carbides at the carbon-enriched grain boundaries [90]. The extent of transformation of martensite into tempered martensite is affected by the local thermal cycles and thus can be controlled by adjusting the heat input, layer thickness, and scanning strategies. For example, Fig. 3.4.3 shows how to control the tempering of martensite by adjusting the heat input during PBF-L of Fe-0.45C steel [90]. Martensite is tempered due to a higher temperature at a higher heat input and forms nano-sized Fe_3C carbides at the carbon-enriched grain boundaries [90]. ODS steels have martensite and ferrite phases. However, their mechanical properties are primarily affected by the dispersed oxides that are controlled by adjusting the heat input, adding oxide-forming elements, and changing the chemical composition of the steel [250–270]. TRIP steels contain retained austenite within a ferrite matrix that transforms into martensite when stress is applied [272]. The parts often contain round or ellipsoid carbides of W, Mo, V, and Cr [272]. However, the strength and toughness depend on the extent of martensite formed when the stress is applied and thus are not largely affected by the carbide precipitates. Limited work is available in the literature on
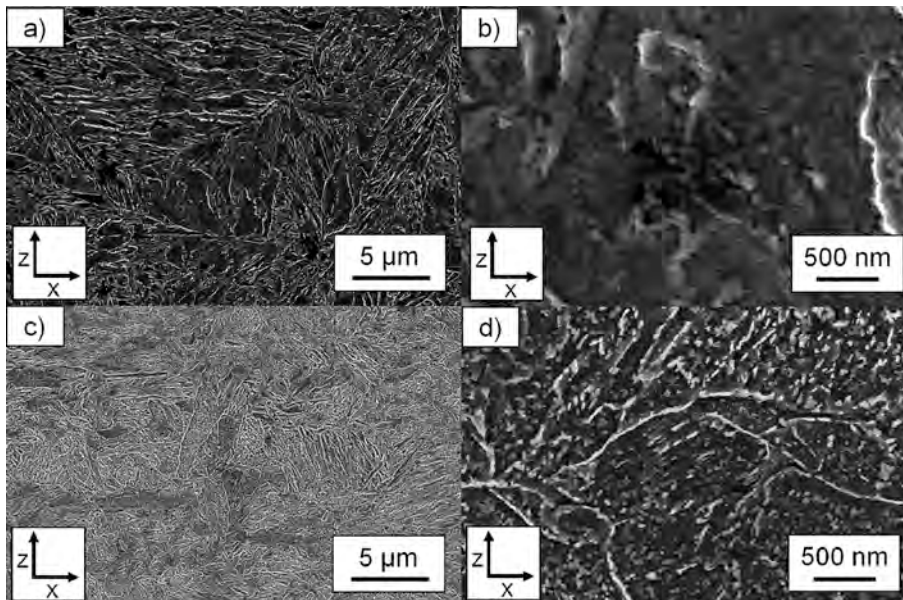
Fig. 3.4.3. Control of martensite by adjusting the heat input during PBF-L of Fe-0.45C steel [90]. (a) SEM image of un-tempered martensite in a specimen made using 60 J/mm³ volumetric heat input. (b) Higher magnification of figure (a) shows no noticeable precipitates. (c) SEM image of tempered martensite in a specimen made using 100 J/mm³ volumetric heat input. (d) Higher magnification of figure (c) shows the presence of nano-sized Fe_3C carbide precipitates.

controlling the phases in additively manufactured TRIP steel parts.

Additively manufactured plain carbon steel parts are susceptible to the lack of fusion (Fig. 3.4.4 (a)), keyhole porosity (Fig. 3.4.4 (b)), and cracking. At low heat energy input, insufficient melting results in the lack of fusion Fig. 3.4.4 (c). Keyholes are formed at a high energy density. Unstable keyholes may collapse and form keyhole pores Fig. 3.4.4 (c). Cracks form at a higher carbon content (Fig. 3.4.4 (c)). High carbon content is related to a higher alloy hardenability and a higher martensite hardness. High local hardness initiates cold cracking during cooling. These cracks propagate due to the accumulation of high stresses during cooling [241]. Fig. 3.4.4 (c) shows a process map indicating the formation of different defects at various heat energy inputs and carbon content. Such maps are immensely useful to select an appropriate combination of process parameters and alloy composition to avoid defects. Additively manufactured ODS steel parts are also susceptible to the lack of fusion [250,259] which can be controlled by increasing the heat input at a higher laser power (Fig. 3.4.5). The same strategy is also used to reduce the lack of fusion in additively manufactured TRIP steel parts [272].

4. Control of grain structure, phases, and defects in aluminum alloys

Printed aluminum alloy parts are used in the automotive, defense, and aerospace industries because of their low weight and good mechanical properties. However, there are several complexities in printing aluminum alloys. They often exhibit long columnar grains that are susceptible to solidification cracking and poor tensile properties. In addition, these parts may contain oxides and other precipitates that degrade the mechanical and chemical properties. In addition, printed aluminum alloy parts are susceptible to lack of fusion, porosity, and composition change due to selective vaporization of the alloying elements. Additive manufacturing of commonly used aluminum alloys is limited by the evolution of undesired grain structure, phases, cracking, and other defects. Therefore, printing aluminum alloy parts containing minimum defects with desired microstructure and properties is challenging. This section reviews the common strategies (Fig. 4.1) to control grain structure, phases, and defects during additive manufacturing of aluminum alloys
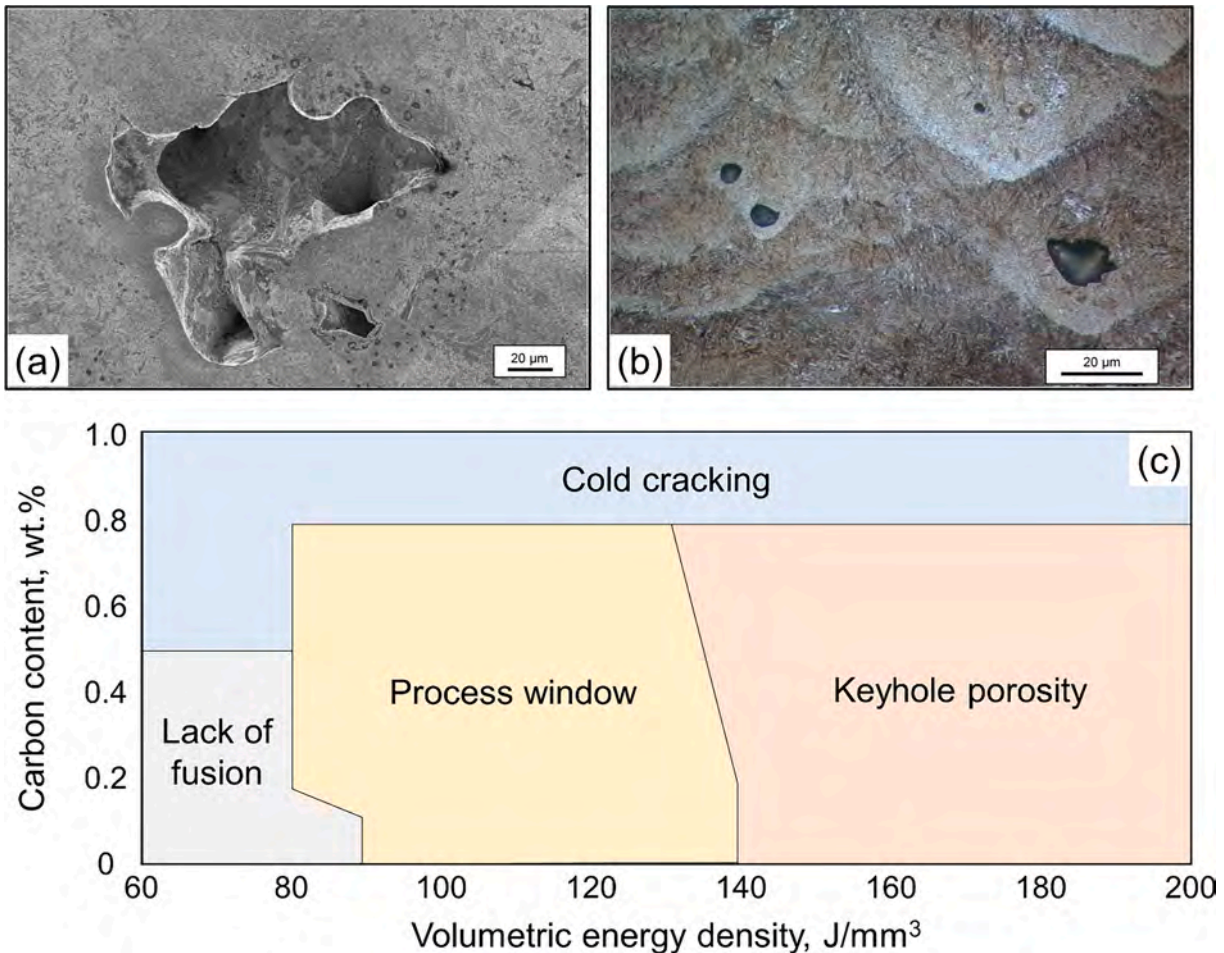
Fig. 3.4.4. (a) Lack of fusion voids in Fe-0.2C part produced using PBF-L [240]. (b) Keyhole pores in Fe-0.75C part produced using PBF-L [240]. (c) Dependence of formation of different defects on heat energy density and carbon content during PBF-L of plain carbon steels. The figure is made using the data reported in [241].
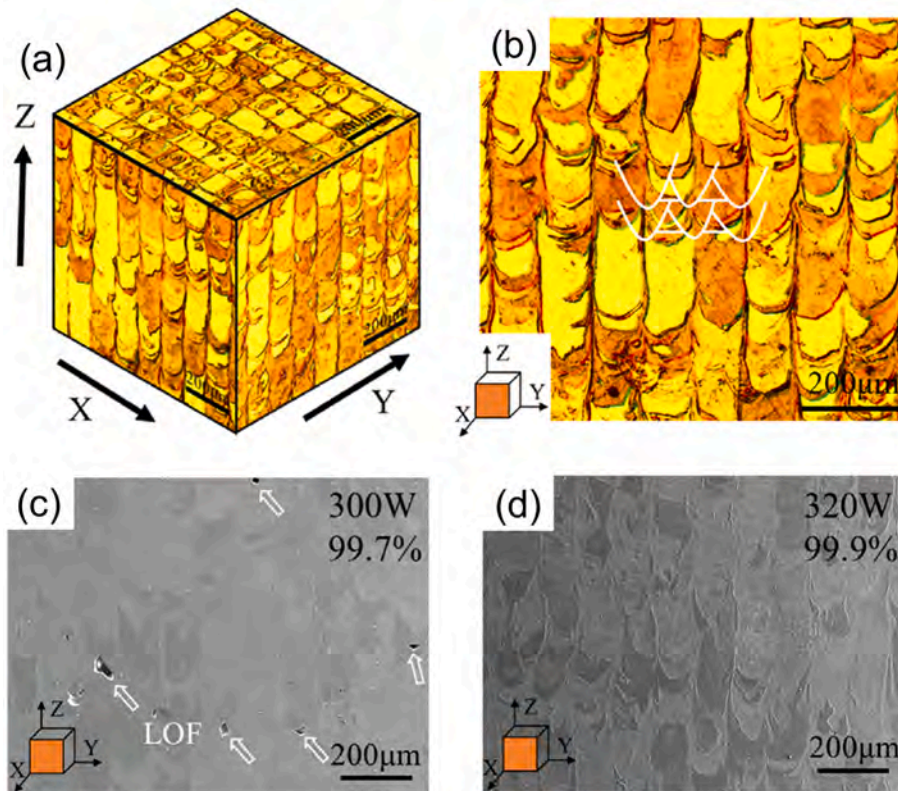
Fig. 3.4.5. Optical micrograph and SEM images of ODS steel parts made by PBF-L [250]. (a) Three-dimensional microstructure using optical micrography, (b) transverse cross-sectional microstructure, and SEM images of parts made using (c) 300 W and (d) 320 W laser power. Figure (c) indicates the presence of the lack of fusion (LOF) defects.

[273–275]. Table 4.1 provides selected examples of controlling grain structure, phases, and defects in additively manufactured aluminum alloy parts.

4.1. Strategies to control grain structure

Additively manufactured aluminum alloy parts often contain long columnar grains that are known to degrade mechanical properties and cause solidification cracking. Several control techniques are emerging to modify the long columnar grains to form small equiaxed grains as discussed below.

4.1.1. Addition of inoculants and grain refiners to achieve columnar to equiaxed transition

High melting point elements such as zirconium and scandium are added [276–279] as inoculants to promote several nucleation sites for the formation of equiaxed grains. For example, the addition of 1 vol% of zirconium in AA 7075 processed using PBF-L promoted heterogeneous nucleation resulting in small equiaxed grains [104]. The formation of equiaxed grains significantly improved the tensile properties of the part. Only 2 wt% of zirconia [280] can act as grain refiners and change the long columnar grains (Fig. 4.2 (a)) into smaller equiaxed grains (Fig. 4.2 (b) and (c)) that are beneficial for improving tensile properties [281]. Titanium and vanadium have also been used for grain refinement during AM of aluminum alloys [282].

The addition of zirconium or scandium can form Al_3Zr [283,284] or Al_3Sc [285–288] precipitates, respectively, from the liquid before the Al-rich primary solidification phase forms. These precipitates are known to be very effective for grain refinement during solidification by promoting heterogeneous nucleation. For example, zirconium creates two types of metastable Al_3Zr precipitates. First, sub-micrometer particles form upon solidification and act as grain refining agents, nucleating fine aluminum grains that improve tensile properties. Second, Al_3Zr nano-precipitates form in the solid alloy during heat treatment that precipitation-strengthen the alloy leading to a significant increase in the tensile strength over the as-fabricated value. Similar observations were also made in fusion welding [289,290]. However, the exact mechanism of the formation of these precipitates is not fully understood and more work is needed to uncover it.

Micro and nanoparticles of high melting point ceramic materials such as titanium carbide (TiC) and titanium boride (TiB_2) are often added as grain refiners or inoculants during casting and fusion welding. They are also used in the additive manufacturing of aluminum alloys [291–296]. For example, TiC nanoparticles were used as grain refiners during PBF-L of pure aluminum [297], AA 7075[296],
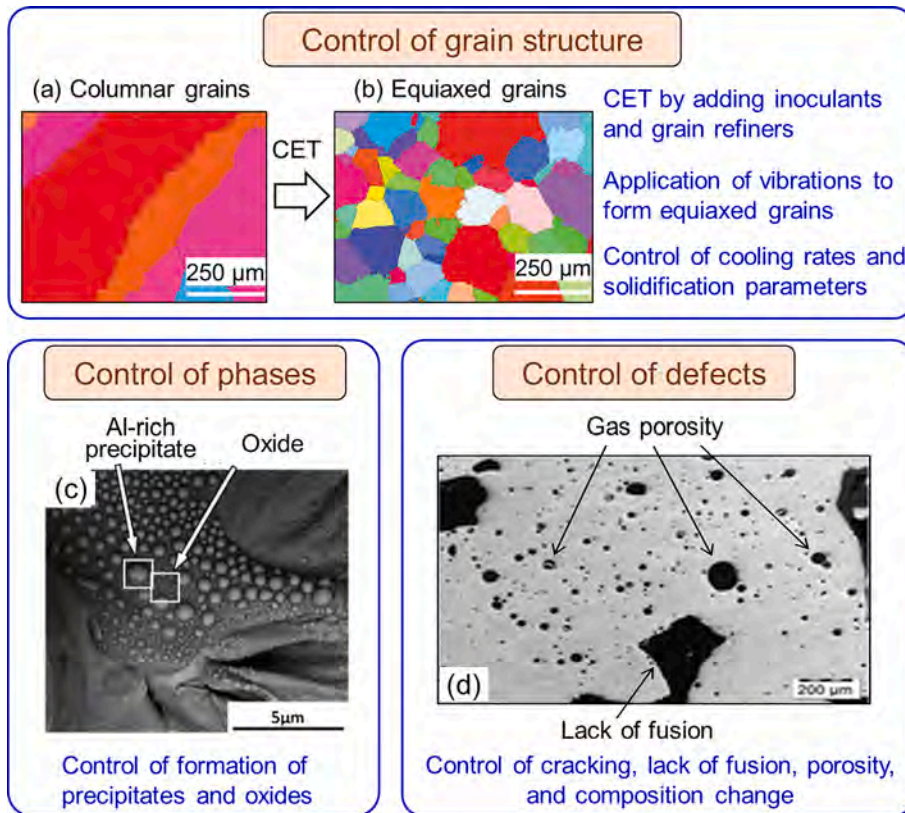
Fig. 4.1. Common techniques to control grain structure, phases, and defects in additively manufactured aluminum alloys. Figures (a) and (b) show results taken from [273] and figures (c) and (d) are adapted from [275] and [274], respectively.

and an Al-Cu-Ag-Mg-Ti alloy [298], DED-L of AA 5024 [299], and DED-GMA of AA 7075 [300] and AA 2219 [301]. However, the shape, size, and optimum amount of these additives are selected by experimental trials. More work is needed to examine the attributes of the additives needed to act as effective inoculants. The shape, size, and amount of the inoculant particles and their cost are important factors in the selection of inoculants.

4.1.2. Application of external vibrations to form equiaxed grains

External forces such as ultrasonic vibration and mechanical agitation can be used to change large columnar grains to small equiaxed grains that are beneficial for improving tensile properties. The mechanical vibration of the entire system has been used to break the columnar grains [302]. Thermal fluctuations in the pool could also be increased by such mechanical vibration, which could in turn increase remelting of dendrite arms at their roots. The remelted dendrite arms, if they survived, could grow into equiaxed grains and cause grain refining. The goal is to achieve many small grains (Fig. 4.3) by adjusting the amplitude and frequency of the vibration. However, the amplitude and frequency are selected based on trial and error. In addition, the efficacy of different types of ultrasonic waves (transverse or longitudinal) needs to be investigated. Plastic deformation by cold working using either mechanical hammering (or peening) [303] or laser shock peening [304] is used to produce refined grains. However, both methods interrupt the deposition process to apply the deformation and thus require longer processing times.

4.1.3. Control of cooling rates and solidification parameters

Grain morphology (columnar or equiaxed dendrites) is controlled by the ratio of the temperature gradient to the solidification growth rate. A high ratio favors the formation of columnar grains. In addition, the product of the temperature gradient to solidification growth rate represents the cooling rate during solidification which affects the fineness of the microstructure, such as the dendrite-arm spacing or cell spacing. Process conditions are adjusted to achieve the required temperature gradient and solidification growth rate to attain the desired solidification morphology and grain size. Substrate preheating and high heat input reduce the temperature gradient which is favorable for the formation of equiaxed grains. Rapid cooling at a fast scanning speed results in smaller, but more elongated, grains [305]. Inter-layer cooling can control the net heat content in the part and thus affect the temperature gradient. Decreasing power progressively during DED-GMA can reduce the heat input, enhance the cooling rate, and produce fine grains [306].

Table 4.1

Selected examples of controlling grain structure, phases, and defects in additively manufactured aluminum alloy parts.

Objective	Alloy	AM process	Description of control strategy	References
Control of grain structure	AA 7075	PBF-L	Addition of 1 vol% Zr promoted heterogenous nucleation and resulted in equiaxed grains	[104]
	Al-Mg-Zr alloy	PBF-L	Addition of Zr formed Al_3Zr precipitates that helped in heterogeneous nucleation and formation of equiaxed grains	[283,284]
	Al-Mg alloy	PBF-L	Addition of Sc formed Al_3Sc precipitates that helped in heterogeneous nucleation and formation of equiaxed grains	[287,288]
	Pure Al	PBF-L	TiC nanoparticles were added as grain refiners that resulted in equiaxed grains	[297]
	AA 7075	PBF-L		[296]
	AA 5024	DED-L		[299]
	AA 7075	DED-GMA		[300]
	AA 2219	DED-GMA		[301]
	Al-Mg alloy	DED-GMA	Vibration of the entire system was used to break the columnar grains	[302]
	AA 2319	DED-GMA	Laser shock peening was used during the process to break the columnar grains	[304]
	Al-5Si alloy	DED-GMA	Pulsing or arc was used to refine grains	[307]
Control of phases	AA 4043	DED-GMA	Post-process heat treatment reduced silicon-rich, globular precipitates	[315]
	AA 2319	DED-GMA	Post-process heat treatment reduced Mn, Cu, and Si-rich secondary phases and improved mechanical properties	[314]
Defect control	AA 7075	PBF-L	Addition of grain refiners promoted columnar to equiaxed transition and reduced solidification cracking	[104]
	AA 7075	PBF-L	Addition of 4 wt% Si refined grains and reduced solidification cracking	[331]
	AA 6061	PBF-L	Substrate preheating reduced temperature gradient and stress accumulation and minimize solidification cracking	[345]
	AlSi10Mg	PBF-L	Lack of fusion voids were minimized by increasing the pool size by enhancing the heat source power, decreasing the scanning speed, and reducing the hatch spacing	[353]
	Al-Zn-Mg alloy	DED-GMA	Gas pores were minimized by varying the arc polarity and pulsing the arc	[354]
	Al-Mg alloy	DED-GMA	Low arc current or rapid scanning resulted in low temperature and reduced composition change due to selective vaporization	[113]
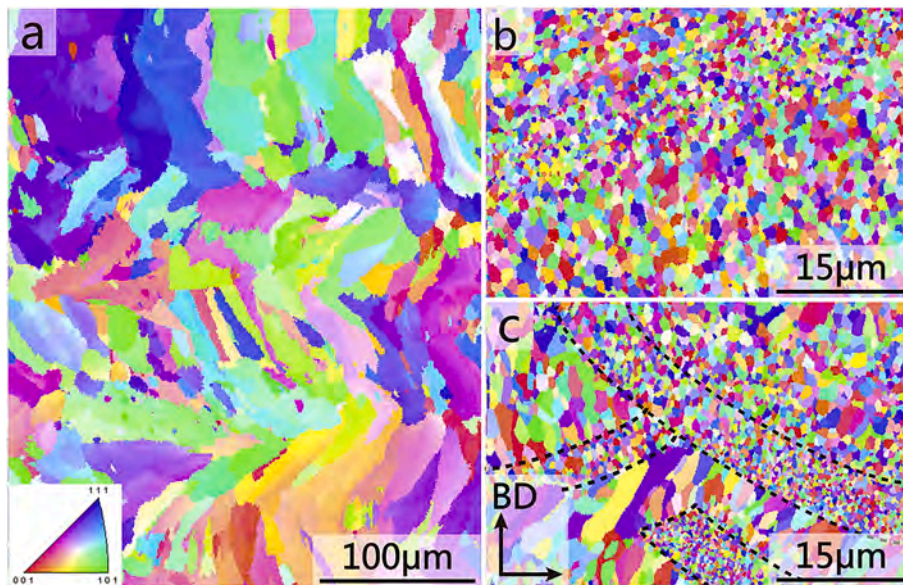
Fig. 4.2. EBSD inverse pole figure (IPF) maps of AA 2024 fabricated by PBF-L showing (a) coarse grains and showing fine grains after zirconium addition using laser scanning speeds of (b) 5 m/min and (c) 15 m/min, respectively [281].
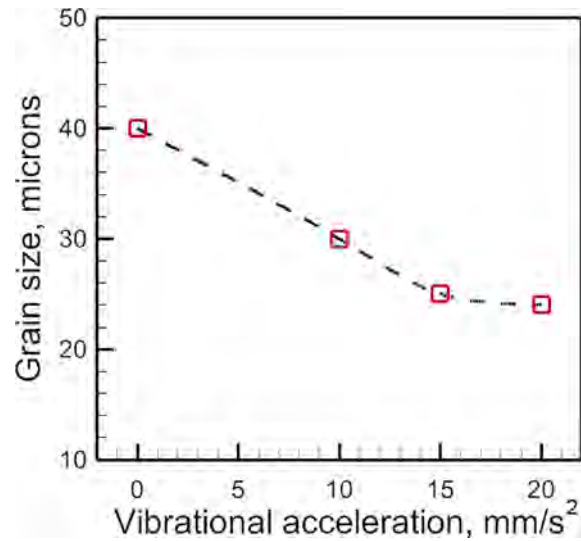
Fig. 4.3. Reduction in grain size with an increase in vibration acceleration during DED-GMA of aluminum-magnesium alloy with the provision for an external ultrasonic vibration source. The plot is made using the data reported in [302].

4.1.4. Other methods to control grain structure

Pulsing [307] of arc source in DED-GMA is effective at reducing the grain size. DED-GMA of aluminum alloys using cold metal transfer (CMT) technologies allows control of overall heat input which results in faster cooling and smaller dendrite arm spacings.
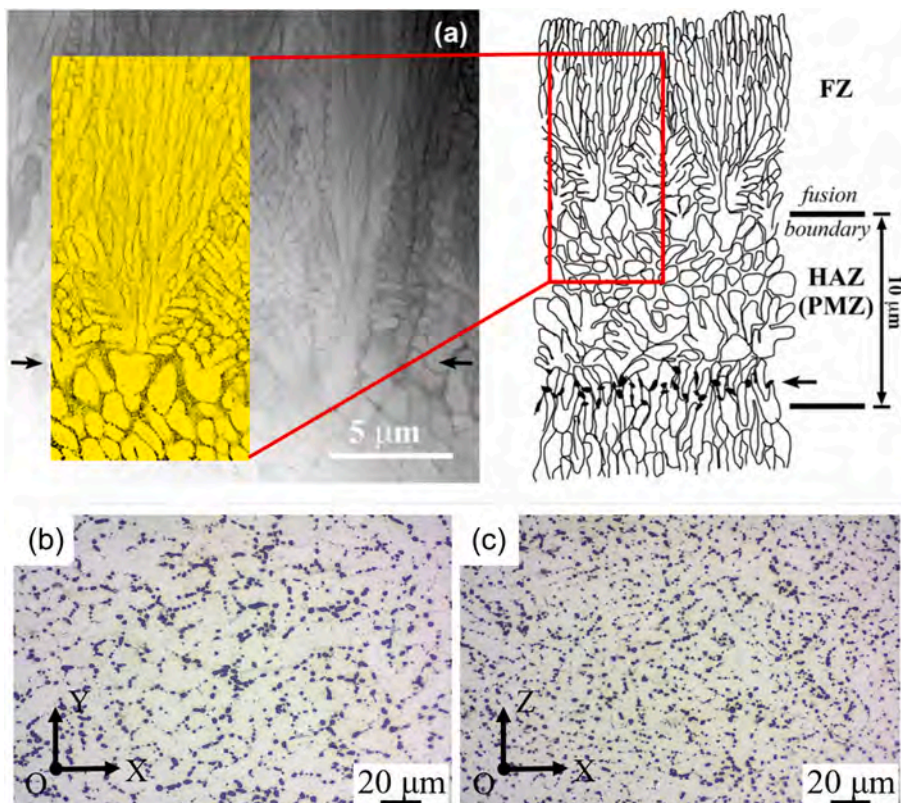
Fig. 4.4. (a) The bright-field STEM image of a printed AlSi10Mg alloy part shows the cellular structure as it forms during solidification into the fusion zone from the fusion boundary. The schematic to the right shows an overall view of the boundary structure. The characteristic layer of coarsened silicon deposits is marked with arrows that define the bottom boundary of the heat-affected zone [313]. AA 4043 parts made by DED-GMA [315] containing silicon-rich (b) globular precipitates and (c) smaller precipitates with uniform distribution after heat treatment.

Several process variants [308–312] such as conventional CMT, CMT-Pulse (CMT-P), CMT-Advanced (CMT-ADV), and CMT Pulse Advanced (CMT-PADV) can provide a progressively decreasing heat input. All the variants permit control of the current waveforms. The PADV version operates in a variable polarity mode, with cathodic cleaning of substrate oxides in the electrode positive mode. Increases in arc pressure with the variable polarity mode are claimed to cause dendrite fragmentation with subsequent formation of equiaxed grains of random texture. Further investigation is needed to provide an improved understanding of the effects of arc pressure and polarity on dendrite fragmentation.

4.2. Phase control strategies

Precipitates are the most common phases formed during the additive manufacturing of aluminum alloys. For example, rapid cooling rates during the solidification of an additively manufactured AlSi10Mg alloy [313] resulted in a small dendrite spacing in the middle of the fusion zone with uniformly distributed, nanoscale silicon-rich precipitates. The precipitates were found within the primary α-grains. A thin, distinct boundary layer containing larger α-grains and extended regions of the nanocrystalline precipitates of eutectic material was found near the fusion boundary (Fig. 4.4 (a)). Iron-rich precipitates were found to affect the mechanical properties of AA 2319 parts made by DED-GMA [314].

In-situ and post-process heat treatments are commonly used to control precipitates in additively manufactured aluminum alloy parts. For example, AA 4043 parts made by DED-GMA [315] contained silicon-rich, globular precipitates (Fig. 4.4 (b)) that are reduced by post-process heat treatment (Fig. 4.4 (c)). The heat treatment also resulted in a more uniform distribution of the precipitates. The multiple thermal cycles inherent with most AM processes provide an opportunity for in-situ heat-treating much like that experienced during temper bead welding during arc welding. The effects of multiple thermal cycles during AM processes are referred as intrinsic heat-treating. For Al alloys that are precipitation strengthened, this approach would require either very fast cooling of each pass after solidification to keep solute in solution or subsequent thermal cycles that reach temperatures high enough to re-solutionize. Note that the choice of process parameters to provide these thermal cycles must also yield fully dense deposits without defects. One method for developing a set of parameters to meet all the requirements is process simulation. In addition, post-process heat treatments to dissolve unwanted phases or to provide spheroidization of features for improved mechanical properties are possible for AM of Al alloys. However, post-process heat treatment adds extra cost.

4.3. Control of common defects

Additively manufactured aluminum alloy parts are susceptible to common defects such as cracking, lack of fusion, porosity, and composition change. For example, AA 2139 parts suffered from evaporative loss of magnesium that significantly reduced the hardness [316]. Elongated pores due to lack of fusion were observed in printed AA 1100 parts [317]. Al 5083 parts made by DED-L exhibited gas porosity, evaporative loss of magnesium, and the presence of pure magnesium HCP phase surrounded by a matrix of FCC aluminum, all of which affected the structure and properties of parts [318]. AlSi10Mg parts made by PBF-L have been found to have defects such as porosity that degrade the mechanical properties [319–321]. Porosity was also observed in aluminum alloys 1100, 4043, 4943, 4047, and 5356 parts made by DED-GMA [322]. This section reviews commonly used control strategies to mitigate these defects in additively
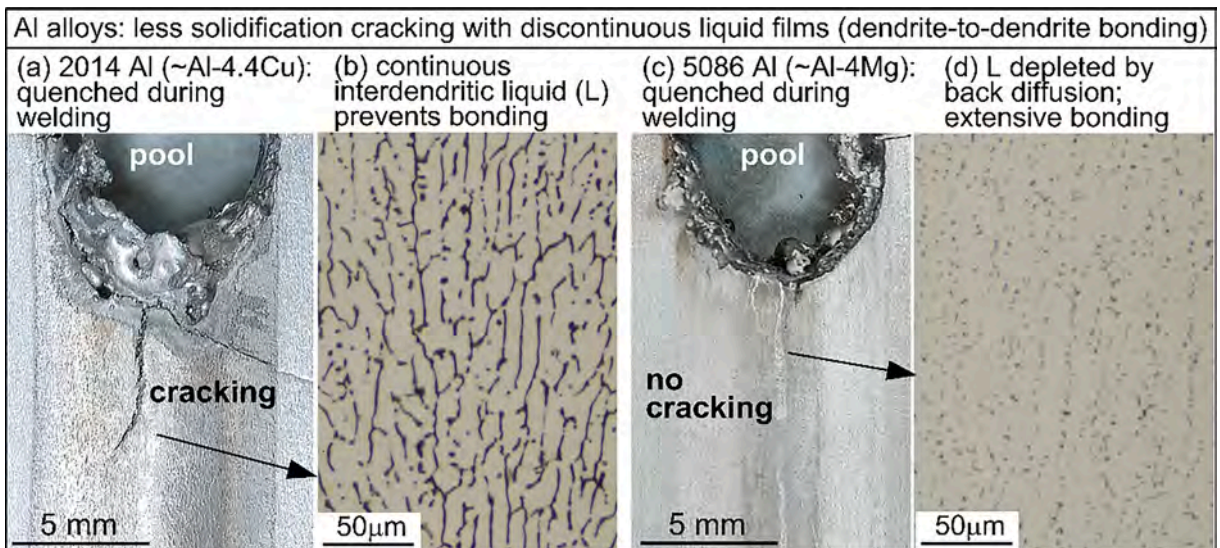
Fig. 4.5. New mechanism of resistance to solidification cracking shown by quenching Al alloys during welding: (a) (b) 2014 Al (~Al-4.4Cu) showing continuous interdendritic liquid films as easy paths for cracking; (c) (d) 5086 Al (~Al-4 Mg) showing grain-boundary liquid depleted by back diffusion of Mg into Al-rich dendrites and explaining its greater crack resistance than 2014 Al [330].

manufactured aluminum alloy parts.

4.3.1. Solidification cracking

Solidification cracks are often visible in the fusion zone, along grain boundaries, and the fracture surfaces show dendrites or cells [103]. Significant progress has been made in understanding solidification cracking in casting and fusion welding of aluminum alloys that are also applicable for additive manufacturing [323,324]. A simple index $|dT/d(f_S)^{1/2}|$ was used to evaluate the susceptibility to solidification cracking [325], where T is temperature and f_S is the fraction of solid. It was suggested that the maximum $|dT/d(f_S)^{1/2}|$ up to $(f_S)^{1/2} = 0.99$ (i.e., $f_S = 0.98$) is a convenient option for the index. This is because the maximum $|dT/d(f_S)^{1/2}|$ usually occurs near $(f_S)^{1/2} = 1$ and because beyond $f_S = 0.98$, the grains can bond to each other extensively to resist cracking [326]. Commercial thermodynamic software and database can be used to calculate the T versus $(f_S)^{1/2}$ curves and obtain values of $|dT/d(f_S)^{1/2}|$. For instance, "Pandat" [327] and "PanAluminum" commercial packages [328] can be used to calculate the index of an Al alloy based on its composition. It is interesting to note that the crack susceptibility of one alloy relative to a similar alloy different in composition in arc welding has been found similar to that in laser- or electron-beam welding [329]. For example, the crack-susceptibility ranking of 6061 Al > 7075 Al > 2219 Al observed in arc welding was also observed in electron-beam welding. Both back diffusion and reactions that consume the interdendritic liquid can help resist solidification cracking. They can increase f_S at a given T to flatten the T-$(f_S)^{1/2}$ curve and hence significantly reduce $|dT/d(f_S)^{1/2}|$. This mechanism has been verified in different Al alloys.

The Al-Mg alloy system, based on its low eutectic temperature ($T_E = 450\,°C$), can be expected to be significantly more susceptible to solidification cracking than the Al-Cu alloy system ($T_E = 548\,°C$). Indeed, the much lower T_E of Al-Mg alloys makes its T versus $(f_S)^{1/2}$ curves much steeper, suggesting a higher crack susceptibility. However, Fig. 4.5 shows that 5086 Al (~Al-4 Mg) resists solidification cracking much better than 2014 Al (~Al-4.4Cu) [330]. Liquid Wood's metal at 75 °C was poured from a glass beaker onto the weld pool and its surroundings to freeze and capture the elevated-temperature microstructure of the mushy zone and simultaneously induce transverse tension in it to cause cracking. In 2014 Al, continuous interdendritic liquid films exist as easy paths for intergranular cracking but not in 5086 Al. The much higher maximum solubility of Mg in solid Al (17.5 wt% Mg) than Cu in solid Al (5.65 wt% Cu) encourages much Mg back diffusion into Al-rich dendrites to deplete the interdendritic liquid. This is consistent with the dramatic flattening of the T versus $(f_S)^{1/2}$ curves of Al-Mg alloys and a significant reduction in both $|dT/d(f_S)^{1/2}|$ and crack susceptibility [330].

In commercial Al alloys, Si, Cu, Mg, Zn, and Li are common alloying elements. Al-Si alloys, including AlSi10Mg, have low susceptibility to solidification cracking. Al-Si alloys are widely used in casting, with excellent castability due to their narrow freezing temperature range (a high eutectic temperature of 577 °C) and good fluidity (high fraction of eutectic). Hyer et al. [102] investigated solidification cracking in PBF-L of Al-Si alloys, including six binary Al-Si alloys and AlSi10Mg and Al12Si. Only Al-Si alloys with 1.0 and 2.0 wt% Si were found to exhibit solidification cracking, consistent with the prediction based on the index $|dT/d(f_S)^{1/2}|$. The addition of silicon can prevent cracking in aluminum alloys by increasing the fraction eutectic that forms and reducing the
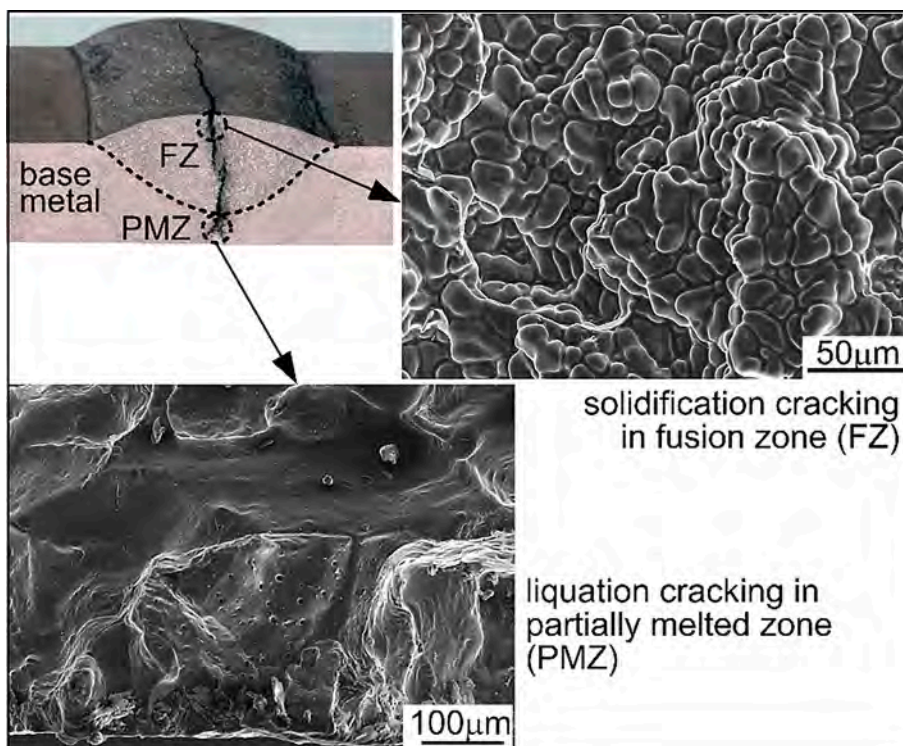
Fig. 4.6. Liquation cracking vs. solidification cracking in bead-on-plate, gas-metal arc weld of 6061 Al [347].

solidification temperature range. In some aluminum alloys such as AA 2024 and AA 7075, silicon addition can result in precipitation hardening to achieve high strengths. However, the amount of silicon is significantly less than that used for casting and filler metal in welding to minimize cracking. For example, the addition of 4 wt% of silicon in AA 7075 during PBF-L resulted in fine grains at the fusion boundary more likely due to epitaxy and competitive growth [331]. A new alloy composition with 6.5 wt% of silicon was developed by mixing AA 7068 powders with Al10SiMg which was found to minimize cracking [332]. Selection of process parameters [333–335], scan strategy [336], and modeling [337] to understand and reduce solidification cracking during PBF-L of aluminum alloys have been demonstrated.

The most effective control of solidification cracking is to avoid the composition range of the highest crack susceptibility. For a binary Al alloy system (e.g., Al-Si, Al-Cu, Al-Mg, or Al-Li) the crack susceptibility curve can be used as a guide, which shows the crack susceptibility as a function of the solute content. The composition range near the solute content corresponding to the highest crack susceptibility should be avoided. For a ternary (e.g., Al-Mg-Si, Al-Cu-Mg, or Al-Cu-Si) or quaternary (e.g., Al-Si-Mg-Cu, Al-Zn-Mg-Cu or Al-Li-Mg-Cu) Al alloy system, a crack susceptibility map can be used as a guide to avoiding the composition range of the highest crack susceptibility. Crack susceptibility curves or maps have been determined experimentally for Al alloys. They also have been calculated based on the index $|dT/d(f_S)^{1/2}|$, including binary [338,339], ternary [340], and quaternary [100] Al alloy systems and verified against experimental results. New alloys are being developed to reduce cracking during additive manufacturing [341,342].

If high-strength Al alloys with compositions susceptible to solidification cracking [343,344] have to be used for AM, grain refining should be considered. Reduction of cracking during solidification by grain refining has been demonstrated in casting [345] and welding of Al alloys. In powder bead fusion of 6061 Al, preheating of the powder bed has been shown to eliminate solidification cracking [346]. Preheating reduces the temperature gradients and thermally induced tensile stresses and solidification cracking.
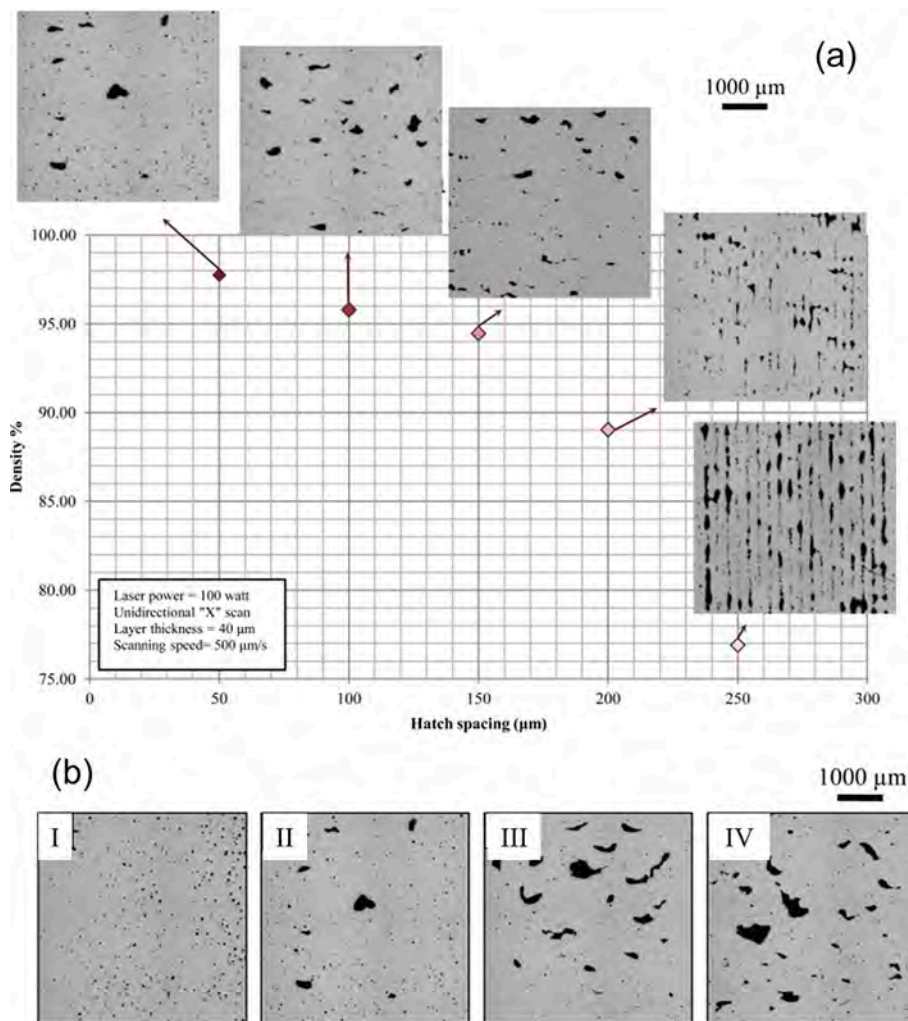
Fig. 4.7. (a) An increase in hatch spacing results in more lack of fusion voids and decreases part density during PBF-L of AlSi10Mg [353]. (b) Evolution of lack of fusion voids with scanning speeds (I) 250 mm/s, (II) 500 mm/s, (III) 750 mm/s, and (IV) 1000 mm/s during PBF-L of AlSi10Mg [353].

Substrate preheating was effective to reduce cracking in PBF-L of AA 6061 by reducing the temperature gradient and accumulated stress [345]. Different scanning strategies were used to attain desired cooling rates and solidification parameters to control microstructure and reduce cracking in AM of aluminum alloys [346]. Significant progress has been made to mitigate the solidification cracking by controlling the solidification morphology, designing new alloys, and making changes in the additive manufacturing process. In addition to the persistent problems of solidification cracking, AM of aluminum alloys also suffer from other defects as explained below.

4.3.2. Liquation cracking

Liquation cracking occurs in the partially melted zone (PMZ) of an alloy, where localized liquid formation (i.e., liquation) occurs along grain boundaries as well as at isolated spots within grains. Fig. 4.6 compares solidification cracking and liquation cracking in a 6061 Al weld [347]. Both are intergranular. However, the fracture surface is dendritic with the former but smooth with the latter. Liquation cracking can occur if the PMZ is under significant tension, e.g., by the solidifying/contracting mushy zone nearby. Alloys with a wider freezing temperature range are more crack susceptible. In arc welding, a suitably designed filler metal can be used to eliminate liquation cracking. A simple criterion was proposed by Kou and coworkers and verified experimentally. It states that cracks occur if the weld-metal f_S > base-metal f_S after f_S reaches about 0.3. This criterion has been verified for Al and Mg alloys [111,112,348].

In some systems, water cooling was found to reduce liquation cracking [349]. It was suggested columnar grains grew more nearly
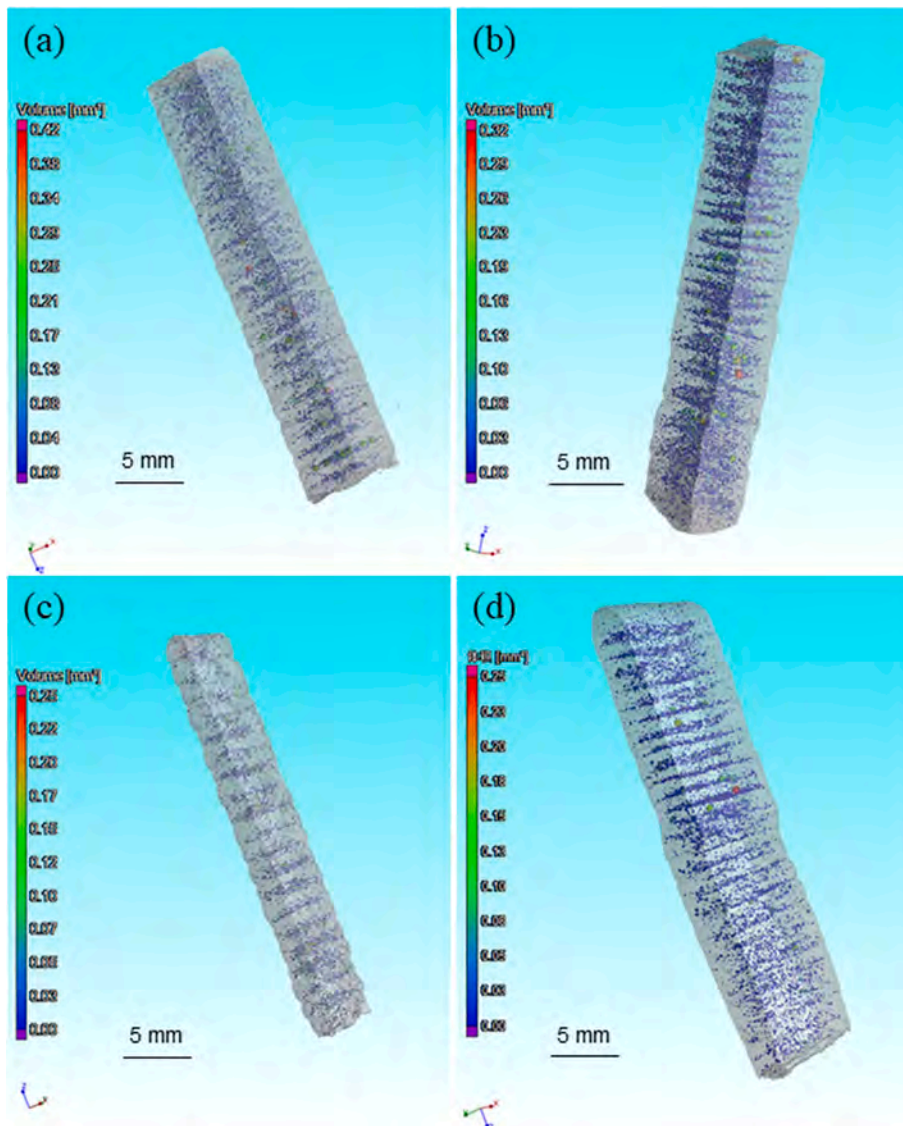
Fig. 4.8. Gas porosity during wire arc additive manufacturing of an Al-Zn-Mg alloy using cold metal transfer with (a) varying polarity, (b) fixed polarity, (c) varying polarity with arc voltage pulsing, and (d) fixed polarity with arc voltage pulsing [354].

vertically upward with water cooling, and this reduced the grain-boundary angle and hence the undercooling of the grain boundary liquid. In welding, the explanation can be straightforward, that is, water cooling reduces the extent of liquation and hence liquation cracking. The Laves/γ eutectic can remain liquid well below the liquidus temperature (~1355 °C), e.g., 1000 °C [350], thus allowing liquid films between grains to persist to promote both solidification and liquation cracking.

4.3.3. Lack of fusion and porosity

Additively manufactured aluminum alloy parts are susceptible to the lack of fusion voids and porosity both of which significantly degrade the mechanical properties of the parts [351,352]. Improper fusion adherence among the neighboring tracks results in the formation of lack-of-fusion voids [351,352]. Moisture from the atmosphere and the gas entrapped inside the gas-atomized powders often cause gas porosity inside the component [351,352]. Gas pores are spherical and their size is much smaller (<20 μm) than the typical lack of fusion voids. In contrast, the lack of fusion pores are often irregular in shape and often they are much bigger than the gas pores [274].

Lack of fusion is affected by the extent of overlap between two consecutive tracks. The extent of overlap between tracks can be controlled by adjusting the molten pool size and the distance between two neighboring tracks. A high hatch spacing that indicates more distance between two neighboring tracks reduces the overlap between two tracks [353] and increases the lack of fusion voids (Fig. 4.7 (a)). Parts made with small hatch spacing can reduce the lack of fusion voids but it needs more number of hatches to be deposited which decreases the productivity. Therefore, an estimation of an optimum hatch spacing is needed that reduces the lack of fusion voids without significantly affecting productivity. A selection of an optimum hatch spacing is often done by time-consuming and expensive experimental trials or by using mechanistic models. For the same hatch spacing, the lack of fusion voids can be reduced by increasing the pool size by increasing the heat source power or decreasing the scanning speed [353]. For example, the amount of lack of fusion voids during PBF-L of AlSi10Mg can be reduced (Fig. 4.7 (b)) by decreasing the scanning speed [353]. However, increasing heat input for reducing the lack of fusion voids may cause other issues such as distortion or accumulation of high residual stresses.

Aluminum alloys often react with moisture and produce hydrogen gas that is entrapped inside the molten pool and results in gas pores [274]. Moisture content can be reduced by drying up the powders by preheating. Therefore, preheated powders often show less gas porosity in parts. However, preheating powders adds an extra step and increases production costs. Since Zn has a low boiling point, additively manufactured parts of Al-Zn-Mg alloys such as high-strength 7xxx aluminum alloys often contain gas pores of Zn vapors (Fig. 4.8). These alloys are often used to print structural components using wire arc additive manufacturing where pores are reduced [354] by varying the arc polarity and pulsing the arc (Fig. 4.8). However, the exact mechanism of how pulsing and varying polarity reduces gas pores is not fully understood and needs further research. In addition, since aluminum alloys have low yield strength, gas pores often initiate cracks under high solidification stress [355]. Reduction of lack of fusion voids and gas pores in additively manufactured aluminum alloy parts remains an important challenge to improve the mechanical properties of parts. Post-process hot isostatic pressing can reduce the voids but adds an extra cost.
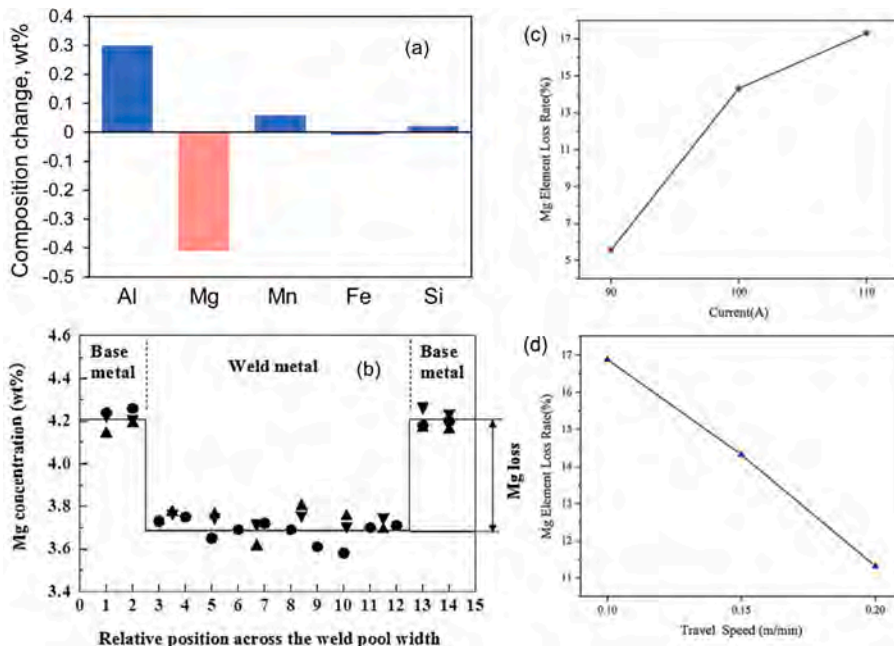
Fig. 4.9. (a) Composition change (in wt%) of major constituting elements during DED-EB of aluminum 2139 alloy. The plot is made using the data from [316]. (b) A reduction in Mg in the fusion zone during fusion welding of aluminum alloy 5182 [358]. The data were taken on three weld pool cross-sections of the same welding condition: laser power 3.0 kW, welding speed 105.8 mm/s, and beam defocusing 1.5 mm. Variations in Mg loss with (c) arc current and (d) travel speed during wire arc additive manufacturing of an aluminum alloy [113].

4.3.4. Composition change due to selective vaporization of alloying elements

Aluminum alloys often contain magnesium, zinc, copper, manganese, silicon, and some other elements in small quantities. These elements have very different vapor pressures. Therefore, they vaporize at different rates from the molten pool depending on their concentration and vapor pressure over the alloy. This selective vaporization of different alloying elements results in a change in the composition of the part from the feedstock [113,316,318,356,357]. Composition change can degrade the microstructure and corrosion resistance and may cause defects such as cracking.

The Fig. 4.9 (a) shows the composition change of major constituting elements during DED-EB of aluminum 2139 alloy [316]. Mg shows the maximum change in composition for the aluminum alloy considered. Similarly, depletion of magnesium [358] in the weld zone in bead-on-plate autogenous conduction mode laser welding of thin aluminum alloy 5182 plates (4.2 wt%Mg, 0.2%Si, 0.35% Mn, 0.07% Zn, 0.15%Cu, 0.1% Ti and balance Al) can be observed in Fig. 4.9 (b). These results indicate that relatively low boiling point elements, such as Mg, and Zn, selectively vaporize out of the molten pool more readily than other elements. The vaporization rate depends on the temperature distribution on the surface of the fusion zone. Reducing the temperature by reducing power or increasing speed can alleviate the severity of composition change. For example, Fig. 4.9 (c) and (d) indicate that loss in Mg during wire arc additive manufacturing of an aluminum alloy can be significantly reduced by reducing the arc current or by scanning faster [113].

5. Control of grain structure, phases, and defects in nickel alloys

5.1. Polycrystalline nickel alloys

A variety of polycrystalline parts of nickel-base alloys have been printed by fusion-based additive manufacturing processes. These alloys can be organized into three categories [359]: solid-solution strengthened alloys containing various substitutional elements such as Cr, Fe, Mo, Nb, and W, precipitation strengthened alloys containing precipitate forming elements such as Ti, Al, and/or Nb that form strengthening precipitates such as γ' ($Ni_3(Ti, Al)$) and γ'' (Ni_3Nb), and specialty alloys such as NiTi with shape memory effect and Ni-15Fe-5Mo with unique magnetic properties. The precipitation-strengthened alloys are further divided into two groups based on their fusion weldability [359]: weldable (e.g., Inconel 718 and Hastelloy X) and unweldable (e.g., CM247LC). This section is focused on the AM of solid-solution and precipitation strengthened nickel alloys. Detailed information on AM of shape memory and magnetic materials may be found in recent review articles by Elahinia et al. [360] and Chaudhary et al. [361], respectively.

Table 5.1 highlights selected literature articles on AM of various nickel alloys. INVAR, technically a Fe base alloy, is included since the solidified matrix phase is also FCC (γ-austenite). While sharing the same layer-by-layer printing approach, there are significant differences in the different AM processes [362–375] shown in Table 5.1. Particularly, due to the need for lightly sintering each layer of

Table 5.1
Nickel alloys printed by additive manufacturing. XRD stands for X-ray diffraction, and SEM stands for the scanning electron microscope.

Alloy	AM process	Salient features of the as-built microstructure	Reference
Solid-solution strengthened alloys			
Inconel 625	PBF-EB	Columnar grains parallel to the build direction; thin γ'' precipitates	[364]
Inconel 625	PBF-L	Columnar grains with strong $\langle 001 \rangle$ texture; no carbides or other precipitate phases detected by XRD or SEM	[365]
Inconel 625	DED-L	Columnar dendrites which grew epitaxially from the substrate; no precipitates detected by XRD or SEM	[366]
Hastelloy C-276	DED-GTA	Columnar dendrites; P (rho) phase precipitates	[408]
INVAR (Fe-36 wt % Ni)	PBF-L	Columnar γ grains grown epitaxially beyond several layers with texture near $\langle 001 \rangle$; nanosized α precipitates	[367]
Weldable precipitation strengthened alloys			
Inconel 718	PBF-EB	Columnar to equiaxed transitions by rapidly changing the electron beam heat source between point and line heating	[380]
Inconel 718	PBF-L	Fine columnar dendrites; precipitates comprising mostly Laves phase along with a small amount of NbC carbide	[409]
Inconel 718	DED-L	Columnar grains with spatial heterogeneity; γ'' precipitates formed at the bottom region of the build due to repeated heating and cooling	[368]
Hastelloy X	PBF-L	Columnar grains; nanoscale precipitates enriched in Al, Ti, Cr, and O	[369]
Hastelloy X	PBF-EB	Columnar grains with a strong texture in $\langle 001 \rangle$ direction; Mo-rich M_6C and Cr-rich $M_{23}C_6$ carbides	[370]
Hastelloy X	DED-GMA	Columnar grains near the substrate transitioned into cellular grains higher in the bead; Mo carbide	[371]
Haynes 282	PBF-L	Columnar grains aligned with the build direction; (Ti, Mo)C carbide particles, and no γ' precipitates detected	[372]
Haynes 282	DED-L	Columnar dendrites; γ', (Ti, Mo)C, and Mo-rich M_6C precipitates	[67]
Nimonic 263	PBF-L	Fine columnar grains with high dislocation density; some small MC carbides, and no γ' precipitates detected	[413]
Unweldable precipitation strengthened alloys			
Inconel 713LC	PBF-L	Columnar grains oriented in the build direction with some equiaxed grains on the upper surface; Cracks due to solidification cracking and ductility dip cracking	[414]
Inconel 738LC	PBF-L	Columnar grains with a preferential alignment of $\langle 001 \rangle$ along the build direction; very fine carbide and γ' precipitates	[362]
CM247LC	PBF-L	Fine, columnar grains with the preferential alignment of $\langle 001 \rangle$ along the build direction; fine MC carbides and very fine γ' precipitates; cracking particularly near the periphery of the samples	[373]
Rene 142	PBF-EB	Columnar grains; cuboidal γ' with volume fraction of 59%, and HfC precipitates; cracks observed	[374]
CMSX-4	PBF-EB	Polycrystalline, columnar grains; cuboidal γ' with volume fraction of 72%	[363]
CMSX-4	PBF-L	Polycrystalline, columnar grains; small Laves precipitates enriched in Re, W, and Ta, and no γ' precipitates detected by SEM; cracks observed	[375]

powder before melting, PBF-EB "inherently" operates with a high preheat, making it suitable to mitigate cracking issues. Such high-temperature preheating is not common for the other AM processes. The heat input in PBF-L, DED-L, and DED-GMA generally increase, resulting in a larger molten pool and lower cooling rate [3,4].

The existing literature on AM of nickel alloys has the following common features.

(i) The matrix phase, γ, tends to solidify in the form of fine, columnar dendrites. Such grain morphology results from the local solidification conditions. Fusion-based AM processes, especially PBF-L and PBF-EB, are characterized by very localized melting (e.g., molten pool having a width of the order of 0.1 mm) and fast travel (e.g., travel speed of the order of 1 m/s). Consequently, both the solidification rate (R) and the temperature gradient at the liquid/solid interface (G) are very high [3,4]. As shown in Fig. 5.1(a), the combination of high R and G results in columnar dendrites. Moreover, the scale or size of columnar grains decreases as the product of G and R, which corresponds to the cooling rate, increases. The high R and G values in PBF AM thus lead to fine dendrites with a primary dendrite arm spacing of the order of 1 μm.

(ii) Commonly, the as-built microstructure in PBF processes has a strong texture with the ⟨001⟩ direction aligned with the build direction. The solidification process during AM of nickel alloys is dominated by epitaxial growth from the substrate or the previously deposited layer. During the epitaxial growth, the dendrites for which the easy growth directions (i.e., ⟨001⟩ for FCC metals) are aligned with the maximum heat flow direction are favored. As shown in Fig. 5.1(b), the molten pool for PBF has the appearance of a flat tail where the maximum heat flow direction is vertically aligned with the build direction due to the fast travel speed [3,4]. As a result, dendritic grains oriented in ⟨001⟩ directions grow vertically resulting in a strong texture. On the other hand, the molten pool for DED has a more curved tail, and as a result, the grains grow in an inclined direction.
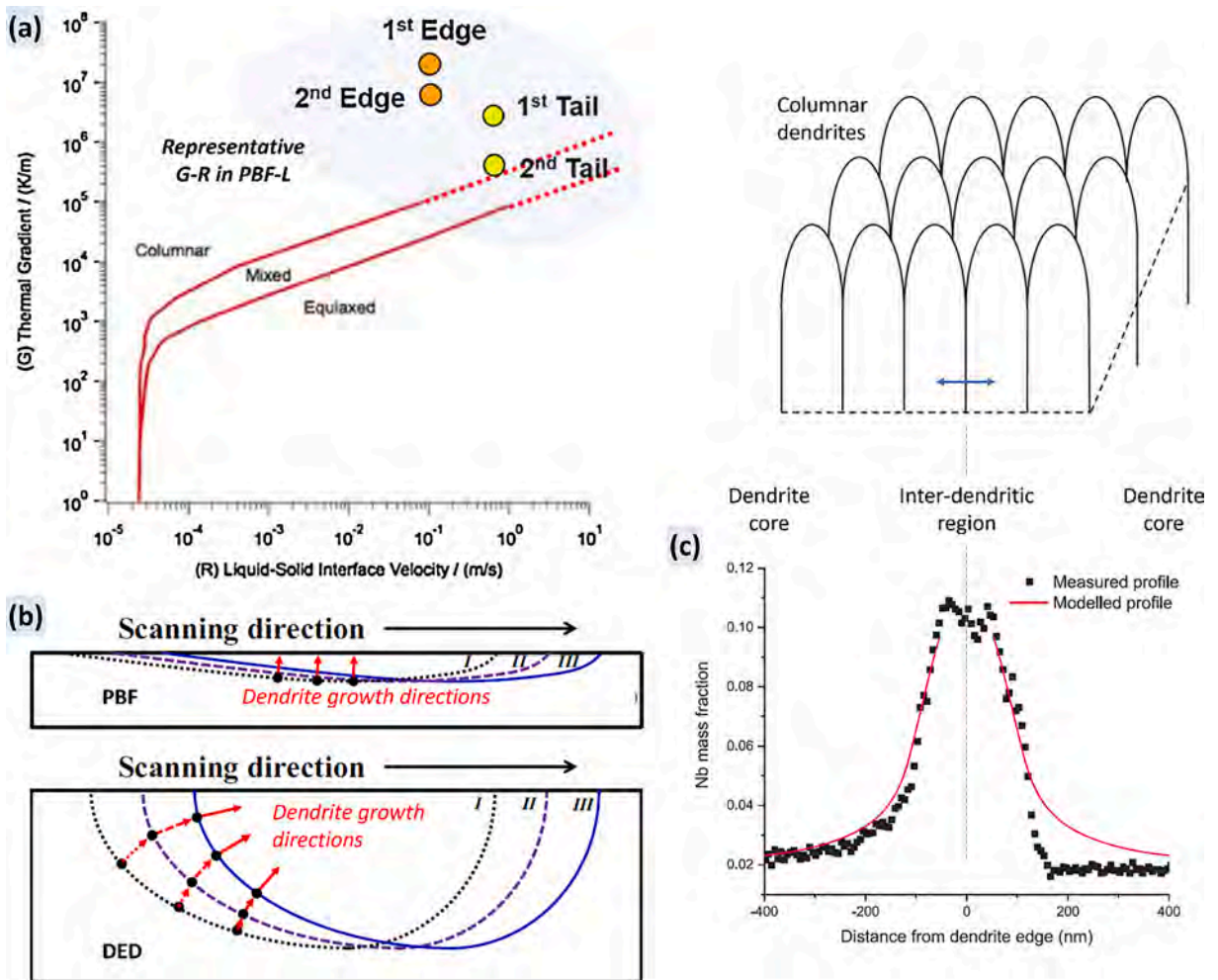
Fig. 5.1. (a) solidification map of IN718 superimposed with representative G and R values during solidification in PBF-L [4,383], (b) schematic illustration of dendrite growth directions in the central longitudinal plane during PBF versus DED [3], and (c) concentration profile of Nb from dendrite core to inter-dendritic region due to micro-segregation [376].

(iii) Micro-segregation is prevalent due to non-equilibrium solidification. An example [376] of the segregation of Nb from the dendrite core to the inter-dendritic region in an as-built IN718 is shown in Fig. 5.1(c). In addition to Nb, alloying elements such as C, Ta, and Al tend to segregate into the inter-dendritic region. Such micro-segregation results in the formation of carbides and topologically close-packed (TCP) phases such as Laves.

(iv) Whether or not the strengthening precipitates (γ' and γ") formed in the as-built microstructure depends on the local temperature experienced by the material. Due to the low preheat and rapid cooling in PBF-L, a discernable amount of γ' or γ" is generally not formed. On the other hand, in-situ "aging" can occur due to high preheat in PBF-EB or significant heat build-up in DED-L, resulting in the formation of γ' or γ".

(v) Compared with fusion welding, cracking issues in unweldable precipitation strengthened alloys printed by AM are generally less due to the low heat input and resulting fine microstructure and high preheat in PBF-EB.

The as-built microstructure and defects result from the complex interactions of materials and processing conditions. Detailed information on the mechanical properties of nickel alloys printed by PBF can be found in a recent review article by Sanchez et al. [377]. Strategies to improve the build quality in terms of grain structure, phases, and defects are reviewed here.

5.1.1. Strategies to control grain structure

5.1.1.1. Control spatial distribution of solidification conditions. The solidification mode can be altered by adjusting the local solidification conditions especially G and R. For PBF-EB of IN718, a transition from columnar to equiaxed solidification mode was achieved by rapidly changing the electron beam heat source between point and line heating [378–380]. As shown in Fig. 5.2, the solidification map is superimposed with the G and R values calculated using a fast analytical solution to the heat conduction equation. Most points in Region 1 where the processing parameters minimized the solidification cooling rate fell within the G-R space for equiaxed solidification mode. On the other hand, Region 2 where the cooling rate was maximized had more points in the columnar morphology zone. The grain structure for both regions corroborated well with the experimental data. Similarly, by controlling the local solidification conditions in the G-R space such as in the product form of $G^{-m}R^{-n}$ (where m and n are material parameters), Raghavan et al. [381] were able to alter the primary dendrite arm spacing from 4 to 10 μm using spot melt scanning patterns in PBF-EB of IN718. Rather than utilizing the spot melting, Helmer et al. [382] showed that the grain refinement was observed in PBF-EB of IN718 when the travel speed was increased and the hatch spacing was reduced correspondingly. Additionally, by altering electron beam power and scanning speed in PDB-EB of IN718, Ding et al. [379] were able to achieve the as-built microstructure ranging from fully columnar grains to mixtures of columnar and equiaxed grains. Fig. 5.4.

As mentioned previously, the common as-built microstructure in PBF of nickel alloys is columnar grains with a strong texture [383–385]. The strong texture can lead to severe anisotropy in mechanical properties [3], which is generally undesirable for structural applications. The laser scanning strategy has been varied to control the size and texture of the grains. Keshavarzkermani et al. [383] investigated the effect of four laser scanning patterns on the as-built microstructure of Hastelloy X printed by PBF-L. Fig. 5.3(a) shows two of the scanning strategies: Stripe Uni and Stripe Rot. The former resulted in the largest average grain size of 734 μm and the strongest texture due to repetitive heat flow patterns created in the successive layers. On the other hand, Stripe Rot scanning resulted in the smallest average grain size of 85 μm and the most randomly distributed texture due to the highest randomness in the heat flow directions [383]. Similar work was recently reported by Nadammal et al. [385] where the effect of four laser scanning patterns on the as-built microstructure of IN718 printed by PBF-L was studied. They also found that the 67° rotational strategy, similar to the Stripe
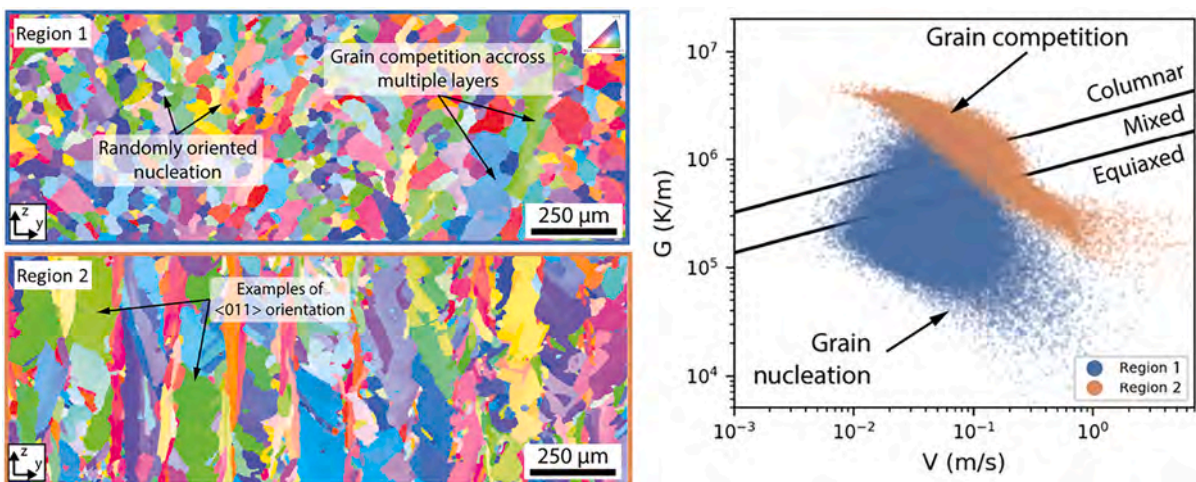
Fig. 5.2. The transition from columnar to equiaxed solidification mode achieved by controlling the spatial distribution of solidification conditions during PBF-EB of IN718 [378].
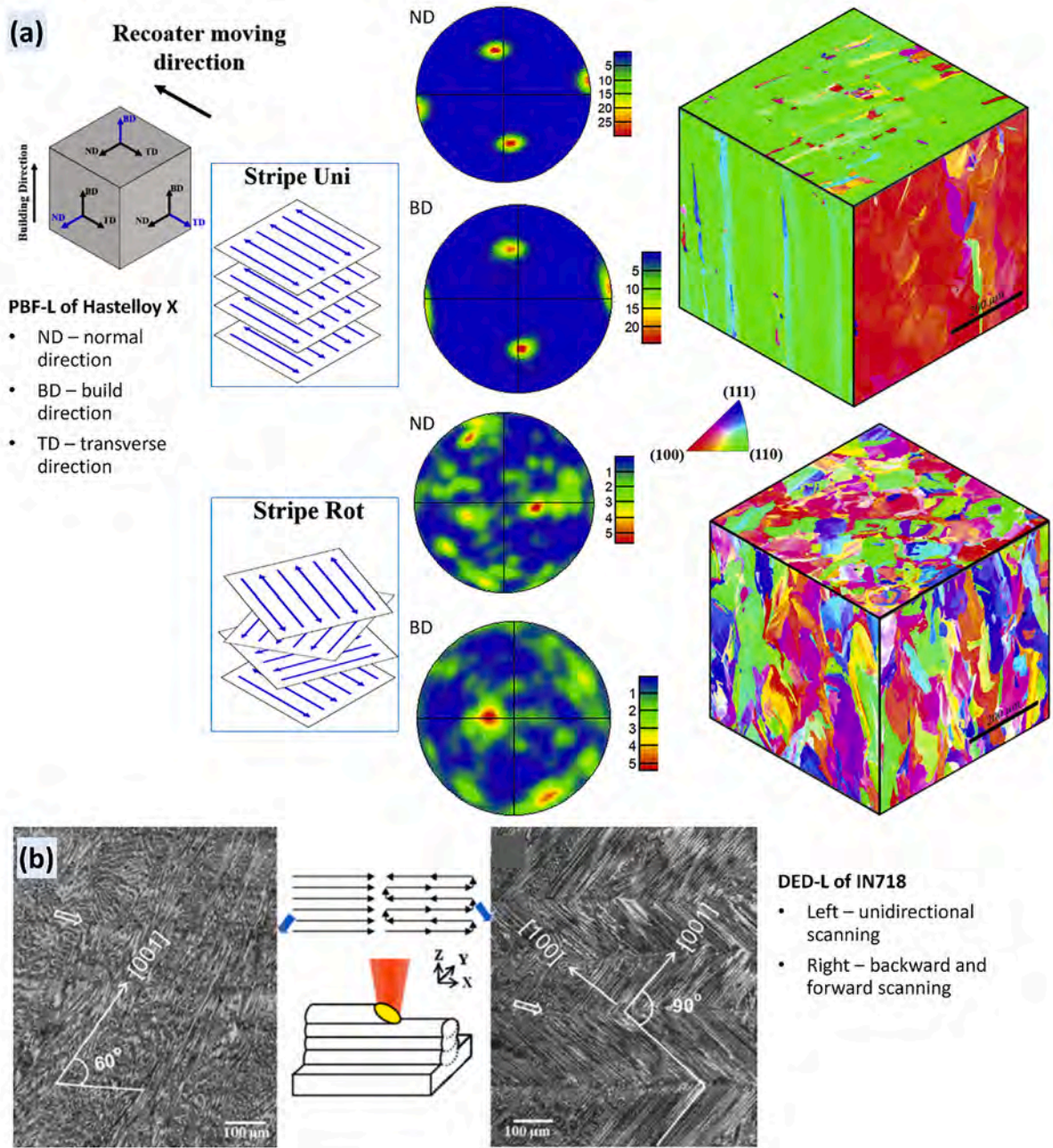
Fig. 5.3. (a) Stripe Uni versus Stripe Rot scanning strategies in PBF-L of Hastelloy X [383]. The former resulted in a large grain size of 734 μm and strong texture, whereas the latter resulted in a small grain size of 85 μm and most randomly distributed texture, and (b) Unidirectional versus backward and forward scanning patterns in DED-L of IN718 [392]. The former resulted in a strong ⟨001⟩ texture that was inclined at 30° to the build direction, whereas the latter developed a rotated cube texture.

Rot in [383] weakened the texture by forming finer microstructural features.

For PBF-L of IN738LC, an unweldable nickel alloy, Geiger et al. [386] studied scanning strategies with three different rotation angles: 90°, 45° and 67°. On a plane parallel to the build direction, all three rotation angles resulted in columnar grains with strong ⟨001⟩ texture aligned with the build direction. On a plane perpendicular to the build direction, the scanning strategy with 67° rotation angle resulted in a uniform mixture of grains with ⟨001⟩ and ⟨011⟩ orientations, whereas the 90° and 45° rotation angles resulted in grains with predominately ⟨001⟩ orientation.

Unlike the above studies on PBF-L [383–389] where the laser power was held constant, Popovich et al. [390]. studied PBF-L of IN718 printed with two laser powers: 250 and 950 W. As expected, the high laser power resulted in much coarser columnar grains than
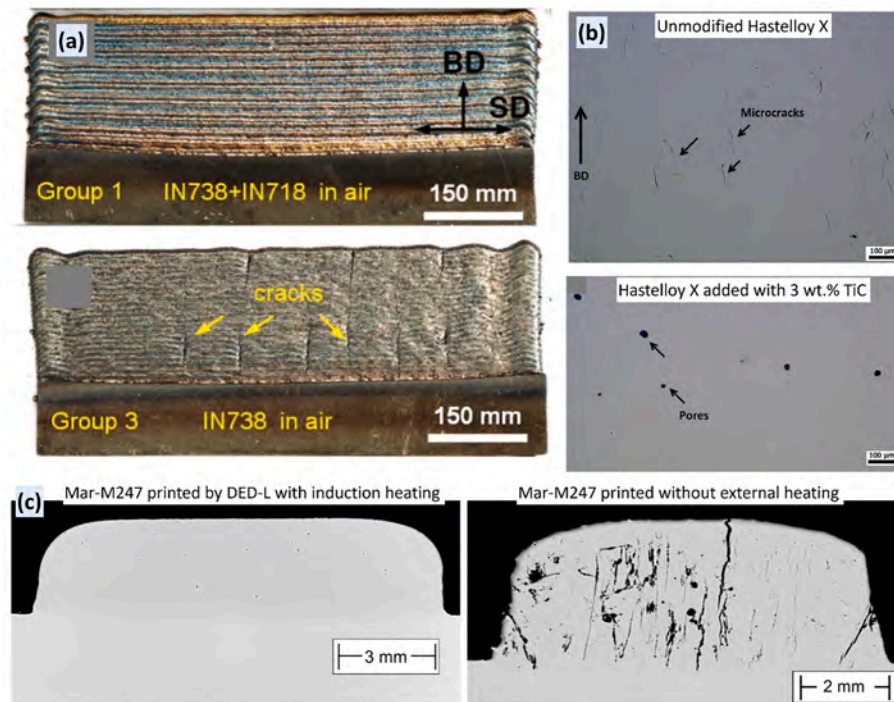
Fig. 5.4. Reduction of solidification cracking by (a) periodic deposition of an IN718 layer after every 2 layers of IN738 [415], (b) addition of 3 wt% TiC nanoparticles [399], and (c) application of induction heating [420] to preheat the substrate. Courtesy of figure (c): Dr. André Seidel from Institute for Machine Tools and Forming Technology IWU.

the lower laser power. An interesting part of their study is the printing of the graded sample where different parts along the built height were printed with a laser power of either 250 or 950 W, resulting in a sharp transition in the microstructure.

The effective laser power was altered by using a pulsed laser instead of a continuous wave laser in the DED-L of IN718 by Xiao et al. [391]. The pulsed laser resulted in a refined dendrite microstructure, which was attributed to a faster cooling rate and shorter solidification time of the molten pool. For the DED-L of IN718, Dinda et al. [392] studied the effect of laser beam scanning patterns on dendrite growth morphology. As shown in Figure 5.3(b), the unidirectional laser beam scanning pattern developed a strong ⟨001⟩ texture that was inclined at 30° to the build direction and 60° with the scanning direction. On the other hand, a backward and forward scanning pattern developed a rotated cube texture. The bidirectional scanning strategy breaks the long columnar grains and results in a zig-zag pattern of the orientation of the primary dendrites with about 15° misorientation with the primary heat flow direction [156]. As described earlier, the formation of different textures is largely affected by how well dendrites with ⟨001⟩ orientation are aligned with the maximum heat flow direction [3].

5.1.1.2. Formation of equiaxed grains by adding inoculants. The addition of inoculants or grain refiners represents a metallurgical approach to increase the number of nucleation sites and thus new grains. A variety of inoculants have been tested for grain refinement in additively manufactured nickel alloys. The inoculants can be divided into the following three groups.

The first group is yttria (Y_2O_3), which is the primary strengthening agent utilized in a special class of nickel alloys known as oxide dispersion strengthened (ODS) nickel alloys. Tan et al. [393] studied DED-L of an ODS nickel alloy where the nickel alloy powder (Ni-21Cr-0.85Fe-0.57Ti-0.25Al by wt.%) was mechanically alloyed with 0.6 wt% YH_2 powder. During the high-energy mechanical alloying process, Y and O dissolved into the powder. Dispersed oxides in the form of Y-O and Al-O oxide cores surrounded by Cr-rich shells were generated after DED-L although the oxide's size and number density were larger than those in a reference material prepared by the standard hot extrusion process using the same mechanical alloyed powder. Additionally, the as-built microstructure mainly comprised columnar dendrites growing along the build direction. When compared to another DED-L sample using nickel alloy powder without mechanical alloying, the oxides formed in DED-L with mechanically alloyed powder refined the columnar grains. Kenel et al. [394] mechanically alloyed a Ni-Cr-Al-Ti model alloy powder with 0.5 to 1 wt% Y_2O_3 nano-powder, and the alloyed powder was printed by PBF-L. It was observed that most Y_2O_3 dispersoids were consumed by processes such as reaction with Al or Al_2O_3 to form a liquid $Y_4Al_2O_9$ slag. Nevertheless, some of the added Y_2O_3 dispersoids were successfully distributed through the solidified matrix as nano-dispersoids without coarsening, noticeably reducing grain size compared to the unmodified base alloy. Additional information on AM of oxide-dispersion strengthened nickel alloys may be found in a recent review article by Wilms [395].

The second group of added inoculants is various ceramic particles, resulting in the formation of metal matrix composites after printing. Ghodsi et al. [396] used a powder decoration method to produce composite IN625 particles with submicron yttria-stabilized

zirconia (YSZ) particles uniformly distributed on the surface. Compared to the unmodified IN625, the YSZ added IN625 resulted in the formation of small grains, thus supporting the role of YSZ as a nucleation agent. TiC particles were added to Inconel 625 for DED-L by Hong et al. [397], IN718 for PBF-L by Gu et al. [398], and Hastelloy X for PBF-L by Han et al. [399]. All those studies used ball milling or high-speed mixing to "coat" the nickel alloy powder with nanoparticles of TiC. After printing, TiC particles were found to be uniformly dispersed along the grain boundaries and inside the grains, and grain refinement was observed in the nickel alloys added with TiC. TiB_2 particles were added to Hastelloy X for PBF-L by Yang et al. [400] and to Inconel 625 for DED-L by Zhang et al. [401]. Grain refinement was observed in the former but absent in the latter; the difference is likely caused by the different heat input and alloy composition used in those two studies.

The third group of added inoculants is based on carbon. Wang et al. [402] coated IN625 powder with multi-walled carbon nanotubes (MWCNTs), and the coated powder was used to print rectangular bars by PBF-L. A very low concentration of MWCNTs was observed inside the γ matrix. Moreover, there was a significant enrichment of Mo and Nb around the MWCNT, indicating the formation of carbides on the boundary between MWCNT and the metal matrix. Nevertheless, the addition of MWCNTs resulted in grain refinement for IN625. In another study by Chen et al. [403], the powders of precipitation strengthened nickel alloy K418 were coated with graphene nanoplatelets (GNPs) by plasma-assisted ball milling and then printed by PBF-L. It was found that the majority of GNPs were uniformly dispersed within the γ grains. The columnar grains of the as-built K418 sample were transformed into approximately equiaxed grains by the addition of GNPs.

5.1.1.3. Modification of alloy composition. Kong et al. [404] studied the effect of Nb on the grain size for IN718 printed by DED-L. A dual-feed system was used to deliver a mixture of two IN718 powders: one containing 1.0 wt% Nb and the other containing 8.0 wt% Nb. By controlling the delivery rate of each powder, the Nb content of the fabricated samples was varied. It was found that the grain size rapidly decreased from 300 μm to 70 μm as the Nb content increased from 1 to 6 wt%. The grain refinement was attributed to the solute drag or pinning effect of Nb as well as increased nucleation sites with a higher amount of Nb.

5.1.1.4. Breaking up long columnar grains by external agitations. The application of high-intensity ultrasound to the liquid metal for refining the solidification grain structure is well studied in the casting and welding literature [405]. A key mechanism for grain refinement is the acoustic cavitation process during which bubbles are created. When a bubble collapses, intense, localized shock waves are emitted, fracturing the already solidified dendrites. The fractured dendrite pieces are carried away by the acoustic stream and serve as heterogeneous nuclei, promoting the formation of fine equiaxed grains.

Todaro et al. [273] deposited IN625 powder by DED-L onto a 4140 stainless steel substrate (sonotrode) that was vibrating at 20 kHz along the build direction. A substantial reduction in grain size was observed in the deposit with ultrasonic vibration when compared to the standard one without ultrasound. The effect of ultrasonic vibration on IN718 printed by DED-L was studied by Wang et al. [406]. The part was deposited also on a substrate that vibrated along the build direction. Three ultrasound frequencies, 25, 33, and 41 kHz, were evaluated. The grain size was reduced from 7 μm at 25 kHz to 4 μm at 41 kHz and the aspect ratio was decreased as well.

5.1.1.5. Comparison of different grain structure control approaches. Following the classification scheme used in [390], the existing approaches for controlling the solidification grain structure can be divided into three categories: thermal, metallurgical, and mechanical. The thermal approach largely relies on the manipulation of processing parameters to control the spatial variation of solidification conditions (e.g., G and R) and consequently the extent of columnar versus equiaxed grains. The advantage of the thermal approach is that they are readily implementable and can be applied to different materials. On the other hand, the extent of control can be limited especially for PBF-L and DED processes. Even for PBF-EB which offers high flexibility in controlling G and R, the scanning strategies developed on simple geometries may produce different grain structures when printing complex geometries [407].

The addition of inoculants or modification of alloy composition represents the metallurgical approach toward controlling the grain structure. Such an approach can be very effective in refining the grain structure. However, coating the nickel alloy powder with the desired inoculant is commonly done through an elaborative process such as ball milling. Moreover, the addition of inoculants into the molten pool can increase the formation of defects. Modification of alloy composition [387,404,408] can result in a nickel alloy whose composition falls outside of the industry specification. For example, the standard specification for IN718 limits Nb plus Ta to 4.75 to 5.50 wt% [387]. The study by Kong et al. [404] had an Nb concentration from 1.0 to 6.0 wt%.

Introducing ultrasonic vibration to the molten pool represents the mechanical approach to controlling the grain structure. This approach can be highly effective and does not require any modification to the alloy metallurgically. However, additional equipment is needed. Moreover, the existing studies in [273,380,406,409] printed small samples on a substrate that was vibrating ultrasonically. Scaling up this approach to large and heavy parts would require further study.

5.1.2. Phase control strategies

As shown in Table 5.1, the as-printed phases of nickel alloys include the FCC (γ) matrix phase and various precipitates such as carbides, Laves, γ' and γ". The formation of carbides and Laves is largely affected by the non-equilibrium solidification process, especially micro-segregation of alloying elements into the interdendritic region. For example, for the most frequently studied alloy in AM, IN718, Laves phase, a topologically close-packed phase with a nominal composition of Ni_2Nb, is ubiquitously present in the as-printed microstructure due to the Nb segregation into liquid during non-equilibrium solidification. These precipitates are commonly observed at the interdendritic regions or grain boundaries as they form near the final stage of solidification. The carbides formed range from NbC in IN718 [409], (Ti, Mo)C in Haynes 282 [372,393,394], Mo-rich M_6C and Cr-rich $M_{23}C_6$ in Hastelloy X [370], to HfC in

Rene 142 [374]. On the other hand, the formation of strengthening precipitates γ' and γ" via solid-state phase transformation, is largely affected by the preheating or heat build-up in the part. In addition to these precipitates, the as-printed microstructure has been found to contain oxide inclusions due to the reaction of alloying elements particularly Al with the oxygen in the build chamber in both PBF-L (inert gas) and PBF-EB (high vacuum) [384,388].

The phases formed are affected by the thermodynamics and kinetics of phase transformations, which in turn are affected by the alloy's composition. In the study by Kong et al. [404],Laves precipitates were not detected in the as-built microstructure when the Nb content was below 2 wt%, and they were detected at higher Nb contents. However, much of the work to date on controlling alloy compositions is focused not on controlling phases but instead on controlling defects, especially cracking, as discussed in the next section.

The majority of work on controlling phases is thermally based. It has been applied to both precipitates formed during solidification and those formed via solid-state phase transformations [391,410]. The size of Laves particles, closely correlated to that of the γ dendrites, is largely affected by the cooling rate. For example, for the DED-L of IN718, Xiao et al. [391] observed long chain-like Laves particles along the boundaries of coarse columnar dendrites in a continuous-wave laser. When a pulsed laser was used and the resultant cooling rate was high, fine, disperse Laves particles formed along the boundaries of refined dendrites.

The fast-traveling heat source used in AM results in a cooling rate that is generally too fast for solid-state transformations to take place. However, the high preheat inherent to PBF-EB and the heat build-up in DED can expose the material locally to evaluated temperatures over an extended time. Upon slow cooling from the evaluated temperatures, strengthening precipitates γ" and γ' can form in the as-built microstructure. For example, cuboidal γ' with a volume fraction of 59% was observed in the as-built microstructure of Rene 142 printed by PBF-EB [374]. Additionally, Sames et al. [389] intentionally heated the top surface of a completed build by a scanning electron beam and achieved in-situ solution treatment and aging of IN718.

5.1.3. Control of common defects

Common defects in additively manufactured nickel alloys include porosity due to lack of fusion or keyhole instability, spattering due to ejection of liquid metal droplets or powder particles, surface roughness caused by stair-step effect, instabilities of the molten pool, or partially melted powder particles attached to the surface, and various cracking issues [3,4]. Porosity defects are commonly mitigated by printing process optimization. Moreover, defects such as porosity, spattering, and surface roughness can be mitigated by additional post-fabrication processing such as hot isostatic pressing (HIP) or machining. The following discussion is thus focused on the control and mitigation of cracking, which is the most detrimental defect hindering the qualification of many high-temperature nickel superalloys for AM.

5.1.3.1. Cracking. Similar to welding, fusion-based additive manufacturing subjects a nickel alloy, especially that containing a high amount of γ' forming elements (e.g., Al and Ti) to a wide range of cracking issues including solidification cracking, liquation cracking, ductility dip cracking, and strain age cracking [3,4]. Compared to welding, the susceptibility to cracking for AM is generally lowered due to the fine microstructures common in PBF and the high preheat inherent to PBF-EB. However, obtaining crack-free parts remains difficult for unweldable, precipitation strengthened nickel alloys, and cracking remains an important issue for nickel alloys.

Mechanisms for crack formation are complex but they typically involve the thermally-induced tensile stress and the material's resistance to cracking at high temperatures [359]. The approaches to control and mitigate cracks tackle one or both of these factors, and they can be divided into two categories: metallurgical based, and processing based.

Designing alloy compositions that can produce crack-free parts by AM lies at the heart of the metallurgical-based approach. Tang et al. [410] performed a comprehensive alloys-by-design study where the effect of alloying composition on various cracking susceptibilities was computed computationally. For example, the susceptibility to solidification cracking was analyzed based on the freezing temperature range and solidification cracking index, and the susceptibility to solid-state cracking was analyzed based on the temperature and extent of γ' precipitation. Their analyses led to the development of a new experimental alloy that contained 1.29 wt% Al and 2.22 wt% Ti. The alloy printed by PBF-L was free of cracks, and the heat-treated material had a low-temperature strength comparable to but somewhat lower creep performance than CM247LC. Jena et al. [411] studied LW 4275 nickel superalloy which contained 5.1 wt% Al but no Ti. The alloy printed by PBF-L was also free of cracks. After post-fabrication heat treatment, γ' with volume fraction of 48% was formed. Compared to conventional alloys such as IN738 and Rene 80, the printed LW 4275 had somewhat inferior creep properties but superior ultimate tensile strength and elongation.

For nickel alloys that are considered weldable but can still suffer from cracking, tighter control of the alloy composition can reduce the cracking issue in AM. For example, Harrison et al. [412] controlled the composition of a modified Hastelloy X in such a way that the concentration of solid solution strengthening elements (e.g., W) was slightly increased and that of the tramp elements (e.g., Mn) was slightly decreased when compared to a standard Hastelloy X. The modified alloy, which composition was still within the pertinent industry specification, displayed a 65% reduction in solid-state crack density when compared to the standard alloy.

Instead of modifying the feedstock composition as in [67,410–414], Zhang et al. [415] modified the local composition in-situ during the DED-L of IN738. An IN718 layer was deposited every 2 layers of IN738 to create a layered, composite material that was free of cracks, as shown in Figure 5.4(a). Since the printing of IN718 did not interrupt the epitaxial growth of grains, the mechanisms for crack mitigation were attributed to the disruption of γ' precipitates as well as the thermal stress on IN738 alleviated by the softer IN718.

The addition of inoculants represents another group microstructure-based approach to control solidification cracking [416]. As discussed earlier, Han et al. [399] studied the addition of TiC particles to Hastelloy X for PBF-L. The addition of 3 wt% TiC

nanoparticles [399] refined the grains and thus increased grain boundaries, which in turn mitigated intergranular microcracks, as shown in Figure 5.4(b). The addition of 2 wt% TiB_2 particles to Hastelloy X was also found to refine the grains and mitigate the cracks in PBF-L [417].

Controlling scanning strategies and processing parameters is commonly used for mitigating cracking issues. Catchpole-Smith et al. [418] studied the effect of scanning strategies on cracking in CM247LC printed by PBF-L. The cracks were identified as solidification and liquation cracks. It was found that the fractal scanning strategy where the laser traveled in a tortuous path based on Hilbert or Peano-Gosper area filling curve reduced the crack length density when compared to the conventional island scanning strategy. No significant difference in microstructure was observed between the two scanning strategies, and thus the reduction in cracking was attributed to the prevention of stress build-up when the fractal scanning strategy was used. It is noted that cracking was not eliminated in their study. Kontis et al. [419] used a higher scanning speed and a reduced hatch spacing to obtain a fine-grained microstructure in an unweldable nickel alloy containing 5.30 wt% of Ti and 8.70 wt% of Al printed by PBF-EB. They identified that liquation cracking was caused by micro-segregation of B, Cr, and Mo to high-angle grain boundaries (HAGBs). The cracks were mitigated for a fine-grained equiaxed or a columnar microstructure with a grain width smaller than 100 μm. It is expected that the high preheat of 1050 °C (1323 K) used in their study helped with the mitigation of cracks. The importance of build temperature on crack formation was studied in PBF-EB of CMSX-4 by Ramsperger et al. [363]. It was found that the pyramid-shaped samples contained cracks at the lower build temperature of 940 °C (1213 K) and did not contain cracks at the higher build temperature of 1040 °C (1313 K).

The application of external heating is another processing-based approach. Seidel et al. [420] used induction heating to preheat the substrate's top surface temperature to 900 °C (1173 K) for DED-L of Mar-M247 and CM247LC alloys. Such high preheat decreased the temperature gradient between the melt pool and the substrate and consequently the thermally induced tensile stress. As a result, solidification and liquation cracking was significantly reduced, as shown in Figure 5.4(c). They further demonstrated the use of high preheats for printing a miniature turbine blade made of CM247LC. The preheat temperature was increased to 1100 °C (1373 K). Lee et al. [416] also used a high preheat of 1025 °C (1298 K) for PBF-EB of Mar-M247. Asymmetric cracking was observed in cylindrical parts built at tilting angles from 30 to 50°. The microstructural factor for cracking was ruled out, and the thermally induced tensile stress was identified as the cause of cracking. The studies by Seidel et al. [420] and Lee et al. [416] indicate that the use of high preheat is necessary but may not be sufficient to fully mitigate cracking when printing un-weldable nickel alloys. The thermally induced stress still needs to be managed.

Kalentics et al. [417] applied laser shock peening after printing every *n*-th layer, where $n = 3$, 10, or 20, during PBF-L of CM247LC. Compared to untreated alloy, a significant reduction in bulk crack density by up to 95% was obtained using laser shock peening. It was postulated that the crack reduction was caused by the introduction of a compressive stress field near the laser shock-peened surface. Vertical cracks formed during printing would be closed by such a compressive stress field. Upon deposition of additional layers, the closed cracks were reheated and diffusion caused the cracks to be healed.

In summary, the elimination of cracks remains a significant challenge for AM of unweldable nickel alloys. Designing new alloy compositions with sound printability is most desirable. While a tremendous stride has been made in the alloy design considering various cracking susceptibilities, the published literature shows that the creep properties of new printable alloys are yet to match those of conventional high γ' nickel alloys, e.g., CM247LC and IN738. The use of high preheat is essential to mitigate solidification or liquation cracking although the thermally induced stress needs to be carefully managed to avoid cracking.

5.1.3.2. Lack of fusion, porosity, and composition change. Additively manufactured nickel alloy parts are susceptible to the lack of fusion voids and gas porosity both of which significantly degrade the mechanical properties of the parts [421–423]. Improper fusional
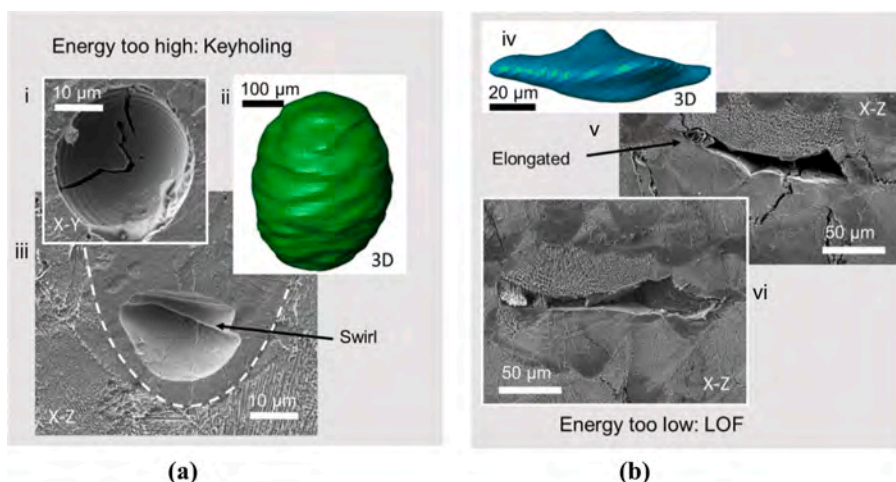
Fig. 5.5. (a) keyhole pores formed at very high energy of the heat source and (b) lack of fusion (LOF) voids formed at very low energy during PBF-L of a nickel alloy IN713C. The image i is an SEM of a keyhole pore. Image ii shows an XCT reconstruction of the pore. Image iii shows an SEM image on a different plane. Image iv shows an XCT reconstruction of a lack of fusion void. Image v and image vi show SEM images of the void [424].

bonding among the neighboring tracks results in the lack of fusion voids. Moisture from the atmosphere and the gas entrapped inside the gas-atomized powders often cause gas porosity inside the component. Pores can also be generated from the gas bubble originating from a collapse of a keyhole. The shape and size of pores and voids can vary significantly. Fig. 5.5 shows the morphologies of keyhole pores and the lack of fusion voids during PBF-L of a nickel alloy IN713C [424]. Keyhole pores are spherical but elongated in shape and their size varies significantly. In contrast, the lack of fusion pores are often irregular in shape and often they are bigger than the gas pores. Pores are observed in optical micrographs of Inconel 718 samples produced by PBF-L with varying laser power and laser scan speed [425]. Keyhole pores are found at a very high laser power or slow scan rates. In contrast, at low power or high speed, the lack of fusion voids are formed due to insufficient melting. Therefore, optimum combinations of powers and speeds are necessary to print void-free parts. Printing parts using smaller hatch spacing can significantly reduce the lack of fusion in Inconel 718 parts made by PBF-L [425].

Nickel alloys generally consist of nickel, chromium, molybdenum, aluminum, iron, and some other elements in small quantities. These elements have very different vapor pressures. Therefore, they vaporize at different rates from the molten pool. This selective vaporization of different alloying elements results in a change in the part composition compared with the feedstock. For example, Fig. 5.6 shows that the composition of the constituting elements changes significantly during PBF-L of Inconel 718 [114]. Composition change can degrade the microstructure and corrosion resistance and may cause defects such as cracking. An optimum set of processing conditions need to be found to reduce composition change which is often done by using well-tested mechanistic models.

5.2. Single crystals of nickel alloys

In a single crystal (SX) part, the crystal lattice of the entire component is continuous with no grain boundaries [426]. The absence of defects related to the grain boundaries can provide the single crystal components with unique mechanical properties such as superior high temperature creep resistance [426]. That is why single crystal parts are used in high-temperature applications such as turbine blades in a jet engine [427]. Printing single crystals using additive manufacturing (AM) is a recent concept and is getting popularity because of its unique advantage of repairing cracks in expensive turbine blades with desired microstructure and properties. The literature on AM of SXs is growing and therefore it is necessary to include the fundamentals of printing SXs and their structure, properties, and performance in this review. This section describes the commonly used AM processes for the manufacturing of SX parts. In addition, theories for directional solidification to maintain single crystallinity are discussed. Furthermore, a comprehensive comparison of the mechanical properties of printed SXs and conventionally processed SXs is provided. Finally, control strategies for stray grain formation and defects in SX are reviewed.

5.2.1. Theories of printing single crystals

Deposition and repair of single crystals require close control of process variables to achieve solidification growth rates and temperature gradients. The main task is to avoid equiaxed grain formation by controlling solidification parameters, such as appropriate temperature gradient (G) and solidification growth rate (R). In addition, providing a high power density ensures sufficient depth of melting to have epitaxial growth with the underlying crystal. In addition to thermal control of G and R values, SX solidification also requires appropriate seeding. In such solidification, a solid grain is nucleated from the liquid onto a substrate in contact with the liquid. The substrate (or the seed) provides direction to the new grain growth and if appropriate thermal conditions are met, this grain can become an SX grain. A noteworthy point is this mode of solidification requires the partial or complete melt back of the substrate which provides seeding for the grain growth. Hence, the substrate must be an SX one if SX solidification is required. However, having an SX substrate does not guarantee SX solidification if the thermal conditions are not adequate and appropriate. This requirement was later
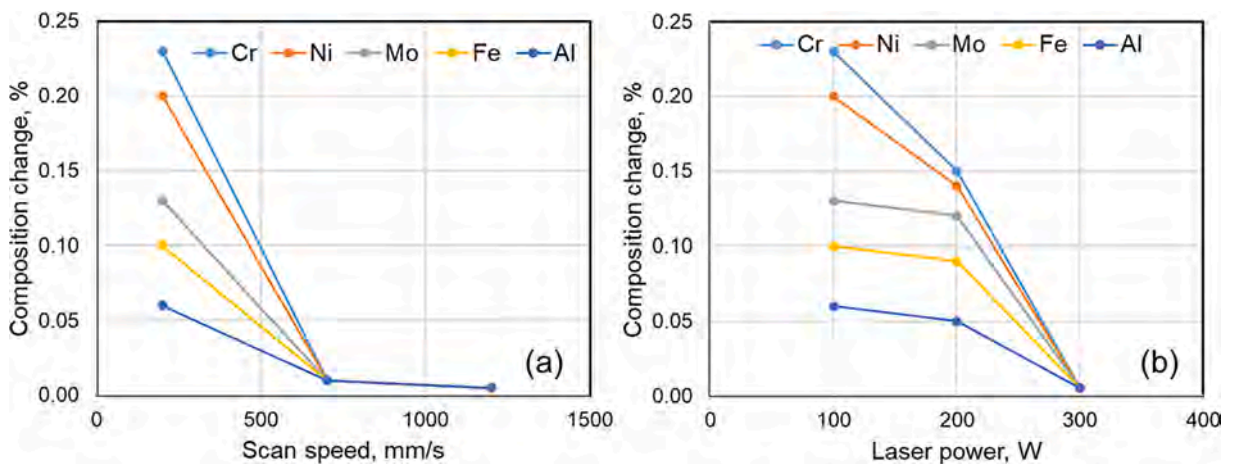
Fig. 5.6. Change in concentration of elements for (a) varying scan speed, (b) varying power during PBF-L of Inconel 718. The figure is made using data reported in [114].

proved to be wrong by Gotterbarm et al. [428] who successfully deposited SX Inconel® on EQ Inconel® via a novel scan strategy during E-PBF.

A good starting point is to use a well-tested model [185,429–431] of heat transfer and fluid flow that can provide solidification parameters from process variables so that maps of solidification growth rates and temperature gradients can be constructed from process variables. Plots of solidification growth rates versus temperature gradients can then be used to avoid equiaxed grains and achieve deposition of repair of single crystals. In addition, sufficient depth of the fusion zone can ensure epitaxy with the previously deposited layer.

5.2.2. AM processes for printing single crystals

Both powder bed fusion and directed energy deposition processes [2,3,8] are used to print single crystal alloy parts. For example, nickel alloy CMSX-4 is printed using PBF-L [432–434], DED-L [435], and PBF-EB to make single crystal parts [436–440]. DED-L is also used to make single crystal parts [441] of another nickel alloy Rene N5. Table 5.2 summarizes the recent applications of different AM processes to print single crystal parts. The most important criteria to print a single crystal is to maintain a particular temperature gradient [29,442,443] and solidification growth rate [29,442,443] throughout the process to facilitate directional solidification [441]. Desired temperature gradient and solidification growth rate to grow single crystals are often achieved by preheating the powder bed [436–440] and using complex combinations of scanning patterns and scanning speeds [435,441].

5.2.3. Recent examples of printed single crystals of nickel alloys

Additively manufactured single crystals can be of different sizes. For example, Fig. 5.7 (a) shows a longitudinal section of a 75 mm long and 12 mm diameter CMSX-4 single crystal cylinder [440] fabricated using PBF-EB. The horizontal section of the SX cylinder as well as the EBSD mapping shown in Fig. 5.7 (b) also indicate the single crystallinity of the component. Additively manufactured single crystals can be grown from both single-crystalline as well as polycrystalline substrates of different shapes and sizes. SXs of nickel-base superalloys such as CMSX-4 and Rene are manufactured and repaired using AM [432–434]. Since most of the nickel base superalloys exhibit FCC structure, AM build direction [440] is commonly along ⟨001⟩. Several researchers have printed components with dendrites aligned along ⟨001⟩ with very small misorientation angle among them and termed them as single crystals [441]. In those cases, dendritic arm spacing is an important microstructural feature that controls the mechanical properties of the component [441]. In SXs of nickel alloys, secondary phases such as laves phase are often observed [441]. Recent examples of additively manufactured single crystals of nickel alloys along with their important features are summarized in Table 5.2.

5.2.4. Properties of printed vs conventionally processed SXs

Single crystal AM parts often show poor tensile strength due to a lack of grain boundary strengthening [440]. Often unwanted secondary phases form in additively manufactured SXs which also affect the tensile properties of the part [440]. Due to the absence of grain boundaries, tensile properties of additively manufactured SXs are generally isotropic unlike common AM parts [440].

There are two main reasons why additively manufactured SXs are better than those processed conventionally. First, cracks in expensive, single-crystal turbine blades can be repaired by AM by depositing material inside the crack where the deposited material has the same microstructure as the original component [432,433]. Second, printed single crystal parts are often found to have high

Table 5.2
Selected examples of additive manufacturing of single crystal of nickel alloys.

AM process	Alloys	Descriptions and features	References
PBF-L	CMSX-4	Rapid scanning of the laser beam (up to 2 m/s) and high-resolution raster scanning (20 to 200 μm hatch spacing) were used to achieve the temperature gradient of 10^4 to 10^5 K/m necessary for directional solidification.	[432,433]
PBF-L	CMSX-4	A bi-directional raster scanning pattern combined with a rapid scanning in the order of one m/s was used to achieve directional solidification	[434]
DED-L	Rene N5	Around 5 mm tall parts were deposited that exhibited stray grains near the top.	[435]
PBF-L	Rene 142	A raster scanning pattern by a very focused beam was implemented to achieve the directional solidification. SX of around 10 mm in length and 1.5 mm in thickness was deposited for repairing a SX part.	[444]
PBF-EB	CMSX-4	A preheating temperature of 1270 K combined with a unique bi-directional scanning strategy where the scanning direction is rotated by 90° between two consecutive layers was used to achieve the directional solidification. Around 50 mm long SX was made. However, the part suffered from γ´ precipitates.	[436]
PBF-EB	CMSX-4	The powder bed was preheated to 1273 K. In addition, a 'cross snake hatch strategy' was used where the scanning direction is rotated by 90° between two consecutive layers. Both helped to obtain the directional solidification. Processed parts were cylindrical with 12 mm in diameter and 78 mm in height. However, the parts suffered from porosities.	[437]
PBF-EB	CMSX-4	A preheating temperature of 1273 K and a special scanning strategy were used to achieve directional solidification.	[438]
PBF-EB	CMSX-4	The bed was preheated to 1223 K to achieve directional solidification. However, the details of the scanning pattern used were not provided. Parts are 5 × 5 × 5 mm³ cubes. However, the parts suffered from γ´ precipitates.	[439]
PBF-EB	CMSX-4	A preheating temperature of 1273 K and a 'cross snake hatch strategy' were used where the scanning direction is rotated by 90° between two consecutive layers. Both helped to obtain the directional solidification. SX cylinders of 75 mm in length and 12 mm in diameter were produced.	[440]
DED-L	Rene N5	Processing conditions were optimized to achieve single crystallinity by trial and error. Further details were not provided.	[441]
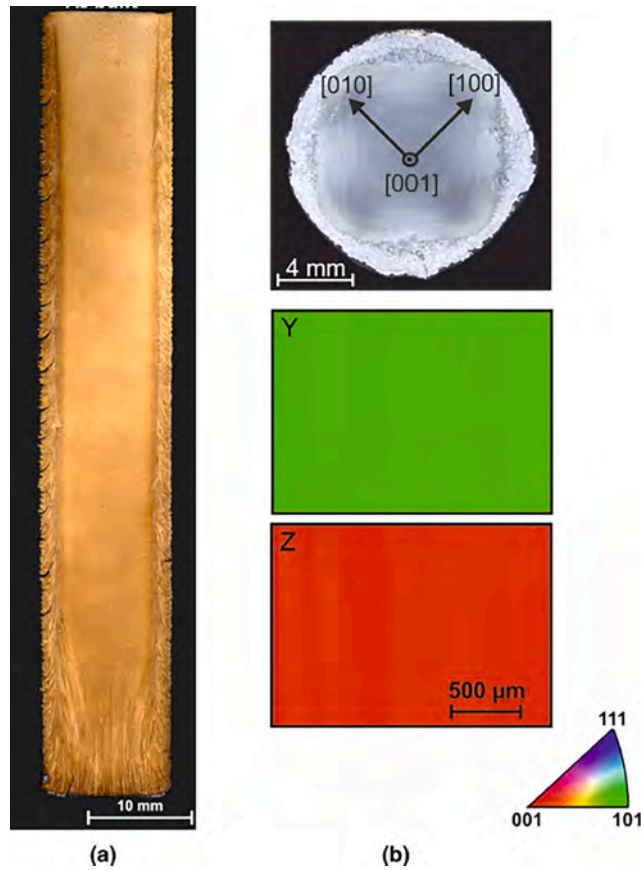
Fig. 5.7. A single crystal part of a nickel alloy, CMSX-4 made by PBF-EB. (a) Vertical cross-section, and (b) horizontal cross-section and EBSD mapping [440]. Y and Z directions are along the radial and height directions, respectively.

temperature creep properties (Fig. 5.8) comparable to those in conventionally processed components [436].

AM is used to repair SX turbine blades that require superior high temperature creep properties [436,444]. It depends on consistency in the microstructure of the repaired part with the original component. However, the formation of stray grains and unwanted secondary phases often significantly degrade the creep properties of the repaired components [435,445]. With an appropriate post-process heat treatment, additively manufactured SXs can achieve superior fatigue life compared to conventionally processed SX components [440]. However, often internal cracks in the repaired part can be a source of stress concentration and significantly reduce
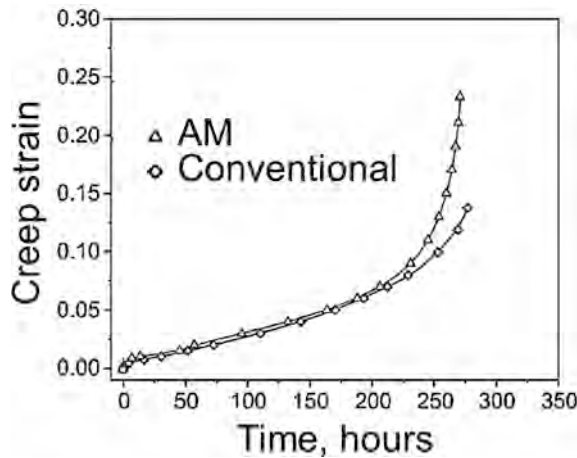
Fig. 5.8. A single crystal CMSX-4 part made by PBF-EB shows comparable high temperature creep properties to conventionally processed single crystal [440].

fatigue life.

5.2.5. Prevention of stray grain formation and defects

Printing of single crystal parts is often hindered by the formation of stray grains [435,445] primarily near the top edge of the deposit (Fig. 5.9). Stray grains may form due to heterogeneous nucleation originating from free powder particles near the top surface (Fig. 5.10) of the deposit [435,445]. High convective and radiative heat losses from the top surface that disrupts directional solidification may also form stray grains [435,445–447]. For example, Liang et al. [435] showed depositions of an SX that contains stray grains near the top of the deposited part, as shown in Fig. 5.9. Prediction of temperature gradient and solidification growth rate can be effective to estimate conditions for stray grain formation [446,447]. Post-process heat treatments or machining of the regions with stray grains are often necessary to achieve a complete single crystal component. In addition, cracking [445] due to solidification shrinkage [448] is another major issue in AM of single crystal parts. Furthermore, it is also challenging to predict appropriate preheat temperature, heat input, and scanning strategy to achieve directional solidification to grow single crystals [445].

Printing of SX is a recent concept and the literature on this topic is growing. Currently, only nickel and titanium alloys can be printed to fabricate single crystals. Wider acceptance of AM for printing SXs also depends on the solution to the major problems associated with the process. The use of well-tested mechanistic models and machine learning can be an option in the future to help alleviate these problems and make the printing of single crystals for various alloys economically viable.

6. Control of grain structure, phases, and defects in titanium alloys

Additive manufacturing allows cost-effective fabrication of Ti-alloy parts because of a low buy-to-fly ratio compared to traditional manufacturing processes. In addition, the mechanical properties of Ti alloys can be modified extensively by alloying, heat-treating, and deformation processing. They are immune to corrosive attacks by many acids and chlorides and are non-toxic and biocompatible. The combination of lightweight, sound mechanical properties, corrosion resistance, and high-temperature endurance makes Ti alloys suitable for aerospace, biomedical, and other applications. However, the printed titanium alloy parts exhibit grain structures and phases that are very different from their wrought counterparts produced with conventional manufacturing methods. In addition, additively manufactured Ti alloy parts suffer from common defects. Therefore, an understanding of how to control the grain structure, phases, and defects is essential. This section of the review focuses on control strategies of grain structure, phases, and defects (Fig. 6.1) during AM of titanium alloys. Table 6.1 provides selected examples of controlling grain structure, phases, and defects in additively manufactured titanium alloy parts. Given their widespread use, at first, we focus on $\alpha + \beta$ alloys, in particular the Ti-6Al-4 V alloy. Then an assessment of controlling grain structure, phases, and defects in metastable β alloys is discussed owing to their importance in aerospace and biomedical applications.

6.1. Control of grain structure, phases, and defects in $\alpha + \beta$ alloys

6.1.1. Strategies to control grain structure

In titanium alloys, large columnar β grains (BCC) form after solidification. During cooling, below a critical β-transus temperature, α grains (HCP) form within the prior β grains structure [449]. AM of Ti alloys involves the formation of large columnar prior β grains
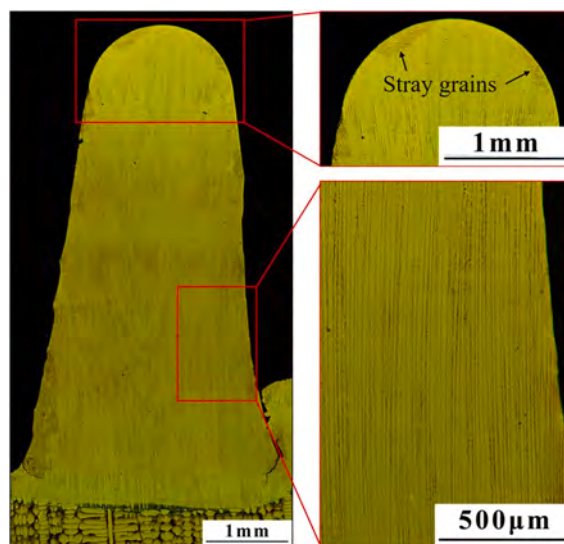
Fig. 5.9. Microstructure of a multi-layer SX deposit formed by L-DED [435], using a set of processing parameters selected according to the processing–microstructure maps involving powder feeding indicating the presence of stray grains near the top of the part.
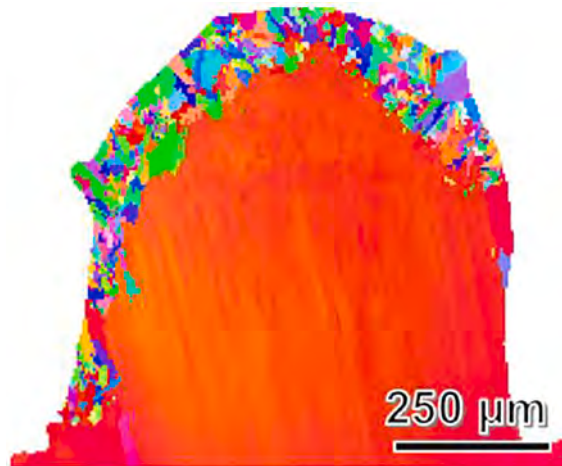
Fig. 5.10. A nickel-based super alloy single crystal part made by DED-L containing stray grains near the top surface of the deposit [445].

[449] that extend several layers or passes. This configuration results in anisotropic mechanical properties and is therefore undesirable. In addition, the mechanical properties of the Ti alloy parts are also affected by the shape and size of the α grains. Several attempts have been made to break the long columnar prior β grains into smaller equiaxed grains and to control the shape and size of α grains to improve the mechanical properties of parts. These methods are reviewed below.

6.1.1.1. Control of solidification morphology. The solidification morphology (columnar or equiaxed) is affected by the ratio of the temperature gradient at the solid/liquid interface (G) and the solidification growth rate (R). At low values of G/R, equiaxed dendritic grains may nucleate in the constitutionally supercooled region just ahead of the solid/liquid interface (see section 2). The scale of the microstructure is indicated by the product GR which is known as the cooling rate. Therefore, control of solidification structures can be done by adjusting G and R. During AM, G and R are affected by the heat input. In AM, heat input per unit length increases with increasing power and decreasing scanning speed.

The effects of heat inputs in controlling the formation of columnar grains have been demonstrated in several studies [450–453]. Zhai et al. [451] conducted a systematic investigation of the microstructure of Ti-6Al-4 V wall builds (2″ x ½" x ½") using two laser powers. Overall, the structures coarsened with the increasing height of the wall. The width of the columnar grains increased with greater distance from the substrate as did the layer height in both high and low power builds due to heat accumulation. The width of the entire HAZ at the substrate/deposit interface was found to be wider with higher laser power (Fig. 6.2). It was reported that the high power reduced the cooling rate and resulted in a coarser microstructure. The formation of columnar prior β grains was compared [450] for DED-L and DED-GMA of wall builds of Ti-6Al-4 V about 250 mm long and 7.5 mm wide. Columnar grains were observed extending over many layers in both processes due to continued epitaxial growth from prior layers. However, there was a clear difference in the width of the columnar grains with much larger grains seen in the DED-GMA samples due to the much higher heat input compared to DED-L. Waryoba et al. [454] compared the solidification structures of Ti-6Al-4 V parts made using laser and electron beam-assisted AM processes. The higher energy density of the electron beam process exhibited slower cooling and resulted in coarse α basketweave structures with large prior β grain size with a columnar morphology. In contrast, the lower energy density of the laser process resulted in a fine α basketweave structure within transformed columnar grains. However, the prior β grain size of the columnar structure was finer. Thus, the grain structure can be effectively controlled by adjusting the heat input. However, care should be taken in adjusting the heat input because it may result in the formation of defects.

6.1.1.2. Grain refinement by controlling undercooling. The control of grain refinement is based on two parameters: P and Q. P is a supercooling parameter and is expressed as $P = mC_o(k-1)/k$ where k is the partition coefficient, m is the slope of the liquidus, and C_o is the alloy composition [455]. The second parameter Q is referred to as the growth restriction factor and is given by: $Q = mC_o(k-1)$. The parameters P and Q are related by: $P = Q/k$. Q can be interpreted as the initial rate of development of constitutional supercooling (CS) concerning fraction solid or $Q = |d\Delta T_c/df_s|_{f_s \to 0}$ where f_s is the fraction of solid. Also, from the plot, it is apparent that P is the amount of supercooling at steady-state growth. Note that both Q and P increase with increasing solute content. Debate continues over which parameter is most useful, although Q has been found to relate to the final grain size via a relationship of the form $d_{gs} = a + b/Q$ where a and b are constants.

The theories described above were extended by St. John and coworkers [456–458] to include other key factors to develop the Interdependence Theory. The theory assumes that a series of successive nucleation events must take place continuously in front of the advancing solid/liquid (s/l) interface to allow the uniform formation of equiaxed grains. Briefly, the theory holds that the final grain size is determined by three factors: (i) the distance that a previously nucleated grain must grow to establish sufficient constitutional supercooling (CS) ahead of an s/l interface to enable the nucleation of the next grain; (ii) the distance from this s/l interface to the point
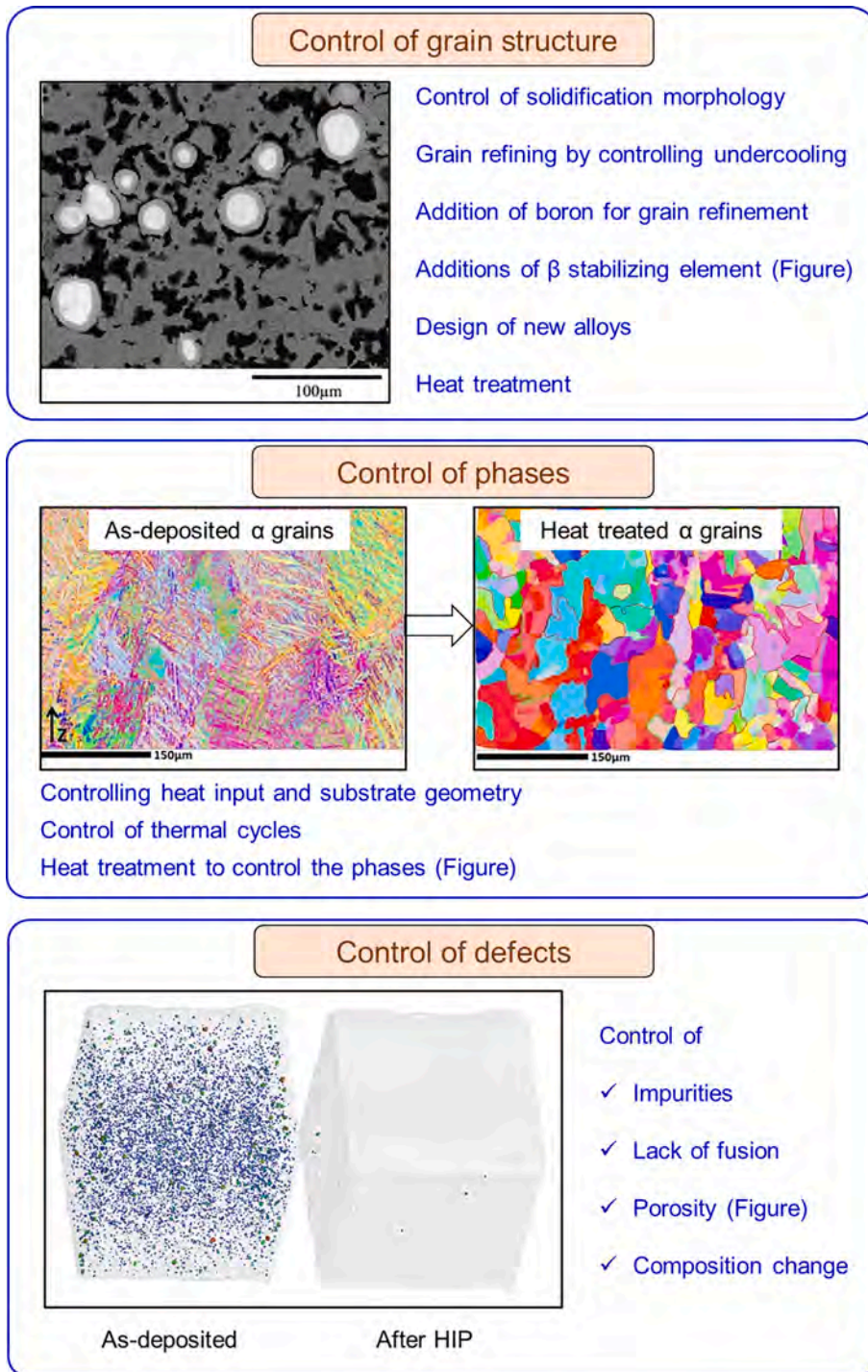
Fig. 6.1. Common techniques to control grain structure [466], phases [474,475], and defects [482] in additively manufactured titanium alloys. Here, HIP indicates hot isostatic pressing.

where this critical amount of CS has been generated; and (iii) the additional distance to the nearest most potent nucleant particle. A distribution of nucleant particle sizes is considered, with the potency of a particle to promote nucleation of a new grain considered to be greater as the particle radius increases.

The Fig. 6.3 (a) illustrates one of the key points of the theory [458]. A new grain has nucleated successfully at the left and is growing radially. As it grows and rejects solute ahead of the s/l interface, a CS region is set up as shown. Here, ΔT_n Sd and X_{Sd} represent the

Table 6.1

Selected examples of controlling grain structure, phases, and defects in additively manufactured titanium alloy parts.

Objective	Alloy	AM process	Description of control strategy	References
Control of grain structure	Ti-6Al-4 V	DED-L	Low laser power increased the cooling rate and reduced the size of columnar β grains	[451]
	Ti-6Al-4 V	DED-GMA	Additions of up to 0.13 wt% B eliminated resulted fine equiaxed α grains and thinner columnar β grains	[462,463]
	Ti-6Al-4 V	PBF-L	β stabilizing elements V and Fe refined columnar β grains	[464]
	Ti-6Al-4 V	DED-GMA	W, Nb, or Mo particles were added that formed supercooled regions around the particles, resulted in heterogeneous nucleation, and refined grains	[466]
	Ti-Cu (up to 8.5 wt%)	DED-L	This alloy was designed to have a high constitutional supercooling to mitigate the formation of columnar grains	[467]
	Ti-6Al-4 V	DED-GMA	Post-process heat treatment refined α grains	[468]
Control of phases	Ti-5553 alloy	PBF-L	Post-process heat treatment resulted in precipitation of α phase that improved mechanical properties	[490]
	Ti-5553 alloy	PBF-L	Low heat input produced single-phase β microstructures with small amounts of ω phase which improved hardness	[498]
	Ti-6Al-4 V	PBF-L	Low energy density resulted in α' martensitic or α/α'microstructures that increased the strength and hardness	[469]
	Ti-6Al-4 V	DED-L	Low laser power resulted in rapid cooling and produced martensitic α' microstructures	[451]
	Ti-6Al-4 V	DED-PA	Low laser power resulted in martensitic α' microstructures	[470]
	Ti-6Al-4 V	DED-L	Post-process vacuum annealing heat treatment produced α + β microstructures that can improve the toughness	[451]
	Ti-6Al-4 V	PBF-L	Post-process heat treatment refined the lath structure occurred due to epitaxial recrystallization from α'/α interfaces in the α' substructure that contained β phase	[474]
Control of defects	Ti-6Al-4 V	PBF-L	Low hatch spacing ensured overlaps among neighboring tracks and reduced the lack of fusion defects	[119,481]
	Ti-6Al-4 V	PBF-L	High laser power increased the pool dimensions, improved fusional bonding, and reduced the lack of fusion defects	[480]
	Ti-5553 alloy	PBF-L	High heat input resulted in larger pool and better fusional bonding, and reduced the lack of fusion defects	[498]
	Ti-6Al-4 V	PBF-L	Post-process hot isostatic pressing reduced the number of voids	[482]
	Ti-6Al-4 V	PBF-EB	Change in aluminum composition due to selective vaporization was reduced by adjusting the heat treatment	[485]

undercooling required for nucleation, distribution of particle sizes, and average interparticle spacing, respectively. The theory assumes that nucleation occurs on the most potent particles. Without describing all the mathematical details, the ΔT_n versus Sd curve that describes the potency and distribution of particle sizes [457] is shown in Fig. 6.3 (b). The key point that underpins the utility of the theory is that the location of the next nucleation event can be predicted as the intersection of the undercooling required for nucleation, ΔT_n versus Sd curve with the actual local temperature in the melt pool (T_A), as shown in Fig. 6.3 (b) [457]. The location of the ΔT_n versus Sd curve will shift to the left as the amount of solute is increased. The curve will also evidently shift to the left for larger particles. Using this approach, the average grain size can be estimated as the distance from the center of the already growing grain and the position of the new nucleation event. For the microstructure to be comprised completely of equiaxed grains, a wave of repeated nucleation must occur as the solid/liquid interface moves with each nucleation event triggering a new constitutionally supercooled region to allow replication and continuation [459].

6.1.1.3. Addition of boron for grain refinement. The addition of boron for grain refinement in titanium alloys was widely practiced in casting and fusion welding. For example, it was found that additions of B up to 0.4% significantly refined the microstructure of cast Ti alloys [460] which improved the tensile strength and toughness. In a different study, it was found that additions up to ∼ 0.1 wt% B provided a large decrease in grain size in cast Ti-6Al-4 V and Ti-6Al-2Sn-4Zr-2Mo (Ti-6242S) alloys [461]. The grain size ranged from ∼ 1700 μm for no B additions to ~200 μm for 0.1% B. The grain refinement occurs due to a change in the undercooling behavior because of the boron addition. In AM, grain refinement due to boron addition was reported for DED-GMA of Ti-6Al-4 V [462,463]. Additions of B (up to 0.13 wt%) eliminated grain boundary-α and colony-α and generated a uniform microstructure of fine equiaxed α-grains in both as-deposited and heat-treated conditions. Prior-β grains remained columnar with B additions but become thinner due to the larger solidification temperature range and growth restricting effect of B. Boron additions were claimed to generate narrower columnar grains due to lateral solute rejection during epitaxial growth from previous layers [462,463]. However, the amount of boron needed to refine the grains are currently selected by trial-and-error and requires a quantitative formalism based on scientific principles.

6.1.1.4. Additions of β stabilizing element for grain refinement. The elements that stabilize β are added to refine grains during AM of titanium alloys [25,453,464–466]. For example, additions of V and Fe for grain refinement during PBF-L of Ti-6Al-4 V have been reported [464]. The in-situ additions of β-stabilizing elements V and Fe resulted in an alloy with a composition close to the β alloy, Ti-10 V-2Fe-3Al. Instead of α' microstructure expected during PBF-L of Ti-6Al-4 V, the additions of Fe and V yielded an α + β micro-structure containing up to ∼ 63% β. Heat-treatment below the β transus permitted precipitation of the nanoscale α phase in the β matrix and produced high strength and good ductility [464]. W, Nb, and Mo were added by Tedman-Jones et al. [466] for grain refinement.
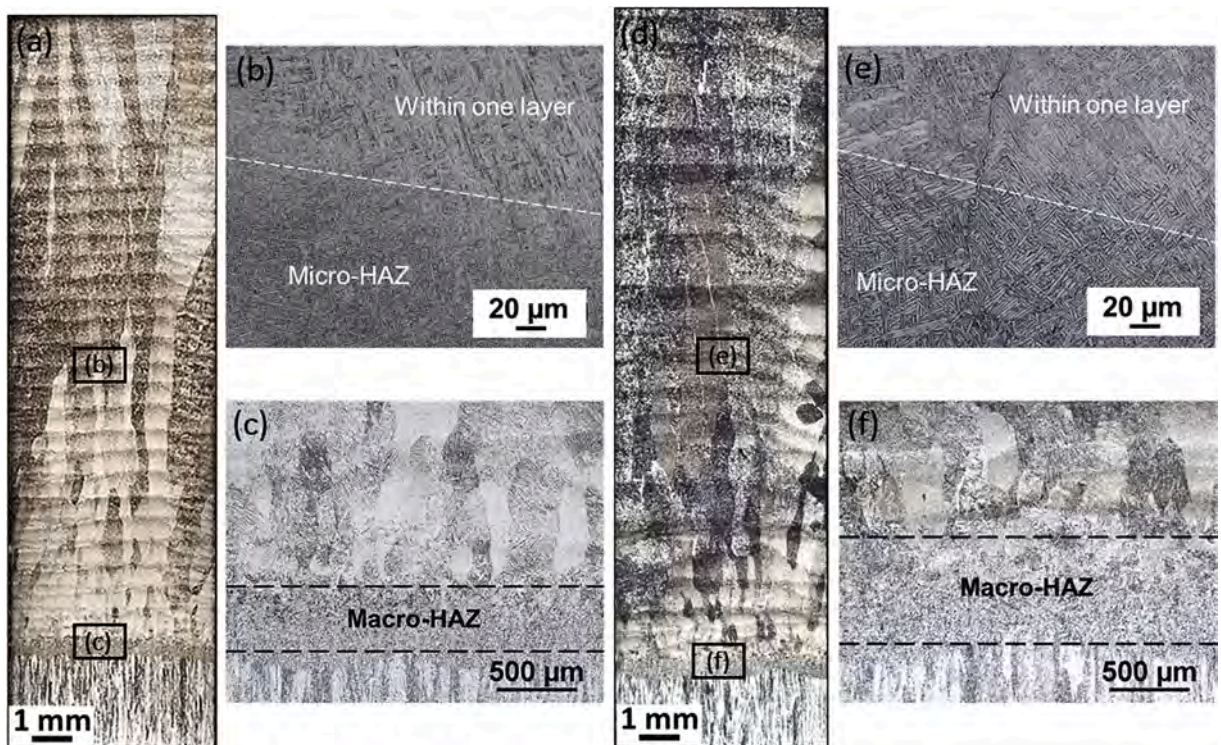
Fig. 6.2. (a,d) Cross-sectional views of the micrographs of Ti-6Al-4 V parts made by DED-L using low and high laser powers, (b,e) micro-HAZ, and (c,f) macro-HAZ [451].

These elements have higher melting points than Ti and exhibit a bcc crystal structure like Ti at temperatures near their melting points. Small powders of these elements added to the Ti-6Al-4 V act as nucleating sites for grain refinement. A supercooled region formed around the W, Nb, or Mo particles due to their dissolution causing the particles to act as sites for nucleation and subsequent growth of fine grains (Fig. 6.4). Care should be taken to select an optimum initial particle size that will maximize the number of nucleation sites and promote grain refinement during solidification while not dissolving too quickly during AM [466].

6.1.1.5. Design of new alloys for controlling grain structure. Ti-Cu (up to 8.5%) alloy [467] was designed to have a high constitutional supercooling capacity because of the partitioning of Cu during solidification, which can mitigate the formation of columnar grains. The as-deposited Ti-Cu alloy specimens had a fully equiaxed fine-grained microstructure [467]. The cooling rate was slower and diffusional transformations dominated microstructural development. In these cases, a fine eutectoid lamellar structure (α + Ti$_2$Cu) formed with some hyper-eutectoid primary Ti$_2$Cu particles of larger size. Reheating above the eutectoid temperature (792 °C) during multilayer deposition removed the α' phase formed initially and produced the very fine eutectoid lamellae. Samples of alloys containing up to 8.5% Cu could be produced, and the α phase was supersaturated (2.8% Cu vs 2.0% solubility limit from the phase diagram) indicating that further strengthening could be achieved with additional heat treatment. The alloys also displayed improved mechanical properties, comparable to wrought Ti-6Al-4 V alloys [467]. Cu is an inexpensive alloying element relative to many other elements used in Ti alloys, making these new alloys even more attractive. However, the density of Cu is almost twice that of Ti. Therefore, care should be taken to maintain the density of the alloy for critical applications where the part weight is a critical factor such as in aerospace industries.

6.1.1.6. Heat treatment for controlling grain structure. Heat treatments below the β-transus temperature (sub-transus) offer the potential for improved ductility while maintaining high strength. Wang et al. [468] produced Ti-6Al-4 V samples using the DED-GMA process and performed different sets of sub-transus heat treatments indicated by (a), (b), and (c) in Fig. 6.5. The figure describes the microstructural evolution for each heat treatment. The microstructure for this heat treatment was comprised of fine discontinuous α_{GB}, α_p, and dispersed α_s where the subscripts for the α phase refer to the following: GB is grain boundary, p is primary, and s is secondary. In heat treatment (a), rapid cooling due to the water quenching formed α' martensite. Relatively slower cooling [468] in the air formed α_p. Dispersed secondary α phase was formed in heat treatments (b) and (c) which improved the strength and ductility. Two mechanisms of α_p break-up during heat treatment were identified [468]. The mechanisms included termination migration involving chemical potential gradient-driven diffusion and boundary splitting or shearing across the lath. The solute concentration gradient within a groove undergoing migration was observed. Although post-process heat treatment can significantly improve the grain structure and mechanical properties, they add costs.
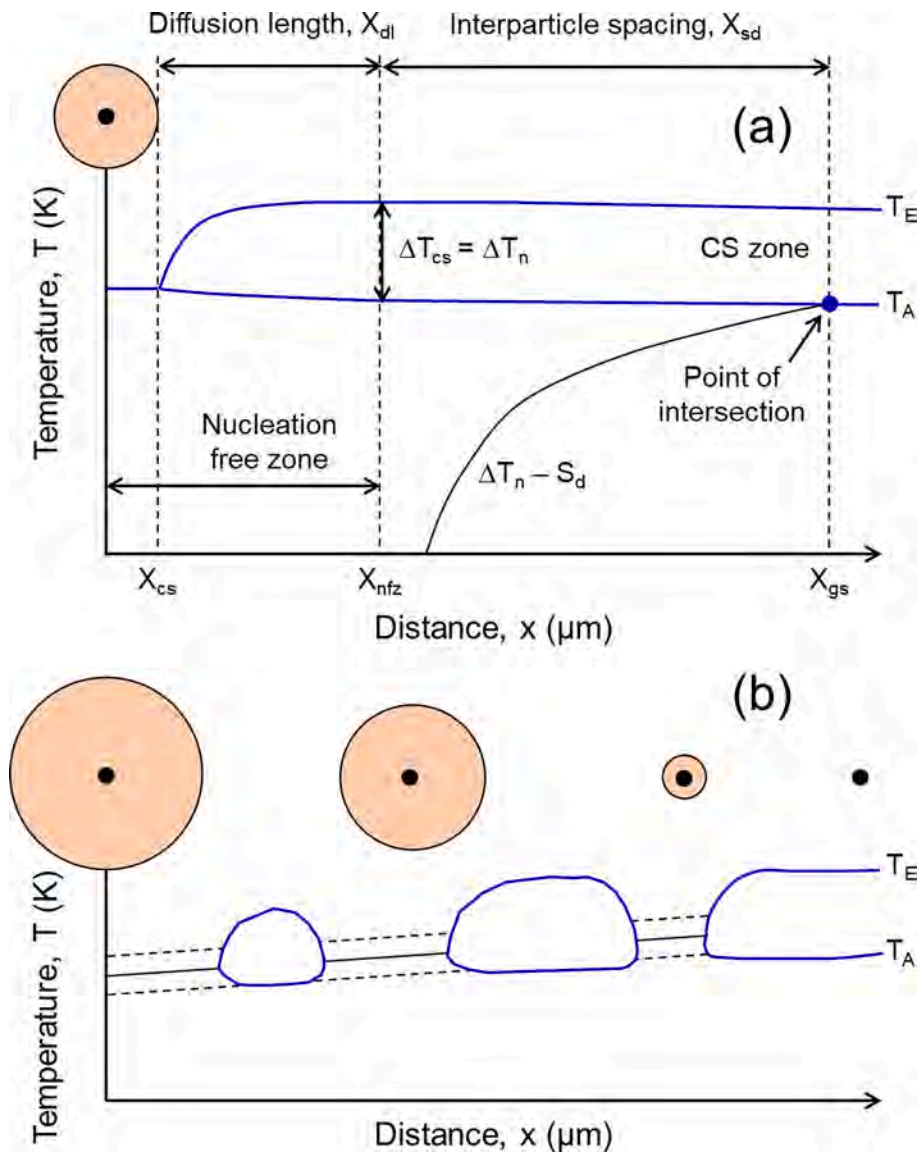
Fig. 6.3. (a) A new grain has nucleated successfully on left and is growing radially. As it grows and rejects solute ahead of the solid/liquid interface, a constitutional supercooling (CS) region [458] is set up as shown. the ΔTn versus Sd curve that describes the potency and distribution of particle sizes. Here, ΔTn and Sd represent the undercooling required for nucleation [457] and distribution of particle sizes, respectively. T_E and T_A indicate the equilibrium liquidus temperature and actual temperature, respectively. The suffix 'nfz' represents nucleation-free zone. (b) Growth of particles. Here, the suffix 'min' indicates the minimum value. We have redrawn this figure.

6.1.2. Phase control strategies

Pure titanium experiences an allotropic transformation from a body-centered cubic (bcc) phase (β phase) to a hexagonal close-packed (hcp) phase (α phase) on cooling at approximately 885 °C (β transus temperature) [449]. The β transus temperature of titanium alloys varies depending on the composition. For example, the β transus temperature for the Ti-6Al-4 V alloy is ~ 975 °C ± 25 °C depending on the amount of O and Fe impurities [449]. Alloy designations for Ti alloys are based on their equilibrium crystal structures at ambient temperature and broadly include α, $\alpha + \beta$ metastable β and stable β alloys depending on the balance of α stabilizers (Al, O, N and others) and β stabilizers (V, Cr, Nb and others). Beta (β) stabilizing alloy elements can be further classified as those that promote either isomorphous or eutectoid phase diagrams. Some alloy additions (ex. Sn, Zr) have little influence on the stability of either phase and are added for purposes of solid solution strengthening. Formation of an hcp α' phase by a martensitic reaction is also possible at faster cooling rates from the β phase field [449]. Moreover, an α'' phase with an orthorhombic structure can form in binary and higher-order systems containing Ti and β stabilizing transition metals (TM) at alloying levels greater than found for α' phases. At higher content of β stabilizing alloy additions, metastable β' and ω (omega) phases can also form at high cooling rates. Finally, secondary α (α_S) may be found that are heated to the β phase field and then quickly cooled again before all α is dissolved. The α_S phase typically
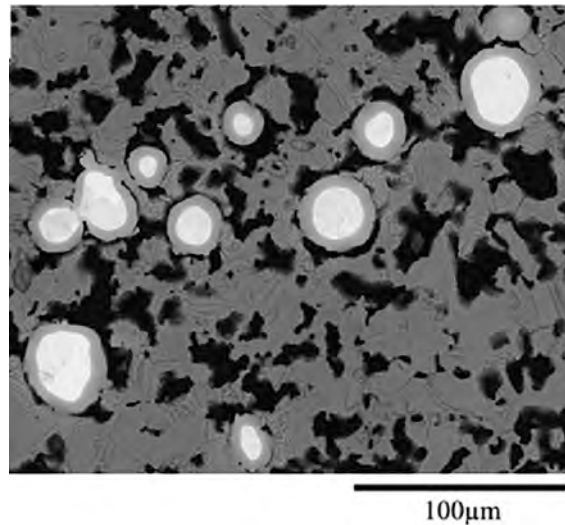
Fig. 6.4. A supercooled region formed around the W, Nb and Mo particles due to their dissolution causing the particles to act as sites for homogeneous nucleation and subsequent growth of fine grains [466] during DED-GMA of Ti-6Al-4 V.

forms on the existing (or remaining) primary α phase [449]. The control strategies for phase formation during AM of titanium alloys are reviewed below.

6.1.2.1. Controlling heat input and substrate geometry. Heat input and its influence on cooling rates play a key role in controlling microstructural features during AM of titanium alloys. High energy density during PBF-EB exhibited slower cooling and resulted in an α + β microstructure in Ti-6Al-4 V parts [469]. In contrast, rapid cooling at relatively lower energy density during PBF-L resulted in α' martensitic or α/α'microstructures [469]. In Ti-6Al-4 V parts made by DED-L, lower laser power resulted in rapid cooling and produced martensitic α' microstructures [451]. In contrast, coarse fully α + β lamellar structures were observed in high power deposits [451]. A similar observation was also made during the DED-PA of Ti-6Al-4 V [470]. Thus, the formation of α and β phases in additively manufactured Ti alloy parts can be controlled by adjusting the heat input.

Thicker substrates conduct more heat than thinner substrates. Therefore, substrate dimensions can influence heat flow, impact the deposit geometry and cooling rates, and produce spatial variations in microstructures [471] and several attempts have been made to control the phase formation by adjusting the substrate geometry. For example, Lin et al. [470] used this approach to control the phase formation during DED-PA of Ti-6Al-4 V (Fig. 6.6). Rapid three-dimensional heat conduction through the substrate resulted in martensitic α' and fine α + β basketweave phases near the substrate. However, the α' disappeared and the phases coarsened as the built height increased. Therefore, the formation of martensitic α' or α + β basketweave phases were affected by the heat conduction through the substrate which can be controlled by adjusting the substrate geometry. Similar observations were also made by Zhai et al. [451] during the DED-L of Ti-6Al-4 V. For these cases, variations in cooling rates at different substrate thicknesses controlled the phases. Mechanistic models need to be developed to simulate the 3D heat transfer and predict the appropriate substrate thickness to achieve cooling rates that can provide the desired grain size and phases.

6.1.2.2. Control of thermal cycles. Additively manufactured parts experience repeated heating and cooling due to multiple thermal cycles during multi-layer deposition. The formation of phases in printed Ti alloy parts is affected by thermal cycles in three distinct temperature regimes [470] in the solid-state: (1) above the β-transus; (2) below the β-transus but high in the two-phase a + β phase field; and (3) a temperature too low for any transformations. After solidification and cooling into the two-phase a + β field, primary α forms within a β matrix. However, this structure is erased, at least partially, as the α partly dissolves during the next heating cycle. The extent of dissolution depends on the time and temperature. Microstructural changes cease when peak temperatures in the thermal cycles become too low for diffusional transformation. Often rapid cooling forms α' martensite, when thermal cycle minima fall below the Martensite start temperature (M_s) for the alloy [470]. The formation of these phases is affected by the multiple thermal cycles and thus can be controlled by adjusting the processing conditions [472,473]. For example, Fig. 6.7 shows the spatial variations in phase formation depending on the local thermal cycles during DED-GMA of Ti-6Al-7Nb alloy [472]. A banded microstructure was found below the β-transus temperature. The low-temperature region occurred two or three layers below the last pass due to the high heat input of the DED-GMA process and was not apparent in the last few passes. The lighter etching band resulted from local enrichment of Nb in the matrix when $α_S$ formed and was not homogenized during later heating due to its lower diffusivity. Thermal cycles can be controlled by adjusting layer thickness, heat input, scanning patterns, and inter-pass dwell time to control the phase formation. However, care should be taken because adjustment of these process variables may also result in other issues such as the formation of defects.
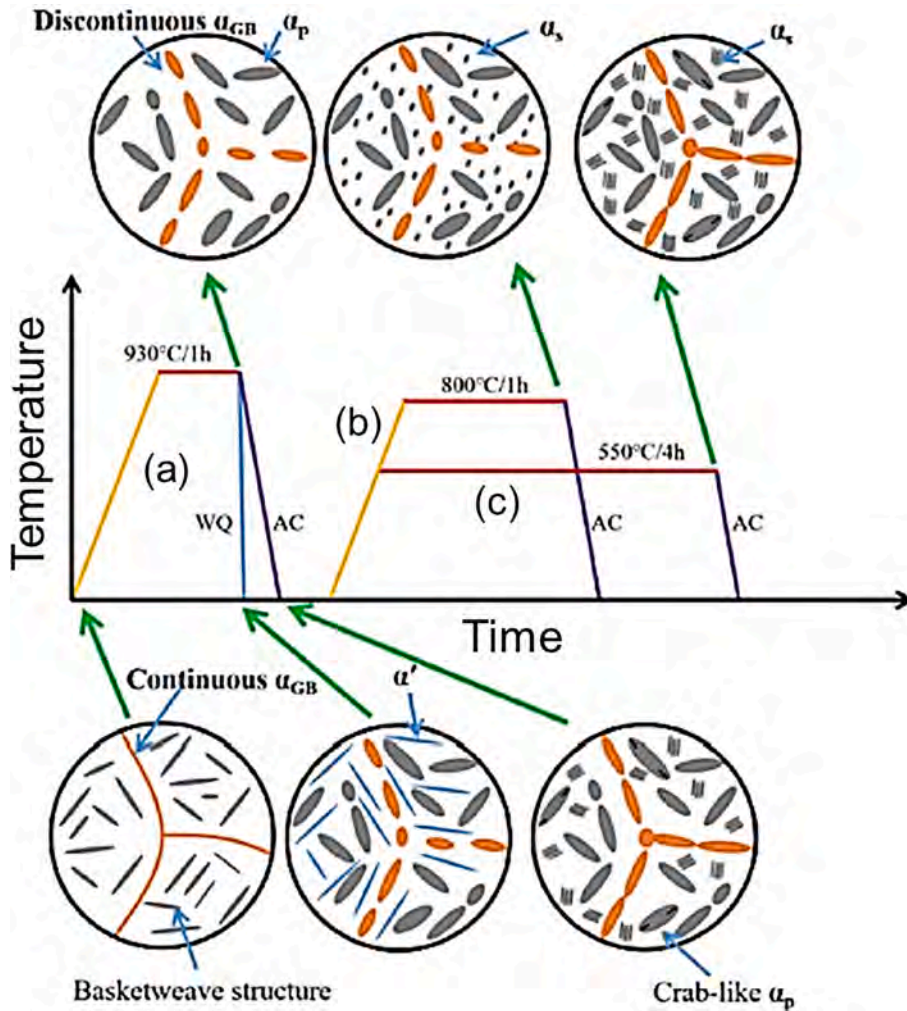
Fig. 6.5. Schematic illustration of microstructure evolution during solution and aging treatment [468]. Three types of heat treatments (a), (b), and (c) were used. Here, suffixes 'p', 's', and 'GB' denote primary, secondary, and grain boundaries, respectively. WQ: Water quenching, AC: Air cooling.

6.1.2.3. Heat treatment to control the phases. Several attempts have been made to control the phases in printed Ti-alloy parts by using post-process heat treatments. For example, the DED samples of Ti-6Al-4 V [451] were subjected to a vacuum annealing heat treatment (760 °C for 1 h followed by air cooling). The annealing process decomposed the martensitic α' phase present in the as-deposited samples and resulted in a fine α + β microstructure. Zou et al. [474,475] showed that the heat treatment of PBF-L samples of Ti-6Al-4 V significantly changed the microstructure from that in the as-deposited parts (Fig. 6.8). The refinement of the lath structure occurred due to epitaxial recrystallization from α'/α interfaces in the α' substructure that contained residual β phase. The EBSD images provided evidence of the early stages of nucleation and growth of new recrystallized β with high angle boundaries. The authors also indicate that the high dislocation density in the α' martensite provided the driving force for the nucleation of new variants. Grain boundary α was also observed in all the specimens due to slow cooling after the heat treatment. From the discussion above, it is evident that the post-process heat treatment can be used to control the phases in the additively manufactured Ti alloy parts. However, the challenge remains in selecting an appropriate combination of heat treatment time and temperature. In addition, post-process heat treatment adds an extra cost that is often not desirable.

6.1.3. Control of common defects

Ti alloys are very sensitive to the pickup of impurity elements such as C, N, O, and H during processing which can cause severe embrittlement issues. In addition to embrittlement, the pickup of gaseous impurities during AM can also lead to porosity problems due to lower solubility in the solid. The extremely strong chemical affinity of the Ti alloy for O, N, C, and H often mandates the use of vacuum or nearly complete inert environments during fusion-based AM processes. In addition, additively manufactured titanium alloy parts are susceptible to other defects such as lack of fusion, porosity, and composition change. This section reviews the controlling strategies for these defects.
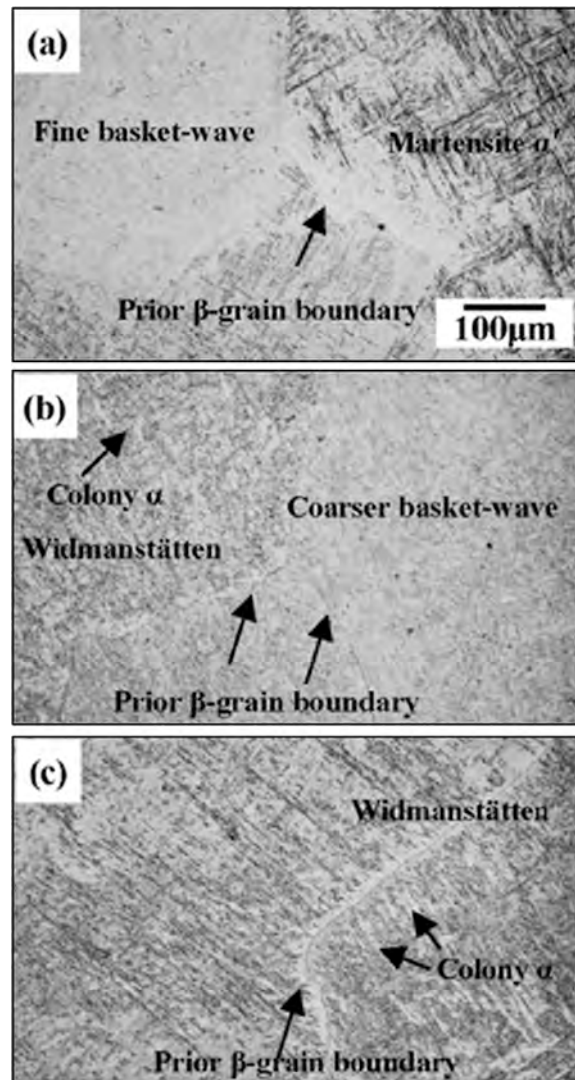
Fig. 6.6. Optical micrograph of normal microstructure compared to layer band of the wall from (a) the bottom region (b) the middle region, and (c) the top region [470].

6.1.3.1. Reducing impurities by gas shielding effects. Ti alloys are very sensitive to the pickup of C, N, O, and H from the atmosphere. Inadvertent additions of these elements not only lead to porosity but embrittlement. Therefore, measures must be undertaken to shield the melt pool from contamination either by vacuum or proper inert gas shielding. Powder feedstocks, with their much greater surface-to-volume ratio relative to wire feedstocks, are expected to contain significantly greater amounts of O in terms of their surface oxide content. Moreover, they will typically have extensive amounts of physically or chemically adsorbed moisture depending on the local humidity levels. Carroll et al. [452] carried out DED-L of Ti-6Al-4 V using powder feedstocks in an argon chamber. They observed a pickup of 0.0124 wt% O but no extensive gas-derived porosity or embrittlement.

Bermingham et al. [476] performed experiments with DED-GMA of Ti-6Al-4 V to study the effects of absorbed oxygen. If no shielding was used a thick brown oxide was formed. In those cases, the samples were allowed to cool to ambient temperature after each pass, and the oxide layer was removed using glass bead blasting before producing the next pass. This process can avoid the accumulation of oxygen and decrease embrittlement but reduce productivity. If no inter-pass glass bead blasting was used the surface oxides appeared to be dissolved uniformly into the next pass. Therefore, it is recommended that an inert shielding gas should be used during AM of Ti alloys to reduce the impurities and the resultant embrittlement and porosity.

6.1.3.2. Controlling the lack of fusion and porosity. The low thermal diffusivity of titanium alloys is of particular interest relative to heat flow during AM and subsequent effects on defect evolution due to cooling rates. Titanium alloys are not susceptible to solidification or liquation cracking during AM. Moreover, Ti alloys are much less reflective to infrared laser beams relative to Al alloys, and coupling or back reflection issues during laser-based AM processes are not typically concerning. However, lack of fusion and porosity
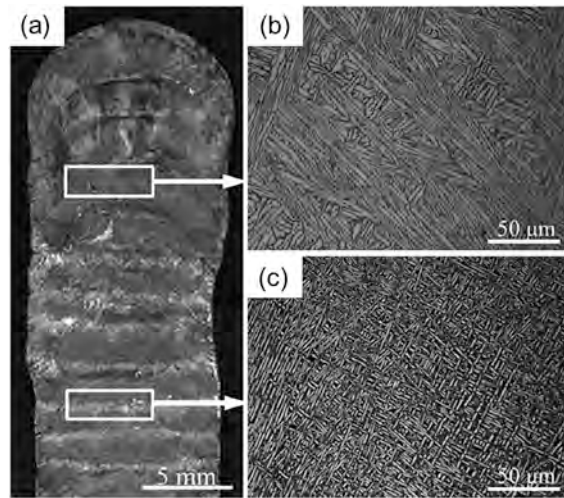
Fig. 6.7. Microstructure of a titanium alloy built (a). The microstructure near the top and bottom are shown in (b) and (c), respectively [472].
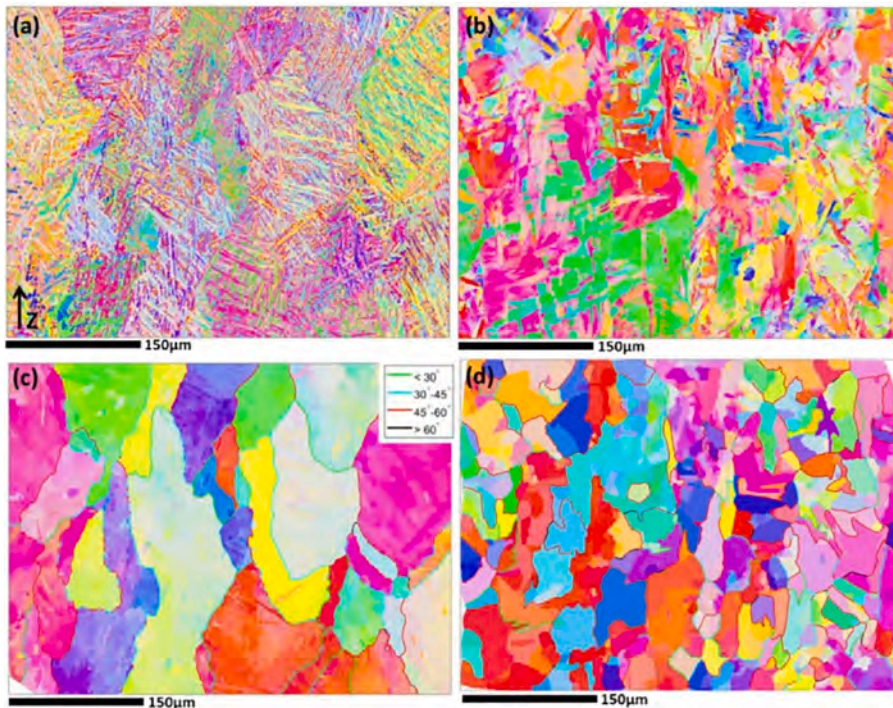
Fig. 6.8. Typical α-orientation maps of Ti-6Al-4 V in (a) as-built condition and (b) after heat treatment. Reconstructed β-orientation maps of Ti-6Al-4 V in (c) as-built condition and (d) after heat treatment [474,475].

[121,477–479] are important issues in additively manufactured titanium alloy parts.

The Fig. 6.9 shows the morphology of the lack of fusion void, gas pore, and keyhole pore during PBF-L of Ti-6Al-4 V [480]. Improper fusional bonding among the neighboring tracks results in the lack of fusion voids that are irregular in shape (Fig. 6.9 (a)). Moisture from the atmosphere and the gas entrapped inside the gas-atomized powders often cause gas porosity inside the component. Gas pores are spherical (Fig. 6.9 (b)) and their size varies significantly. PBF-L is often performed in keyhole mode at a very high energy density. An unstable keyhole may collapse and the vapor bubble is entrapped inside the part to cause keyhole pores. These pores are elongated in shape (Fig. 6.9 (c)). All these three types of voids or pores significantly degrade the mechanical properties of parts [477].

Lack of fusion is affected by the extent of overlap between two consecutive tracks. The extent of overlap between tracks can be controlled by adjusting the molten pool size and the distance between two neighboring tracks. Lack of fusion defects are found to be
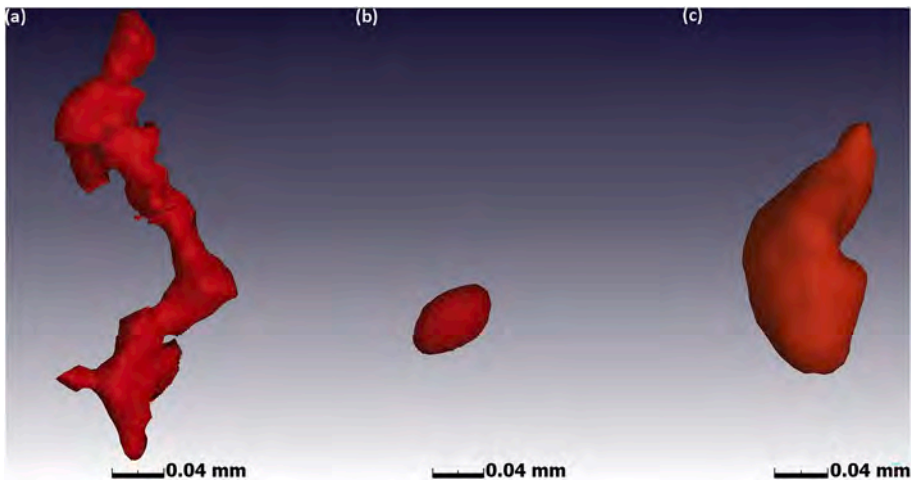
Fig. 6.9. Morphologies of (a) lack of fusion void, (b) gas pore, and (c) keyhole pore during PBF-L of Ti-6Al-4 V at 800 mm/s, power values 120 W, 160 W, 360 W. Build direction is vertical in all images [480].

dependent on layer thickness (L), hatch spacing (H), molten pool depth (D), and width (W). The lack of fusion voids can be prevented by achieving a proper combination of these four variables [124]. For example, at a constant laser power and scanning speed which indicate fixed values of pool width and depth, volume % of lack of fusion void in Ti-6Al-4 V parts made using PBF-L [119] increases with hatch spacing (Fig. 6.10 (a)). Lack of fusion defect in Ti-6Al-4 V parts made using PBF-L [481] was also found to increase with the hatch spacing. In contrast, the lack of fusion can be reduced by printing parts with thinner layers (Fig. 6.10 (b)). High laser power results in both wider and deeper pools that can reduce the lack of fusion as shown in Fig. 6.11 (a-c) for Ti-6Al-4 V components made using PBF-L [480]. The selection of appropriate combinations of processing conditions to avoid the lack of fusion is often performed by using mechanistic models of additive manufacturing.

Moisture or gas produced during the process can be entrapped inside the molten pool and after solidification, they remain inside the component as gas pores. Post-process hot isostatic pressing can reduce the number of voids [482]. For example, Fig. 6.11 (d-e) show that the pores in Ti-6Al-4 V parts made using PBF-L can be reduced using hot isostatic pressing [482] but adds an extra cost. Gas pores originating inside the molten pool can come out of the pool before solidification driven by the buoyancy and convective flow of molten metal. Therefore, the number of gas pores and their distributions are often affected by the convective flow of liquid metal inside the molten pool. Fig. 6.12 explains the molten pool dynamics and their effects on pore distribution [483] during DED-L of Ti6Al2Sn4Zr2Mo. Generally, the molten metal flows from the center (low surface tension) to the periphery (high surface tension) of the
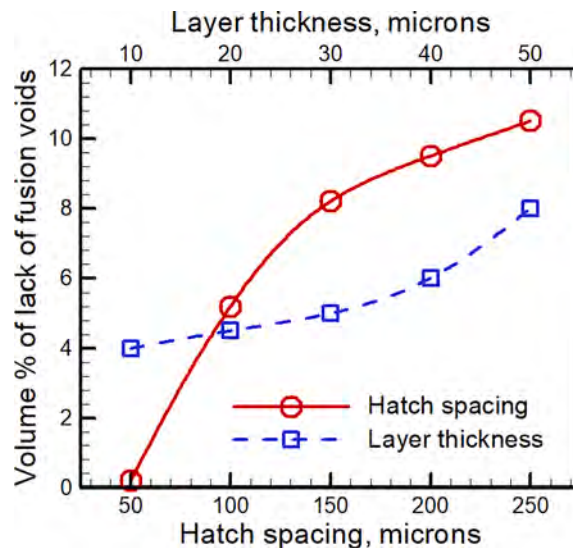
Fig. 6.10. Variation in volume % of lack of fusion void in Ti-6Al-4 V parts made using PBF-L with (a) hatch spacing at a constant layer thickness of 30 μm and (b) layer thickness at a constant hatch spacing of 100 μm. Laser power and scanning speed are 100 W and 750 mm/s, respectively. The plot is made using the data reported in [119].
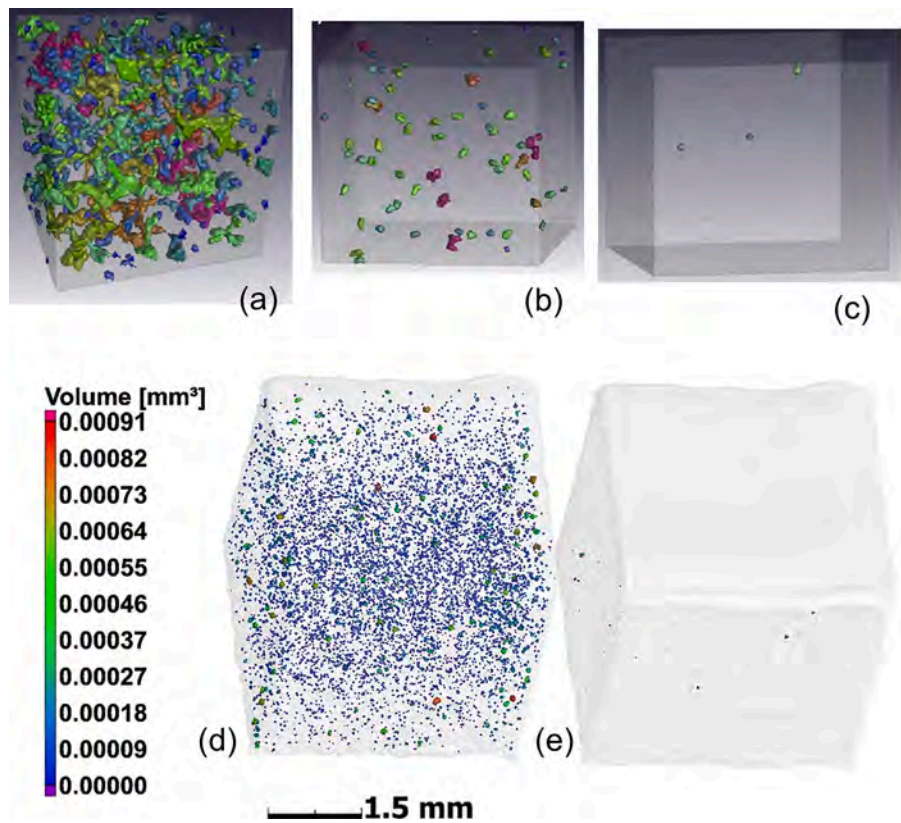
Fig. 6.11. Lack of fusion void distribution measured using X-ray CT in a Ti-6Al-4 V component made using PBF-L using (a) 160 W, (b) 185 W, and (c) 210 W of laser power [480]. Pores in Ti-6Al-4 V parts made using PBF-L (d) as-printed and (e) after hot isostatic pressing [482].

pool. Time-resolved radiographs show the effect of flow patterns on the distribution of the pores. The distribution of the pores can be significantly different if the flow pattern is reversed. Often, the presence of oxygen which is a surface-active element can change the flow pattern and result in a different pore distribution. The number of gas pores that remains in the part and their distributions are affected by the pore size, viscosity of the molten liquid, convective flow, and solidification time. An in-depth quantitative formulation is needed to correlate these variables with the number of gas pores in the additively manufactured parts. The reduction of voids and pores in additively manufactured titanium alloy parts remains an important challenge to improving the mechanical properties of parts.

6.1.3.3. Minimizing composition change due to selective vaporization of alloying elements. Constituting elements of titanium alloys have very different vapor pressures at high temperatures. Therefore, they vaporize at different rates from the molten pool. This selective vaporization of different alloying elements results in a change in the composition of the part from the feedstock [484]. Composition change can degrade the microstructure and corrosion resistance. Experimental results [485] confirm the considerable loss of aluminum for the PBF-EB of Ti-6Al-4 V builds. The experimentally measured concentration of aluminum for various speeds and powers is shown in Fig. 6.13. In all cases, the concentration of aluminum in the build was significantly lower than that in the powder. As shown in the figure, both the energy of the beam and the scanning speed was varied, and for a given linear energy density, a higher scanning speed produced a higher aluminum composition change. Because faster scanning normally results in a shallower, longer molten pool with a larger surface area, the more pronounced composition change is consistent with the fact that a higher surface area to volume ratio will produce more vaporization per unit volume. A careful selection of process parameters, the spatial distribution of the energy of the heat source, and control of temperature are key to reducing the loss of volatile alloying elements.

6.2. Control of grain structure, phases, and defects in metastable β alloys

6.2.1. Metastable β alloys and their applications in additive manufacturing

Metastable β titanium alloys contain higher amounts of body-centered-cubic (bcc) forming elements such as V, Nb, Hf, and Ta which expand the β-bcc phase field and shift it to lower temperatures [486]. Additional alloying elements such as W, Fe, and Cr enhance eutectoid reactions of β titanium and ordered compounds, creating microstructures that are highly sensitive to thermal processing and heat-treating conditions. These alloys tend to have high strength-to-weight ratios with good corrosion resistance and are often used in aerospace applications but tend to be expensive, which limits their use to high-value-added components. There are
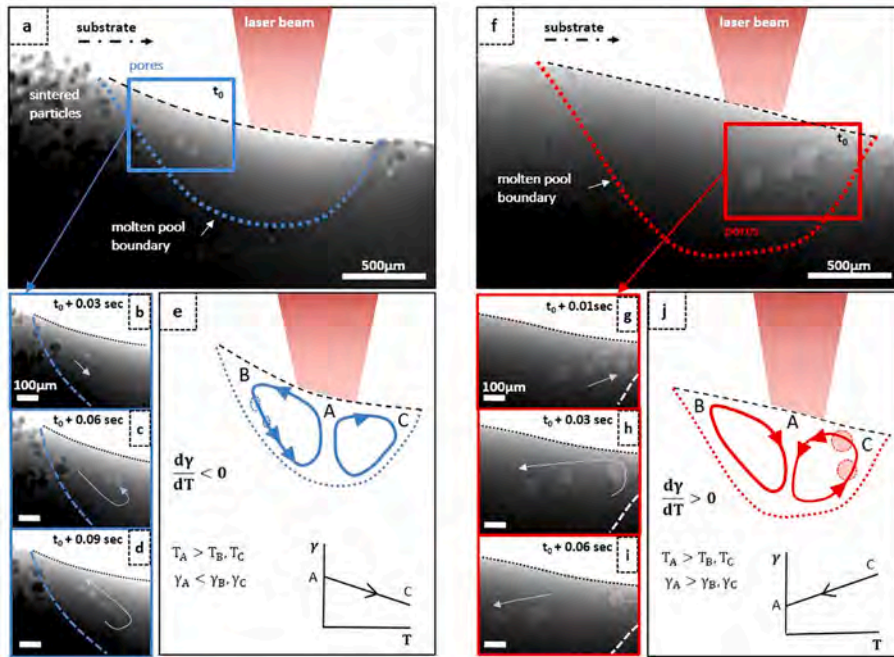
Fig. 6.12. Molten pool dynamics and its effects on pore distribution during DED-L of Ti6Al2Sn4Zr2Mo under (a) radially outward fluid flow and b) radially inward flow. Time-resolved radiographs showing pore behavior in (b) to (d) for the condition of (a) and in (g) to (i) for the condition of (f). (e) Schematic diagram describes the molten metal flow pattern as a function of surface tension (γ) and temperature (T) in a negative surface tension gradient. (j) Schematic diagram describes the molten metal flow pattern as a function of γ and temperature T in a positive surface tension gradient [483].
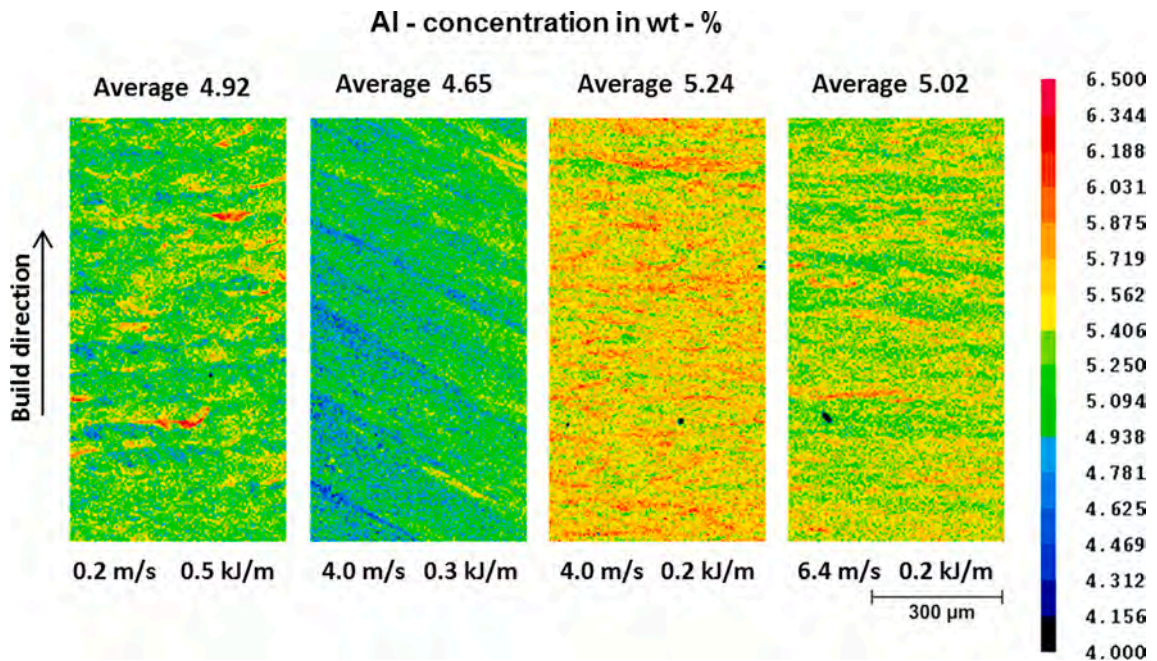
Fig. 6.13. Experimentally measured concentration of aluminum [485] for the deposition of Ti-6Al-4 V by PBF-EB.

several alloys with different degrees of metastability depending on the relative amounts of alloying elements. The β stabilizing effectiveness of a given alloy can be approximated by a molybdenum equivalent, where each alloying element is assigned a multiplier for its β stabilizing ability relative to molybdenum [486]. Metastable titanium alloys have Mo-equivalent values between

approximately 10 and 30, and the processing conditions to create a given microstructure can be related to this value. For example, to create a single-phase β -titanium microstructure at room temperature, a metastable titanium alloy with a low Mo- equivalent would need to be cooled or quenched more rapidly from the high-temperature β-phase field than an alloy with a higher Mo- equivalent After quenching to metastable β, these alloys are typically heat-treated to precipitate a fine dispersion of the α, plus possibly other phases, which act as a strengthening mechanism and partially stabilizes the alloy to further transformation. In conventional processing of wrought metastable β titanium alloys, heat treatments can vary from a single temperature for stress relieving or annealing, to duplex or triplex temperature schedules with peak temperatures that may be above or below the β transus, while cooling conditions can be varied to produce a wide range of microstructures and properties.

Alloy C, β C, β 21S, and Ti-5Al-5 V-5Mo-3Cr (Ti-5553) are some of the more prominent alloys, listed in order of highest to lowest Mo equivalent. These alloys largely retain their bcc structure to room temperature due to their lower transus temperatures and the sluggish transformation to α owing to the lower diffusion rates of the β-stabilizing alloying elements. By definition, metastable β alloys do not form α' martensite even on rapid cooling due to their higher alloy content and correspondingly lower M_S temperature and can be heat-treated to strength levels comparable to those for Ti-6Al-4 V but with greater ductility and toughness when optimally processed [487,488]. Metastable β alloys [487,488] typically have lower elastic moduli than α titanium, or near-α titanium alloys and are normally slightly denser owing to the additions of heavier β-stabilizing alloying elements. Their strength in the solution-annealed condition is modest and allows machining and forming before strengthening by heat treatment below their β-transus temperature (composition specific). In addition to strengthening by the formation of α phase, and precipitation of other phases that include β' and ω during heat treatment, with ω phase potentially being a precursor to α phase formation also affects the strength and ductility of the final component [489].

The Fig. 6.14 shows optical micrographs of a metastable β phase Ti-5553 alloy that has been laser powder bed processed and heat-treated to different conditions [490,491]. In the as-built, and stress-relieved condition at 300 °C shown in Fig. 6.14 (a), the microstructure at this magnification appears as single-phase grains that are patterned and multi-sized due to the nature of the layer-by-layer LPB process [490]. If this alloy had been rapidly quenched from the β phase field, this microstructure would be 100% β, however, in the as-built or stress-relieved condition, there may be secondary phases in the microstructure that are too small to be observed at these
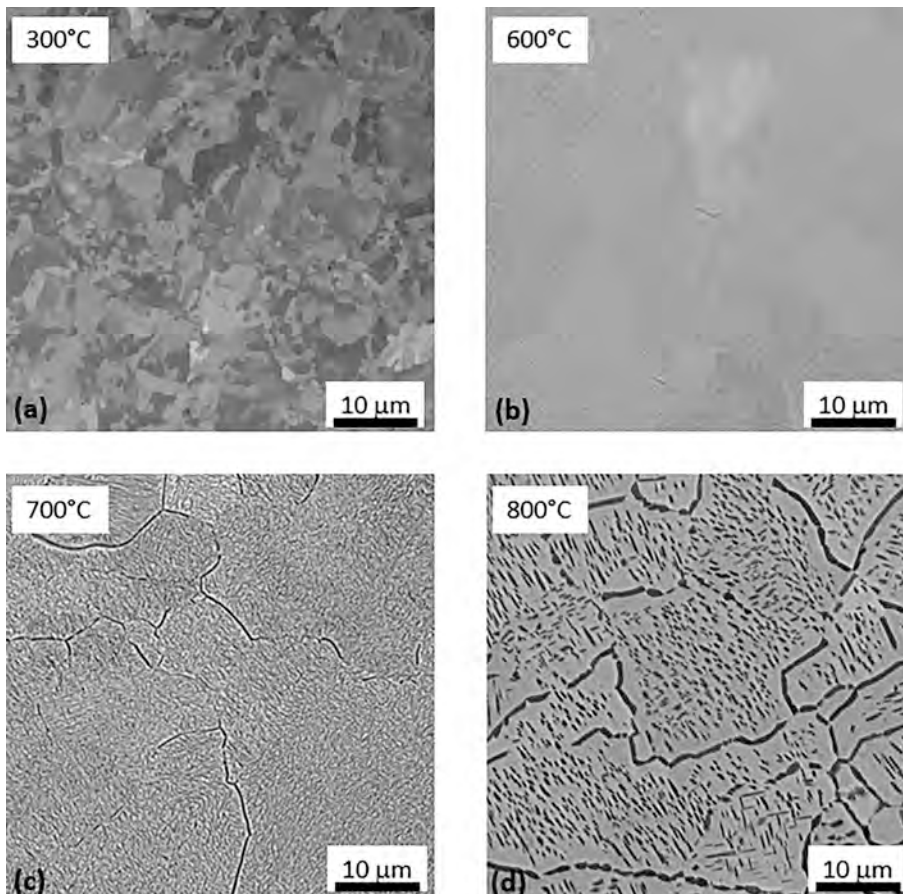
Fig. 6.14. Backscattered electron images of PBF-L processed Ti-5Al-5 V-5Mo-3Cr showing (a) stress relieved condition at 300C, and b-d) heat treated to higher temperatures [490]. Precipitates of α phase become visible at (b) 600 °C and coarsen at (c) 700 °C and (d) 800 °C [490]. The α phase (dark) forms on grain boundaries and is also dispersed throughout the β grains.

magnifications. Upon heat treatment at higher temperatures, the α phase nucleates, grows, and becomes visible at 600 °C (Fig. 6.14 (b)) and above, where it is observed to be present both within β grains and along the β grain boundaries. As the heat treatment temperature increases to 700 °C (Fig. 6.14 (c)) and 800 °C (Fig. 6.14 (d)), there is a coarsening of the microstructural features and an increase in the size of the α phase. At 800 °C the microstructure consists of approximately 25% α in what appears to be a β phase matrix, thus there is an optimum post-build heat treatment for this alloy since these microstructural features affect both strength and ductility.

The use of metastable β alloys has been focused on two principal areas of application: (1) for traditional aerospace components, as summarized by Cotton et al. [486], and (2) for biomedical purposes such as implants and prosthetic devices [487]. The development of metastable β alloys for aerospace applications preceded their consideration for bio-medical use. These efforts led to the commercialization of several successful alloys including β-C, β − 21S, and Ti15V3Cr3Sn3Al. Ti alloys are bio-inert and are often selected for biomedical applications including various implants. The development of metastable β alloys for biomedical applications followed a two-stage path with time [488]. Initial efforts in the bio-medical field were aimed at (α + β) Ti-6Al-4 V alloys but issues with their higher modulus caused issues with stress shielding and loosening with attendant failure issues [488]. This concern prompted bio-medical researchers to turn to metastable β alloys owing to their lower moduli. During this first stage, alloys used for aerospace were natural starting points. The focus of alloy development was on lowering the modulus of metastable β alloys to match more closely with that of bones (~30 GPa) to avoid stress shielding. However, these alloys could not achieve both low modulus and high strength. This issue led to research aimed at finding alloys with low modulus and high strengths in the second stage of development, often containing considerable Nb content.

PBF-EB of the β alloy Ti-24Nb-4Zr-8Sn formed [492] a lamellar α'' (orthorhombic Martensite) phase in the β matrix with a specific orientation relationship between the two phases, $[100]_\beta$ // $[100]_{\alpha''}$. The presence of the α'' produced high hardness and strength but can lead to poor fatigue properties. The hardness of the material was ~ 25% greater than that of an arc melted alloy. PBF-L of Ti-24Nb-4Zr-8Sn scaffolds for biomedical applications has been performed by Li et al [493]. Production of scaffold structures has also been considered to provide stiffness matching with bones with Ti-6Al-4 V. The porous scaffolds also assist with bone integration (osseointegration) and contribute to better implant performance since it permits control of component stiffness to match the bone modulus. Issues with the evaporation of Sn (high vapor pressure) in the β alloy caused porosity in the scaffolds which caused the fracture of some of the struts on straining. Development of alternate alloys with little or no Sn may prove helpful. The presence of unmelted particles also contributed to strut failure [493].

Ti-26 Nb β alloy parts were made by DED-L by Wei et al. [494]. Heat treatment after deposition at 650° C (sub-transus) revealed the presence of some α-phase which disappeared above 850 °C (supra-transus). Like in the last study, unmelted Nb particles were found in the as-deposited sample due to the low laser power (750 W) used for this study. Some solidification segregation was also visible in the deposits, as seen in the micrographs in Fig. 6.15. The position of α peaks in the XRD spectra shifted to lower values of diffraction angle (commonly called 2θ) with annealing due to Nb dissolution which caused an increase in lattice parameter. The extent of Nb dissolution increased with increasing heat treatment temperatures. Fine acicular α_S was found in the inter-dendritic regions after heat treatments
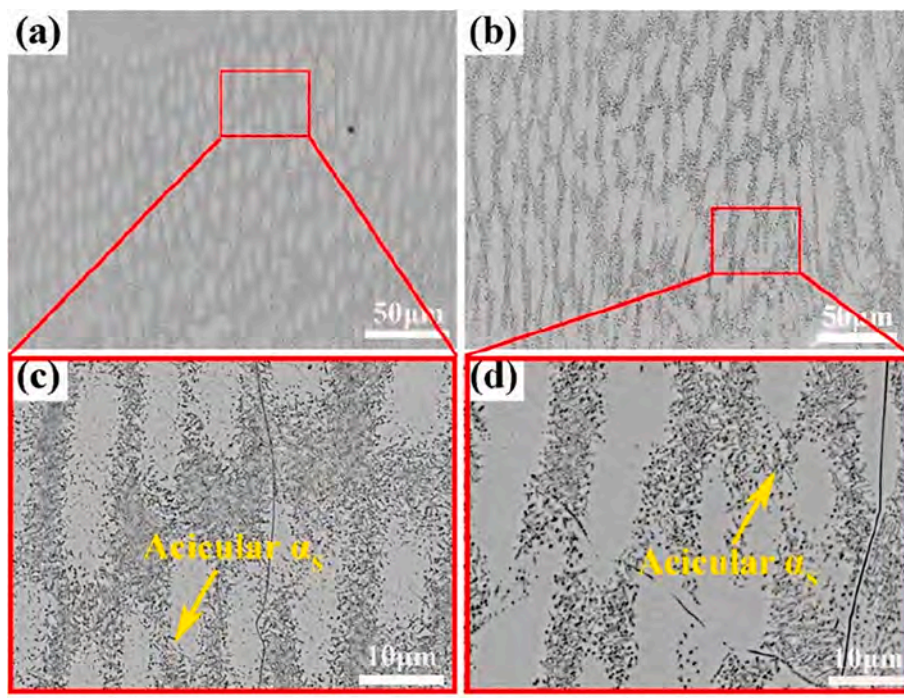
Fig. 6.15. Microstructure of annealed samples of DED-L of Ti-26Nb β alloy at different temperatures for 0.5 h (a) 650 deg. C and (b) 750 deg. C. (c) and (d) are the high magnification images of (a) and (b), respectively [494].

due to the residual effects of segregation. High strength was achieved in Ti-35Nb-7Zr-5 T (a metastable β alloy) parts made by PBF-L by Raghunandan et al. [495]. The presence of geometrically necessary dislocations (GNDs) near grain boundaries from fast cooling and ⟨200⟩ texture of the β grains were claimed to contribute to the high strength. The as-deposited microstructure was characterized by a cellular solidification microstructure. In addition, DED-GMA of a metastable β alloy called β-C [496] and DED-GMA of Ti-35Nb-15Zr metastable β alloy [497] have also been reported. Several strategies to control grain structure, phases, and defects during AM of these alloys are discussed below.

6.2.2. Control strategies for grain structure, phases, and defects

Metastable β alloys have been used to fabricate components using different processes such as PBF-L, PBF-EB, DED-GMA, and DED-L where the part temperature fluctuates with layer-by-layer processing conditions. Because of this and the sensitivity of these alloys to heat treating, the alloy composition and processing conditions are critical in producing a component with the desired as-built or post-build heat-treated properties for optimum performance. In addition, since these titanium alloys, in general, tend to have low ductility, they are particularly sensitive to internal defects that may cause stress concentrations, reduce strain to failure, and reduce fatigue life [492,493].

Heat treating of metastable β alloys can precipitate α phase at the grain boundaries and interior of the grains. These effects have a strong influence on mechanical properties as illustrated in Fig. 6.16 for a PBF-L processed Ti-5553 alloy [490]. Initially, in the as-built condition, the alloy has a moderate ultimate strength of about 800 MPa, with good ductility and nearly 18% elongation to failure. Heat treating at temperatures in the 400–600 °C range for 1 hr, increases strength above 1,000 MPa, but the ductility drops to below 2%, which is not acceptable for most engineering applications, and there are associated large changes in the elastic modulus. Heat treating to higher temperatures overages the microstructure, recovering some of the ductility with a corresponding loss in strength, and places the microstructure in a more stable condition. Bakhshivash et al. [498] demonstrated this on a Ti-5553 build using different heat inputs as defined by a volumetric energy density (VED, measured in energy per unit volume of melted metal, of the PBF-L processing parameters. Low VEDs produced substantially single-phase β microstructures with small amounts of ω phase, while higher VEDs aged underlying layers of the build. At medium VED, the build has a consistent hardness of approximately 300 Vickers, but at high VED only the topmost layers have this hardness, while lower layers in the build have α phase precipitates and Vicker's hardness values of approximately 500 due to significant aging during the build.

One solution to preventing the overaging of metastable β alloys during the build is to limit the heat input. However, several tradeoffs must be considered. First, lower heat inputs typically slow the build speed and increase the part cost. The lack of fusion defects can form if insufficient heat is present to properly remelt previous tracks. Fig. 6.17 shows a typical lack of fusion defect in a PBF-L processed Ti-5553 alloy [491], which would affect the mechanical properties of the joint. Therefore, optimization of printing parameters is critical for metastable β titanium alloys to avoid defects on the low heat input end, and avoid the formation of α phases on the high heat input end of the processing parameter window. Fig. 6.17 further shows another important consideration, which is surface roughness. In this part, the thin vertical truss element has ridges and valleys with ~ 0.1 mm surface roughness with additional powder particles attached. This roughness creates stress risers which are undesirable but can be improved using lower heat inputs. For example, it is found that the surface roughness significantly varies for a PBF-L Ti-5553 part manufactured with low, medium, and high VED [498]. It is clear that surface roughness improves with lower VED, but this effect also needs to be optimized to avoid the lack of fusion defects at lower heat inputs.

Metastable β titanium alloys can also be joined together by welding [486,499] and welded in the AM condition [490], which
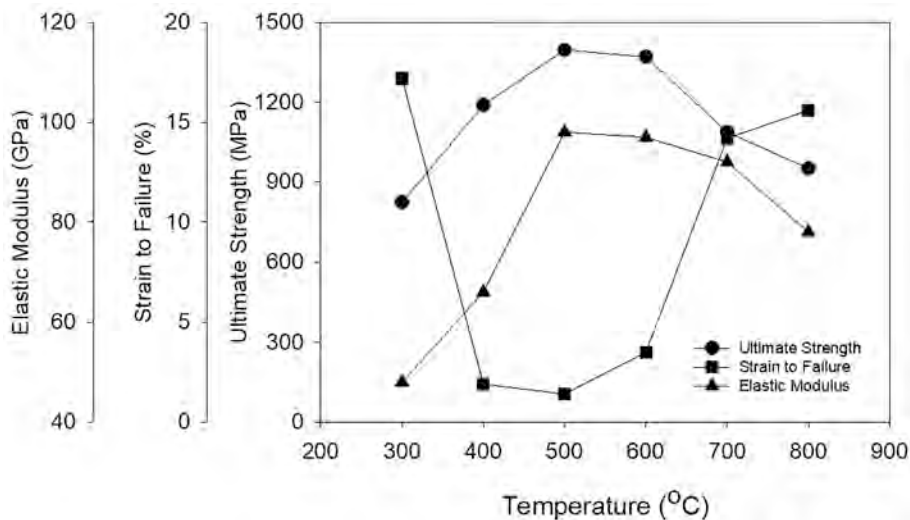
Fig. 6.16. The effect of heat treating in the 400–600 °C range for 1 h on the mechanical properties of metastable Ti-5Al-5 V-5Mo-3Cr PBF-L alloy showing an increase in strength and corresponding dip in ductility, with corresponding changes to the elastic modulus [490].

Fig. 6.17. Lack of fusion bulk defects, and rough surface of a Ti-5553 laser PBF processed lattice structure component [491].

provides opportunities to repair defects in AM parts and join smaller AM parts together to make structures larger than can be built in a powder bed. Pulsed laser beam welding of the Ti-5553 component at a short pulse duration was performed [490] where the fusion zone of the weld was defect-free with what appears to be a single phase β-titanium microstructure [490,491]. The fusion zone grains grow epitaxially from the AM base metal microstructure as would be expected for a fusion weld, with what appears to be minimal heat-affected zone changes to the surrounding AM microstructure. Marvel et al. [499] produced electron beam welds in a metastable β Ti-5553 alloy at slower cooling rates, where in situ aging produced precipitation of ω and α phases in the microstructure of both the weld and base metal regions. Post-build heat treating to recover the microstructure is possible, but complicated multi-stage heat treating schedules may be required [499]. Such post-build heat treatments of AM components are dependent on the initial AM processing parameters and the specific alloy composition but may be required to achieve optimal metastable β titanium properties.

7. Control of grain structure, phases, and defects in copper alloys

Copper and copper alloys are used for many different types of applications that make use of copper's exceptional thermal and electrical conductivity, as well as its ability to form high-strength, wear-resistant, and corrosion-resistant alloys [500]. However, pure copper can be difficult to deposit by welding [501] and can be difficult to additively manufacture because its high thermal conductivity rapidly draws heat away from the melt zone [502,503]. Creating a melt pool in copper requires intense heat sources to counteract its high thermal conductivity, and the ensuing rapid cooling of the melt pool often results in macroscopically rough solidified surfaces. Other challenges for producing AM parts from copper include the high solubility of oxygen in liquid copper, which causes porosity in melt zones, and copper's high reflectivity to infrared laser wavelength radiation, which reduces energy absorption during laser-based AM processes. Nevertheless, progress has been made in developing additively manufacturing high purity copper, copper alloys, and functionally graded composites containing copper.

7.1. Strategies for grain structure, phases, and defect control in high purity copper

Components that require high thermal and electrical conductivity use high purity copper because even small amounts of many impurities lower the conductivity [500]. Some exceptions exist where small amounts of elements such as Cr are added for strength or second-phase particulates such as alumina are added for high temperature creep resistance [500]. The copper feedstock needs to be deoxidized and free of copper oxide phases to minimize porosity formation in the melt pool, and oxygen-free high conductivity (OFHC) copper, which is available in both powder and wire forms, is often used for PBF and DED applications. Copper components such as metal injection tool molds, semiconductor cooling applications, and other heat exchanging devices are targeted areas for PBF-L [503,504] and PBF-EB [505,506] where higher powers may be required compared to other metals and alloys [3,507]. In addition, shorter laser wavelengths are beneficial for laser processing due to the poor coupling of infrared laser wavelengths that are typically used in PBF-L [502], and low powder bed temperatures are required due to the tendency for high purity copper particles to sinter

together [506].

Even with high purity powders, substantial porosity of > 20 vol% has been observed in PBF-L fabricated copper components [502,503]. Fig. 7.1 shows an example of this porosity, which both reduces the mechanical integrity of the component and lowers its bulk thermal properties. This type of porosity is most frequently related to the difficulties of keeping a steady and continuous melt pool established and incomplete wetting into preexisting layers, leaving the lack of fusion defects in the microstructure. Through careful PBF-L processing parameter development, porosity and lack of fusion defects in pure copper can be significantly reduced but porosity is difficult to eliminate. DED-GMA using wire feedstock of OFHC copper can be used to manufacture components from copper but requires significant attention to the processing parameters for starting and maintaining a stable melt pool, particularly before the part reaches a steady-state preheated condition when wetting into previous layers can be difficult. Fig. 7.2 shows a cross-section through a DED-GMA wall built from OFHC copper where spherical porosity exists and is common in these builds. If required, hot isostatic pressing is successful in reducing porosity and producing more dense parts in binder-jet fabricated pure copper and may be useful to close internal voids made by other AM techniques.

7.2. Strategies for grain structure, phases, and defect control in copper alloys

For applications where strength and corrosion resistance is desired, copper is alloyed with Sn, Zn, Ni, Al, Si, and other elements to create a variety of high strength, wear-resistant, and corrosion-resistant alloys in the bronze, brass, and cupronickel alloy systems [500]. Additive manufacturing of copper alloys faces similar challenges as pure copper, with the additional complexity of alloying element segregation and the potential for cracking in some alloy systems. Many different AM methods have been used to produce copper alloy components including PBF-L [502,508–513], PBF-EB [514–516], DED-GMA [517–525], and DED-L [526] with varying degrees of success. Bronze alloys of different compositions manufactured by PBF-L tend to be stronger than their cast counterparts due to the refinement of the microstructure created during the high cooling rates associated with PBF-L [3,508,512,513]. Post-build heat treating of PBF-L Cu-Sn bronze and DED-GMA bronze samples further increases the strength and ductility of the alloy through solid solution strengthening and have properties comparable to conventionally processed materials [508,512,527].

PBF-L was used to fabricate structures from a Cu-Ni-Sn alloy which displayed a highly refined microstructure with grain boundary precipitates that strengthened the alloy with favorable ductility so that it could be used in the as-built condition [513]. Nickel aluminum bronze (NAB) is a Cu-Al-Ni alloy commonly used for naval applications due to its high strength and corrosion resistance in seawater, and forms a martensitic microstructure during PBF-L that requires higher temperature heat treating for optimum performance, but when properly built and heat-treated can equal the properties of cast and wrought NAB alloys [510]. Precipitation hardening copper alloys containing small amounts of Cr, Zr, and Ti can be processed with small amounts of porosity at 97.9% density by PBF-L and subsequently heat-treated for increased strength [511]. The columnar grains in bronze alloys tend to grow parallel to the build direction in both PBF-L and DED-GMA and create higher strength properties parallel to the build direction than perpendicular to the build direction [511,527]. Fig. 7.3 (a) shows the microstructure of a DED-GMA silicon-bronze (3%Si-Cu) alloy wall where the elongated grains can be seen growing upward in the build direction [528]. A similar texture is seen in PBF-EB fabricated bronze alloys [514–516]. Reduced strength and ductility relative to conventional hot rolled and heat-treated alloys are sometimes attributed to porosity in the sample that may be reduced by subsequent hot isostatic pressing [511].

Many conventionally manufactured bronze components are castings that are physically too large to be made in powder beds and require higher deposition rates than are possible by PBF. Alternative DED wire-based (DED-GMA and DED-EB) [141] and powder-based DED-L [3] are high deposition rate processes that ideal for large AM parts since they do not have size restrictions of powder beds. The majority of the DED work has been performed using DED-GMA on NAB alloys with typical compositions containing Cu9% Al5%Ni plus other minor alloying elements to enhance strength or corrosion resistance [518–525]. Even higher deposition rates are
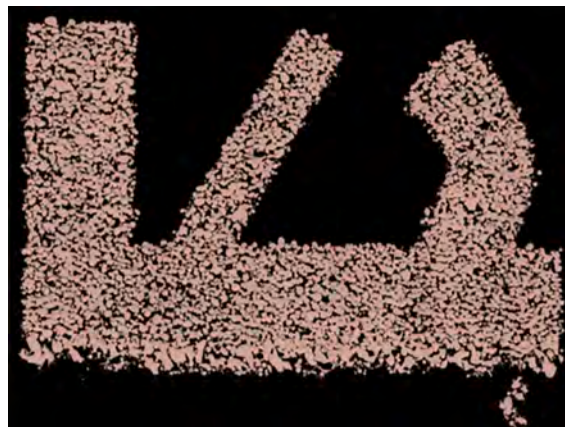
Fig. 7.1. Fabrication of high purity copper by PBF-L showing excessive porosity when non-optimal processing parameters result in the lack of fusion defects in the microstructure [502].
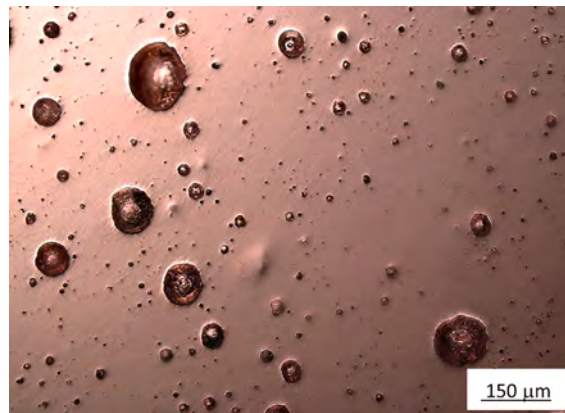
Fig. 7.2. An optical micrograph of oxygen-free high conductivity copper processed by DED-GMA showing spherical porosity that is commonly observed and difficult to eliminate (as polished) [528].
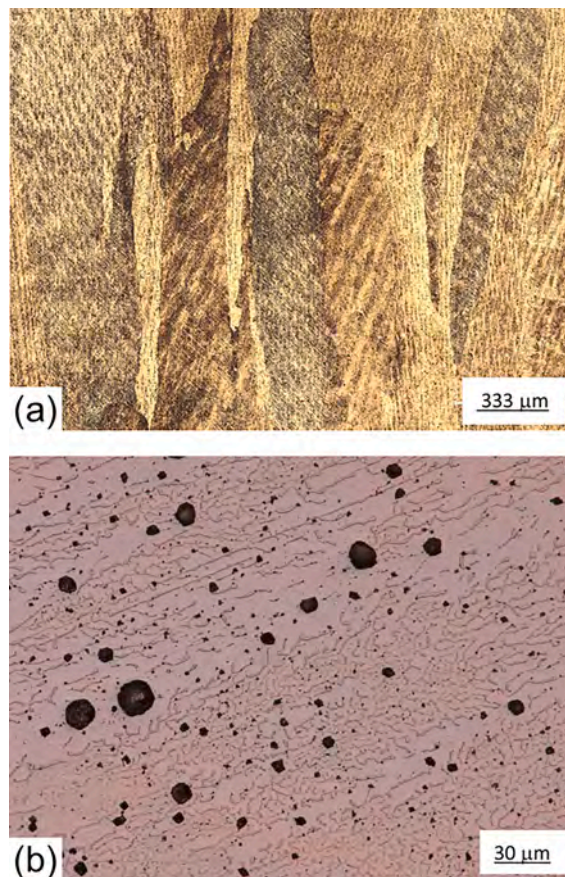
Fig. 7.3. (a) An optical microstructure of DED-GMA deposited silicon-bronze with columnar grains growing upward, parallel to the vertical build direction (etched in dilute nitric acid) [528]. (b) An optical micrograph of an in situ Cu 6 wt%Ni alloy specimen created by a DED-GMA dual wire process with Ni being added to the copper GMA melt pool using a secondary Ni cold wire feed at a controlled wire feed rate. Porosity is present and is similar to what is observed in pure copper (etched with FeCl$_3$ in HCL aqueous solution) [528].

being developed using dual wire rather than conventional single wire DED methods [523]. Dual wire processes are also being explored for in-situ alloying using DED-GMA [522] and also DED-EB [529] processes. A DED-GMA build microstructure produced by in-situ alloying with two dissimilar metal wires is shown in Fig. 7.3 (b), where a transition from an OFHC copper build to an in-situ alloyed Cu-6 wt%Ni alloy was produced. In this case, a cold Ni wire was fed into the copper GMA melt pool at a controlled rate to

produce the desired composition [528]. Nickel will alloy with copper, being miscible in both the liquid and solid phases, and the microstructure has both nickel and copper rich regions due to the high melting point of nickel and incomplete homogenization in the weld pool during cooling to room temperature. Practical limits for this process in Cu-Ni are approximately 3–12 wt% Ni, where higher Ni alloy content would require a preheated hot-wire for homogeneity. Some porosity is present in the microstructure, particularly near the edge of the melt pool in this sample.

The wire-based AM processes are very similar to welding [141] and many bronze alloy welding filler metals have been developed that tend to work well in AM processes, producing dense 3D AM parts without cracking and minimal porosity. Fig. 7.4 shows the microstructure of an aluminum bronze alloy (6.6%Al-Cu) wall produced by DED-GMA [528]. This alloy builds very well with no cracks in thin walls and does so with minimal porosity, but it does form columnar grains along the build direction. The typical DED-GMA microstructure of copper alloys shows a degree of microsegregation and/or second-phase formation as seen in silicon bronze (Fig. 7.3 (a)). Post-build heat treating is sometimes used to homogenize the microstructure and reduce the number of intermetallic phases that form at grain boundaries for improved strength and ductility [521,522]. Such heat treatments are also used in attempts to reduce mechanical anisotropy related to the large columnar grains that form in the build [525,527]. Ultrasonic vibration during the DED build has been explored as a means to break up the columnar grain structure and build at lower inter-pass temperatures to reduce anisotropy [519]. It should be noted that not all bronze alloys will build without problems and that brittle intermetallic phases, or low melting point compounds can form during the build which will result in cracking [530,531]. One example is shown in Fig. 7.5 where a 3%Si bronze alloy was deposited using DED-GMA in a thin-wall bowl-shaped part configuration which developed cracks in the columnar grain boundaries. The cracks traversed many layers parallel to the build direction [528].

8. Functionally graded materials

Functionally Graded Materials (FGMs) refer to materials with spatially varying properties through gradual changes in composition and microstructure. AM is well suited to produce FGMs owing to its two intrinsic features: the layer-upon-layer printing process, and the selective melting of spatial regions where the scanning strategies and printing parameters can be readily altered. AM of FGMs can create components in ways not easily achievable by conventional manufacturing. These components including bimetallic joints and graded transitions have important commercial applications that can benefit from multi-material performance in some cases and cost savings in others. Additionally, FGMs fabricated by AM have been explored for high-throughput testing of material properties such as radiation damage in stainless steels [532], magnetic, electrical, and mechanical properties of Co-Fe-Ni alloys [533], and corrosion behavior of stainless steels [534].
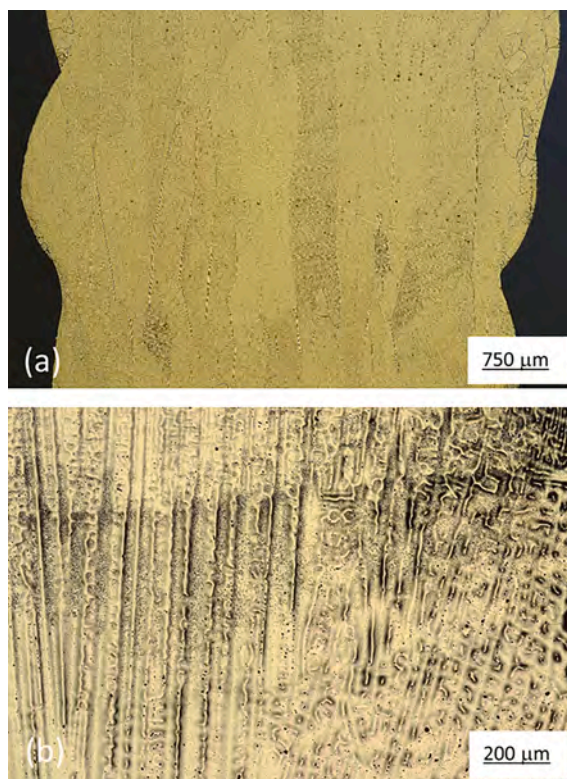
Fig. 7.4. Optical micrographs of columnar grains forming in DED-GMA 6.6%Al-Cu bronze alloy. a) As-deposited edge of the part (light nitric acid etch). B) Elongated dendritic microstructure parallel to the build direction (etched in dilute Cr-IV oxide aqueous solution) [528].

Fig. 7.5. An optical micrograph showing cracking in a DED-GMA 3 wt%Si bronze alloy 3D shape, where the cracks form at the columnar grain boundaries growing parallel to the build direction (etched in nitric acid) [528].

This section is focused on metallic FGMs produced by AM using multiple feedstock materials, which is an area for increased research activities. As it has been the subject of several recent review articles [3,4,535–538], the section provides a succinct review of printing FGMs using the five feedstock materials discussed in the previous sections, i.e., steels, aluminum alloys, nickel alloys, titanium alloys and copper alloys. Additionally, recent advances in printing functionally graded copper composites are critical reviewed and used as an example to illustrate the common challenges in controlling phases and defects in printing FGMs.

8.1. AM methods for printing functionally graded materials

FGMs fabricated by AM can be achieved using a single or multiple (two or more) feedstock materials. For a single feedstock material, altering the local composition during printing has been achieved by adjusting beam energy to evaporate volatile elements (e. g., Al in Ti alloy) [539,540] or modifying shield gas composition (e.g., the addition of N_2) to induce gas-molten metal reactions [541,542]. Clearly, the composition range that can be varied using a single feedstock material is limited. On the other hand, AM using multiple feedstock materials, commonly referred to as multi-material additive manufacturing, can achieve wide composition and microstructure gradients.

Between the two most widely used AM processes for metal printing, DED is much more amenable to using multiple feedstocks than PBF. For example, different mixing ratios of feedstocks can be readily achieved by adjusting the feed speed of dual wires in DED-GMA
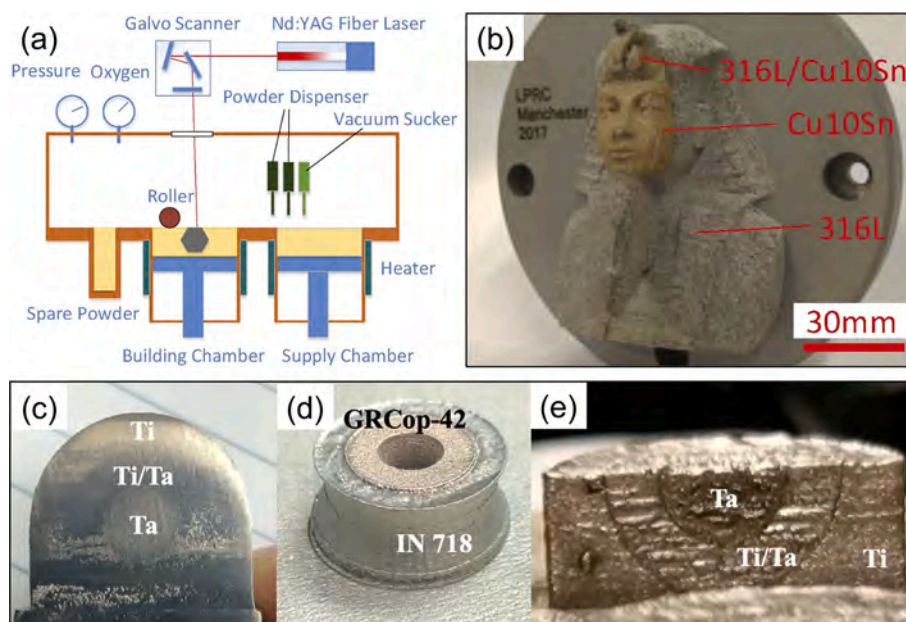
Fig. 8.1. a) Schematics of a blade + ultrasonic hybrid powder spreading system equipped with a micro-vacuum powder suction device for multi-material PBF-L [546] and b) a multi-material sample printed by the system in (a) [546]. (c-e) Printed structures with Ti to Ta grading in both the vertical and horizontal planes and compositional grading between Inconel 718 and GRCop-42 copper alloy [547 548].

[543] or multiple powder streams in DED-L [544]. In-situ alloying of different feedstock mixtures in the melt pool then yields spatial variations in compositions potentially along all three directions (i.e., build height and within layers) [544]. However, the geometric complexity and accuracy printed by DED are usually limited and inferior to those printed by PBF.

For PBF of FGMs, advanced powder spreading systems are necessary to dispense powder particles of different materials onto the powder bed. Wei and Li reviewed various powder spreading systems for multi-material PBF-L such as a blade-based dual powder recoater and an ultrasonic-based dual powder dispenser [535]. Fu et al. discussed the potential application of those powder spreading systems for PBF-EB under vacuum conditions [545]. Moreover, they demonstrated the feasibility of an interesting approach to producing Cu-W graded material, where Cu and W powders with different particle sizes were used and the layer thickness was varied to control the Cu/W ratio in a layer. The composition gradient is commonly realized along the build direction (i.e., 1D functional grading). Wei et al. developed a blade + ultrasonic hybrid powder spreading system equipped with a micro-vacuum powder suction device shown in Fig. 8.1 (a) [546]. They demonstrated the feasibility of realizing the composition variations within layers and along the build direction (i.e., 3D functional grading), as shown in Fig. 8.1 (b). Walker et al. also demonstrated 3D functional grading using a PBF-L machine equipped with special powder hoppers to place materials at specified locations and a vacuum pump to selectively remove the prior powder [547]. Printed structures with Ti to Ta grading in both the vertical and horizontal planes and compositional grading between Inconel 718 and GRCop-42 copper alloy [547 548] are shown in Fig. 8.1 (c-e). It is evident that Ta that has a higher melting point than Ti showed rough structure under the same heat input.

8.2. Common challenges for controlling microstructure in functionally graded materials

AM of FGMs using various dissimilar metal combinations involving steels, aluminum alloys, nickel alloys, titanium alloys, and copper alloys has been studied in the literature although the resultant part quality varies greatly depending on the specific combinations [535,537]. Similar to dissimilar metal welding, a primary challenge for AM of FGMs is the lack of metallurgical compatibility between some dissimilar metals. The AM processes work well when the metallurgy of the dissimilar metal combination is known to be compatible and can be accomplished without forming brittle intermetallic phases or low melting point alloys that can result in liquation cracking [549,550]. The issue of forming brittle intermetallics is particularly challenging for the dissimilar combinations of titanium alloys to steels, titanium alloys to nickel alloys, titanium alloys to aluminum alloys, and aluminum alloys to steels. For example, Zhang and Bandyopadhyay used DED-L to print bimetallic Ti6Al4V + Al12Si structures [551]. The transition region showed high hardness due to the formation of Ti$_3$Al intermetallic phase and exhibited brittle failure modes during compression tests.

A wealth of information about weldable alloys and compatible combinations is available in the existing welding literature where dissimilar metal welding, weld cladding, and weld surfacing consumables and procedures have already been developed for a wide variety of applications [552]. For traditionally non-weldable combinations of metals such as the aforementioned titanium to nickel alloys, intermediate layers have been used to prevent cracking or other defects at the interface in DED-L builds [553,554]. In these cases, AM parameter development tends to be more involved than when building similar metal parts to ensure good bonding and minimal defects in the dissimilar metal interface and the transition zone, but high-quality parts have been demonstrated using different methods to create bimetallic transitions in otherwise incompatible alloys.

Another main challenge for AM of FGMs arises from the large differences in two feedstock materials' thermo-physical properties including melting temperatures, thermal conductivity, and coefficients of thermal expansion. Additionally, in laser-based AM processes, the laser absorptivity of the two constituent metal powders can be different. These differences have been attributed to causing various defects such as the lack of fusion, unmelted powder particles, porosity, and cracking in AM of FGMs, a problem especially prevalent for FGMs of copper alloys to steels and cooper alloys to nickel alloys [535]. One strategy for mitigating these defects is to utilize composition-dependent adjustment of process parameters such as increasing the heat source power as the composition is transitioned from lower to higher melting point alloys [537].

With the continued advances in AM hardware and scan strategies, printing defect-free, quality FGMs is increasingly realized. As these FGMs are put to service, they can be subjected to unique failure modes that are uncommon to single alloys fabricated by AM. For example, dissimilar joints of ferritic steels to austenitic stainless steels are common in structures used in chemical and power generation industries. From a metallurgical perspective, the two materials are compatible and mix together well. However, during long-term high-temperature service, it is well documented that carbon diffuses away from the ferritic side towards the austenitic side, resulting in the formation of carbides in the austenitic side near the interface, which in turn promote creep cavity formation [555]. Zuback et al. studied the carbon diffusion kinetics in an FGM from 2.25Cr-1Mo ferritic steel to austenitic Alloy 800H [556]. It was found that the carbon diffusion rate was significantly reduced by replacing the dissimilar joints with the compositionally graded joints. Moreover, they pointed out the importance of optimizing the grading based on the chemical potential of carbon rather than carbon concentration itself since the chemical potential of carbon was not a linear function of composition.

Corrosion properties are important for the in-service performance of additively manufactured materials [557]. For single alloys fabricated by AM, corrosion properties have been studied for aluminum alloy [558], copper alloy [559], titanium alloy [560], etc. For FGMs fabricated by AM, galvanic corrosion which is common in dissimilar metal welds can be important. For example, Kong et al. studied the corrosion properties of nickel Inconel 718 alloy with different TiC contents printed by DED-L [561]. It was found that the corrosion rate increased slightly with increasing TiC content due to the galvanic effect. However, to date, galvanic corrosion of FGMs especially those between aluminum alloys and other dissimilar metals (e.g., steels) remains largely unexplored. Further research is thus needed to ensure that FGMs fabricated by AM do not fail prematurely in service due to the issues such as carbon migration and galvanic corrosion.
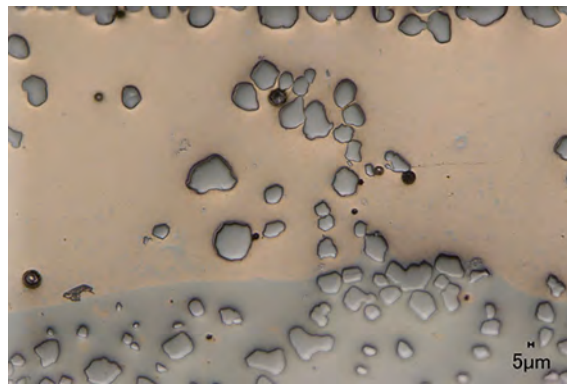
Fig. 8.2. DED-L copper-tungsten composite produced on a stainless steel substrate. This image shows the transition from the 2nd to 3rd pass on the stainless steel substrate located below. The tungsten particles are wet by the copper and incorporate into the liquid melt pool (as polished) [528].
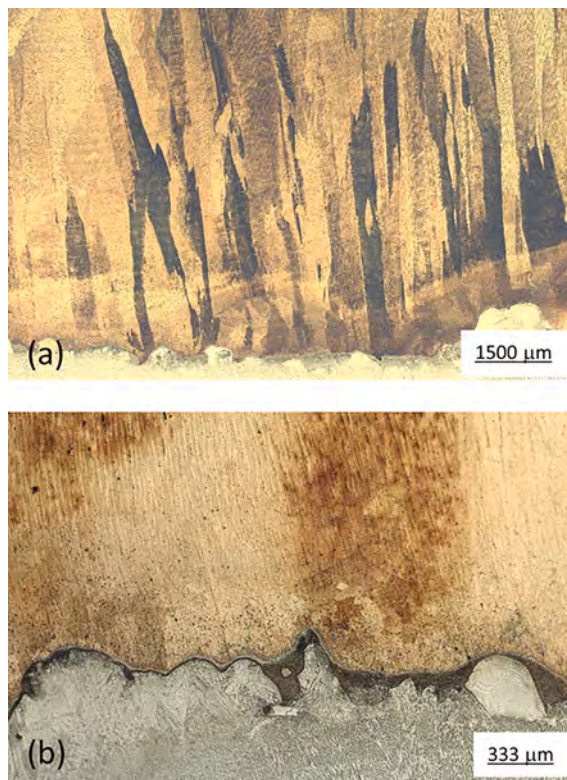
Fig. 8.3. a) Optical macrostructure of a dissimilar metal DED-GMA bimetallic transition interface between 308L SS (bottom) and columnar grains of the silicon-bronze, b) higher magnification microstructure of the interface region (etched in nitric acid) [528].

8.3. Functionally graded copper composites

Compositionally graded copper composites and bimetallic parts provide a means to transition the material composition and properties from copper or copper alloys to another metal [526,529,531,544,556,562–565]. Smooth graded transitions between the two dissimilar metals are accomplished using the DED-L powder method where the composition can be adjusted on multiple thin layers by altering the ratio of two or more powder feeders on each layer where they form an in-situ alloy in the melt pool [3,544,556]. Fig. 8.2 shows a transition from a 304L stainless steel base plate (bottom) to a copper/tungsten composite made by the DED-L process [566]. In this micrograph, copper and tungsten powders were mixed and deposited onto the stainless steel base plate in multiple layers to produce a graded density composite, similar to an aluminum/tungsten-particulate composite produced using the same technique [544].

More abrupt transitions can be made directly from one metal to copper or copper alloys by PBF or DED using a dissimilar metal
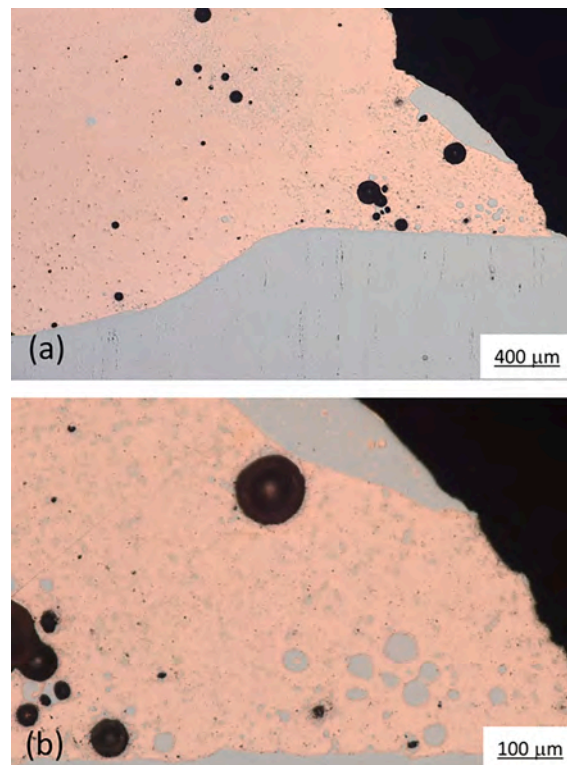
Fig. 8.4. a) Optical microstructure of DED-GMA thin wall dissimilar metal build in OFHC copper, transitioning from a 304L SS base plate, and b) higher magnification view of the edge of the build showing globules of copper in the stainless steel, and stainless steel in the copper (as polished) [528].

build plate or using different feedstocks, to create bimetallic parts by wire or powder methods [3,526,531,562–564]. Wire-based DED additive manufacturing for bimetallic parts is developed directly from traditional welding methods using arc, laser, or electron beam heat sources to melt and deposit a dissimilar filler metal [141]. Examples include transitions from a steel substrate to silicon bronze alloy made by the DED-GMA technique [562], and stainless steel to copper AM transition using DED-EB [529]. Copper and copper alloy bimetallic joints are created between many different metal combinations. For example, maraging steel to a copper build plate [564], a Cu-Cr-Nb oxidation-resistant alloy to an Inconel 718 build plate [526], Inconel 625 to a copper build plate [563] using the DED-L process, and 316L stainless steel to a Cu-Sn bronze alloy using PBF-L with a dual powder arrangement [531] have all been demonstrated. Fig. 8.3 (a) and (b) show a DED-GMA transition between 308 stainless steel to silicon-bronze at low and high magnifications, respectively[528]. The transition region between the two alloys occurs over approximately 500 μm, which is less than the bead height for each deposited layer and is crack-free and porosity free. Although dissimilar metal transitions between bronze and stainless steel using DED-GMA have shown some propensity for cracking at the interface due to the formation of intermetallic compounds [549], this particular transition was crack-free, possibly as the result of low residual stress in the thin wall that was built in this case. Fig. 8.3 (b) also illustrates the elongated bronze grains that initiate very close to the transition region and grow vertically upward in the build direction.

The Fig. 8.4 (a) shows the microstructure of a 308L stainless steel to OFHC copper transition joint produced by DED-GMA [528]. The copper wets the stainless steel base metal, forming a braze-like interface between the two metals, and some of the stainless steel melts into the copper as can be seen by the gray-colored elements in the copper matrix. Other than the presence of some spherical porosity, the transition produced a sound crack-free part [528]. Fig. 8.4 (b) shows the globular morphology of stainless steel in the copper, and copper in the stainless steel, at higher magnification. The globular morphology indicates the presence of liquid phase immiscibility that can occur in Cu-Fe alloys where a metastable liquid phase miscibility gap is known to be present [567,568]. An unusual feature is that the stainless steel droplets can migrate up multiple weld beads during the build, and were observed near the edge of the build through > 10 copper layers, which could be troublesome for some applications where pure copper is desired.

In summary, challenges remain to produce fully dense parts and smooth surfaces in copper-based FGMs due to copper's propensity to form porosity and because of its high thermal conductivity. The metallurgy of some copper alloys produces sound deposits with other alloys, while others can develop solidification-related cracking, so it is important to select known weldable alloys and ones that respond well to the AM process being used. The above examples of functionally graded copper composites printed by PBF and DED processes using powder and wire feedstocks underscore the common challenges in AM of FGMs especially those involving dissimilar metals with mismatched thermo-physical properties and limited metallurgical compatibility.
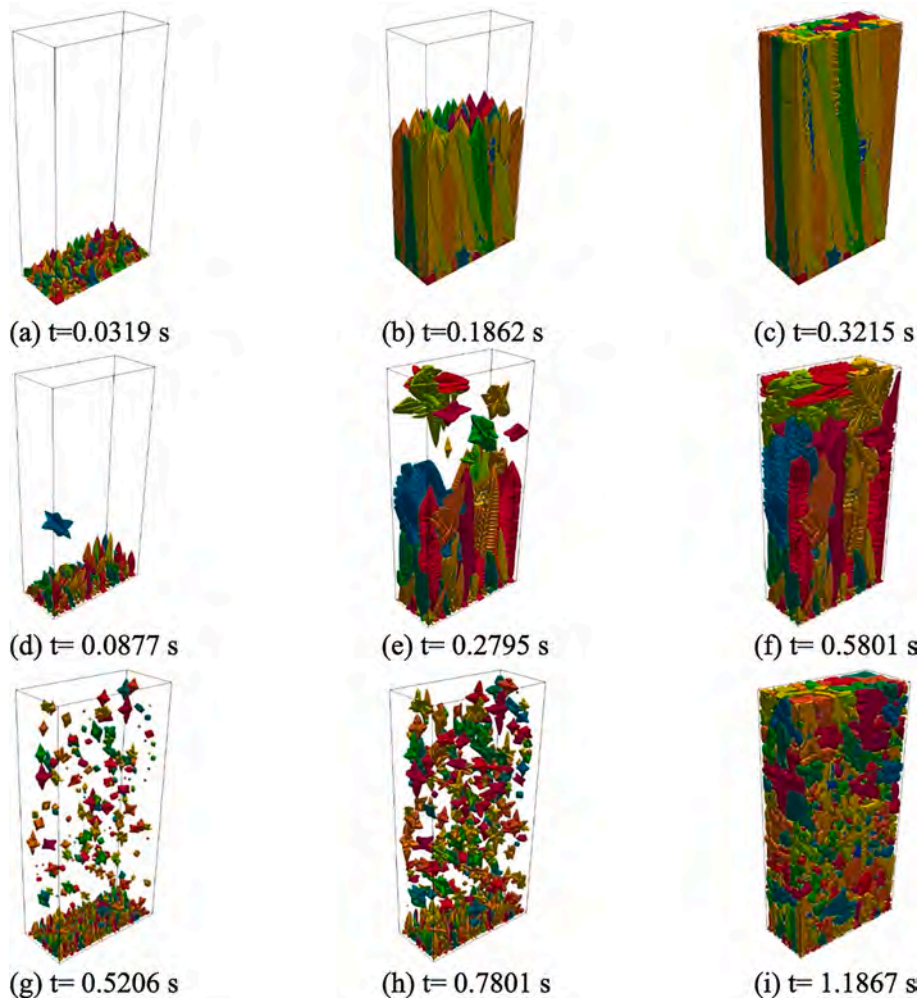
Fig. 9.1. Dendrite growth during solidification of PBF-L of IN718 simulated using phase field model [570]. Results are shown with time for different solidification regimes: (a–c) columnar: G = 2 K/m and R = 10^{-3} m/s, (d–f) mixed: G = 10^4 K/m and R = 0.01 m/s, (g-i) equiaxed: G = 100 K/m and R = 0.1 m/s.

9. Emerging tools for controlling grain structure, phases, and defects

Mechanistic models have provided insight into the microstructure variations and defect formation based on scientific principles that could not have been achieved in any other way [1,4]. However metallic materials are notoriously complex, and most mechanistic models are computationally intensive. However, analytical models are also used in the understanding of various aspects of microstructure as discussed in section 2. Currently, model-based understanding of the evolution of microstructures and defects has been rather limited. In addition, in many metallic systems, the physical processes in the evolution of microstructure and defects are still evolving. Furthermore, a specific defect such as cracking may originate from multiple mechanisms. As a result, mechanistic models cannot be built in many cases because of the lack of mechanistic understanding. In such cases, data-driven techniques such as machine learning, dimensional analysis, and statistical methods can provide important trends of the effects of process parameters on grain structure, phases, and defects often without the need for phenomenological understanding. This section reviews the applications of mechanistic models as well as data-driven techniques to control grain structure, phases, and defects in AM.

9.1. Mechanistic model-based control

9.1.1. Models to control grain structure

9.1.1.1. Phase-field model. Phase-field models are used to predict solidification structure during additive manufacturing. They solve the Allen-Cahn and Cahn–Hilliard equations and can track the interfaces of different phases. Sub-grain level features can be simulated for controlling solidification structures during laser PBF. For example, Park et al. [569] proposed a phase-field model to simulate the
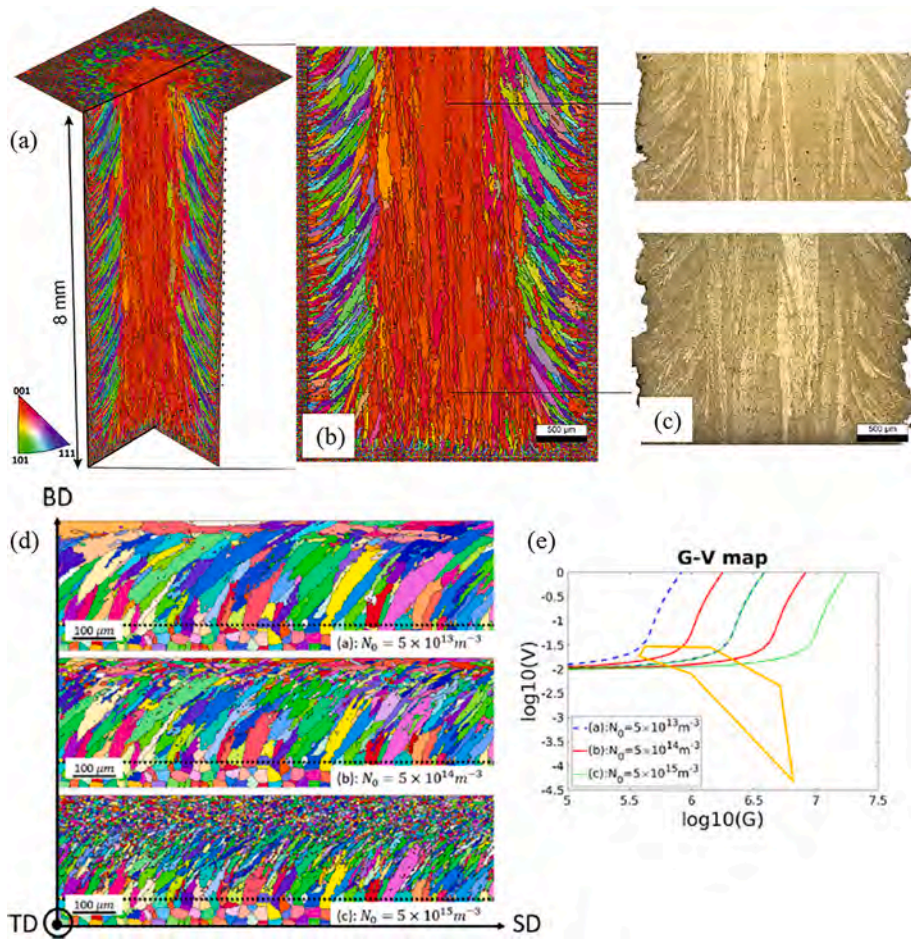
Fig. 9.2. Grain growth and CET during solidification AM simulated using Cellular Automata: (a) 3D section view of the numerically predicted microstructure, (b) and (c) comparison of the simulated and experimental results with a longitudinal section cut [579]. (d) Differences in grain structure at different nucleation density [582]. (e) The G-V map was obtained with different values of N_0 [582].

solidification process during laser PBF of AlSi10Mg. The model considered both the epitaxial effect of the previously deposited layer and the deviation of the growth direction from the local heat flow direction. The knowledge of the grain structure evolution for a given set of processing conditions allows appropriate selection of processing conditions including the scanning strategy. Nabavizadeh et al. [570] developed a three-dimensional hybrid phase-field - lattice Boltzmann model to simulate columnar-to-equiaxed transition in Inconel 718 alloy during directional solidification (Fig. 9.1). Based on the model, a CET solidification map was developed for different temperature gradients and growth rates [570] which can be used to identify conditions to achieve the desired solidification morphology. Yang et al. [571] proposed a phase-field model to simulate the grain nucleation and growth in molten pools, epitaxial growth from powder particles, substrate, and previous tracks, grain re-melting and re-growth in overlapping zones, and grain coarsening in heat-affected zones during laser PBF of 316L [571]. The simulation of the spatiotemporal variations of the 3D microstructure by the phase-field model provides a useful route for visualization, which is challenging experimentally. The mechanisms for the formation and transition of various sub-grain and grain structures revealed by the simulations can be useful for the determination of control strategies targeting specific microstructures.

9.1.1.2. Cellular automata and Monte Carlo models. Modeling of microstructure during additive manufacturing using Cellular Automata mainly focuses on the solidification process [572–581]. The morphologies, sizes, and orientations of the grains have been simulated. For example, Koepf et al. [579] used a Finite-Element (FE) model with a Cellular Automata (CA) model to predict the microstructure evolution during PBF-EB of CMSX-4, as shown in Fig. 9.2 (a)-(c). Since the grain morphology and the texture could be calculated, the modeling provides a tool to connect process variables with the grain structure and texture. Li et al. [582] used a mesoscale Cellular Automata model with a macro-scale thermal model to predict the three-dimensional grain structure in the direct laser deposition process of stainless steel 304, as shown in Fig. 9.2 (d)-(e). It was found that the nucleation parameters (N_0, the number of nucleating sites, ΔTc, the extent of undercooling) can significantly affect the grain structure. An increase of N_0 and/or a decrease of ΔTc will encourage the occurrence of equiaxed grains, while a decrease of N_0 and/or an increase of ΔTc will promote columnar grains.
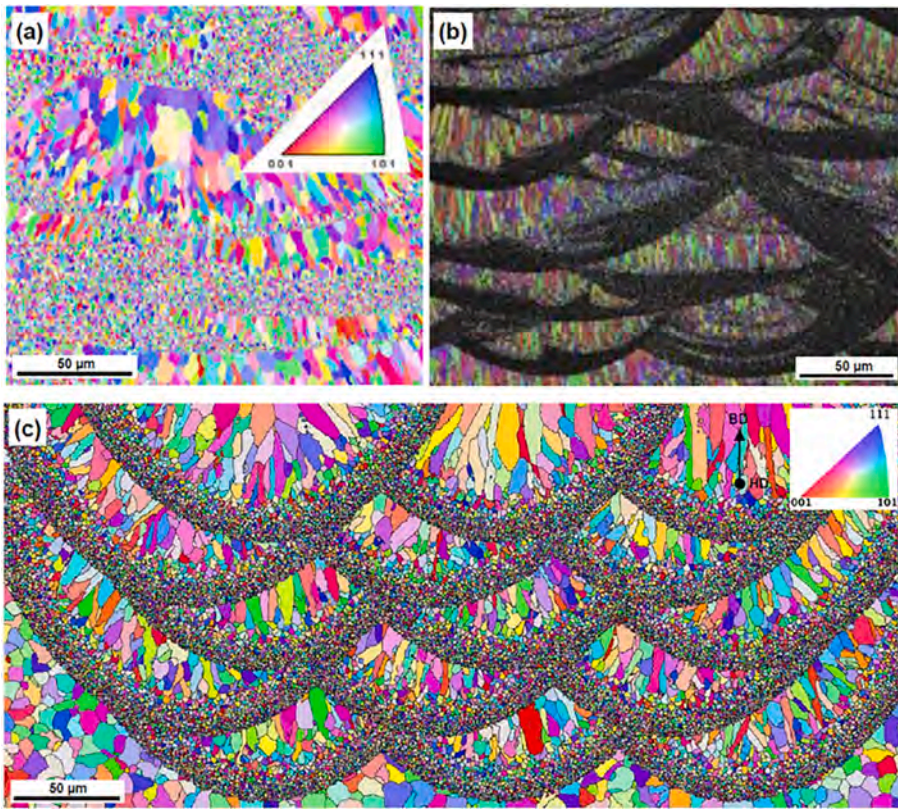
Fig. 9.3. Microstructures of PB-LBM processed (a) Scalmalloy® and (b) Al-Mn-Sc alloy, and (c) simulated microstructure of Sc-modified aluminum alloys [573].
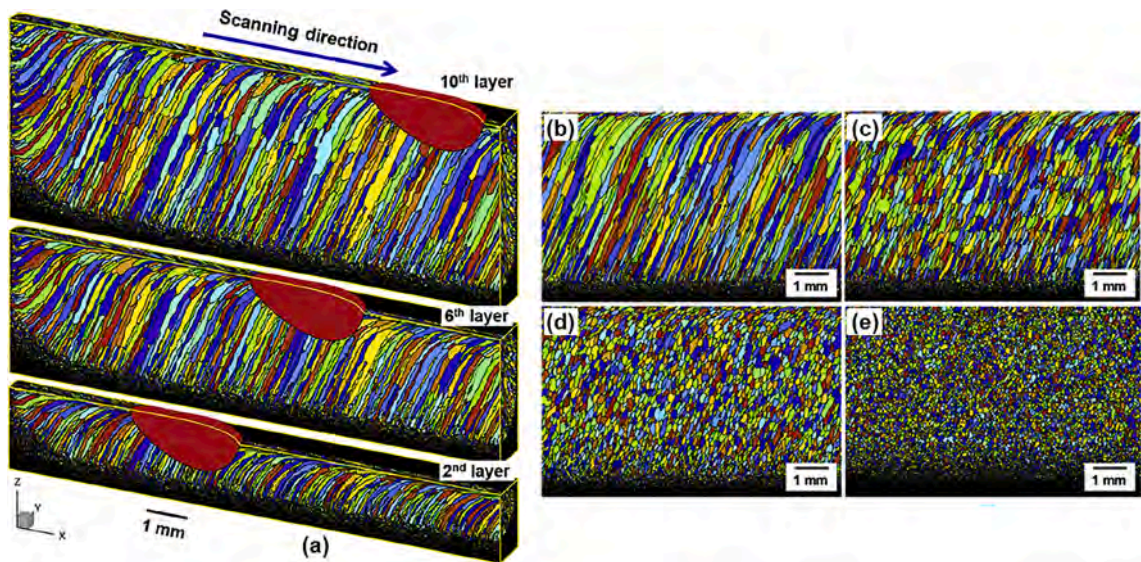
Fig. 9.4. Evolution of grain structure simulated considering the localized solidification conditions at the trailing edge of the moving molten pool, and the solid-state growth due to multiple thermal cycles using the Monte Carlo method [36]. The results are for DED-L of Inconel 718.

The model is useful to study the effect of the variation in nucleation density due to the addition of inoculants or grain refiners on solidification morphology and grain growth. Mohebbi et al. [573] used the CA model to simulate the grain growth process during laser PBF of aluminum alloys. The formation of the bimodal grain structure was well reproduced, as shown in Fig. 9.3. Such well-tested CA
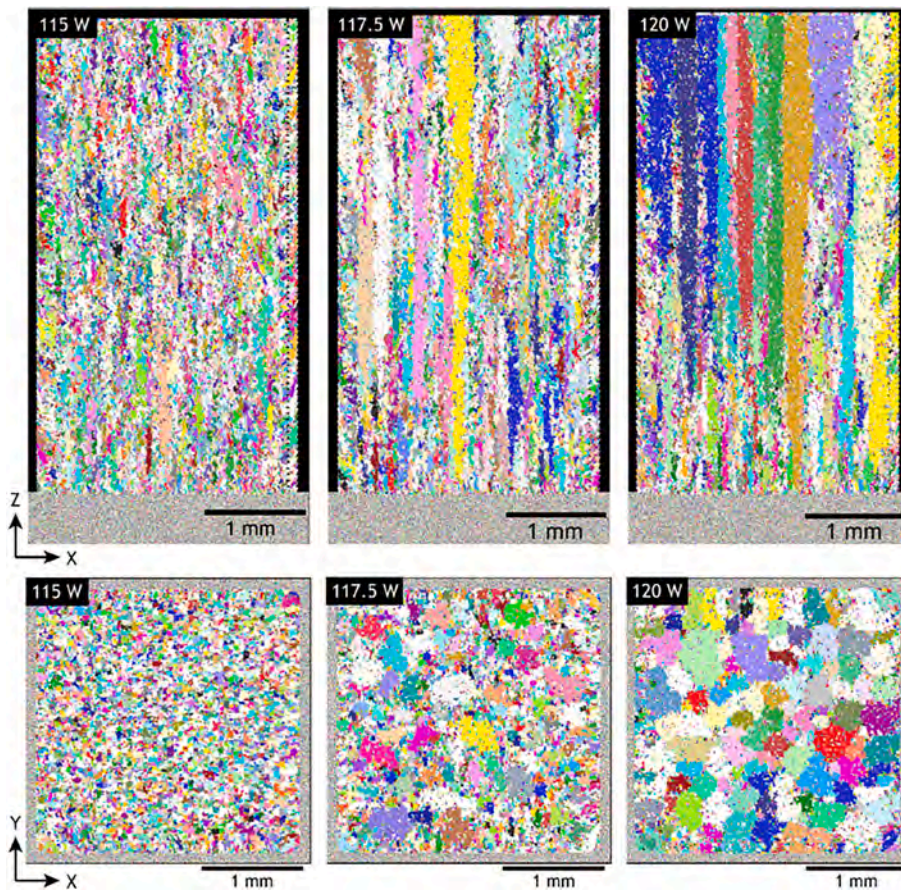
Fig. 9.5. Cross-sections parallel to the build direction (top), and cross-sections perpendicular to the build direction (bottom), for simulated microstructures built at three absorbed powers during laser PBF of SS 316L, using the Monte Carlo method [585].

models can be used to identify processing conditions for achieving the desired grain structure during PBF of aluminum alloys.

Monte Carlo (MC) models were used to predict grain growth during additive manufacturing [36,583–586]. MC models are based on probabilistic approaches and are suitable for the simulation of grain boundary migration considering the variations of interface energies. However, grain growth during solidification largely depends on the solidification conditions determined by the moving molten pool. For example, Wei et al. [36] reported the comprehensive grain growth model considering both the solidification and the solid-state heating and cooling processes (Fig. 9.4). The transient solidification process was simulated considering the moving solidification front. Grain growth during ten layers of deposition is shown in Fig. 9.4 (a). Moreover, the evolution of the grain structure in the solid metal during repeated thermal cycles was simulated using an MC model. The calculations show the variation in the grain structures in various planes within a three-dimensional structure as shown in Fig. 9.4 (b)-(e). Rodgers et al. [585] simulated the grain growth during laser PBF of SS 316L parts on a scale of several millimeters with complex scan patterns used in AM (Fig. 9.5). It was found that columnar grains are both more likely to be elongated along the build direction and have a larger cross-sectional area perpendicular to the build direction at high laser powers. The three-dimensional variations of grain structure provide a key to understanding the anisotropic mechanical properties observed in additively manufactured parts.

The above results imply that the spatial variations of the grain structure can be simulated by high-fidelity 2D and 3D Cellular Automata and Monte Carlo models. Moreover, the transient solidification conditions, the resultant grain structure, and the solidification texture can be examined. The visualization of the simulated transient microstructural features in the 3D domain and virtually any 2D sections can provide valuable information that is difficult to obtain experimentally through the characterization of specimens. Thus, the use of mechanistic models for grain growth provides the ability to simulate grain structure and understand the effects of the AM process conditions.

9.1.2. Kinetic modeling of phase transformation to control phases

9.1.2.1. Johnson Mehl Avrami model. The Johnson Mehl Avrami (JMA) model can describe the rate of phase transformation during the heating and cooling processes for the solid-state phase transformations [82,587 180,588,589]. JMA model uses analytical equations and applies to various alloys supported by corresponding materials properties and phase transformation parameters. For example,
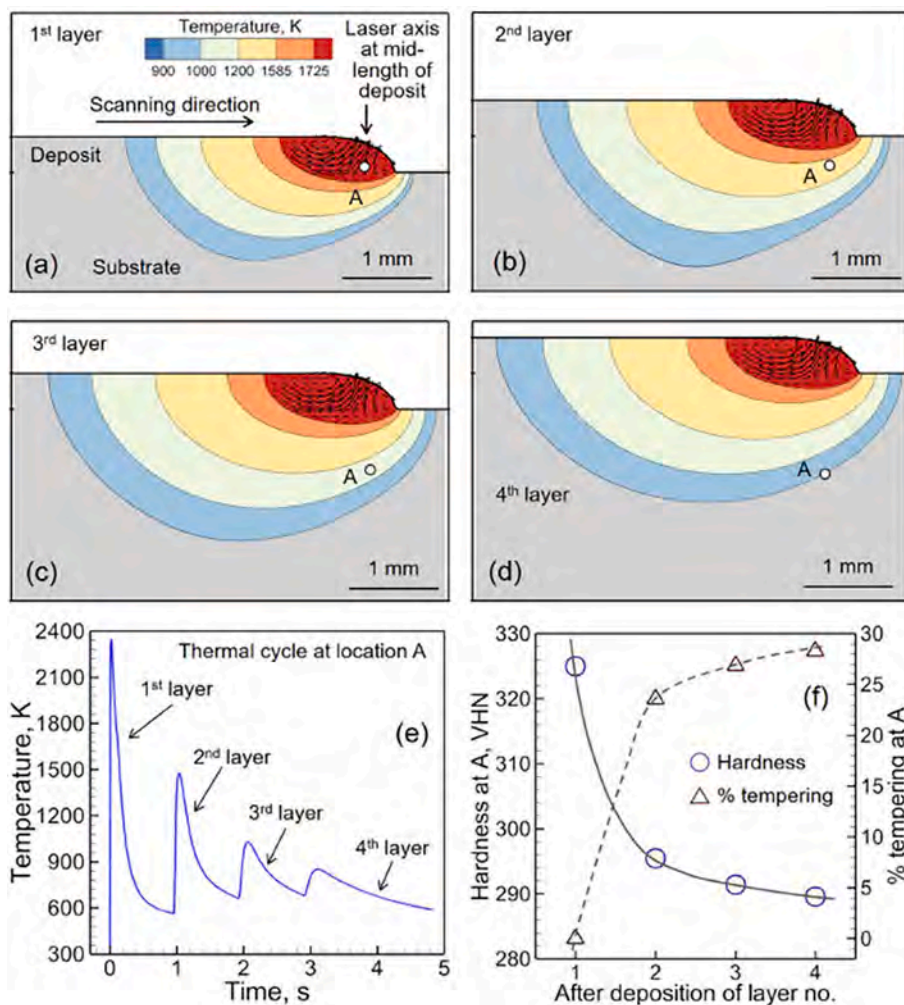
Fig. 9.6. Temperature fields, thermal cycles, computed percentile of tempered martensite using JMA equations, and the resultant hardness of H13 tool steel printed using DED: (a) 1st, (b) 2nd, (c) 3rd, and (d) 4th layer. (e) Thermal cycle calculated at the location 'A' while depositing the 4 layers. (f) Calculated variation in hardness and percentage tempering of martensite at location 'A' during the deposition of 4 layers [180].

Mukherjee et al. [180] predicted the transformation of martensite during laser DED of a tool steel using JMA kinetics and computed 3D, transient temperature fields [180]. Fig. 9.6 (a-d) show the temperature distributions on a selected plane and at a monitoring location 'A' in the first layer (Fig. 9.6 (e)). Considering the repeated heating and cooling cycles during the deposition, and the phase transformation kinetics, the hardness at various locations was predicted (Fig. 9.6 (f)) as a function of time. These models can compute the kinetics of phase transformations taking into account the multiple thermal cycles and they provide a means to understand the evolution of microstructure and properties.

Lu et al. [588] simulated the evolution of precipitates in IN718 during the DED-GMA process, using the JMA model. It was found that the distribution of micro-hardness in the mid-section of the sample was consistent with the distribution of γ''/γ' strengthening phases fraction calculated by the model. More γ''/γ' strengthening phases were present in the middle/upper region than in other regions, which indicates that proper transformation temperature and longer transformation time enhanced the transformation extent of γ'' and γ' phases at the local region of the build. Since the JMA model uses analytical equations and does not capture the phenomenological features of the phases such as the morphologies and dimensions, other mechanistic models such as phase-field models are required for a more detailed understanding of the phase transformation processes during AM.

9.1.2.2. Phase-field model. Phase-field models can predict solid-state phase transformations. For instance, Shi et al. [590] used a phase-field model to compute the precipitation and dissolution of secondary-phase α (α') precipitate during repeated thermal cycles during laser PBF of Ti-6Al-4 V. Moreover, Shi et al. [590] developed a multiscale model integrating a powder-scale transient heat transfer and fluid flow model, a Cellular Automaton model for the simulation of solidification grain structure and texture, and phase-field modeling of precipitation and dissolution of secondary-phase precipitates during repeated thermal cycles [590]. It was found that successive layers exert a cyclic thermal influence leading to in situ decompositions of a near α' martensitic structure or precipitation of
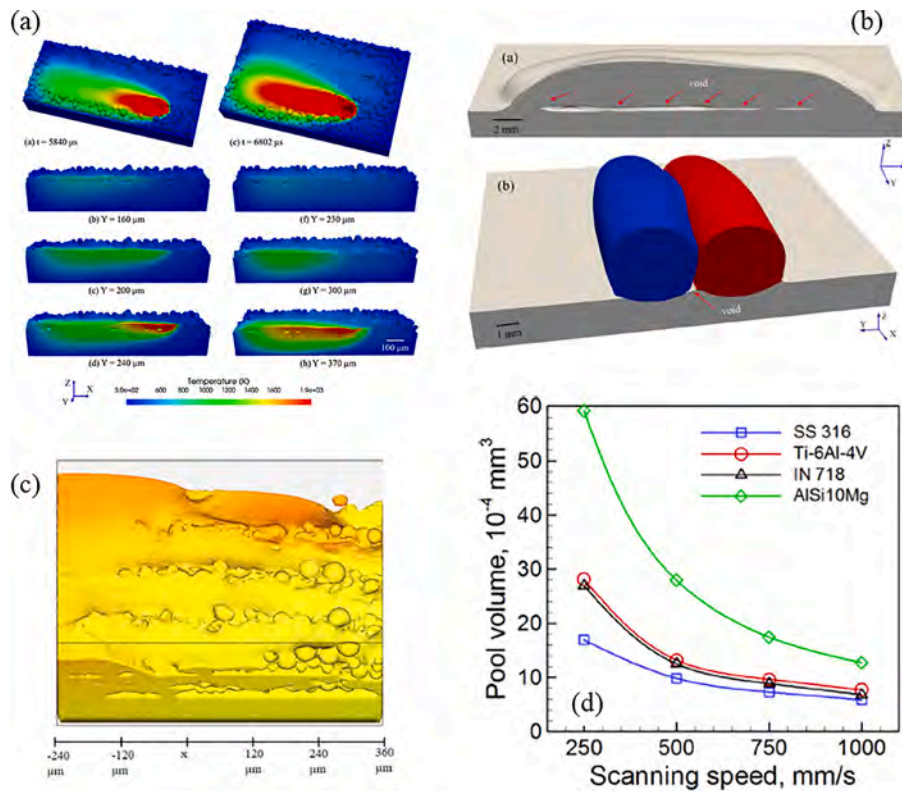
Fig. 9.7. Lack of fusion defects generated from various AM processes: (a) inter-track voids in PBF-L [592], (b) inter-track voids in DED-L [593], (c) inter-layer lack of fusion in PBF-L [594], (d) various molten pool volumes for PBF-L using different materials [431].

the equilibrium α precipitate. In other words, the formation of the secondary phases can be controlled by adjusting the thermal cycles via changing the heat source power, speed, layer thickness, and scanning pattern.

Although phase-field models have been applied to various aspects of microstructure control in AM, their engineering applications are restricted due to the low computational efficiency and the high computation cost. For example, the running process of the phase-field model with 17.88 million cells took 311 h for the simulation of a physical time of 0.009 s, using parallel computations on an NVIDIA Tesla M2090 GPU [571]. The intensive computational resources required by the phase-field models imply that considerable research efforts are still needed for the engineering applications of the phase-field models for real-time feedback for microstructure control.

9.1.3. Models for controlling defects

The mechanical properties of the AM parts are affected by the microstructure. For example, strength and ductility are influenced by the formation of fine equiaxed grains. On the other hand, defects such as lack of fusion, porosity, and cracking damage the integrity of AM parts on different scales, which adversely influence their mechanical properties. Therefore, it is critical to mitigate printing defects via experimental and modeling approaches. In situ observations of the printing process such as synchrotron XRD and high-speed imaging can obtain valuable data. However, the observation domain and correlated physical information are often incomplete due to the complex and highly transient nature of the AM processes. Mechanistic models are capable of revealing the highly transient physical processes involving the transport of mass, energy, and momentum on multiple scales. These underlying transport processes are helpful in the understanding of the formation and control of defects.

9.1.3.1. Models to control lack of fusion and keyhole pores. The most common printing defects for all materials may be the lack of fusion and pores [1,4,591]. Fig. 9.7 shows several examples of lack of fusion during DED-L and PBF-L. It can be observed that such defects can occur on at least three scales: (i) the feedstock material scales such as powder-related voids for PBF [592] as shown in Fig. 9.7 (a); (ii) the track scale such as inter-track voids during DED [593] as shown in Fig. 9.7 (b), (iii) the layer scale such as inter-layer voids during PBF [594] as shown in Fig. 9.7 (c). Moreover, since the alloys have different thermophysical properties, the molten pool shapes and sizes for different alloys can vary significantly under identical process parameters, as shown in Fig. 9.7 (d). These differences in the molten pool shape and size make the susceptibility to lack of fusion to be different for different alloys. The inappropriate selection of hatch spacing and layer thickness would similarly cause a lack of fusion. The utilization of the mechanistic models can reveal the mechanisms of formation of lack of fusion and provide a means of avoiding the defects cost-effectively based on scientific principles.
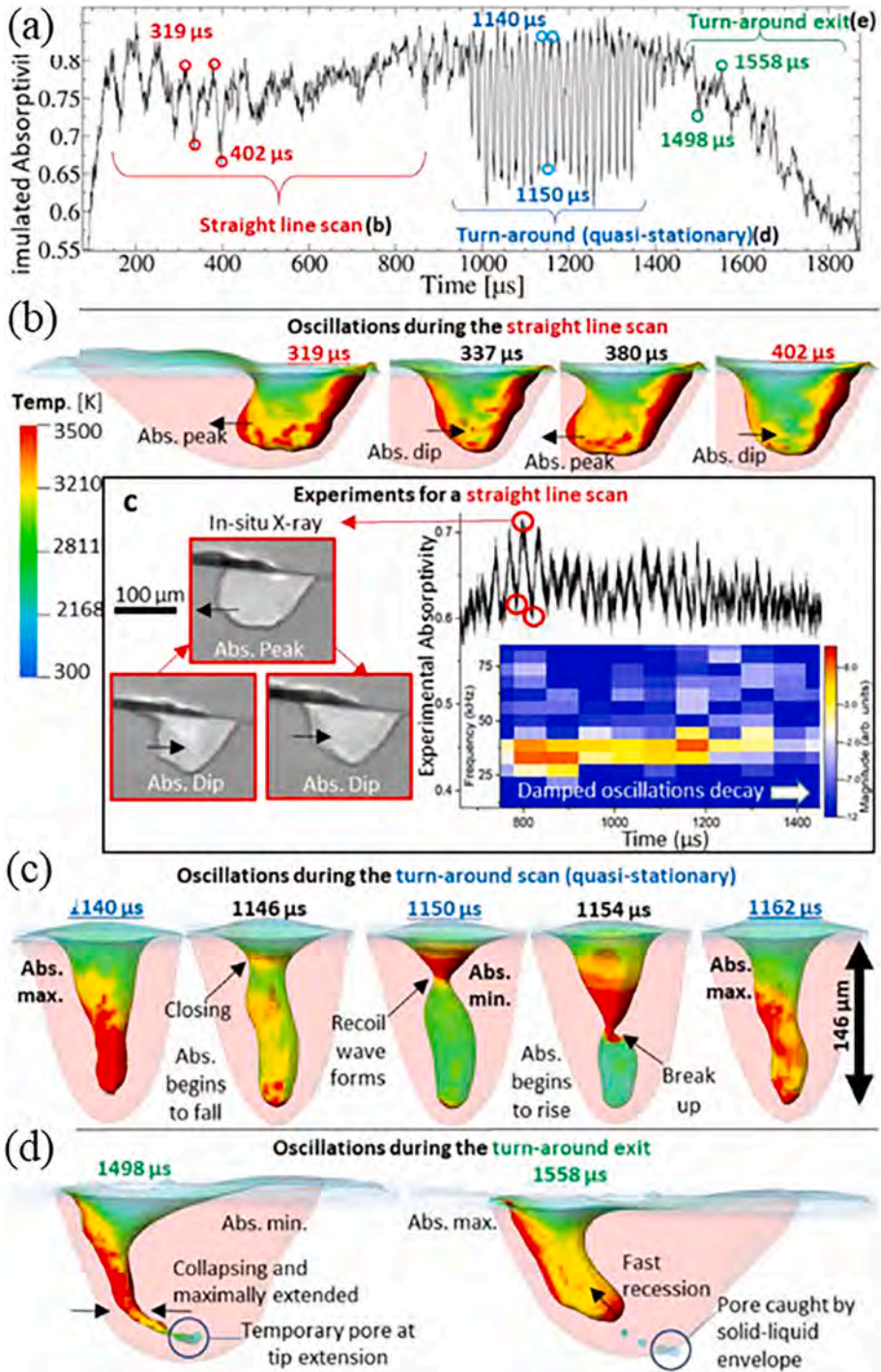
Fig. 9.8. Keyhole-induced pores during PBF-L: (a)-(d) pores generated due to the oscillation of keyhole and molten pool [670].
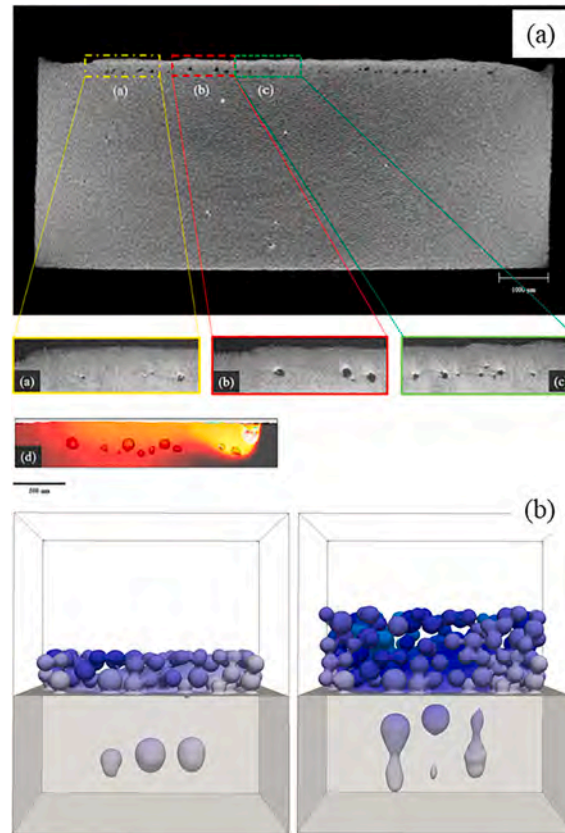
Fig. 9.9. Keyhole-induced pores during PBF-L: (a) pores generated at the bottom of the track during single-track printing [596], (b) pores generated and reformed during two-layer and three-track printing.

Several examples of keyhole-induced pores in laser PBF products are shown in Fig. 9.8. A keyhole can be formed under the laser beam due to the action of recoil pressure. The instability of the keyhole may result in the formation of porosity. Note that the keyhole geometry may vary drastically due to the complex interaction of the laser beam with the powder feedstock and molten pool metal, with the absorption of the laser energy changing periodically as shown in Fig. 9.8 (a) and (b). Keyhole-induced pores are more frequently observed near the turning point of adjacent tracks (Fig. 9.8 (c) and (d)). With the help of high spatiotemporal resolution mechanistic models, it can be inferred that lower power or slower acceleration at the turn-around exit can prevent the above pores [595]. Fig. 9.9 (a) shows pores generated near the bottom of the printed track, in which condition process parameters were inappropriately selected. Fig. 9.9 (b) shows the initial generation and subsequent reformation of keyhole-induced pores in a typical multi-layer and multi-track condition [596]. These results prove that a sudden shut-off of the laser beam in the condition of a deep keyhole melting mode would cause various residual pores in the deposit during the layerwise printing processes. Adjustment of the processing conditions such as the laser power guided by an appropriate model can prevent the occurrence of keyhole-induced pores [597].

9.1.3.2. Models to control cracking. Modeling and experiments have shown that the crack propagation directions vary with scanning strategy and hatch spacings during laser PBF [99] (Fig. 9.10). Columnar grains grow in a curved pattern from the boundary towards the centerline of the molten pool. For small hatch spacings, only transverse cracks were observed. The absence of longitudinal cracks near the centerlines was due to the remelting of the centerline region with significant overlap. In other words, longitudinal centerline cracks were initially generated, but with the following elimination upon the printing of the subsequent adjacent track. Note that columnar grains in two adjacent tracks grew with different orientations [99] due to the bidirectional laser scanning strategy. Thus, the transverse cracks generated in each track exhibited opposite directions owing to the changes in the directions of motion of the molten pool and the resultant maximum heat flow directions at the trailing edges of the molten pools. The results show that the models can help control the gain structure and solidification cracking.

The Fig. 9.11 (a) shows the synchrotron x-ray imaging of the hot cracking behavior of AA6061 during laser PBF. It was found that hot cracks occur underneath the surface. The cracks originate near the back of the melt pool and the initial crack propagation speed is of order 1 m/s but decreases rapidly during crack propagation [598]. These results can provide valuable support for the validation of simulations of solidification cracking. Pores are favorable sites for crack initiation; while trapped-gas pores tend to form when the laser beam scans across the cracks when cracks are present in the material [598]. Modeling and experiments [599] have established the important effects of both the alloy composition and processing conditions on the evolution and control of solidification cracking during
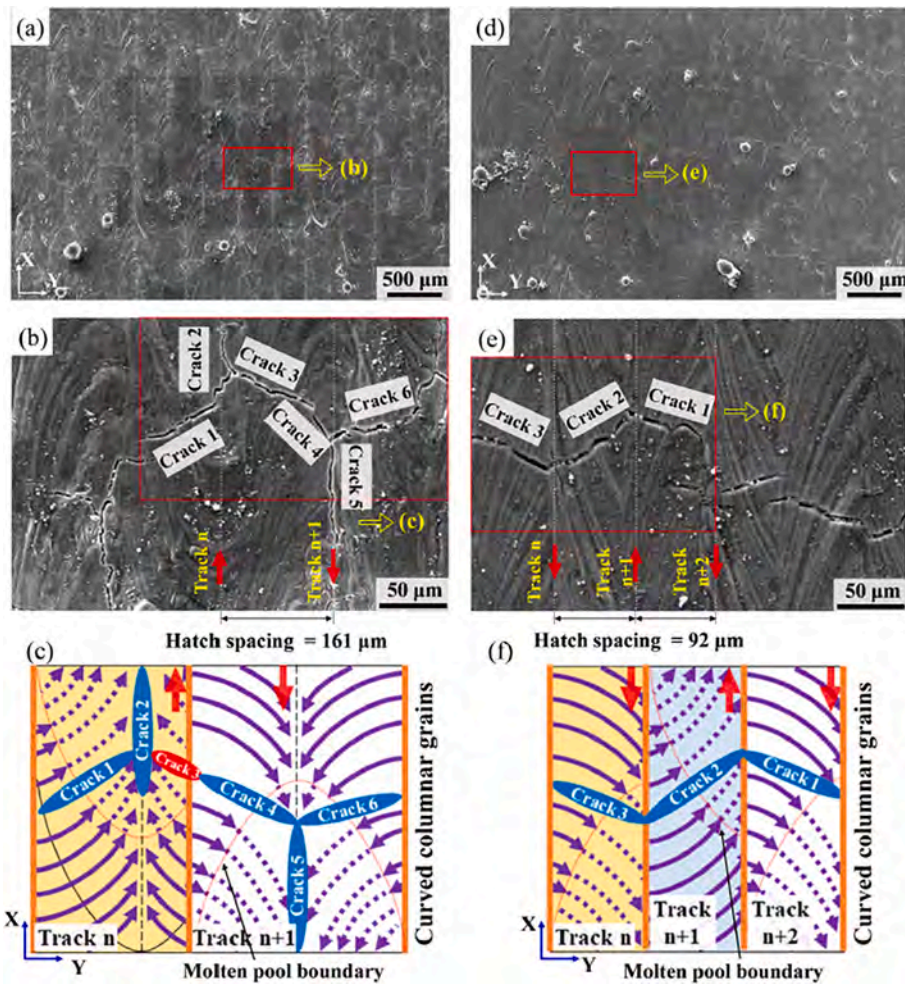
Fig. 9.10. Solidification cracking in multi-track builds deposited using bidirectional laser scanning strategy with different hatch spacings. Laser power: 270 W, scanning speed: 600 mm/s. (a)–(c) Hatch spacing: 161 μm. (d)–(f) Hatch spacing: 92 μm. (a), (b), (d), and (e) The top view of the deposit with different magnifications. The white dotted lines in (b) and (e) represent the centerlines of the tracks. (c) and (f) Schematics of the propagation paths of the solidification cracks with grain growth directions depending on the curvatures of the trailing edges of the moving molten pool [99].

PBF-L of Al-Cu alloys (Fig. 9.11 (b) and (c)). It has been shown that model-based adjustment of the scanning speed, hatch spacing, and alloy composition can mitigate solidification cracking.

The prevention of solidification cracking involves several factors including the chemical compositions of the alloy, the grain structure generated upon solidification, and the stress conditions during the rapid heating and cooling encountered during the AM processes [32,99]. Solidification cracking is affected by the specific chemical compositions and the resultant large intergranular liquid films at the final stages of solidification [600]. Therefore, adjustment of the chemical composition of the alloy can reduce the solidification cracking. For instance, Montero Sistiaga et al. [601] obtained a crack-free high strength aluminum alloy specimen with the addition of 4 wt% Si.

The generation of the cracks can be mitigated by controlling the grain structure and promoting CET. Parts with fine equiaxed grains are less susceptible to solidification cracking than those with coarse columnar grains [600]. Although promoting CET by modifying feedstock materials is an effective method of controlling solidification cracking [602,603], the modification of the chemical compositions of a given alloy may not be practical in many conditions. Therefore, it is worthwhile to explore other mitigation strategies such as process control guided by mechanistic modeling [99]. Another critical factor for the high solidification cracking susceptibility is the stress and strain conditions. High-fidelity mechanistic models for the quantitative assessment of these factors would be useful but they are still evolving.

9.1.3.3. Models to control composition change. During additive manufacturing of metallic materials, alloying elements vaporize from the molten pool. The rate of vaporization is the highest under the heat source where the temperature is the maximum. The vaporization is most pronounced for the electron beam processes because of the combination of low chamber pressure and high temperatures that
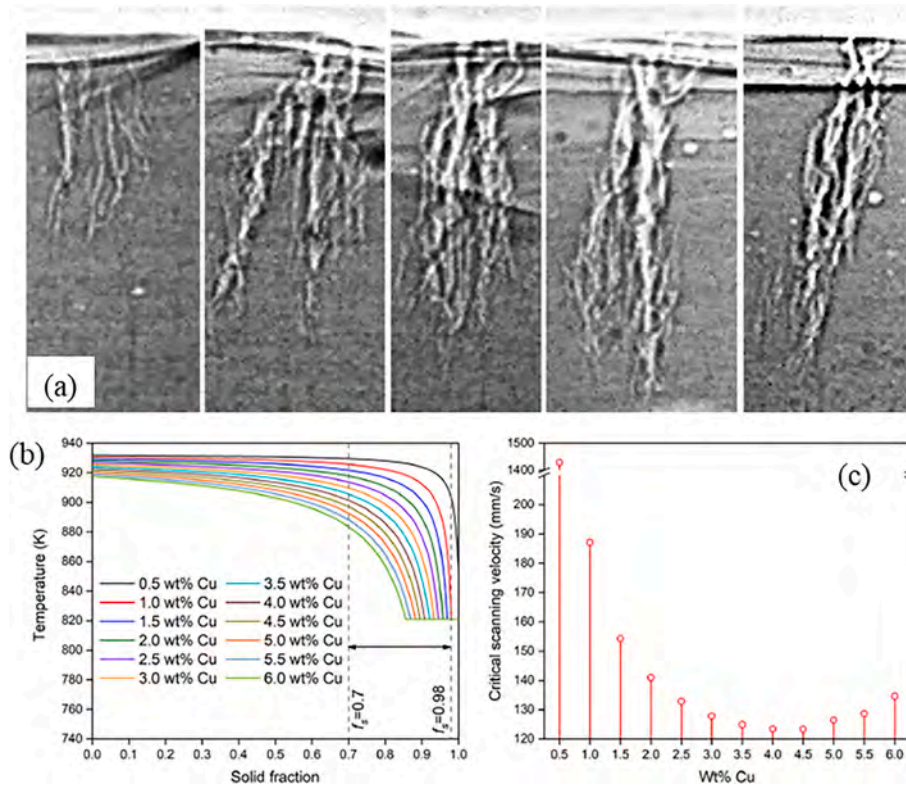
Fig. 9.11. Observation and computation for solidification cracking: (a) in situ observation of solidification cracking using ultra high-speed X-ray visualization [598], (b) susceptibilities to solidification cracking for aluminum alloys with different chemical compositions, temperature solid fraction curves obtained from JMatPro [599].

promotes rapid vaporization of alloying elements. All elements do not vaporize at the same rate due to their differences in vapor pressures. Selective vaporization of alloying elements often results in a significant change in the composition of the part from that of the feedstock[118,485,604]. Composition change is an important defect since it affects the microstructure, properties, and corrosion resistance.

It is well-known that composition change is significantly affected by the ratio of pool top surface area to pool volume. In addition, the rate of vaporization depends on the local temperature. Heat transfer and fluid flow calculations can calculate the molten pool dimensions and the temperature field since they affect the composition change. In addition, these calculations need data on the variations in the vapor pressure on elements with temperature. These calculation methods are well-established in the fusion welding literature [131] and can be adopted for the AM processes. For example, Knight's model [605] was used to compute the change in the composition of alloying elements from SS316 during PBF-L, DED-L, and DED-GMA. A significant loss of manganese was observed followed by a less pronounced loss of chromium. It was shown how the model can be used to adjust laser power and scanning speed to reduce the composition change. A similar approach was also used to compute composition change in PBF-L of Ti-6Al-4V [606]. The temperature fields in the molten pool computed using a finite element method were combined with an evaporation model which computes the local vaporization rates of alloying elements. Aluminum was found to be the most susceptible to composition change.

There are very few models of additive manufacturing that consider vaporization and the resulting composition change of alloys. The rich knowledge base of composition change in fusion welding can help to develop such models for different additive manufacturing processes. Though the trends predicted by these models are also qualitatively observed in additive manufacturing experiments, rigorous validation of these models for a quantitative prediction of composition change remains to be undertaken.

9.2. Data-driven approaches

As discussed in the previous section, comprehensive numerical mechanistic models of grain growth and the evolution of phases have been used to understand the process and microstructure relationships to control grain structure and phases. In addition, there are physics-based models to control defects in AM parts. These models can provide accurate results but are often computationally intensive. Therefore, they often cannot be used in real-time. In contrast, data-driven techniques such as machine learning, dimensional analysis, and statistical methods are fast and can provide important trends of the effects of process parameters on grain structure, phases, and defects. Therefore, they are increasingly used since they are often easy to use, effective, and insightful.

Machine learning can make reliable and reproducible predictions [607–609] by learning from existing data. It can extract useful

Simulated grain growth

(b)
Size distribution by ML

(c)
ML results match with model
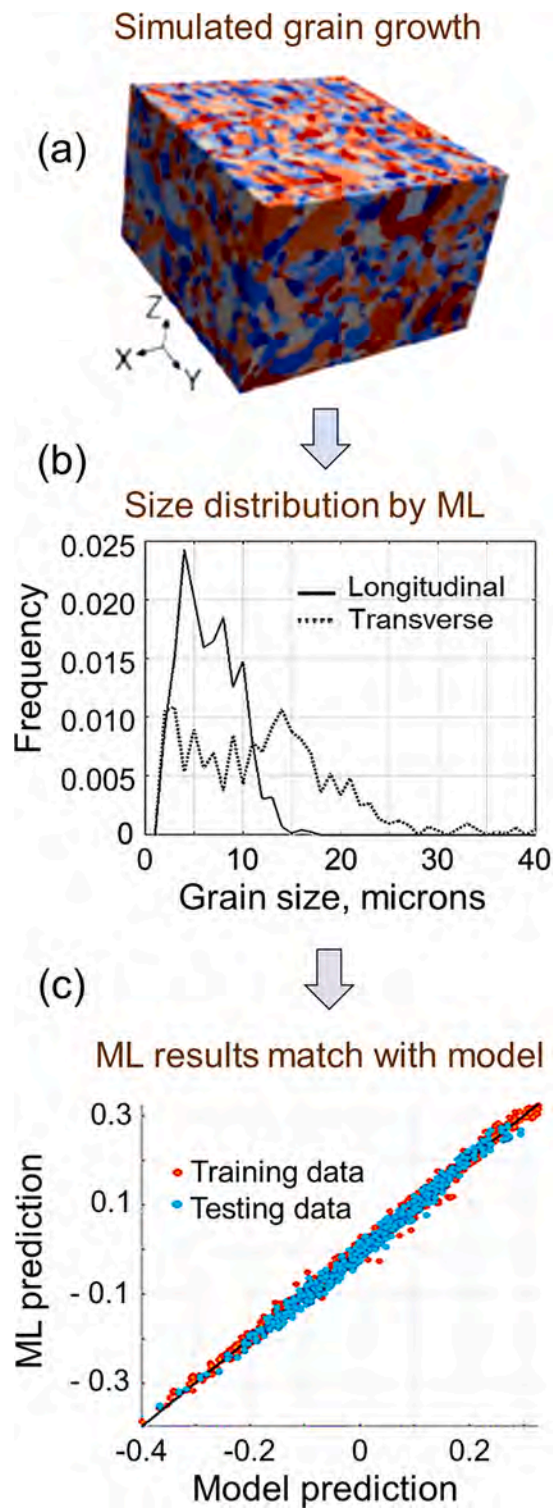
Fig. 9.12. (a-c) An example of the application of machine learning in microstructure control [610]. The grain growth results (figure (a)) computed using a Monte Carlo model provide grain size versus frequency data in longitudinal and transverse directions (figure (b)). These data are used to train a neural network that could then calculate grain growth during DED- L (figure (c)).

Table 9.1
Examples of grain structure control in AM using several data-driven techniques.

Control methods	Examples	References
Machine learning (ML)	A combination of principal component analysis (PCA) based ML and Monte Carlo grain growth model is used to control the grain size during DED-L	[610]
	A combination of artificial neural network-based ML and Monte Carlo grain growth model is used to control α grain size during DED-EB of Ti-6Al-4 V	[611]
	A combination of neural network-based ML and phase-field model is used to control ferrite and austenite fractions during AM of stainless steel 316	[612]
	A neural network-based ML trained using experimental data is used to control the grain orientation of columnar β grains during DED-L of Ti-6Al-4 V	[613]
	Image analysis and random forest-based ML are used to control the size of α grains during PBF-L of Ti-6Al-4 V.	[614]
	A combination of a thermal-fluid dynamics model and a self-organizing map-based data mining model is used to control the secondary dendritic arm spacing during DED-L of Inconel 718.	[615]
	A neural network and principal component analysis based ML trained using data extracted from EBSD results are used to control grain-size during AM of copper	[616]
Dimensional analysis	Dimensionless heat input is proposed and used to identify conditions to control secondary dendritic arm spacing in stainless steel 316 parts made by DED-L	[617]
	Marangoni number is used to identify conditions to control the distribution of titanium carbide particles in the Inconel 625 matrix made by DED-L	[618]
	Fourier number is used to identify conditions to control the cooling rates and solidification parameters during DED-L of stainless steel, Ti-6Al-4 V, and Inconel 718	[617]
	Back of the envelope calculations using the Gaumann equation are used to control solidification morphology during PBF-EB of Inconel 718	[429]
Statistical methods	An analysis of variance (ANOVA) developed using experimental data is used to control the size of α grains during PBF-EB of Ti-6Al-4 V	[620]
	An ANOVA developed using experimental data is used to control the size of both α and β grains during PBF-EB of Ti-6Al-4 V	[621]
	An ANOVA developed using experimental data is used to control the size of α grains during DED-L of Ti-6Al-4 V	[622,623]
	A non-linear regression developed using experimental data is used to control the grain size during PBF-L of AlSi10Mg	[619]
	A linear regression developed using experimental data and results from a cellular automata grain growth model is used to control the size of β grains during DED-L of Ti-6Al-4 V	[624]
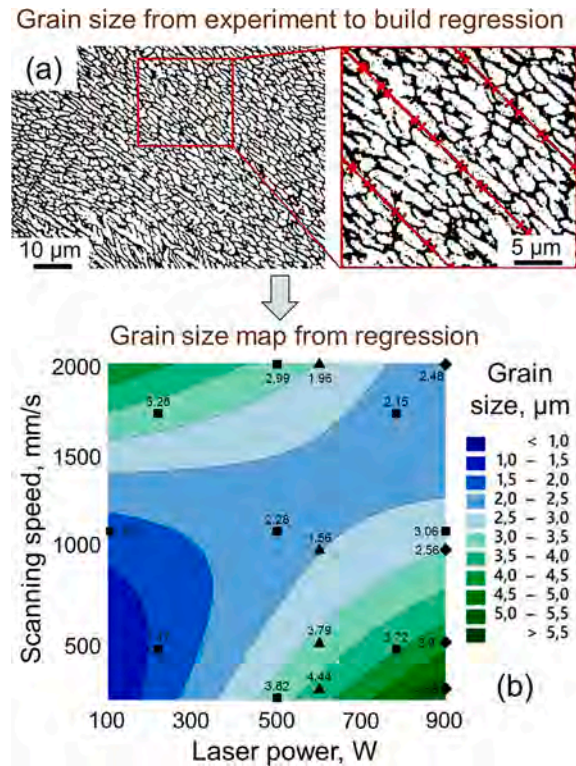
Fig. 9.13. An example of the application of regression-based statistical analysis [619] for controlling the control the grain size during PBF-L of AlSi10Mg. The grain size data is extracted from the microstructure (figure (a)) and is used to develop the regression which is used to make a grain size process map (figure (b)).
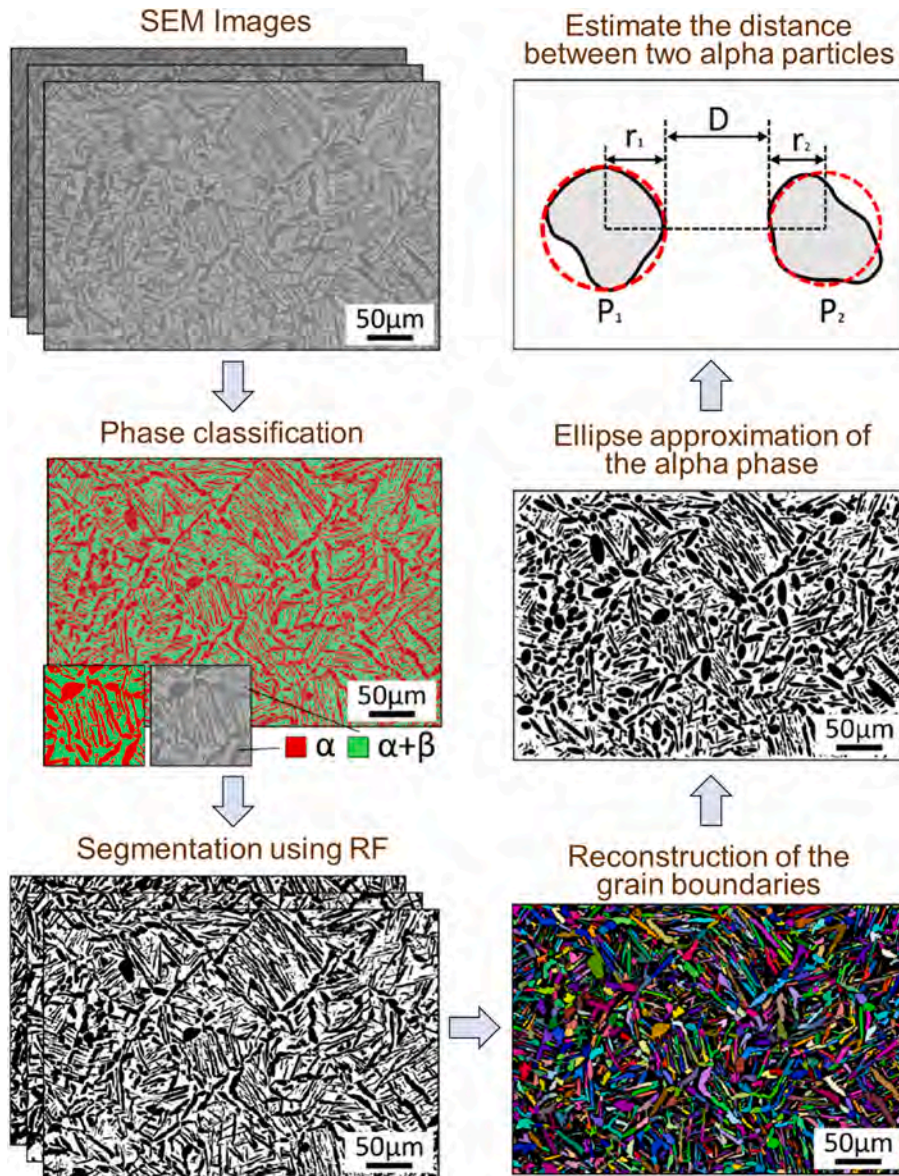
Fig. 9.14. An example of using Random Forest-based machine learning for controlling the formation of the α phase and its size and distribution during PBF-L of Ti-6Al-4 V [614].

information and relations from the data without any need for phenomenological understanding. The powerful, open-source codes for machine learning support their applications for solving many complex problems in AM including the control of grain structure, phases, and defects. There are two types of machine learning algorithms used in AM, supervised and unsupervised [608]. In supervised machine learning, variables are mathematically correlated to the material response such as grain size for microstructure prediction. The algorithm trained with both the input and output data can reveal the hidden relationship. The commonly used supervised machine learning algorithms for AM are neural networks, decision trees, Bayesian Networks, K-nearest neighbor, and support vector machines. Unlike supervised machine learning, unsupervised machine learning determines features from the data. It can be used to identify unique features from the digital images of the microstructure, such as classifying various types of precipitates during AM. In this subsection, applications of machine learning, dimensional analysis, and statistical methods to control grain structure, phases, and defects in AM parts are discussed.

9.2.1. Machine learning, dimensional analysis, and statistical methods to control grain structure

Features of grain structure in AM parts such as grain size, distribution and orientation, and dendritic arm spacing are used to train machine learning algorithms that can compute appropriate processing parameters to achieve the desired grain structure. Input data to
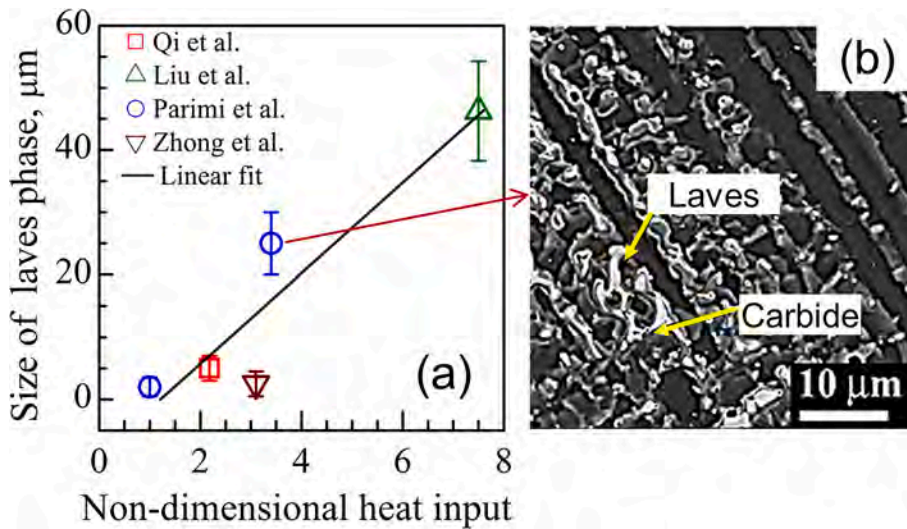
Fig. 9.15. (a) A non-dimensional heat input [617] is correlated with the size of laves phases in Inconel 718 parts made by DED-L. This non-dimensional heat input is further used to identify conditions for controlling the size of laves phase. The data are taken from the literature [628–631]. (b) An example of microstructure indicating the laves phase in Inconel 718 part [628].
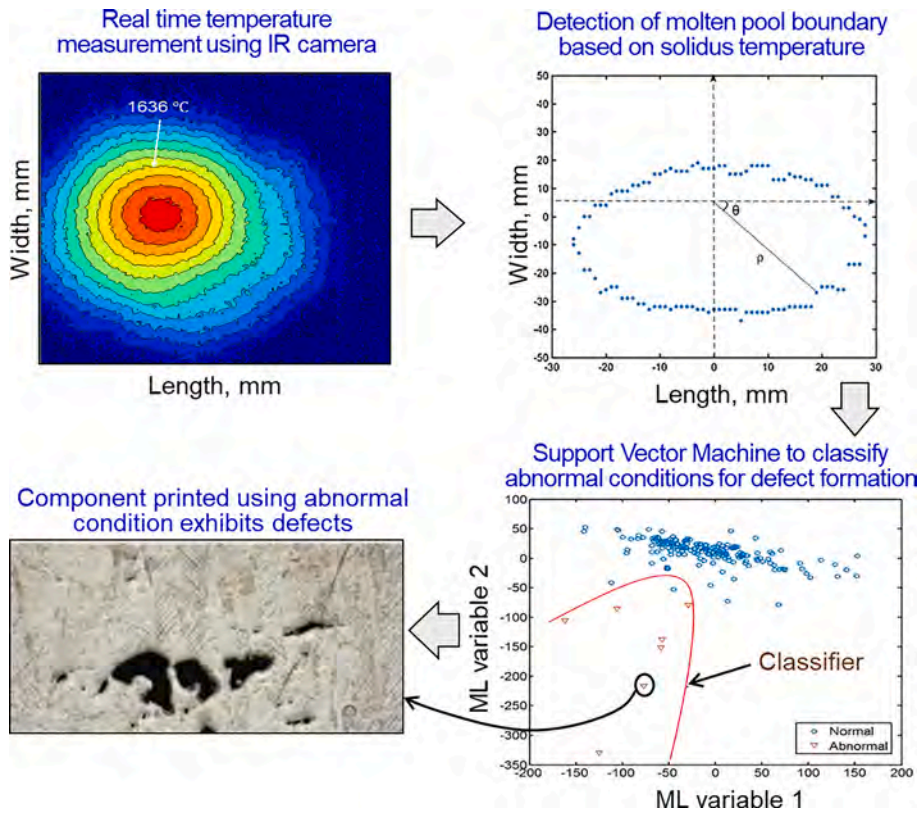
Fig. 9.16. An example of using a support vector machine-based machine learning to control the lack of fusion defects in Ti-6Al-4 V parts made by DED-L [632].

train machine learning can also be generated from well-tested mechanistic models of grain growth and the evolution of solidification structure. For example, Fig. 9.12 (a) to (c) provide an example of using the computed data to train a machine learning algorithm that is subsequently used to control the grain structure [610]. A 3D Monte Carlo-based grain growth model calculates the grain structure in
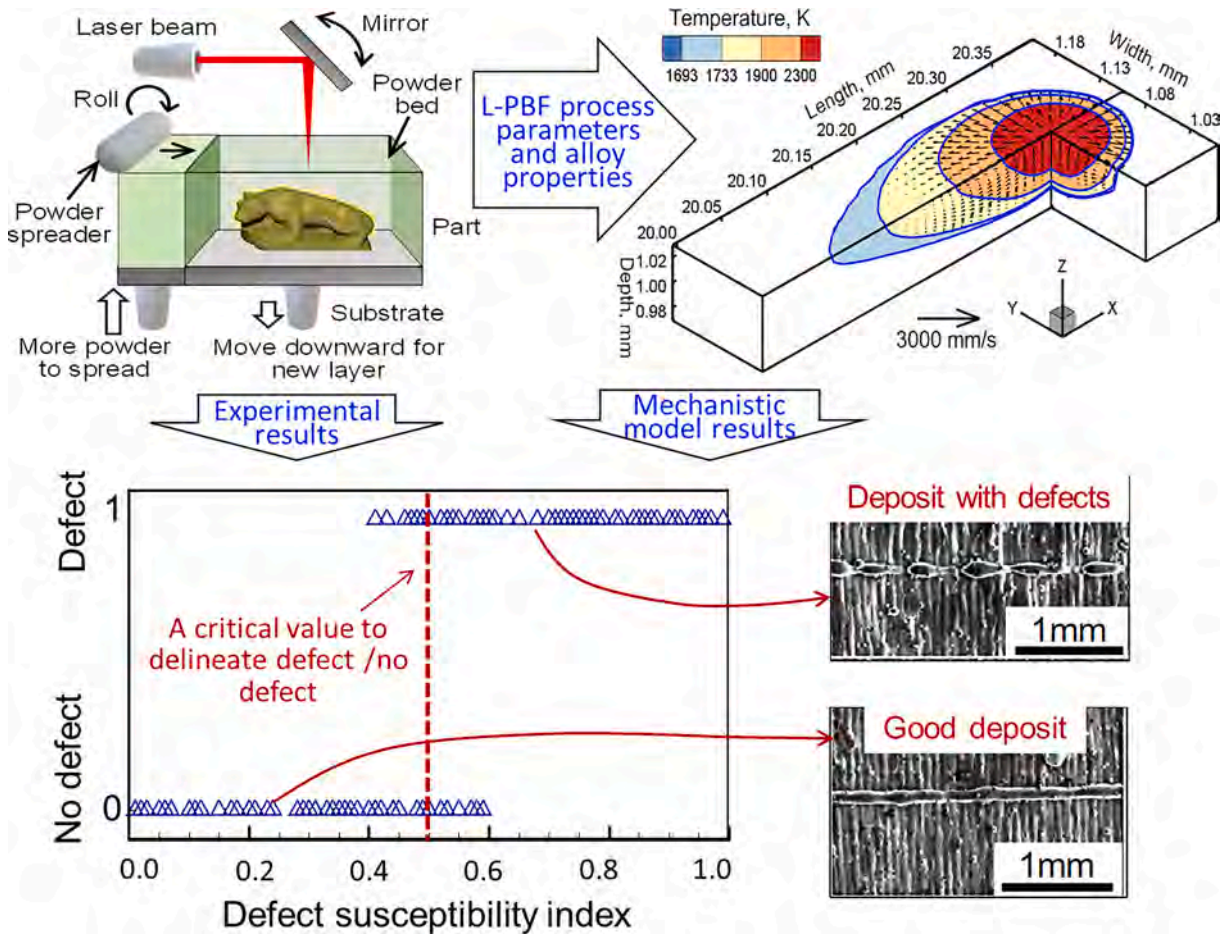
Fig. 9.17. An example of using machine learning to control balling defects in alloy parts made by PBF-L [238]. Experimental data, results from heat transfer and fluid flow calculations, and machine learning results are combined to propose an easy-to-use balling susceptibility index to identify process conditions for avoiding balling.

3D (Fig. 9.12 (a)). From the computed 3D grain structure, frequency versus grain size data are extracted (Fig. 9.12 (b)). These data are then used to train a neural network that could correctly and rapidly predict the grain size (Fig. 9.12 (c)). The well-trained neural network can predict the grain size the same as what is computed using the computationally intensive Monte Carlo model (Fig. 9.12 (c)). Several examples [610–616] of the use of machine learning for grain structure control in AM are provided in Table 9.1. Although progress has been made in the applications of machine learning algorithms to control grain structure in AM parts, they are in their initial stages of development and need more research.

In AM, important variables often simultaneously affect the temperature field, cooling rates, and solidification parameters and thus the grain structure of the part. Therefore, combinations of multiple variables in dimensionless forms are often used to understand the evolution of the grain structure of AM parts [617]. These dimensionless variables reduce the number of parameters that need to be investigated. In addition, these variables express important physical meanings that cannot be represented by any single variable. Commonly used dimensionless numbers for grain structure control in AM [429,617,618] are indicated in Table 9.1.

Factors affecting the microstructure of AM parts such as thermal cycle, cooling rates, and solidification parameters are significantly impacted by the rate of heat dissipation from the part as well as the heat storage in the component. A dimensionless Fourier number (F) is defined as the ratio of the heat dissipation rate to heat storage rate as [617]:

$$F = \alpha/VL \tag{12}$$

where α, V and L indicate the thermal diffusivity, scanning speed, and characteristic length, respectively. The characteristic length is often taken as pool depth [617]. An AM process with a high Fourier number exhibits rapid heat dissipation and fast cooling that can result in a fine grain structure [617]. In addition, a low Fourier number in AM process results in a small ratio of the temperature gradient to solidification growth rate which favors the formation of equiaxed grains [617].

Cooling rates during solidification, temperature gradient, and solidification growth rate that affect the solidification structures are affected by the shape and size of the molten pool. It is well-known that the molten pool shape and size are impacted by the molten

metal convection often quantified by the dimensionless Marangoni number [617].

$$Ma = -\frac{d\gamma}{dT}\frac{w\Delta T}{\mu\alpha}$$ (13)

where μ is the viscosity, α is the thermal diffusivity of the alloy, w is the characteristic length of the molten pool, which is taken as the width of the molten pool, ΔT is the difference between the maximum temperature inside the pool and the solidus temperature of an alloy, and $\frac{d\gamma}{dT}$ is the sensitivity of surface tension gradient with respect to temperature. The vigorous convective flow of the molten metal characterized by a high Marangoni number can often break long columnar grains and the fragmented grains can act as heterogeneous nucleation sites for the equiaxed grains.

Solidification morphology depends on the ratio of the temperature gradient (G) and solidification growth rate (R). The values of G and R can be computed from a well-tested heat transfer and fluid flow model. The values of these parameters can be used in an experimentally determined morphology map such as Fig. 2.1 in section 2 to determine the morphology. Analytical calculations have also been proposed to predict the solidification morphologies such as the one proposed by Hunt [31]. Other equations have also been proposed such as the Gaumann equation to estimate the ratio G^n/R [429]:

$$\frac{G^n}{R} = a\left[\frac{1}{n+1}\left(-\frac{4}{3}\frac{\pi N_0}{\ln(1-\phi)}\right)^{1/3}\right]^n$$ (14)

where a, n, and ϕ are alloy-specific constants. Depending on the alloy used, a varies between 1 and 10 $K^2 s/m$, and the value of n is generally 1 or 2 and $\phi < 0.0066$ for fully columnar grain growth. N_0 is the nucleation density whose value is in the order of 10^{14} m^{-3}. $\frac{G^2}{R}$ and $\frac{G}{R}$ have threshold values that determine the columnar to equiaxed transition. However, the accuracy of these calculations depends on the correctness of the values of the constants that are not generally available for many alloys.

Statistical methods such as linear and non-linear regressions and analysis of variance are often used to control the grain structure. For example, Fig. 9.13 shows that a regression-based statistical analysis [619] was used for controlling the grain size during PBF-L of AlSi10Mg. The grain size data is extracted from the microstructure and is used to develop the regression which is used to make a grain size process map. Such process maps can guide engineers to adjust important variables to control grain size. Several examples [619–624] of the use of statistical methods for grain structure control in AM are provided in Table 9.1.

9.2.2. Machine learning and dimensional analysis for controlling phases

Machine learning [614,625–627] has been used to control the formation of secondary phases that affect the mechanical properties and corrosion resistance of additively manufactured parts. For example, Fig. 9.14 shows how SEM images of Ti-6Al-4 V parts made by PBF-L were used in image processing-based machine learning to control the formation α phase and its size and distribution [614]. The SEM images in the figure show two phases α and β with different contrasts. The ratio of the area of the two phases was evaluated by random forest-based machine learning. It could classify each image pixel to the particular class with the highest probability. After image segmentation using random forest, the missed borders (grain boundaries) between the α and prior-β phases were reconstructed by using an additional image processing technique. It facilitated the visualization of the individual α particles. Then, ellipses were fitted into each segmented α particle and their minor axis values were estimated and averaged for all particles in the analyzed images. The size of the α phases was then correlated to the processing conditions. This method provided a helpful way to control the shape, size, and distribution of the α phase.
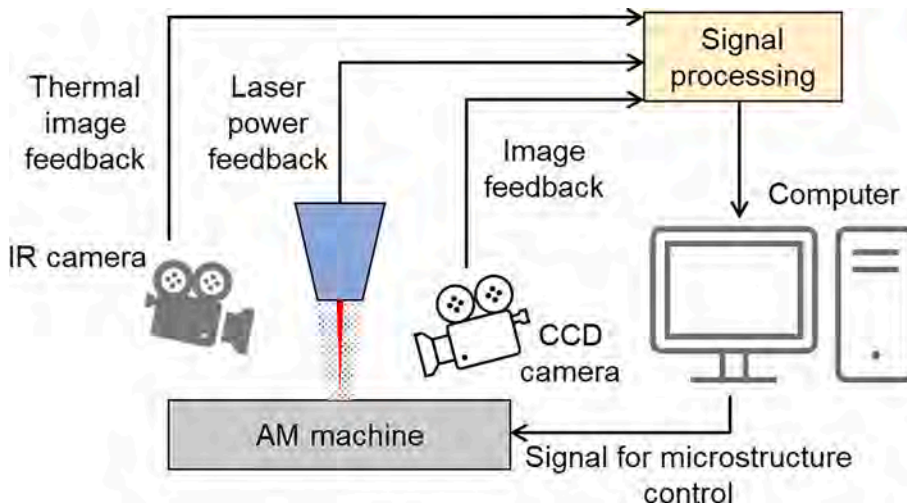
Fig. 9.18. An example of using closed-loop control for in-situ control of microstructure. Here, A charge-coupled device (CCD) camera and an infrared (IR) camera were used to monitor the AM process. The sensing signal was sent to a real-time control system that provided a control signal to the machine to adjust the process parameters for in-situ microstructure control.

Dimensionless numbers are also used to control the formation of phases in AM parts. Heat input which is the ratio of heat source power to scanning speed significantly affects the temperature field, cooling rates, and solidification parameters and thus has a profound impact on the microstructure of AM parts. A dimensionless heat input (Q^*) is proposed as [617]:

$$Q^* = (P/V)/(P_R/V_R) \tag{15}$$

where P and V refer to the laser power and the scanning speed, respectively. P_R and V_R represent the reference laser power and scanning speed that provide the lowest heat input per unit length among the range of process parameters. The dimensionless heat input, Q^*, indicates a measure of the energy supplied per unit length of the part. High heat input results in a slow cooling that allows sufficient time for the growth of the laves phases in nickel alloys (Fig. 9.15 (a-b)). The laves phases are hard and brittle secondary phases that significantly degrade the mechanical properties of AM parts [628–631]. Dimensionless heat input can help to select the optimum combination of power and speed to minimize the formation of the harmful laves phases [617].

9.2.3. Reduction of defects using machine learning

Common defects in additive manufacturing such as balling, cracking, porosity, lack of fusion, distortion, and surface roughness are often controlled by using machine learning. For example, a support vector machine-based machine learning was used to minimize the lack of fusion defects in Ti-6Al-4 V parts fabricated using DED-L [632]. Fig. 9.16 shows that the temperature field during the DED-L process was monitored using an IR camera. A molten pool boundary was extracted from the temperature field by tracking the solidus temperature contour. A support vector machine was trained using the data extracted from the molten pool results. The trained support vector machine was used to classify the processing conditions into two categories, normal and abnormal, based on the probability of lack of fusion defect formation. Defects were found in the components printed using the abnormal processing conditions responsible for the defect formation.

Machine learning was also used to reduce balling defects during PBF-L [238]. Fig. 9.17 shows that the machine learning algorithm was trained using both the experimental data on balling formation as well as several computed variables that represent the mechanism of balling formation. These variables were calculated using a heat transfer and fluid flow model. A balling susceptibility index was proposed and derived using the machine learning results that provided a threshold value delineating the defect and no defect cases. The index was proved to identify conditions for reducing balling defects during PBF-L of several engineering alloys. In addition, feature selection-based machine learning was used to provide the hierarchical influence of important variables on the balling defect. This hierarchy is helpful to guide engineers about which variables to tune in for controlling balling defects.

Examples of reducing defects in AM parts using machine learning include the control of the anomalies in powder spreading by a recoater during powder bed fusion [633]. In this case, a neural network-based machine learning was used to correlate the imperfection of the powder bed resulting from recoater streaking and hopping with part defects. The use of image processing and pattern recognition-based deep learning methods are increasingly used to control defects in AM. For example, an image processing-based technique was used to detect anomalies during the powder spreading of PBF-L to control defects [634]. In all of these aforementioned examples, machine learning has provided useful guidelines to control the common AM defects, the physics behind the formation of which is often not known.

9.3. In-situ control of grain structure, phases, and defects

As discussed, in the previous sections of this review, grain structure, phases, and defects are primarily controlled by alloy design, post-processing, and adjusting the processing conditions guided by experimental trials, mechanistic modeling, or data-driven techniques. However, in-situ control methods are also becoming increasingly popular where grain structure, phases, and defects are controlled during the printing process. Primarily, there are three main methods for in-situ control: (1) in-situ alloying [635–639] where alloying elements, inoculants, or grain refiners are added during printing to control the grain structure and phases, (2) application of external agitation during printing such as ultrasound [27,640–645], mechanical vibration [302,646,647], magnetic field [648–651], and external heating [652,653] to control microstructure and defects, and (3) in-situ adjustment of processing conditions [654–663] using a closed-loop feedback system. Applications of these three methods to control grain structure, phases, and defects are reviewed below.

In the in-situ alloying process [635–639], elements, inoculants, or grain refiners are added to the molten pool in powder form. Powders of high melting point elements, ceramic particles, and grain refiners are added to break the long columnar grains into smaller equiaxed grains to improve mechanical properties and reduce solidification cracking. For example, this process is used for grain refinement in AM of stainless steel 316 [637] and Ti alloys [638]. However, the addition of powders during a process with very rapid scanning needs precise control. External agitation such as ultrasound [27,640–645], mechanical vibration [302,646,647], magnetic field [648–651], and external heating [652,653] are used during printing to control microstructure and defects. Ultrasound treatment is used to break long columnar grains to improve mechanical properties and prevent solidification cracking in stainless steels, titanium alloys, and nickel base superalloys [27,642–645]. Mechanical vibrations [302,646,647] are also used for the same purpose. Mechanical vibrations are easier and cheaper to use than ultrasonic vibrations. However, precise control of the vibration amplitude and frequency can be done using ultrasound. External magnetic fields used in DED-GMA [649,650] affect the arc source and thus the heat input and cooling rates to alter the grain structure and phases. Magnetic fields in laser AM processes [648,651] affect the molten pool shape and size and controls the cooling rate and solidification parameters. Application of external heating [652,653] using an auxiliary heat source alters the effective heat input and cooling rates to control the grain structure and phases. Selection of the controlling

parameters of these external sources, such as the frequency and amplitude of the ultrasound, is done by experimental trial-and-error. There is a need to develop mechanistic models of AM processes with external agitations to predict the desired parameters without time-consuming and expensive trials.

Process parameters are adjusted during printing [654–663] to achieve the desired microstructure and reduce defects. Generally, a closed-loop feedback system is used that analyses the data captured by sensors during the process and provides feedback to the controller to adjust the processing conditions in real-time. Fig. 9.18 provides an example of where this method was used to control the microstructure during DED-L [654]. A real-time closed-loop control process was developed and used to control the microstructure. An infrared-based thermal imaging system was developed to monitor the thermal process in real time. The developed system was capable of capturing the real-time cooling rate and melt pool temperature. The solidified grain structures were correlated with in situ thermal measurements to identify the appropriate procedure to control the microstructure. A closed-loop controller was developed and used to control the cooling rate in real-time. This method requires the setting up of additional accessories and sensors which may not be possible for all AM machines and require a high level of expertise.

10. Research needs

This review cites many examples where the current generally accepted understanding of microstructure and properties has been challenged [664], new alloys and applications are explored [665], and mechanisms are investigated for achieving the exciting combination of properties of metallic materials never before believed to be possible [145]. There are several variants of metal printing and each is affected by many process variables such as heat source power, scanning speed, deposition rate, and other variables that vary widely depending on the printing process and the alloy being printed [666]. Consequently, the parameter space window is large in additive manufacturing in comparison with more mature manufacturing processes such as welding and casting. Because of the complexities of the AM processes, more work is needed for the achievement of a significantly better understanding of the relation between the processing, microstructure, properties, and performance. The following are some of the focus areas to maintain and enhance the pace of progress.

10.1. Microstructural features that overcome strength-ductility trade-off

The microstructure of many commonly used alloys such as stainless steels, titanium alloys, and high-strength aluminum alloys contains multiple phases and precipitates in different length scales [3]. The microstructure is characterized by various phases, solidification structures containing cellular, dendritic morphologies, precipitates, and various defects that range in size from nano to mesoscale, and compositional variations owing to segregation and loss of alloying elements [3]. The various constituents in the microstructure vary in size by a factor of more than a million and the resulting heterogeneous hierarchical microstructures strongly influence the mechanical properties of the parts. Like in welding and casting, the phase transformations are strongly influenced by the thermal cycles, except there are multiple thermal cycles in additive manufacturing. Tempering of the phases during additive manufacturing during progressive deposition of layers of metallic materials occurs depending on the local heat transfer conditions that vary with the location within the part and time [180]. Moreover, the heating and cooling rates can be much more intense in additive manufacturing than in welding and casting. The resulting extensive variations of phase compositions, solidification microstructures, and defects such as dislocations have resulted in combinations of properties not attainable by other manufacturing processes. Examples include the simultaneous improvements of both strength and ductility in many cases, thus defying the commonly accepted norm of strength-ductility tradeoff where an increase in strength is commonly accompanied by a decrease in ductility [145,664]. While the hierarchical microstructure and the solidification morphology have been cited for the unique combination of properties, more work is needed for uncovering the mechanisms so that microstructures can be routinely tailored to achieve improved performance of parts.

10.2. Solidification morphology control

The solidification morphology depends on the ratio of the local temperature gradient, G, and the solidification growth rate, R [617]. These two parameters are dependent on a variety of factors that determine the local heat transfer condition, feedstock properties, and process variables. The cooling rates vary by five orders of magnitude depending on the linear heat input, which is the ratio of heat source power to the scanning speed [666]. The diversity in spatial and temporal variations of G and R and repeated thermal cycles present an unusual challenge for understanding the evolution of the solidification structure of printed metals. Many of the previous studies of morphology control originated from the lessons from casting and welding. For example, the addition of nucleants is commonly practiced in the foundry to achieve an equiaxed structure [667]. By adopting this time-tested practice, zirconia nano-particles have been added to break up the growth of columnar dendrites to an equiaxed structure to prevent solidification cracking in printed aluminum alloy parts [104]. However, there is no direct way to predict the number of nucleation sites obtained by adding a certain amount of nucleant. In addition, the type of the nucleant, its size, and the amount are determined by trial and error and alternatives are being explored to achieve equiaxed morphology. One such method is the use of ultrasonic energy to break up the columnar grains [273]. The strength of the iron and aluminum alloy parts has also been attributed to the cellular structures. Although morphology control has been practiced in welding and casting for a long time, the implementation of the lessons to achieve equiaxed grains by adding expensive inoculants or applying ultrasonic energy to improve 3D printed parts needs more work.

10.3. Texture

Since texture affects the mechanical properties of additively manufactured parts, particularly the yield strength and fatigue properties, it is important to seek a better understanding of the evolution of texture in AM samples. The heat source power, scanning speed, hatch spacing, and scanning pattern all play a part in influencing texture. In solidified alloys, the texture is aligned to the heat flow direction [156], and grains tend to continue from layer to layer along the heat flow direction. In thin parts, the heat flow direction is often towards the base plate and the solidification texture in cubic materials is parallel to the build direction [156]. Textured microstructure often results in anisotropy in properties that can affect mechanical performance in multi-axial loading. The effect of anisotropy on mechanical properties is not well understood and more work needs to be done [149].

10.4. Defects and their impact on properties

Defects in microstructures are present in different length scales and can affect mechanical properties. For example, the lack of fusion voids adversely affect tensile properties [157]. High thermal stresses may result in distortions and, in extreme cases, may result in delamination and adversely affect fatigue properties. Surface roughness may act as the source of stress concentration that may result in crack initiation under stress [668]. The role that different defects play in crystal plasticity, fracture, and fatigue are also affected by dislocations and other defects in the microstructure. In addition, different types of defects interact with each other and affect mechanical properties in a manner not clearly understood. A better understanding of the evolution of various types of defects and their role in affecting mechanical properties needs more work.

10.5. Creating a printability database

Undesirable microstructural components such as brittle phases and common defects can be largely avoided by an appropriate selection of alloys and process variables [3]. Progressive enrichment of a database that assimilates valuable information about the known susceptibilities of various alloys to defects and undesirable microstructural features will help practicing engineers avoid difficulties before alloys are printed [3]. Defects such as lack of fusion, cracking, surface roughness, porosity, residual stresses, and distortion originate from a combination of the alloy used, printing process, and process parameters [23]. A comprehensive assessment of the ability of a feedstock material to be printed as a sound part by a combination of a printing process and process variables is needed. Such a printability database [605] will help in the selection of an appropriate printing process-alloy combination and avoid poor microstructural features without expensive and time-consuming trial and error testing. The success of the weldability database for fusion welding indicates that a printability database will enable the research results in 3D printing usable in the industry.

10.6. Applications of the emerging digital tools

Additive manufacturing has been designed to use digital technology in production, monitoring, and process control [3]. Validated mechanistic models and machine learning algorithms can reliably predict microstructural features and they have the potential to effectively control and improve the microstructures of parts [1]. The mechanistic models calculate important parameters such as temperature fields, build geometry, and cooling rates from process conditions and thermophysical properties of the alloy. These data are then used in a microstructure model to relate processing conditions and alloy composition with important microstructural features such as phase composition, grain structure and topology, and precipitates [1]. Since the microstructural features are highly sensitive to alloy composition, printing techniques, and process parameters, predictions of these characteristics using verifiable mechanistic models before printing are helpful for their control. However, in many cases, mechanistic information is not available and data-driven machine learning codes can provide quantitative correlation between microstructural features, the processing conditions, and alloy composition [1]. A case in point is the formation of cracking in many aluminum and nickel alloys that occurs via multiple mechanisms [105,669]. In the absence of definitive mechanistic understanding, machine learning codes use data and process conditions without phenomenological understanding to predict the evolution of microstructural features and defects. These algorithms can augment human intelligence based on experience to provide optimization of process variables and product attributes [1].

11. Outlook

11.1. Effect of process parameters on microstructure, grain structure, and texture

Only a handful of the over 5000 alloys have been investigated so far to understand the special features of AM that have a beneficial impact on properties [1]. In addition, new alloys are being developed specifically for additive manufacturing processes to take advantage of their unique features such as multiple thermal cycles to obtain superior properties [665]. Printing of silicon-containing steels [165] to achieve specific crystallographic texture for use in electric motors and transformers or affordable iron alloys containing nickel and cobalt [3] for applications where low thermal expansion coefficients are needed are examples of potentially attractive applications of new alloys with unique microstructures. Small changes in the microstructures of the existing alloys by taking advantage of the rich knowledge base of casting and welding may solve some of the persistent problems in AM [1]. For example, it has been known for a long time that certain additives in high-strength aluminum alloys promote the growth of equiaxed grains and prevent solidification cracking [105]. Developing a comprehensive knowledge base for understanding microstructural features and how they

are related to multiple properties is contributing to the printability database where the alloy-process combinations can be examined for their suitability to print sound components [605]. Apart from revealing the outcome of process-materials combinations, they will also continue to enrich the fundamentals of phase transformations, elemental segregation, formation of metastable phases, grain and sub-grain structures, and defects in mesoscale to as small as the crystal defects that result in unique properties during AM.

11.2. Improved understanding of the unique combination of properties

The serviceability of parts depends on a combination of several properties. Optimizing process combinations to achieve the desired combination of properties will undoubtedly result in a unique combination of properties never before thought possible [3]. Over-coming the strength-ductility tradeoff is a case in point. In most cases, an increase in the strength of alloys is accompanied by a decrease in ductility. However, in certain stainless steel and other alloys, this common paradigm has been overcome and simultaneous improvements in either one or both of the properties have been achieved [145,664]. As we study the underlying mechanisms, the new knowledge will undoubtedly lead to better properties and serviceability of parts.

11.3. New alloys

The crystal structures of the iron, aluminum, nickel, and titanium-based alloys are determined by both the unit cells of the solvent atoms modified by the solutes they contain. Additions of the nature and amount of solutes have been the basis to control the solidification behavior, grain morphology, phase compositions, and mechanical properties of the alloys [1]. However, the microstructures of metallic materials are notoriously sensitive to external impulses such as cooling rates and stresses [3]. The existing iron, aluminum, nickel, and titanium-based alloys that are used in AM were not designed specifically for additive manufacturing [3]. Most variants of additive manufacturing involve multiple thermal cycles that affect the microstructure and properties of metallic parts. Process models that can predict thermal cycles are emerging [1]. However, it is anticipated that relating process variables with microstructure and properties of parts is a slow process because of the large number of process variables, their wide range, and the alloy-specific nature of microstructure and properties [666]. Advanced modeling can assist in controlling thermal cycles that are useful for insight into the evolution of microstructure. In addition, the development of new alloys and functionally graded materials will continue [665] that when exposed to the AM conditions can result in microstructures and properties that will meet the performance needs of the parts for qualification.

11.4. Fewer defects

Lack of fusion defects, cracking, residual stresses and distortion, various types of porosity, surface roughness, waviness, balling, and change in chemical composition and crystal defects such as dislocations are important microstructural features of additively manufactured parts [23]. Multiple defects in mesoscale and smaller, all the way to the atomic scale profoundly affect the properties and serviceability of parts. Post-processing such as heat treatments and hot isostatic pressing will continue to be used to mitigate defects such as porosity, lack of fusion, and residual stresses but these steps compromise the cost competitiveness of parts, and progress is being made to mitigate defects [3]. Defects in all scales also play a part in affecting mechanical properties in a complex manner. Although significant progress has been made recently to quantitatively understand the origin of the defects and the hierarchical influence of various process variables, at present, there is a scarcity of quantitative frameworks for understanding the correlation between the process variables with the defects and mechanical properties of parts. Continuing progress in the applications of mechanistic modeling and machine learning has the potential to narrow down the process parameter window to control defects and improve the serviceability of parts [1].

11.5. Improved integration of digital tools

There are many examples of how important parameters which affect product quality such as the temperature and velocity fields, cooling rates, solidification morphology, and the scale of microstructure can be computed using verifiable mechanistic models [1]. These parameters are difficult to measure experimentally because of the small size of the fusion zone and the strong spatially variable, transient nature of the temperature field. When mechanistic models are combined with experimental data [1], the scientific basis for the understanding of the evolution of microstructure and properties can be uncovered. As the benefits of the use of mechanistic models are more widely appreciated, the selection of parameters for the printing of sound parts will be guided by scientific principles thus avoiding time-consuming and expensive trial and error [1].

Machine learning is a natural fit for additive manufacturing because of its origin in digital technology. From product design to process planning, to production monitoring and control to connecting process variables to product attributes, machine learning will serve a more important role than its current usage [1]. An integrated data collection system by a vision system can gather data during the printing of each layer and machine learning can use the temperature fields and materials states to reduce production errors. Control of microstructure and properties are perhaps the most important features that will be impacted by machine learning because currently there is no reliable way to predict complex properties of metallic materials from phenomenological understanding [105]. Microstructures of additively manufactured metallic materials are complex because of the diversity of phases, grain and sub-grain structures, segregated elements, metastable phases, very fine oxides and other precipitates, and high concentrations of dislocations near grain boundaries. These diverse features of the microstructures make the correlation between the microstructure and properties complex.

Machine learning when the quality and volume requirements of data are met and appropriate precautions are exercised for the prediction errors provides a potential alternative to correlate microstructure with multiple properties and improve the serviceability of parts based on scientific principles [1,105].

Declaration of Competing Interest

The authors declare that they have no known competing financial interests or personal relationships that could have appeared to influence the work reported in this paper.

Data availability

No data was used for the research described in the article.

References

[1] DebRoy T, Mukherjee T, Wei HL, Elmer JW, Milewski JO. Metallurgy, mechanistic models and machine-learning in metal printing. Nat Rev Mater 2021;6: 48–68.
[2] DebRoy T, Mukherjee T, Milewski JO, Elmer JW, Ribic B, Blecher JJ, et al. Scientific, technological and economic issues in metal printing and their solutions. Nat Mater 2019;18:1026–32.
[3] DebRoy T, Wei H, Zuback J, Mukherjee T, Elmer J, Milewski J, et al. Additive manufacturing of metallic components–process, structure and properties. Prog Mater Sci 2018;92:112–224.
[4] Wei HL, Mukherjee T, Zhang W, Zuback JS, Knapp GL, De A, et al. Mechanistic models for additive manufacturing of metallic components. Prog Mater Sci 2021;116.
[5] DebRoy T, Bhadeshia H. Innovations in Everyday Engineering Materials: Springer 2021.
[6] Gu DD, Shi XY, Poprawe R, Bourell DL, Setchi R, Zhu JH. Material-structure-performance integrated laser-metal additive manufacturing. Science 2021;372: 932.
[7] Ngo TD, Kashani A, Imbalzano G, Nguyen KTQ, Hui D. Additive manufacturing (3D printing): A review of materials, methods, applications and challenges. Composites Part B-Engineering. 2018;143:172–96.
[8] Herzog D, Seyda V, Wycisk E, Emmelmann C. Additive manufacturing of metals. Acta Mater 2016;117:371–92.
[9] Sames WJ, List FA, Pannala S, Dehoff RR, Babu SS. The metallurgy and processing science of metal additive manufacturing. Int Mater Rev 2016;61:315–60.
[10] Gu DD, Meiners W, Wissenbach K, Poprawe R. Laser additive manufacturing of metallic components: materials, processes and mechanisms. Int Mater Rev 2012;57:133–64.
[11] MacDonald E, Wicker R. Multiprocess 3D printing for increasing component functionality. Science 2016;353.
[12] Tofail SAM, Koumoulos EP, Bandyopadhyay A, Bose S, O'Donoghue L, Charitidis C. Additive manufacturing: scientific and technological challenges, market uptake and opportunities. Mater Today 2018;21:22–37.
[13] Frazier WE. Metal Additive Manufacturing: A Review. J Mater Eng Perform 2014;23:1917–28.
[14] Beaman JJ, Bourell DL, Seepersad CC, Kovar D. Additive Manufacturing Review: Early Past to Current Practice. Journal of Manufacturing Science and Engineering-Transactions of the Asme. 2020;142.
[15] Singh S, Ramakrishna S, Singh R. Material issues in additive manufacturing: A review. J Manuf Process 2017;25:185–200.
[16] Liu ZY, Zhao DD, Wang P, Yan M, Yang C, Chen ZW, et al. Additive manufacturing of metals: Microstructure evolution and multistage control. J Mater Sci Technol 2022;100:224–36.
[17] Nguyen HD, Pramanik A, Basak AK, Dong Y, Prakash C, Debnath S, et al. A critical review on additive manufacturing of Ti-6Al-4V alloy: microstructure and mechanical. Journal of Materials Research and Technology-Jmr & T. 2022;18:4641–61.
[18] Zhang D, Liu AB, Yin BZ, Wen P. Additive manufacturing of duplex stainless steels-A critical review. J Manuf Process 2022;73:496–517.
[19] Shahwaz M, Nath P, Sen I. A critical review on the microstructure and mechanical properties correlation of additively manufactured nickel-based superalloys. J Alloy Compd 2022;907.
[20] Kok Y, Tan XP, Wang P, Nai MLS, Loh NH, Liu E, et al. Anisotropy and heterogeneity of microstructure and mechanical properties in metal additive manufacturing: A critical review. Mater Des 2018;139:565–86.
[21] Bajaj P, Hariharan A, Kini A, Kurnsteiner P, Raabe D, Jagle EA. Steels in additive manufacturing: A review of their microstructure and properties. Materials Science and Engineering A-Structural Materials Properties Microstructure and Processing. 2020;772,138633.
[22] Brennan MC, Keist JS, Palmer TA. Defects in Metal Additive Manufacturing Processes. J Mater Eng Perform 2021;30:4808–18.
[23] Mostafaei A, Zhao C, He YN, Ghiaasiaan SR, Shi B, Shao S, et al. Defects and anomalies in powder bed fusion metal additive manufacturing. Curr Opin Solid State Mater Sci 2022;26.
[24] Chadwick AF, Voorhees PW. The development of grain structure during additive manufacturing. Acta Mater 2021;211:116862.
[25] Bermingham MJ, StJohn DH, Krynen J, Tedman-Jones S, Dargusch MS. Promoting the columnar to equiaxed transition and grain refinement of titanium alloys during additive manufacturing. Acta Mater 2019;168:261–74.
[26] Mclean N, Bermingham M, Colegrove P, Sales A, Dargusch M. Understanding the grain refinement mechanisms in aluminium 2319 alloy produced by wire arc additive manufacturing. Sci Technol Weld Join 2022;27:479–89.
[27] Todaro C, Easton M, Qiu D, Brandt M, StJohn D, Qian M. Grain refinement of stainless steel in ultrasound-assisted additive manufacturing. Addit Manuf 2021; 37:101632.
[28] Schneider J. Comparison of microstructural response to heat treatment of Inconel 718 prepared by three different metal additive manufacturing processes. JOM 2020;72:1085–91.
[29] Wei HL, Elmer JW, DebRoy T. Three-dimensional modeling of grain structure evolution during welding of an aluminum alloy. Acta Mater 2017;126:413–25.
[30] Mukherjee T, DebRoy, T. Theory and Practice of Additive Manufacturing (in press). Wiley, New Jersey, USA.
[31] Hunt JD. Steady state columnar and equiaxed growth of dendrites and eutectic. Mater Sci Eng 1984;65:75–83.
[32] Kou S. Welding metallurgy. New Jersey, USA 2003;431:223–5.
[33] Burke J, Turnbull D. Recrystallization and grain growth. Prog Met Phys 1952;3:220–92.
[34] Atkinson H. Overview no. 65: Theories of normal grain growth in pure single phase systems. Acta Metallurgica. 1988;36:469-91.
[35] Mishra S, DebRoy T. Non-isothermal grain growth in metals and alloys. Mater Sci Technol 2006;22:253–78.
[36] Wei HL, Knapp GL, Mukherjee T, DebRoy T. Three-dimensional grain growth during multi-layer printing of a nickel-based alloy Inconel 718. Addit Manuf 2019;25:448–59.
[37] Zhou Y, Ning F, Zhang P, Sharma A. Geometrical, microstructural, and mechanical properties of curved-surface AlSi10Mg parts fabricated by powder bed fusion additive manufacturing. Mater Des 2021;198:109360.
[38] Shi S, Lin X, Wang L, Wang Z, Wei L, Yang H, et al. Investigations of the processing–structure–performance relationships of an additively manufactured AlSi10Mg alloy via directed energy deposition. J Alloy Compd 2023;944:169050.

[39] Karlsson D, Chou C-Y, Pettersson NH, Helander T, Harlin P, Sahlberg M, et al. Additive manufacturing of the ferritic stainless steel SS441. Addit Manuf 2020;
     36:101580.
[40] Chai R, Zhang Y, Zhong B, Zhang C. Effect of scan speed on grain and microstructural morphology for laser additive manufacturing of 304 stainless steel. Rev
     Adv Mater Sci 2021;60:744–60.
[41] Sun L, Jiang F, Huang R, Yuan D, Guo C, Wang J. Anisotropic mechanical properties and deformation behavior of low-carbon high-strength steel component
     fabricated by wire and arc additive manufacturing. Mater Sci Eng A 2020;787:139514.
[42] Dai Y-l, Yu S-f, Huang A-g, Shi Y-s. Microstructure and mechanical properties of high-strength low alloy steel by wire and arc additive manufacturing. Int J
     Miner Metall Mater 2020;27:933–42.
[43] Jiang P, Zhang C, Zhang S, Zhang J, Chen J, Chen H. Additive manufacturing of novel ferritic stainless steel by selective laser melting: Role of laser scanning
     speed on the formability, microstructure and properties. Opt Laser Technol 2021;140:107055.
[44] Sridharan N, Gussev MN, Field KG. Performance of a ferritic/martensitic steel for nuclear reactor applications fabricated using additive manufacturing. J Nucl
     Mater 2019;521:45–55.
[45] Yan X, Yang X, Tian G, Sun D, Liu S, Xiong Z, et al. Modeling and Simulation Investigations on Microstructure Evolution during Additive Manufacturing of
     AlSi10Mg Alloy. Metals. 2022;12:1711.
[46] Jiang R, Mostafaei A, Pauza J, Kantzos C, Rollett AD. Varied heat treatments and properties of laser powder bed printed Inconel 718. Mater Sci Eng A 2019;
     755:170–80.
[47] Kim K-S, Kang T-H, Kassner ME, Son K-T, Lee K-A. High-temperature tensile and high cycle fatigue properties of inconel 625 alloy manufactured by laser
     powder bed fusion. Addit Manuf 2020;35:101377.
[48] Gonzalez J, Mireles J, Stafford S, Perez M, Terrazas C, Wicker R. Characterization of Inconel 625 fabricated using powder-bed-based additive manufacturing
     technologies. J Mater Process Technol 2019;264:200–10.
[49] Nandha Kumar E, Athira K, Chatterjee S, Srinivasan D. Effect of Heat Treatment on Structure and Properties of Laser Powder Bed Fusion Inconel 939.
     International Manufacturing Science and Engineering Conference: American Society of Mechanical Engineers; 2022. p. V001T02A3.
[50] Ghods S, Schultz E, Wisdom C, Schur R, Pahuja R, Montelione A, et al. Electron beam additive manufacturing of Ti6Al4V: Evolution of powder morphology and
     part microstructure with powder reuse. Materialia. 2020;9:100631.
[51] Meier B, Skalon M, Warchomicka F, Belei C, Görtler M, Kaindl R, et al. Effect of the reuse of powder on material properties of Ti6Al4V processed by SLM. In:
     AIP Conference Proceedings: AIP Publishing LLC; 2019. p. 150006.
[52] Ji X, Mirkoohi E, Ning J, Liang SY. Analytical modeling of post-printing grain size in metal additive manufacturing. Opt Lasers Eng 2020;124:105805.
[53] Zhang W, Elmer J, DebRoy T. Integrated modelling of thermal cycles, austenite formation, grain growth and decomposition in the heat affected zone of carbon
     steel. Sci Technol Weld Join 2005;10:574–82.
[54] Wu Y, Zhang S, Cheng X, Wang H. Investigation on solid-state phase transformation in a Ti-47Al-2Cr-2V alloy due to thermal cycling during laser additive
     manufacturing process. J Alloy Compd 2019;799:325–33.
[55] Zhang Z, Ge P, Li J, Ren D, Wu T. Monte Carlo simulations of solidification and solid-state phase transformation during directed energy deposition additive
     manufacturing. Progress in Additive Manufacturing. 2022;7:671–82.
[56] Bailey NS, Shin YC. Multi-track, multi-layer dendrite growth and solid phase transformation analysis during additive manufacturing of H13 tool steel using a
     combined hybrid cellular automata/phase field, solid-state phase prediction models. Int J Adv Manuf Technol 2022;120:2089–108.
[57] Kumara C, Balachandramurthi AR, Goel S, Hanning F, Moverare J. Toward a better understanding of phase transformations in additive manufacturing of Alloy
     718. Materialia. 2020;13:100862.
[58] Du Q, Azar AS, M'hamdi M. Kinetic interface condition phase diagram for the rapid solidification of multi-component alloys with an application to additive
     manufacturing. Calphad. 2022;76:102365.
[59] Seede R, Ye J, Whitt A, Trehern W, Elwany A, Arroyave R, et al. Effect of composition and phase diagram features on printability and microstructure in laser
     powder bed fusion: Development and comparison of processing maps across alloy systems. Addit Manuf 2021;47:102258.
[60] Sprouster DJ, Cunningham WS, Halada GP, Yan H, Pattammattel A, Huang X, et al. Dislocation microstructure and its influence on corrosion behavior in laser
     additively manufactured 316L stainless steel. Addit Manuf 2021;47:102263.
[61] Sarkar S, Mukherjee S, Kumar CS, Nath AK. Effects of heat treatment on microstructure, mechanical and corrosion properties of 15–5 PH stainless steel parts
     built by selective laser melting process. J Manuf Process 2020;50:279–94.
[62] Hatakeyama T, Sawada K, Suzuki M, Watanabe M. Microstructure development of modified 9Cr-1Mo steel during laser powder bed fusion and heat treatment.
     Addit Manuf 2023;61:103350.
[63] Jiang R, Mostafaei A, Wu Z, Choi A, Guan P-W, Chmielus M, et al. Effect of heat treatment on microstructural evolution and hardness homogeneity in laser
     powder bed fusion of alloy 718. Addit Manuf 2020;35:101282.
[64] Misra S, Mohanty I, Raza MS, Chakraborty R, Chatterjee P, Gopal M, et al. Investigation of IR pyrometer-captured thermal signatures and their role on
     microstructural evolution and properties of Inconel 625 tracks in DED-based additive manufacturing. Surf Coat Technol 2022;447:128818.
[65] Chen Y, Yang C, Fan C, Wang M. Microstructure evolution and mechanical properties of a nickel-based superalloy repaired using wire and arc additive
     manufacturing. Mater Charact 2022;193:112315.
[66] Yang J, Liu X, Song M, He L, Bankson S, Hamilton M, et al. Sensitization, desensitization, and carbide evolution of Alloy 800H made by laser powder bed
     fusion. Addit Manuf 2022;50:102547.
[67] Ramakrishnan A, Dinda GP. Microstructure and mechanical properties of direct laser metal deposited Haynes 282 superalloy. Materials Science and
     Engineering a-Structural Materials Properties Microstructure and Processing. 2019;748:347–56.
[68] Zhang H, Wang Y, De Vecchis RR, Xiong W. Evolution of carbide precipitates in Haynes® 282 superalloy processed by wire arc additive manufacturing.
     J Mater Process Technol 2022;305:117597.
[69] Zhang K, Kan WH, Zhu Y, Lim SCV, Gao X, Sit CK, et al. Achieving ultra-high strength rapidly in Ti-3Al-8V-6Cr-4Mo-4Zr alloy processed by directed energy
     deposition. Mater Des 2022;224:111325.
[70] Pauzon C, Markström A, Dubiez-Le Goff S, Hryha E. Effect of the Process Atmosphere Composition on Alloy 718 Produced by Laser Powder Bed Fusion. Metals.
     2021;11:1254.
[71] Lervåg M, Sørensen C, Robertstad A, Brønstad BM, Nyhus B, Eriksson M, et al. Additive manufacturing with superduplex stainless steel wire by cmt process.
     Metals. 2020;10:272.
[72] A Hosseini V, Högström M, Hurtig K, Valiente Bermejo MA, Stridh L-E, Karlsson L. Wire-arc additive manufacturing of a duplex stainless steel: thermal cycle
     analysis and microstructure characterization. Welding in the World. 2019;63:975-87.
[73] Haghdadi N, Ledermueller C, Chen H, Chen Z, Liu Q, Li X, et al. Evolution of microstructure and mechanical properties in 2205 duplex stainless steels during
     additive manufacturing and heat treatment. Mater Sci Eng A 2022;835:142695.
[74] Eo D-R, Chung S-G, Yang J, Jung I-H, Cho J-W. Numerical modeling of oxide particle evolution during additive manufacturing. Addit Manuf 2022;51:102631.
[75] Yang X, Tang F, Hao X, Li Z. Oxide evolution during the solidification of 316L stainless steel from additive manufacturing powders with different oxygen
     contents. Metall Mater Trans B 2021;52:2253–62.
[76] El Moghazi SN, Wolfe T, Ivey DG, Henein H. Plasma transfer arc additive manufacturing of 17–4 PH: assessment of defects. Int J Adv Manuf Technol 2020;108:
     2301–13.
[77] Brytan Z, Król M, Benedyk M, Pakieła W, Tański T, Dagnaw MJ, et al. Microstructural and mechanical properties of novel Co-free maraging steel M789
     prepared by additive manufacturing. Materials. 2022;15:1734.
[78] Bojestig E, Cao Y, Nyborg L. Surface chemical analysis of copper powder used in additive manufacturing. Surf Interface Anal 2020;52:1104–10.
[79] Upadhyay MV, Slama MBH, Gaudez S, Mohanan N, Yedra L, Hallais S, et al. Non-oxide precipitates in additively manufactured austenitic stainless steel. Sci
     Rep 2021;11:10393.

[80] Wang K, Sun Z, Liu Y, Lv Y. Investigation of microstructure and mechanical performance of IN738LC superalloy thin wall produced by pulsed plasma arc additive manufacturing. Materials. 2020;13:3924.

[81] Li C, Gu H, Wang W, Wang S, Ren L, Wang Z, et al. Effects of magnesium on the microstructure and properties of Al–Si alloy deposited by wire and arc-based additive manufacturing. Mater Technol 2021;36:793–8.

[82] Sui S, Chen J, Li Z, Li H, Zhao X, Tan H. Investigation of dissolution behavior of laves phase in inconel 718 fabricated by laser directed energy deposition. Addit Manuf 2020;32.

[83] Wang X, Liu P, Ji Y, Liu Y, Horstemeyer M, Chen L. Investigation on microsegregation of IN718 alloy during additive manufacturing via integrated phase-field and finite-element modeling. J Mater Eng Perform 2019;28:657–65.

[84] Chen Y, Guo Y, Xu M, Ma C, Zhang Q, Wang L, et al. Study on the element segregation and Laves phase formation in the laser metal deposited IN718 superalloy by flat top laser and gaussian distribution laser. Mater Sci Eng A 2019;754:339–47.

[85] Sui S, Tan H, Chen J, Zhong C, Li Z, Fan W, et al. The influence of Laves phases on the room temperature tensile properties of Inconel 718 fabricated by powder feeding laser additive manufacturing. Acta Mater 2019;164:413–27.

[86] Conde F, Avila J, Oliveira J, Schell N, Oliveira M, Escobar J. Effect of the as-built microstructure on the martensite to austenite transformation in a 18Ni maraging steel after laser-based powder bed fusion. Addit Manuf 2021;46:102122.

[87] Fleißner-Rieger C, Tunes MA, Gammer C, Jörg T, Pfeifer T, Musi M, et al. On the existence of orthorhombic martensite in a near-α titanium base alloy used for additive manufacturing. J Alloy Compd 2022;897:163155.

[88] Pantawane MV, Sharma S, Sharma A, Dasari S, Banerjee S, Banerjee R, et al. Coarsening of martensite with multiple generations of twins in laser additively manufactured Ti6Al4V. Acta Mater 2021;213:116954.

[89] Ge J, Ma T, Chen Y, Jin T, Fu H, Xiao R, et al. Wire-arc additive manufacturing H13 part: 3D pore distribution, microstructural evolution, and mechanical performances. J Alloy Compd 2019;783:145–55.

[90] Hearn W, Lindgren K, Persson J, Hryha EJM. In Situ Tempering of Martensite during Laser Powder Bed Fusion of Fe-0.45 C Steel. Materialia 2022;23:101459.

[91] Mukherjee T, DebRoy T, Lienert TJ, Maloy SA, Lear CR, Hosemann P. Tempering kinetics during multilayer laser additive manufacturing of a ferritic steel. J Manuf Process 2022;83:105–15.

[92] Ning J, Wen J-H, Zhang L-J, Na S-J. Assessment of the universality of duplex stainless steel powder in laser additive repair based on Schaeffler diagram. Addit Manuf 2022;55:102864.

[93] Ivanova T, Mashlan M, Ingr T, Doláková H, Sarychev D, Sedláčková A. Mössbauer Spectroscopy for Additive Manufacturing by Selective Laser Melting. Metals. 2022;12:551.

[94] Jang J, Van D, Lee SH. Precipitation kinetics of secondary phases induced by heat accumulation in the deposit of Inconel 718. Addit Manuf 2022;55:102831.

[95] Kohout J. An alternative to the JMAK equation for a better description of phase transformation kinetics. J Mater Sci 2008;43:1334–9.

[96] Hong T, DebRoy T. Time-temperature-transformation diagrams for the growth and dissolution of inclusions in liquid steels. Scr Mater 2001;44:847–52.

[97] Hong T, DebRoy T, Babu S, David S. Modeling of inclusion growth and dissolution in the weld pool. Metall Mater Trans B 2000;31:161–9.

[98] Sridar S, Sargent N, Wang X, Klecka MA, Xiong W. Determination of location-specific solidification cracking susceptibility for a mixed dissimilar alloy processed by wire-arc additive manufacturing. Metals. 2022;12:284.

[99] Cao Y, Wei HL, Yang T, Liu TT, Liao WH. Printability assessment with porosity and solidification cracking susceptibilities for a high strength aluminum alloy during laser powder bed fusion. Addit Manuf 2021;46.

[100] Liu JW, Zeng PW, Kou SO. Solidification cracking susceptibility of quaternary aluminium alloys. Sci Technol Weld Join 2021;26:244–57.

[101] Guo B, Zhang Y, Yang Z, Cui D, He F, Li J, et al. Cracking mechanism of Hastelloy X superalloy during directed energy deposition additive manufacturing. Addit Manuf 2022;55:102792.

[102] Hyer H, Zhou L, Mehta A, Park S, Thinh H, Song S, et al. Composition-dependent solidification cracking of aluminum-silicon alloys during laser powder bed fusion. Acta Mater 2021;208.

[103] Kou S. Welding Metallurgy. John Wiley & Sons; 2020.

[104] Martin JH, Yahata BD, Hundley JM, Mayer JA, Schaedler TA, Pollock TM. 3D printing of high-strength aluminium alloys. Nature 2017;549:365 -+.

[105] Mondal B, Mukherjee T, DebRoy T. Crack free metal printing using physics informed machine learning. Acta Mater 2022;226.

[106] Luu DN, Zhou W, Nai SML. Mitigation of liquation cracking in selective laser melted Inconel 718 through optimization of layer thickness and laser energy density. J Mater Process Technol 2022;299:117374.

[107] Chen S, Xu M, Yuan T, Jiang X, Zhang H, Zheng X. Thermal–microstructural analysis of the mechanism of liquation cracks in wire-arc additive manufacturing of Al–Zn–Mg–Cu alloy. J Mater Res Technol 2022;16:1260–71.

[108] Xu M, Zhang H, Yuan T, Yan Z, Chen S. Microstructural characteristics and cracking mechanism of AlCu alloys in wire arc additive manufacturing. Mater Charact 2023;112677.

[109] Zhang X, Chen H, Xu L, Xu J, Ren X, Chen X. Cracking mechanism and susceptibility of laser melting deposited Inconel 738 superalloy. Mater Des 2019;183:108105.

[110] Chun E-J, Jeong Y-S, Seo S-M, Kang H. Liquation cracking susceptibility of remelted and reheated weld metals in CM247LC superalloy using multi-bead Varestraint testing. Sci Technol Weld Join 2022;1–10.

[111] Huang C, Kou S. Liquation cracking in full-penetration Al-Mg-Si welds. Weld J 2004;83:111S–S122.

[112] Yuan T, Chai X, Luo Z, Kou S. Predicting susceptibility of magnesium alloys to weld-edge cracking. Acta Mater 2015;90:242–51.

[113] Yuan T, Yu ZL, Chen SJ, Xu M, Jiang XQ. Loss of elemental Mg during wire plus arc additive manufacturing of Al-Mg alloy and its effect on mechanical properties. J Manuf Process 2020;49:456–62.

[114] Ahsan F, Ladani L. Temperature Profile, Bead Geometry, and Elemental Evaporation in Laser Powder Bed Fusion Additive Manufacturing Process. JOM 2020;72:429–39.

[115] Xin J, Wu D, Shen C, Wang L, Hua X, Ma N, et al. Multi-physical modelling of alloy element transportation in wire arc additive manufacturing of a γ-TiAl alloy. Int J Therm Sci 2022;179:107641.

[116] Shinjo J, Kutsukake A, Arote A, Tang YT, McCartney DG, Reed RC, et al. Physics-based thermal-chemical-fluid-microstructure modelling of in-situ alloying using additive manufacturing: Composition-microstructure control. Addit Manuf 2023;64:103428.

[117] Zhao D, Long D, Niu T, Zhang T, Hu X, Liu Y. Effect of Mg Loss and Microstructure on Anisotropy of 5356 Wire Arc Additive Manufacturing. J Mater Eng Perform 2022;1–10.

[118] Mukherjee T, Zuback JS, De A, DebRoy T. Printability of alloys for additive manufacturing. Sci Rep 2016;6.

[119] Ning JQ, Wang WJ, Zamorano B, Liang SY. Analytical modeling of lack-of-fusion porosity in metal additive manufacturing. Appl Phys A-Mater Sci Process. 2019;125:11.

[120] dos Santos Paes LE, Pereira M, Xavier FA, Weingaertner WL, Vilarinho LO. Lack of fusion mitigation in directed energy deposition with laser (DED-L) additive manufacturing through laser remelting. J Manuf Process 2022;73:67–77.

[121] Coeck S, Bisht M, Plas J, Verbist F. Prediction of lack of fusion porosity in selective laser melting based on melt pool monitoring data. Addit Manuf 2019;25:347–56.

[122] Laleh M, Hughes AE, Yang S, Wang J, Li J, Glenn AM, et al. A critical insight into lack-of-fusion pore structures in additively manufactured stainless steel. Addit Manuf 2021;38:101762.

[123] Jiang M, Mukherjee T, Du Y, DebRoy T. Superior printed parts using history and augmented machine learning. npj Comput Mater 2022;8:184.

[124] Gordon JV, Narra SP, Cunningham RW, Liu H, Chen HM, Suter RM, et al. Defect structure process maps for laser powder bed fusion additive manufacturing. Addit Manuf 2020;36:11.

[125] Sola A, Nouri A. Microstructural porosity in additive manufacturing: The formation and detection of pores in metal parts fabricated by powder bed fusion. Journal of Advanced Manufacturing and Processing. 2019;1:e10021.

[126] Hauser T, Reisch RT, Breese PP, Lutz BS, Pantano M, Nalam Y, et al. Porosity in wire arc additive manufacturing of aluminium alloys. Addit Manuf 2021;41: 101993.

[127] Zhang B, Liu S, Shin YC. In-Process monitoring of porosity during laser additive manufacturing process. Addit Manuf 2019;28:497–505.

[128] Reijonen J, Revuelta A, Riipinen T, Ruusuvuori K, Puukko P. On the effect of shielding gas flow on porosity and melt pool geometry in laser powder bed fusion additive manufacturing. Addit Manuf 2020;32:101030.

[129] Kumar P, Farah J, Akram J, Teng C, Ginn J, Misra M. Influence of laser processing parameters on porosity in Inconel 718 during additive manufacturing. Int J Adv Manuf Technol 2019;103:1497–507.

[130] Pehlke RD. Unit processes of extractive metallurgy. American Elsevier Publishing Co, New York 1973;1973:396.

[131] DebRoy T, David SA. Physical processes in fusion welding. Rev Mod Phys (USA). 1995;67:85–112.

[132] Huang Y, Fleming TG, Clark SJ, Marussi S, Fezzaa K, Thiyagalingam J, et al. Keyhole fluctuation and pore formation mechanisms during laser powder bed fusion additive manufacturing. Nat Commun 2022;13:1170.

[133] Paulson NH, Gould B, Wolff SJ, Stan M, Greco AC. Correlations between thermal history and keyhole porosity in laser powder bed fusion. Addit Manuf 2020; 34:101213.

[134] Zhao C, Parab ND, Li X, Fezzaa K, Tan W, Rollett AD, et al. Critical instability at moving keyhole tip generates porosity in laser melting. Science 2020;370:1080 -+.

[135] Ren Z, Gao L, Clark SJ, Fezzaa K, Shevchenko P, Choi A, et al. Machine learning–aided real-time detection of keyhole pore generation in laser powder bed fusion. Science 2023;379:89–94.

[136] Yeung H, Kim F, Donmez M, Neira J. Keyhole pores reduction in laser powder bed fusion additive manufacturing of nickel alloy 625. Int J Mach Tool Manu 2022;183:103957.

[137] Bajaj P, Hariharan A, Kini A, Kuernsteiner P, Raabe D, Jaegle EA. Steels in additive manufacturing: A review of their microstructure and properties. Materials Science and Engineering a-Structural Materials Properties Microstructure and Processing. 2020:772.

[138] Sun Z, Tan X, Tor SB, Yeong WY. Selective laser melting of stainless steel 316L with low porosity and high build rates. Mater Des 2016;104:197–204.

[139] Yadollahi A, Shamsaei N, Thompson SM, Seely DW. Effects of process time interval and heat treatment on the mechanical and microstructural properties of direct laser deposited 316L stainless steel. Materials Science and Engineering a-Structural Materials Properties Microstructure and Processing. 2015;644: 171–83.

[140] Tucho WM, Lysne VH, Austbø H, Sjolyst-Kverneland A, Hansen V. Investigation of effects of process parameters on microstructure and hardness of SLM manufactured SS316L. J Alloy Compd 2018;740:910–25.

[141] Elmer JW, Vaja J, Carpenter JS, Coughlin DR, Dvornak MJ, Hochanadel P, et al. Wire-Based Additive Manufacturing of Stainless Steel Components. Weld J 2020;99:S8–24.

[142] Raabe D, Tasan CC, Olivetti EA. Strategies for improving the sustainability of structural metals. Nature 2019;575:64–74.

[143] Ziętala M, Durejko T, Polański M, Kunce I, Płociński T, Zieliński W, et al. The microstructure, mechanical properties and corrosion resistance of 316L stainless steel fabricated using laser engineered net shaping. Materials science & engineering A, Structural materials : properties, microstructure and processing. 2016; 677:1–10.

[144] Zhong Y, Liu LF, Wikman S, Cui DQ, Shen ZJ. Intragranular cellular segregation network structure strengthening 316L stainless steel prepared by selective laser melting. J Nucl Mater 2016;470:170–8.

[145] Wang YM, Voisin T, McKeown JT, Ye JC, Calta NP, Li Z, et al. Additively manufactured hierarchical stainless steels with high strength and ductility. Nat Mater 2018;17:63 -+.

[146] Fayazfar H, Salarian M, Rogalsky A, Sarker D, Russo P, Paserin V, et al. A critical review of powder-based additive manufacturing of ferrous alloys: Process parameters, microstructure and mechanical properties. Mater Des 2018;144:98–128.

[147] Hong YJ, Zhou CS, Zheng YY, Zhang L, Zheng JY, Chen XY, et al. Formation of strain-induced martensite in selective laser melting austenitic stainless steel. Materials Science and Engineering a-Structural Materials Properties Microstructure and Processing. 2019;740:420–6.

[148] Shamsujjoha M, Agnew SR, Fitz-Gerald JM, Moore WR, Newman TA. High Strength and Ductility of Additively Manufactured 316L Stainless Steel Explained. Metallurgical and Materials Transactions a-Physical Metallurgy and Materials Science. 2018;49A:3011–27.

[149] Elmer JW, Fisher K, Gibbs G, Sengthay J, Urabe D. Post-build thermomechanical processing of wire arc additively manufactured stainless steel for improved mechanical properties and reduction of crystallographic texture. Addit Manuf 2022;50.

[150] Elmer JW, Gibbs G. Mechanical rolling and annealing of wire-arc additively manufactured stainless steel plates. Sci Technol Weld Join 2022;27:14–21.

[151] Abd-Elghany K, Bourell DL. Property evaluation of 304L stainless steel fabricated by selective laser melting. Rapid Prototyp J 2012;18:420–8.

[152] Yu HC, Yang JJ, Yin J, Wang ZM, Zeng XY. Comparison on mechanical anisotropies of selective laser melted Ti-6Al-4V alloy and 304 stainless steel. Materials Science and Engineering a-Structural Materials Properties Microstructure and Processing. 2017;695:92–100.

[153] Ghayoor M, Lee K, He YJ, Chang CH, Paul BK, Pasebani S. Selective laser melting of 304L stainless steel: Role of volumetric energy density on the microstructure, texture and mechanical properties. Addit Manuf 2020:32.

[154] Riemer A, Leuders S, Thone M, Richard HA, Troster T, Niendorf T. On the fatigue crack growth behavior in 316L stainless steel manufactured by selective laser melting. Eng Fract Mech 2014;120:15–25.

[155] Sun ZJ, Tan XP, Tor SB, Chua CK. Simultaneously enhanced strength and ductility for 3D-printed stainless steel 316L by selective laser melting. NPG Asia Mater 2018;10:127–36.

[156] Wei H, Mazumder J, DebRoy T. Evolution of solidification texture during additive manufacturing. Sci Rep 2015;5:1–7.

[157] Mukherjee T, DebRoy T. Mitigation of lack of fusion defects in powder bed fusion additive manufacturing. J Manuf Process 2018;36:442–9.

[158] Zhao H, DebRoy T. Macroporosity free aluminum alloy weldments through numerical simulation of keyhole mode laser welding. J Appl Phys 2003;93: 10089–96.

[159] Shrestha R, Simsiriwong J, Shamsaei N. Fatigue behavior of additive manufactured 316L stainless steel parts: Effects of layer orientation and surface roughness. Addit Manuf 2019;28:23–38.

[160] Yadollahi A, Shamsaei N. Additive manufacturing of fatigue resistant materials: Challenges and opportunities. Int J Fatigue 2017;98:14–31.

[161] Laleh M, Hughes AE, Yang S, Li JL, Xu W, Gibson I, et al. Two and three-dimensional characterisation of localised corrosion affected by lack-of-fusion pores in 316L stainless steel produced by selective laser melting. Corros 2020;165.

[162] Melia MA, Nguyen HDA, Rodelas JM, Schindelholz EJ. Corrosion properties of 304L stainless steel made by directed energy deposition additive manufacturing. Corros Sci 2019;152:20–30.

[163] Carlton HD, Haboub A, Gallegos GF, Parkinson DY, MacDowell AA. Damage evolution and failure mechanisms in additively manufactured stainless steel. Materials Science and Engineering a-Structural Materials Properties Microstructure and Processing. 2016;651:406–14.

[164] Zhu Y, Zou J, Chen X, Yang H. Tribology of selective laser melting processed parts: Stainless steel 316 L under lubricated conditions. Wear 2016;350–351: 46–55.

[165] Haghdadi N, Laleh M, Moyle M, Primig S. Additive manufacturing of steels: a review of achievements and challenges. J Mater Sci 2021;56:64–107.

[166] Trojan K, Ocelik V, Capek J, Cech J, Canelo-Yubero D, Ganev N, et al. Microstructure and Mechanical Properties of Laser Additive Manufactured H13 Tool Steel. Metals. 2022:12.

[167] Ge J, Fan N, Long Y, Lin J, Lei Y, Yin S. Investigation on H13 buildups produced with wire arc additive manufacturing: Deposition strategies-induced microstructural evolution and mechanical performances. J Alloy Compd 2021;860.

[168] Kahlert M, Brenne F, Vollmer M, Niendorf T. Influence of Microstructure and Defects on Mechanical Properties of AISI H13 Manufactured by Electron Beam Powder Bed Fusion. J Mater Eng Perform 2021;30:6895–904.

[169] Tanvir ANM, Ahsan MRU, Seo G, Bates B, Lee C, Liaw PK, et al. Phase stability and mechanical properties of wire plus arc additively manufactured H13 tool steel at elevated temperatures. J Mater Sci Technol 2021;67:80–94.

[170] Joshi SS, Sharma S, Mazumder S, Pantawane MV, Dahotre NB. Solidification and microstructure evolution in additively manufactured H13 steel via directed energy deposition: Integrated experimental and computational approach. J Manuf Process 2021;68:852–66.

[171] Abdel-latif M, Abdel-Ghany K, El-Mahallawy N, Mattar T. Effect of Laser Speed on Microstructure and Mechanical Properties of AISI H13 Tool Steel Prepared by Laser Powder Bed Fusion Process. J Mater Eng Perform 2021;30:8821–30.

[172] Lei F, Wen T, Yang F, Wang J, Fu J, Yang H, et al. Microstructures and Mechanical Properties of H13 Tool Steel Fabricated by Selective Laser Melting. Materials. 2022:15.

[173] Chen C, Yan K, Qin L, Zhang M, Wang X, Zou T, et al. Effect of Heat Treatment on Microstructure and Mechanical Properties of Laser Additively Manufactured AISI H13 Tool Steel. J Mater Eng Perform 2017;26:5577–89.

[174] Fonseca EB, Gabriel AHG, Araujo LC, Santos PLL, Campo KN, Lopes ESN. Assessment of laser power and scan speed influence on microstructural features and consolidation of AISI H13 tool steel processed by additive manufacturing. Addit Manuf 2020:34.

[175] Telasang G, Majumdar JD, Padmanabham G, Tak M, Manna I. Effect of laser parameters on microstructure and hardness of laser clad and tempered AISI H13 tool steel. Surf Coat Technol 2014;258:1108–18.

[176] Park JS, Park JH, Lee M-G, Sung JH, Cha KJ, Kim DH. Effect of Energy Input on the Characteristic of AISI H13 and D2 Tool Steels Deposited by a Directed Energy Deposition Process. Metallurgical and Materials Transactions a-Physical Metallurgy and Materials Science. 2016;47A:2529–35.

[177] Karmakar DP, Gopinath M, Nath AK. Effect of tempering on laser remelted AISI H13 tool steel. Surf Coat Technol 2019;361:136–49.

[178] Park JS, Lee M-G, Cho Y-J, Sung JH, Jeong M-S, Lee S-K, et al. Effect of Heat Treatment on the Characteristics of Tool Steel Deposited by the Directed Energy Deposition Process. Met Mater Int 2016;22:143–7.

[179] Zhao X, Lv Y, Dong S, Yan S, He P, Liu X, et al. The effect of thermal cycling on direct laser-deposited gradient H13 tool steel: Microstructure evolution, nanoprecipitation behaviour, and mechanical properties. Materials Today. Communications 2020:25.

[180] Mukherjee T, DebRoy T, Lienert TJ, Maloy SA, Hosemann P. Spatial and temporal variation of hardness of a printed steel part. Acta Mater 2021:209.

[181] Brooks J, Robino C, Headley T, Goods S, Griffith M. Microstructure and property optimization of LENS deposited H13 tool steel. 10th Solid Freeform Fabrication Symposium (SFF). Univ Texas, Austin, Tx1999. p. 375-82.

[182] Manvatkar VD, Gokhale AA, Reddy GJ, Savitha U, De A. Investigation on laser engineered net shaping of multilayered structures in H13 tool steel. J Laser Appl 2015;27.

[183] Asberg M, Fredriksson G, Hatami S, Fredriksson W, Krakhmalev P. Influence of post treatment on microstructure, porosity and mechanical properties of additive manufactured H13 tool steel. Materials Science and Engineering a-Structural Materials Properties Microstructure and Processing. 2019;742:584–9.

[184] Kempen K, Vrancken B, Buls S, Thijs L, Van Humbeeck J, Kruth J-P. Selective Laser Melting of Crack-Free High Density M2 High Speed Steel Parts by Baseplate Preheating. Journal of Manufacturing Science and Engineering-Transactions of the Asme. 2014:136.

[185] Ou W, Mukherjee T, Knapp GL, Wei Y, DebRoy T. Fusion zone geometries, cooling rates and solidification parameters during wire arc additive manufacturing. Int J Heat Mass Transf 2018;127:1084–94.

[186] Ou W, Knapp GL, Mukherjee T, Wei Y, DebRoy T. An improved heat transfer and fluid flow model of wire-arc additive manufacturing. Int J Heat Mass Transf 2021:167.

[187] Cui X, Zhang S, Zhang CH, Chen J, Zhang JB, Dong SY. Additive manufacturing of 24CrNiMo low alloy steel by selective laser melting: Influence of volumetric energy density on densification, microstructure and hardness. Materials Science and Engineering a-Structural Materials Properties Microstructure and Processing. 2021:809.

[188] Rodrigues TA, Duarte VR, Tomas D, Avila JA, Escobar JD, Rossinyol E, et al. In-situ strengthening of a high strength low alloy steel during Wire and Arc Additive Manufacturing (WAAM). Addit Manuf 2020:34.

[189] Rafieazad M, Ghaffari M, Nemani AV, Nasiri A. Microstructural evolution and mechanical properties of a low-carbon low-alloy steel produced by wire arc additive manufacturing. Int J Adv Manuf Technol 2019;105:2121–34.

[190] Rafieazad M, Nemani AV, Ghaffari M, Nasiri A. On Microstructure and Mechanical Properties of a Low-Carbon Low-Alloy Steel Block Fabricated by Wire Arc Additive Manufacturing. J Mater Eng Perform 2021;30:4937–45.

[191] Duarte VR, Rodrigues TA, Schell N, Santos TG, Oliveira JP. Miranda RM. Wire and Arc Additive Manufacturing of High-Strength Low-Alloy Steel: Microstructure and Mechanical Properties. Advanced Engineering Materials; 2021. p. 23.

[192] Jiang MG, Chen ZW, Tong JD, Liu CY, Xu G, Liao HB, et al. Strong and ductile reduced activation ferritic/martensitic steel additively manufactured by selective laser melting. Materials Research Letters. 2019;7:426–32.

[193] Liu CY, Tong JD, Jiang MG, Chen ZW, Xu G, Liao HB, et al. Effect of scanning strategy on microstructure and mechanical properties of selective laser melted reduced activation ferritic/martensitic steel. Materials Science and Engineering a-Structural Materials Properties Microstructure and Processing. 2019:766.

[194] Xia Z, Xu J, Shi J, Shi T, Sun C, Qiu D. Microstructure evolution and mechanical properties of reduced activation steel manufactured through laser directed energy deposition. Addit Manuf 2020:33.

[195] Jiang M, Liu C, Chen Z, Wang P, Liao H, Zhao D, et al. Enhanced strength-ductility synergy of selective laser melted reduced activation ferritic/martensitic steel via heterogeneous microstructure modification. Materials Science and Engineering a-Structural Materials Properties Microstructure and Processing. 2021:801.

[196] Zhong W, Sridharan N, Isheim D, Field KG, Yang Y, Terrani K, et al. Microstructures and mechanical properties of a modified 9Cr ferritic-martensitic steel in the as-built condition after additive manufacturing. J Nucl Mater 2021:545.

[197] Graning T, Sridharan N. Benchmarking a 9Cr-2WVTa Reduced Activation Ferritic Martensitic Steel Fabricated via Additive Manufacturing. Metals. 2022:12.

[198] Guo L, Zhang L, Andersson J, Ojo O. Additive manufacturing of 18% nickel maraging steels: Defect, structure and mechanical properties: A review. J Mater Sci Technol 2022;120:227–52.

[199] Bai Y, Yang Y, Wang D, Zhang M. Influence mechanism of parameters process and mechanical properties evolution mechanism of maraging steel 300 by selective laser melting. Materials Science and Engineering a-Structural Materials Properties Microstructure and Processing. 2017;703:116–23.

[200] Tan C, Zhou K, Kuang M, Ma W, Kuang T. Microstructural characterization and properties of selective laser melted maraging steel with different build directions. Sci Technol Adv Mater 2018;19:746–58.

[201] Jaegle EA, Choi P-P, Van Humbeeck J, Raabe D. Precipitation and austenite reversion behavior of a maraging steel produced by selective laser melting. J Mater Res 2014;29:2072–9.

[202] Bodziak S, Al-Rubaie KS, Dalla Valentina L, Lafratta FH, Santos EC, Zanatta AM, et al. Precipitation in 300 grade maraging steel built by selective laser melting: Aging at 510 degrees C for 2 h. Mater Charact 2019;151:73–83.

[203] Casalino G, Campanelli SL, Contuzzi N, Ludovico AD. Experimental investigation and statistical optimisation of the selective laser melting process of a maraging steel. Opt Laser Technol 2015;65:151–8.

[204] Casati R, Lemke JN, Tuissi A, Vedani M. Aging Behaviour and Mechanical Performance of 18-Ni 300 Steel Processed by Selective Laser Melting. Metals. 2016;6.

[205] Jaegle EA, Sheng Z, Kuernsteiner P, Ocylok S, Weisheit A, Raabe D. Comparison of Maraging Steel Micro- and Nanostructure Produced Conventionally and by Laser Additive Manufacturing. Materials. 2017:10.

[206] Kempen K, Yasa E, Thijs L, Kruth JP, Van Humbeeck J. Microstructure and mechanical properties of Selective Laser Melted 18Ni-300 steel. 6th International WLT Conference on Lasers in Manufacturing (LiM). Munich, GERMANY2011. p. 255-63.

[207] Tan C, Zhou K, Tong X, Huang Y, Li J, Ma W, et al. Microstructure and Mechanical Properties of 18Ni-300 Maraging Steel Fabricated by Selective Laser Melting. 6th International Conference on Advanced Design and Manufacturing Engineering (ICADME). Zhuhai, PEOPLES R CHINA2016. p. 404-10.

[208] Mooney B, Kourousis KI, Raghavendra R. Plastic anisotropy of additively manufactured maraging steel: Influence of the build orientation and heat treatments. Addit Manuf 2019;25:19–31.

[209] Chen C, Yan X, Xie Y, Kuang R, Kuang M, Ma W, et al. Microstructure evolution and mechanical properties of maraging steel 300 fabricated by cold spraying. Materials Science and Engineering a-Structural Materials Properties Microstructure and Processing. 2019;743:482–93.

[210] Takata N, Nishida R, Suzuki A, Kobashi M, Kato M. Crystallographic Features of Microstructure in Maraging Steel Fabricated by Selective Laser Melting. Metals. 2018;8.

[211] Wang X, Yang D, Huang Y, Zhou Q, Fan J, Wang K. Microstructure and Mechanical Properties of As-Deposited and Heat-Treated 18Ni (350) Maraging Steel Fabricated by Gas Metal Arc-Based Wire and Arc Additive Manufacturing. J Mater Eng Perform 2021;30:6972–81.

[212] Yang G, Deng F, Zhou S, Wu B, Qin L. Microstructure and mechanical properties of a novel Cu-reinforced maraging steel for wire arc additive manufacturing. Materials Science and Engineering A-Structural Materials Properties Microstructure and Processing 2021;825:141894.

[213] Yang G, Deng F, Zhou S, Wu B, Qin L, Zheng J. Influence of shielding gas nitrogen content on the microstructure and mechanical properties of Cu-reinforced maraging steel fabricated by wire arc additive manufacturing 2022;832:142463.

[214] Porro M, Zhang B, Parmar A, Shin YC. Data-Driven Modeling of Mechanical Properties for 17–4 PH Stainless Steel Built by Additive Manufacturing. Integrating Materials and Manufacturing Innovation. 2022;11:241–55.

[215] Ghaffari M, Vahedi Nemani A, Nasiri A. Microstructure and mechanical behavior of PH 13-8Mo martensitic stainless steel fabricated by wire arc additive manufacturing. Additive Manufacturing 2022;49:102374.

[216] Guo C, Hu R, Chen F. Microstructure and performances for 15–5 PH stainless steel fabricated through the wire-arc additive manufacturing technology. Mater Technol 2021;36:831–42.

[217] Nong XD, Zhou XL, Wang YD, Yu L, Li JH. Effects of geometry, location, and direction on microstructure and mechanical properties of 15–5PH stainless steel fabricated by directed energy deposition. Materials Science and Engineering a-Structural Materials Properties Microstructure and Processing. 2021;821.

[218] Nong XD, Zhou XL. Effect of scanning strategy on the microstructure, texture, and mechanical properties of 15–5PH stainless steel processed by selective laser melting. Mater Charact 2021;174.

[219] Huang EW, Lee SY, Jain J, Tong Y, An K, Tsou N-T, et al. Hardening steels by the generation of transient phase using additive manufacturing. Intermetallics 2019;109:60–7.

[220] Rashid R, Masood SH, Ruan D, Palanisamy S, Rashid RAR, Brandt M. Effect of scan strategy on density and metallurgical properties of 17–4PH parts printed by Selective Laser Melting (SLM). J Mater Process Technol 2017;249:502–11.

[221] Jiang D, Birbilis N, Hutchinson CR, Brameld M. On the Microstructure and Electrochemical Properties of Additively Manufactured Duplex Stainless Steels Produced Using Laser-Powder Bed Fusion. Corrosion 2020;76:13.

[222] Saeidi K, Kevetkova L, Lofaj F, Shen Z. Novel ferritic stainless steel formed by laser melting from duplex stainless steel powder with advanced mechanical properties and high ductility. Mater Sci Enga-Structural Materials Properties Microstructure and Processing. 2016;665:59–65.

[223] Davidson K, Singamneni S. Selective Laser Melting of Duplex Stainless Steel Powders: An Investigation. Mater Manuf Process 2016;31:1543–55.

[224] Iams AD, Keist JS, Palmer TA. Formation of Austenite in Additively Manufactured and Post-Processed Duplex Stainless Steel Alloys. Metallurgical and Materials Transactions a-Physical Metallurgy and Materials Science. 2020;51:982–99.

[225] Sander G, Thomas S, Cruz V, Jurg M, Birbilis N, Gao X, et al. On The Corrosion and Metastable Pitting Characteristics of 316L Stainless Steel Produced by Selective Laser Melting. J Electrochem Soc 2017;164:C250–7.

[226] Eriksson M, Lervaringg M, Soslashrensen C, Robertstad A, Broslashnstad BM, Nyhus B, et al. Additive manufacture of superduplex stainless steel using WAAM. MATEC Web Conf (France). 2018;188:03014 (8 pp.)- (8 pp.).

[227] Wittig B, Zinke M, Juttner S. Influence of arc energy and filler metal composition on the microstructure in wire arc additive manufacturing of duplex stainless steels. Welding in the World. 2021;65:47–56.

[228] Saeidi K, Alvi S, Lofaj F, Petkov VI, Akhtar F. Advanced Mechanical Strength in Post Heat Treated SLM 2507 at Room and High Temperature Promoted by Hard/Ductile Sigma Precipitates. Metals. 2019;9.

[229] Murkute P, Pasebani S, Isgor OB. Metallurgical and Electrochemical Properties of Super Duplex Stainless Steel Clads on Low Carbon Steel Substrate produced with Laser Powder Bed Fusion. Sci Rep 2020;10.

[230] Zhang X, Wang K, Zhou Q, Kong J, Peng Y, Ding J, et al. Element partitioning and electron backscatter diffraction analysis from feeding wire to as-deposited microstructure of wire and arc additive manufacturing with super duplex stainless steel. Materials Science and Engineering A-Structural Materials Properties Microstructure and Processing. 2020;773:138856.

[231] Papula S, Song M, Pateras A, Chen X-B, Brandt M, Easton M, et al. Selective Laser Melting of Duplex Stainless Steel 2205: Effect of Post-Processing Heat Treatment on Microstructure, Mechanical Properties, and Corrosion Resistance. Materials. 2019;12.

[232] Zagade PR, Gautham BP, De A, DebRoy T. Scaling analysis for rapid estimation of lack of fusion porosity in laser powder bed fusion. Science and Technology of Welding and Joining 2023;28:372–80.

[233] Knezovic N, Garasic I, Juric I. Influence of the Interlayer Temperature on Structure and Properties of Wire and Arc Additive Manufactured Duplex Stainless Steel Product. Materials. 2020;13:16.

[234] Ramkumar KD, Kumar PSG, Radhakrishna VS, Kothari K, Sridhar R, Arivazhagan N, et al. Studies on microstructure and mechanical properties of keyhole mode Nd:YAG laser welded Inconel 625 and duplex stainless steel, SAF 2205. J Mater Res 2015;30:3288–98.

[235] Nigon GN, Isgor OB, Pasebani S. The effect of annealing on the selective laser melting of 2205 duplex stainless steel: Microstructure, grain orientation, and manufacturing challenges. Opt Laser Technol 2021;134:13.

[236] Jiang M, Chen YB, Chen X, Toa W, Debroy T. Enhanced Penetration Depth during Reduced Pressure Keyhole-Mode Laser Welding Modeling and experiments took place to understand deeper laser keyholes at lower pressures. Weld J 2020;99:110–23.

[237] Wu BT, Pan ZX, Ding DH, Cuiuri D, Li HJ, Xu J, et al. A review of the wire arc additive manufacturing of metals: properties, defects and quality improvement. J Manuf Process 2018;35:127–39.

[238] Du Y, Mukherjee T, DebRoy T. Physics-informed machine learning and mechanistic modeling of additive manufacturing to reduce defects. Appl Mater Today 2021;24:12.

[239] Narasimharaju SR, Zeng WH, See TL, Zhu ZC, Scott P, J. x,, et al. A comprehensive review on laser powder bed fusion of steels: Processing, microstructure, defects and control methods, mechanical properties, current challenges and future trends. J Manuf Process 2022;75:375–414.

[240] Hearn W. Laser Based Powder Bed Fusion of Plain Carbon and Low-Alloy Steels. Microstructure and Processability: Chalmers Tekniska Hogskola (Sweden) 2021.

[241] Hearn W, Hryha E. Effect of Carbon Content on the Processability of Fe-C Alloys Produced by Laser Based Powder Bed Fusion. Front Mater 2022;8:10.

[242] Navarro M, Matar A, Diltemiz SF. Eshraghi MJJoM, Processing M. Development of a low-cost wire arc additive manufacturing system. 2021;6:3.

[243] Paul AR, Mukherjee M, Raja M, Kundu S, Chatterjee A. Development of near homogeneous mechanical properties in wire arc additive manufacturing process for near-net shaped structural component of low-carbon steel. Proc Inst Mech Eng Part C-J Eng Mech Eng Sci. 2022;236:3497–511.

[244] Lu X, Zhou YF, Xing XL, Shao LY, Yang QX, Gao SY. Open-source wire and arc additive manufacturing system: formability, microstructures, and mechanical properties. Int J Adv Manuf Technol 2017;93:2145–54.

[245] Alhuzaim A. Madigan RBJIJIER. Measurement and Simulation of Low Carbon Steel Alloy Deposit Temperature in plasma Arc Welding Additive Manufacturing. 2014;2:113–27.

[246] Nakamoto T, Shirakawa N, Miyata Y, Inui H. Selective laser sintering of high carbon steel powders studied as a function of carbon content. J Mater Process Technol 2009;209:5653–60.

[247] Rombouts M, Kruth JP, Froyen L, Mercelis P. Fundamentals of selective laser melting of alloyed steel powders. Cirp Annals-Manufacturing Technology. 2006;55:187–92.

[248] Simchi A, Pohl H. Direct laser sintering of iron-graphite powder mixture. Materials Science and Engineering a-Structural Materials Properties Microstructure and Processing. 2004;383:191–200.

[249] Wang JQ, Liu S, Xu B, Zhang JY, Sun MY, Li DAZ. Research progress on preparation technology of oxide dispersion strengthened steel for nuclear energy. Int J Extreme Manuf. 2021;3:14.

[250] Wang Y, Wang B, Luo L, Li B, Liu T, Zhao J, et al. Laser-based powder bed fusion of pre-alloyed oxide dispersion strengthened steel containing yttrium. Additive Manufacturing 2022;58:103018.

[251] Ghayoor M, Mirzababaei S, Lee K, He Y, Chang C-h, Paul BK, et al. Strengthening of 304L stainless steel by addition of yttrium oxide and grain refinement during selective laser melting. 2019 International Solid Freeform Fabrication Symposium: University of Texas at Austin; 2019.

[252] Arkhurst BM, Bae JH, Na MY, Chang HJ, Kim HG, Kim IH, et al. Effect of tellurium on the microstructure and mechanical properties of Fe-14Cr oxide-dispersion-strengthened steels produced by additive manufacturing. J Mater Sci Technol 2021;95:114–26.

[253] Zhong Y, Liu LF, Zou J, Li XD, Cui DQ, Shen ZJ. Oxide dispersion strengthened stainless steel 316L with superior strength and ductility by selective laser melting. J Mater Sci Technol 2020;42:97–105.

[254] Streubel R, Wilms MB, Donate-Buendia C, Weisheit A, Barcikowski S, Schleifenbaum JH, et al. Depositing laser-generated nanoparticles on powders for additive manufacturing of oxide dispersed strengthened alloy parts via laser metal deposition. Jpn J Appl Phys. 2018;57:5.

[255] Donate-Buendia C, Fromel F, Wilms MB, Streubel R, Tenkamp J, Hupfeld T, et al. Oxide dispersion-strengthened alloys generated by laser metal deposition of laser-generated nanoparticle-metal powder composites. Mater Des 2018;154:360–9.

[256] Haodong J, Zhangjian Z, Shaofu L. A new strategy for additive manufacturing ODS steel using Y-containing gas atomized powder. Mater Charact 2022;187.

[257] Qiu C. A new approach to synthesise high strength nano-oxide dispersion strengthened alloys. J Alloy Compd 2019;790:1023–33.

[258] Yan F, Xiong W, Faierson E, Olson GB. Characterization of nano-scale oxides in austenitic stainless steel processed by powder bed fusion. Scr Mater 2018;155:104–8.

[259] Vasquez E, Giroux P-F, Lomello F, Chniouel A, Maskrot H, Schuster F, et al. Elaboration of oxide dispersion strengthened Fe-14Cr stainless steel by selective laser melting. J Mater Process Technol 2019;267:403–13.

[260] Horn T, Rock C, Kaoumi D, Anderson I, White E, Prost T, et al. Laser powder bed fusion additive manufacturing of oxide dispersion strengthened steel using gas atomized reaction synthesis powder. 2022;216:110574.

[261] Donate-Buendia C, Kuernsteiner P, Stern F, Wilms MB, Streubel R, Kusoglu IM, et al. Microstructure formation and mechanical properties of ODS steels built by laser additive manufacturing of nanoparticle coated iron-chromium powders. Acta Mater 2021;206.

[262] Zhai W, Zhou W, Nai SML, Wei J. Characterization of nanoparticle mixed 316 L powder for additive manufacturing. J Mater Sci Technol 2020;47:162–8.

[263] Sun X, Chen F, Huang H, Lin J, Tang X. Effects of interfaces on the helium bubble formation and radiation hardening of an austenitic stainless steel achieved by additive manufacturing. Appl Surf Sci 2019;467:1134–9.

[264] Zhou X, An Z, Shen Z, Liu W, Yao C. Particles control in selective laser melting in-situ oxide dispersion strengthened method. 1st International Conference on New Material and Chemical Industry (NMCI). Sanya, PEOPLES R CHINA2016.

[265] Tatlock GJ, Dawson K, Boegelein T, Moustoukas K, Jones AR. High resolution microstructural studies of the evolution of nano-scale, yttrium-rich oxides in ODS steels subjected to ball milling, selective laser melting or friction stir welding. Conference on Advances in Refractory and Reactive Metals and Alloys (ARRMA). Mumbai, INDIA2016. p. 3086-93.

[266] Saeidi K, Kvetkova L, Lofajc F, Shen Z. Austenitic stainless steel strengthened by the in situ formation of oxide nanoinclusions. RSC Adv 2015;5:20747–50.

[267] Hunt RM, Kramer KJ, El-Dasher B. Selective laser sintering of MA956 oxide dispersion strengthened steel. J Nucl Mater 2015;464:80–5.

[268] Gao R, Zeng L, Ding H, Zhang T, Wang X, Fang Q. Characterization of oxide dispersion strengthened ferritic steel fabricated by electron beam selective melting. Mater Des 2016;89:1171–80.

[269] Boegelein T, Dryepondt SN, Pandey A, Dawson K, Tatlock GJ. Mechanical response and deformation mechanisms of ferritic oxide dispersion strengthened steel structures produced by selective laser melting. Acta Mater 2015;87:201–15.

[270] Walker JC, Berggreen KM, Jones AR, Sutcliffe CJ. Fabrication of Fe-Cr-Al Oxide Dispersion Strengthened PM2000 Alloy Using Selective Laser Melting. Adv Eng Mater 2009;11:541–6.

[271] Lehnert R, Wagner R, Burkhardt C, Clausnitzer P, Weidner A, Wendler M, et al. Microstructural and mechanical characterization of high-alloy quenching and partitioning TRIP steel manufactured by electron beam melting. Materials Science and Engineering a-Structural Materials Properties Microstructure and Processing. 2020;794.

[272] Sander J, Hufenbach J, Bleckmann M, Giebeler L, Wendrock H, Oswald S, et al. Selective laser melting of ultra-high-strength TRIP steel: processing, microstructure, and properties. J Mater Sci 2017;52:4944–56.

[273] Todaro CJ, Easton MA, Qiu D, Zhang D, Bermingham MJ, Lui EW, et al. Grain structure control during metal 3D printing by high-intensity ultrasound. Nature. Communications 2020;11.

[274] Weingarten C, Buchbinder D, Pirch N, Meiners W, Wissenbach K, Poprawe R. Formation and reduction of hydrogen porosity during selective laser melting of AlSi10Mg. J Mater Process Technol 2015;221:112–20.

[275] Tang M, Pistorius PC. Oxides, porosity and fatigue performance of AlSi10Mg parts produced by selective laser melting. Int J Fatigue 2017;94:192–201.

[276] Schuster M, De Luca A, Widmer R, Maeder X, Leinenbach C. Processability, microstructure and precipitation of a Zr-modified 2618 aluminium alloy fabricated by laser powder bed fusion. J Alloy Compd 2022;913:165346.

[277] Leijon F, Johansson E, Lu J, Aling B, Skjervold S, Moverare J. Investigation of Ti1− x (Zr, Ta, V, W) xB2 and Al3Ti1− x (Zr, V) x grain refiners in additively manufactured Al-2 wt% Cu alloys by a high throughput method. Mater Des 2022;222:111093.

[278] Guo Y, Wei W, Shi W, Zhou X, Wen S, Wu X, et al. Microstructure and mechanical properties of Al-Mg-Mn-Er-Zr alloys fabricated by laser powder bed fusion. Mater Des 2022;222:111064.

[279] Qbau N, Nam ND, Ca NX, Hien NT. The crack healing effect of scandium in aluminum alloys during laser additive manufacturing. J Manuf Process 2020;50:241–6.

[280] Zhang H, Zhu HH, Qi T, Hu ZH, Zeng XY. Selective laser melting of high strength Al-Cu-Mg alloys: Processing, microstructure and mechanical properties. Materials Science and Engineering a-Structural Materials Properties Microstructure and Processing. 2016;656:47–54.

[281] Zhang H, Zhu H, Nie X, Yin J, Hu Z, Zeng X. Effect of Zirconium addition on crack, microstructure and mechanical behavior of selective laser melted Al-Cu-Mg alloy. Scr Mater 2017;134:6–10.

[282] Li G, Ruan G, Huang Y, Xu Z, Li X, Guo C, et al. Facile and cost-effective approach to additively manufacture crack-free 7075 aluminum alloy by laser powder bed fusion. J Alloy Compd 2022;928:167097.

[283] Croteau JR, Griffiths S, Rossell MD, Leinenbach C, Kenel C, Jansen V, et al. Microstructure and mechanical properties of Al-Mg-Zr alloys processed by selective laser melting. Acta Mater 2018;153:35–44.

[284] Griffiths S, Rossell MD, Croteau J, Vo NQ, Dunand DC, Leinenbach C. Effect of laser rescanning on the grain microstructure of a selective laser melted Al-Mg-Zr alloy. Mater Charact 2018;143:34–42.

[285] Schmidtke K, Palm F, Hawkins A, Emmelmann C. Process and Mechanical Properties: Applicability of a Scandium modified Al-alloy for Laser Additive Manufacturing. 6th International WLT Conference on Lasers in Manufacturing (LiM). Munich, GERMANY2011. p. 369-74.

[286] Spierings AB, Dawson K, Voegtlin M, Palm F, Uggowitzer PJ. Microstructure and mechanical properties of as-processed scandium-modified aluminium using selective laser melting. Cirp Annals-Manufacturing Technology. 2016;65:213–6.

[287] Spierings AB, Dawson K, Heeling T, Uggowitzer PJ, Schaublin R, Palm F, et al. Microstructural features of Sc- and Zr-modified Al-Mg alloys processed by selective laser melting. Mater Des 2017;115:52–63.

[288] Spierings AB, Dawson K, Kern K, Palm F, Wegener K. SLM-processed Sc- and Zr- modified Al-Mg alloy: Mechanical properties and microstructural effects of heat treatment. Materials Science and Engineering a-Structural Materials Properties Microstructure and Processing. 2017;701:264–73.

[289] Gutierrez A, Lippold J. A proposed mechanism for equiaxed grain formation along the fusion boundary in aluminum-copper-lithium alloys. Weld J 1998;77.

[290] Kostrivas A, Lippold JC. A method for studying weld fusion boundary microstructure evolution in aluminum alloys. Weld J 2000;79:1S–8S.

[291] Sun T, Xiao Y, Luo G, Yang H, Wu Y, Wang M, et al. Roadmap to improve the printability of a non-castable alloy for additive manufacturing. Metall Mater Trans A 2022;53:2780–95.

[292] Liu X, Liu Y, Zhou Z, Zhan Q. Enhanced strength and ductility in Al-Zn-Mg-Cu alloys fabricated by laser powder bed fusion using a synergistic grain-refining strategy. J Mater Sci Technol 2022;124:41–52.

[293] Liu X, Liu Y, Zhou Z, Luo W, Zeng Z. Enhanced printability and strength of unweldable AA2024-based nanocomposites fabricated by laser powder bed fusion via nano-TiC-induced grain refinement. Mater Sci Eng A 2022;856:144010.
[294] Fan Z, Li C, Yang H, Liu Z. Effects of TiC nanoparticle inoculation on the hot-tearing cracks and grain refinement of additively-manufactured AA2024 Al alloys. J Mater Res Technol 2022;19:194–207.
[295] Sokoluk M, Yuan J, Pan S, Li X. Nanoparticles enabled mechanism for hot cracking elimination in aluminum alloys. Metall Mater Trans A 2021;52:3083–96.
[296] Zhou S, Su Y, Wang H, Enz J, Ebel T, Yan M. Selective laser melting additive manufacturing of 7xxx series Al-Zn-Mg-Cu alloy: Cracking elimination by co-incorporation of Si and TiB2. Addit Manuf 2020;36:101458.
[297] Lin TC, Cao CZ, Sokoluk M, Jiang L, Wang X, Schoenung JM, et al. Aluminum with dispersed nanoparticles by laser additive manufacturing. Nature. Communications 2019;10.
[298] Mair P, Kaserer L, Braun J, Weinberger N, Letofsky-Papst I, Leichtfried G. Microstructure and mechanical properties of a TiB 2-modified Al-Cu alloy processed by laser powder-bed fusion. Materials Science and Engineering a-Structural Materials Properties Microstructure and Processing. 2021;799.
[299] Zhao T, Dahmen M, Cai W, Alkhayat M, Schaible J, Albus P, et al. Laser metal deposition for additive manufacturing of AA5024 and nanoparticulate TiC modified AA5024 alloy composites prepared with balling milling process. Opt Laser Technol 2020;131.
[300] Oropeza D, Hofmann DC, Williams K, Firdosy S, Bordeenithikasem P, Sokoluk M, et al. Welding and additive manufacturing with nanoparticle-enhanced aluminum 7075 wire. J Alloy Compd 2020;834.
[301] Jin P, Liu Y, Sun Q. Evolution of crystallographic orientation, columnar to equiaxed transformation and mechanical properties realized by adding TiCps in wire and arc additive manufacturing 2219 aluminum alloy. Addit Manuf 2021;39.
[302] Zhang C, Gao M, Zeng X. Workpiece vibration augmented wire arc additive manufacturing of high strength aluminum alloy. J Mater Process Technol 2019; 271:85–92.
[303] Fang X, Zhang L, Chen G, Huang K, Xue F, Wang L, et al. Microstructure evolution of wire-arc additively manufactured 2319 aluminum alloy with interlayer hammering. Materials Science and Engineering a-Structural Materials Properties Microstructure and Processing. 2021;800.
[304] Sun R, Li L, Zhu Y, Guo W, Peng P, Cong B, et al. Microstructure, residual stress and tensile properties control of wire-arc additive manufactured 2319 aluminum alloy with laser shock peening. J Alloy Compd 2018;747:255–65.
[305] Derekar K, Lawrence J, Melton G, Addison A, Xiang Z, Lei X. Influence of Interpass Temperature on Wire Arc Additive Manufacturing (WAAM) of Aluminium Alloy Components. MATEC Web Conf (France). 2019;269:05001 (6 pp.)- (6 pp.).
[306] Chen F, Yang Y, Feng H. Regional Control and Optimization of Heat Input during CMT by Wire Arc Additive Manufacturing: Modeling and Microstructure Effects. Materials. 2021;14.
[307] Wang D, Lu J, Tang S, Yu L, Fan H, Ji L, et al. Reducing Porosity and Refining Grains for Arc Additive Manufacturing Aluminum Alloy by Adjusting Arc Pulse Frequency and Current. Materials. 2018;11.
[308] Zhang C, Li Y, Gao M, Zeng X. Wire arc additive manufacturing of Al-6Mg alloy using variable polarity cold metal transfer arc as power source. Materials Science and Engineering a-Structural Materials Properties Microstructure and Processing. 2018;711:415–23.
[309] Derekar KS. A review of wire arc additive manufacturing and advances in wire arc additive manufacturing of aluminium. Mater Sci Technol 2018;34:895–916.
[310] Derekar KS, Addison A, Joshi SS, Zhang X, Lawrence J, Xu L, et al. Effect of pulsed metal inert gas (pulsed-MIG) and cold metal transfer (CMT) techniques on hydrogen dissolution in wire arc additive manufacturing (WAAM) of aluminium. Int J Adv Manuf Technol 2020;107:311–31.
[311] Gierth M, Henckell P, Ali Y, Scholl J, Bergmann JP. Wire Arc Additive Manufacturing (WAAM) of Aluminum Alloy AlMg5Mn with Energy-Reduced Gas Metal Arc Welding (GMAW). Materials. 2020;13.
[312] Klein T, Schnall M. Control of macro-/microstructure and mechanical properties of a wire-arc additive manufactured aluminum alloy. Int J Adv Manuf Technol 2020;108:235–44.
[313] Holesinger TG, Carpenter JS, Lienert TJ, Patterson BM, Papin PA, Swenson H, et al. Characterization of an Aluminum Alloy Hemispherical Shell Fabricated via Direct Metal Laser Melting. JOM 2016;68:1000–11.
[314] Dong M, Zhao Y, Li Q, Fei Y, Zhao T, Wang F, et al. Microstructure Evolution and Mechanical Property Anisotropy of Wire and Arc-Additive-Manufactured Wall Structure Using ER2319 Welding Wires. J Mater Eng Perform 2021;30:258–68.
[315] Yang Q, Xia C, Deng Y, Li X, Wang H. Microstructure and Mechanical Properties of AlSi7Mg0.6 Aluminum Alloy Fabricated by Wire and Arc Additive Manufacturing Based on Cold Metal Transfer (WAAM-CMT). Materials. 2019;12.
[316] Brice C, Shenoy R, Kral M, Buchannan K. Precipitation behavior of aluminum alloy 2139 fabricated using additive manufacturing. Materials Science and Engineering a-Structural Materials Properties Microstructure and Processing. 2015;648:9–14.
[317] Hung C-H, Li Y, Sutton A, Chen W-T, Gong X, Pan H, et al. Aluminum Parts Fabricated by Laser-Foil-Printing Additive Manufacturing: Processing, Microstructure, and Mechanical Properties. Materials. 2020;13.
[318] Svetlizky D, Zheng B, Buta T, Zhou Y, Golan O, Breiman U, et al. Directed energy deposition of Al 5xxx alloy using Laser Engineered Net Shaping (LENS (R)). Mater Des 2020;192.
[319] Buchbinder D, Schleifenbaum H, Heidrich S, Meiners W, Bultmann J. High Power Selective Laser Melting (HP SLM) of Aluminum Parts. 6th International WLT Conference on Lasers in Manufacturing (LiM). Munich, GERMANY2011. p. 271-8.
[320] Kempen K, Thijs L, Van Humbeeck J, Kruth JP. Mechanical properties of AlSi10Mg produced by Selective Laser Melting. 7th Conference on Laser Assisted Net shape Engineering (LANE) / International Conference on Photonic Technologies. Furth, GERMANY2012. p. 439-46.
[321] Aboulkhair NT, Tuck C, Ashcroft I, Maskery I, Everitt NM. On the Precipitation Hardening of Selective Laser Melted AlSi10Mg. Metallurgical and Materials Transactions a-Physical Metallurgy and Materials Science. 2015;46A:3337–41.
[322] Haselhuhn AS, Buhr MW, Wijnen B, Sanders PG, Pearce JM. Structure-property relationships of common aluminum weld alloys utilized as feedstock for GMAW-based 3-D metal printing. Materials Science and Engineering a-Structural Materials Properties Microstructure and Processing. 2016;673:511–23.
[323] Tang G, Gould BJ, Ngowe A, Rollett AD. An updated index including toughness for hot-cracking susceptibility. Metall Mater Trans A 2022;53:1486–98.
[324] Mishra RS, Thapliyal S. Design approaches for printability-performance synergy in Al alloys for laser-powder bed additive manufacturing. Mater Des 2021;204: 109640.
[325] Kou S. A Simple Index for Predicting the Susceptibility to Solidification Cracking. Weld J 2015;94:374S–S388.
[326] Fisher DJ, Kurz W. Department of Materials. Switzerland: EPFL-Swiss Institute of Technology Lausanne; 1978.
[327] Computherm L. Pandat—Phase Diagram Calculation Software Package for Multicomponent Systems. Madison, WI: Computherm LLC; 2001.
[328] PanAluminium – Thermodynamic database for Commercial Aluminum Alloys. Computherm LLC, Madison, WI. 2020.
[329] Kou S. Solidification cracking susceptibility associated with a teardrop-shaped weld pool. Sci Technol Weld Join 2021;26:341–7.
[330] Liu JW, Duarte HP, Kou S. Evidence of back diffusion reducing cracking during solidification. Acta Mater 2017;122:47–59.
[331] Xia CZ, Kou SD. Calculating the Susceptibility of Carbon Steels to Solidification Cracking During Welding. Metallurgical and Materials Transactions B-Process Metallurgy and Materials Processing Science. 2021;52:460–9.
[332] Hu B, Li D, Li Z, Xu J, Wang X, Zeng X. Hot Tearing Behavior in Double Ternary Eutectic Alloy System: Al-Mg-Si Alloys. Metallurgical and Materials Transactions a-Physical Metallurgy and Materials Science. 2021;52:789–805.
[333] Riener K, Pfalz T, Funcke F, Leichtfried G. Processability of high-strength aluminum 6182 series alloy via laser powder bed fusion (LPBF). Int J Adv Manuf Technol 2022;1–15.
[334] Elambasseril J, Benoit MJ, Zhu S, Easton MA, Lui E, Brice CA, et al. Effect of process parameters and grain refinement on hot tearing susceptibility of high strength aluminum alloy 2139 in laser powder bed fusion. Progress in Additive Manufacturing. 2022;7:887–901.
[335] Stopyra W, Gruber K, Smolina I, Kurzynowski T, Kuźnicka B. Laser powder bed fusion of AA7075 alloy: Influence of process parameters on porosity and hot cracking. Addit Manuf 2020;35:101270.
[336] Li G, Brodu E, Soete J, Wei H, Liu T, Yang T, et al. Exploiting the rapid solidification potential of laser powder bed fusion in high strength and crack-free Al-Cu-Mg-Mn-Zr alloys. Addit Manuf 2021;47:102210.

[337] Dreano A, Favre J, Desrayaud C, Chanin-Lambert P, Wimmer A, Zaeh MF. Computational design of a crack-free aluminum alloy for additive manufacturing. Addit Manuf 2022;55:102876.
[338] Liu JW, Kou SD. Effect of diffusion on susceptibility to cracking during solidification. Acta Mater 2015;100:359–68.
[339] Liu JW, Kou SD. Crack susceptibility of binary aluminum alloys during solidification. Acta Mater 2016;110:84–94.
[340] Liu JW, Kou S. Susceptibility of ternary aluminum alloys to cracking during solidification. Acta Mater 2017;125:513–23.
[341] Deng S, Zhao H, Li R, Shao J, Li J, Qi L, et al. Composition design of low hot-cracking susceptibility of Al-Zn-Mg-Sc alloy and its formability during laser additive manufacturing. Mater Charact 2022;193:112304.
[342] Zhuravlev E, Milkereit B, Yang B, Heiland S, Vieth P, Voigt M, et al. Assessment of AlZnMgCu alloy powder modification for crack-free laser powder bed fusion by differential fast scanning calorimetry. Mater Des 2021;204:109677.
[343] Li N, Wang T, Zhang L, Zhang L. Crack initiation mechanism of laser powder bed fusion additive manufactured Al-Zn-Mg-Cu alloy. Mater Charact 2023;195:112415.
[344] Dixit S, Liu S. Laser Additive Manufacturing of High-Strength Aluminum Alloys: Challenges and Strategies. Journal of Manufacturing and Materials Processing. 2022;6:156.
[345] Uddin SZ, Murr LE, Terrazas CA, Morton P, Roberson DA, Wicker RB. Processing and characterization of crack-free aluminum 6061 using high-temperature heating in laser powder bed fusion additive manufacturing. Addit Manuf 2018;22:405–15.
[346] Aboulkhair NT, Everitt NM, Maskery I, Ashcroft I, Tuck C. Selective laser melting of aluminum alloys. MRS Bull 2017;42:311–9.
[347] Kou S, Firouzdor V, Haygood IW. Hot Cracking in Welds of Aluminum and Magnesium Alloys. 3rd Workshop on Hot Cracking Phenomena Welds. Ohio State Univ, Columbus, OH2010. p. 3-23.
[348] Cao G, Kou S. Predicting and reducing liquation-cracking susceptibility based on temperature vs. fraction solid. Weld J 2006;85:9S–18S.
[349] Chen Y, Lu FG, Zhang K, Nie PL, Hosseini SRE, Feng K, et al. Dendritic microstructure and hot cracking of laser additive manufactured Inconel 718 under improved base cooling. J Alloy Compd 2016;670:312–21.
[350] Chen Y, Zhang K, Huang J, Hosseini SRE, Li ZG. Characterization of heat affected zone liquation cracking in laser additive manufacturing of Inconel 718. Mater Des 2016;90:586–94.
[351] Aboulkhair NT, Simonelli M, Parry L, Ashcroft I, Tuck C, Hague R. 3D printing of Aluminium alloys: Additive Manufacturing of Aluminium alloys using selective laser melting. Prog Mater Sci 2019;106.
[352] Kotadia HR, Gibbons G, Das A, Howes PD. A review of Laser Powder Bed Fusion Additive Manufacturing of aluminium alloys: Microstructure and properties. Addit Manuf 2021;46.
[353] Aboulkhair N, Everitt N, Ashcroft I, Tuck C. Reducing porosity in AlSi10Mg parts processed by selective laser melting. Addit. Manuf. 2014;1(2014):77–86.
[354] Fang XW, Chen GP, Yang JN, Xie Y, Huang K, Lu BH. Wire and Arc Additive Manufacturing of High-Strength Al-Zn-Mg Aluminum Alloy. Front Mater 2021;8.
[355] Mehta A, Zhou L, Huynh T, Park S, Hyer H, Song S, et al. Additive manufacturing and mechanical properties of the dense and crack free Zr-modified aluminum alloy 6061 fabricated by the laser-powder bed fusion. Addit Manuf 2021;41.
[356] Taheri H, Shoaib MRBM, Koester LW, Bigelow TA, Collins PC, Bond LJ. Powder-based additive manufacturing-a review of types of defects, generation mechanisms, detection, property evaluation and metrology. International Journal of Additive and Subtractive Materials Manufacturing. 2017;1:172–209.
[357] Kenevisi MS, Yu Y, Lin F. A review on additive manufacturing of Al-Cu (2xxx) aluminium alloys, processes and defects. Mater Sci Technol 2021;37:805–29.
[358] Zhao H, Debroy T. Weld metal composition change during conduction mode laser welding of aluminum alloy 5182. Metallurgical and Materials Transactions B-Process Metallurgy and Materials Processing Science. 2001;32:163–72.
[359] Lippold JC, Kiser SD, DuPont JN. Welding metallurgy and weldability of nickel-base alloys. John Wiley & Sons; 2011.
[360] Elahinia M, Moghaddam NS, Andani MT, Amerinatanzi A, Bimber BA, Hamilton RF. Fabrication of NiTi through additive manufacturing: A review. Prog Mater Sci 2016;83:630–63.
[361] Chaudhary V, Mantri S, Ramanujan R, Banerjee R. Additive manufacturing of magnetic materials. Prog Mater Sci 2020;114:100688.
[362] Messe OMDM, Munoz-Moreno R, Illston T, Baker S, Stone HJ. Metastable carbides and their impact on recrystallisation in IN738LC processed by selective laser melting. Addit Manuf 2018;22:394–404.
[363] Ramsperger M, Singer RF, Koerner C. Microstructure of the Nickel-Base Superalloy CMSX-4 Fabricated by Selective Electron Beam Melting. Metallurgical and Materials Transactions a-Physical Metallurgy and Materials Science. 2016;47A:1469–80.
[364] Murr LE, Martinez E, Gaytan SM, Ramirez DA, Machado BI, Shindo PW, et al. Microstructural Architecture, Microstructures, and Mechanical Properties for a Nickel-Base Superalloy Fabricated by Electron Beam Melting. Metallurgical and Materials Transactions a-Physical Metallurgy and Materials Science. 2011;42A:3491–508.
[365] Li S, Wei Q, Shi Y, Zhu Z, Zhang D. Microstructure characteristics of Inconel 625 superalloy manufactured by selective laser melting. J Mater Sci Technol 2015;31:946–52.
[366] Dinda GP, Dasgupta AK, Mazumder J. Laser aided direct metal deposition of Inconel 625 superalloy: Microstructural evolution and thermal stability. Materials Science and Engineering a-Structural Materials Properties Microstructure and Processing. 2009;509:98–104.
[367] Qiu C, Adkins NJE, Attallah MM. Selective laser melting of Invar 36: Microstructure and properties. Acta Mater 2016;103:382–95.
[368] Tian Y, McAllister D, Colijn H, Mills M, Farson D, Nordin M, et al. Rationalization of Microstructure Heterogeneity in INCONEL 718 Builds Made by the Direct Laser Additive Manufacturing Process. Metallurgical and Materials Transactions a-Physical Metallurgy and Materials Science. 2014;45A:4470–83.
[369] Pourbabak S, Montero-Sistiaga ML, Schryvers D, Van Humbeeck J, Vanmeensel K. Microscopic investigation of as built and hot isostatic pressed Hastelloy X processed by Selective Laser Melting. Mater Charact 2019;153:366–71.
[370] Karapuzha AS, Fraser D, Schliephake D, Dietrich S, Zhu Y, Wu X, et al. Microstructure, mechanical behaviour and strengthening mechanisms in Hastelloy X manufactured by electron beam and laser beam powder bed fusion. J Alloy Compd 2021;862.
[371] Dinovitzer M, Chen X, Laliberte J, Huang X, Frei H. Effect of wire and arc additive manufacturing (WAAM) process parameters on bead geometry and microstructure. Addit Manuf 2019;26:138–46.
[372] Shaikh AS, Schulz F, Minet-Lallemand K, Hryha E. Microstructure and mechanical properties of Haynes 282 superalloy produced by laser powder bed fusion. Mater Today Commun 2021;26:102038.
[373] Divya VD, Munoz-Moreno R, Messe OMDM, Barnard JS, Baker S, Illston T, et al. Microstructure of selective laser melted CM247LC nickel-based superalloy and its evolution through heat treatment. Mater Charact 2016;114:62–74.
[374] Murr LE, Martinez E, Pan XM, Gaytan SM, Castro JA, Terrazas CA, et al. Microstructures of Rene 142 nickel-based superalloy fabricated by electron beam melting. Acta Mater 2013;61:4289–96.
[375] Lopez-Galilea I, Ruttert B, He J, Hammerschmidt T, Drautz R, Gault B, et al. Additive manufacturing of CMSX-4 Ni-base superalloy by selective laser melting: Influence of processing parameters and heat treatment. Addit Manuf 2019;30.
[376] Abreu Faria G, Kadirvel K, Hinojos A, Zhang W, Wang Y, Ramirez AJ. On the use of metastable interface equilibrium assumptions on prediction of solidification micro-segregation in laser powder bed fusion. Sci Technol Weld Join 2019;24:446–56.
[377] Sanchez S, Smith P, Xu Z, Gaspard G, Hyde CJ, Wits WW, et al. Powder Bed Fusion of nickel-based superalloys: A review. Int J Mach Tool Manu 2021;165.
[378] Plotkowski A, Ferguson J, Stump B, Halsey W, Paquit V, Joslin C, et al. A stochastic scan strategy for grain structure control in complex geometries using electron beam powder bed fusion. Addit Manuf 2021;46.
[379] Ding X, Koizumi Y, Aoyagi K, Kii T, Sasaki N, Hayasaka Y, et al. Microstructural control of alloy 718 fabricated by electron beam melting with expanded processing window by adaptive offset method. Mater Sciand Engineering a-Structural Materials Properties Microstructure and Processing. 2019:764.
[380] Dehoff RR, Kirka MM, Sames WJ, Bilheux H, Tremsin AS, Lowe LE, et al. Site specific control of crystallographic grain orientation through electron beam additive manufacturing. Mater Sci Technol 2015;31:931–8.
[381] Raghavan N, Simunovic S, Dehoff R, Plotkowski A, Turner J, Kirka M, et al. Localized melt-scan strategy for site specific control of grain size and primary dendrite arm spacing in electron beam additive manufacturing. Acta Mater 2017;140:375–87.

[382] Helmer H, Bauereiss A, Singer RF, Koerner C. Grain structure evolution in Inconel 718 during selective electron beam melting (vol 668, pg 180, 2016). Materials Science and Engineering a-Structural Materials Properties Microstructure and Processing. 2016;676:546 -.

[383] Keshavarzkermani A, Esmaeilizadeh R, Ali U, Enrique PD, Mahmoodkhani Y, Zhou NY, et al. Controlling mechanical properties of additively manufactured hastelloy X by altering solidification pattern during laser powder-bed fusion. Materials Science and Engineering a-Structural Materials Properties Microstructure and Processing. 2019:762.

[384] Gasper AND, Szost B, Wang X, Johns D, Sharma S, Clare AT, et al. Spatter and oxide formation in laser powder bed fusion of Inconel 718. Addit Manuf 2018;24: 446–56.

[385] Nadammal N, Mishurova T, Fritsch T, Serrano-Munoz I, Kromm A, Haberland C, et al. Critical role of scan strategies on the development of microstructure, texture, and residual stresses during laser powder bed fusion additive manufacturing. Addit Manuf 2021:38.

[386] Geiger F, Kunze K, Etter T. Tailoring the texture of IN738LC processed by selective laser melting (SLM) by specific scanning strategies. Materials Science and Engineering a-Structural Materials Properties Microstructure and Processing. 2016;661:240–6.

[387] Specification S. Standard Specification for Precipitation-Hardening Nickel Alloy (UNS N07718) Plate, Sheet, and Strip for High-Temperature Service 1. Annual B ASTM Standard. 2010;7:7–10.

[388] Yu H, Hayashi S, Kakehi K, Kuo Y-L. Study of Formed Oxides in IN718 Alloy during the Fabrication by Selective Laser Melting and Electron Beam Melting. Metals. 2019:9.

[389] Sames WJ, Unocic KA, Helmreich GW, Kirka MM, Medina F, Dehoff RR, et al. Feasibility of in situ controlled heat treatment (ISHT) of Inconel 718 during electron beam melting additive manufacturing. Addit Manuf 2017;13:156–65.

[390] Popovich VA, Borisov EV, Popovich AA, Sufiiarov VS, Masaylo DV, Alzina L. Functionally graded Inconel 718 processed by additive manufacturing: Crystallographic texture, anisotropy of microstructure and mechanical properties. Mater Des 2017;114:441–9.

[391] Xiao H, Li S, Han X, Mazumder J, Song L. Laves phase control of Inconel 718 alloy using quasi-continuous-wave laser additive manufacturing. Mater Des 2017; 122:330–9.

[392] Dinda GP, Dasgupta AK, Mazumder J. Texture control during laser deposition of nickel-based superalloy. Scr Mater 2012;67:503–6.

[393] Tan L, Wang G, Guo Y, Fang Q, Liu Z, Xiao X, et al. Additively manufactured oxide dispersion strengthened nickel-based superalloy with superior high temperature properties. Virtual and Physical Prototyping. 2020;15:555–69.

[394] Kenel C, De Luca A, Joglekar SS, Leinenbach C, Dunand DC. Evolution of Y2O3 dispersoids during laser powder bed fusion of oxide dispersion strengthened Ni-Cr-Al-Ti γ/γˊsuperalloy. Addit Manuf 2021;47:102224.

[395] Wilms MB, Rittinghaus S-K, Goßling M, Gökce B. Additive manufacturing of oxide-dispersion strengthened alloys: Materials, synthesis and manufacturing. Prog Mater Sci 2022;101049.

[396] Ghodsi MZ, Khademzadeh S, Marzbanrad E, Razmpoosh MH, De Marchi N, Toyserkani E. Development of Yttria-stabilized zirconia reinforced Inconel 625 metal matrix composite by laser powder bed fusion. Materials Science and Engineering a-Structural Materials Properties Microstructure and Processing. 2021: 827.

[397] Hong C, Gu D, Dai D, Alkhayat M, Urban W, Yuan P, et al. Laser additive manufacturing of ultrafine TiC particle reinforced Inconel 625 based composite parts: Tailored microstructures and enhanced performance. Materials Science and Engineering a-Structural Materials Properties Microstructure and Processing. 2015;635:118–28.

[398] Gu D, Zhang H, Dai D, Xia M, Hong C, Poprawe R. Laser additive manufacturing of nano-TiC reinforced Ni-based nanocomposites with tailored microstructure and performance. Composites Part B-Engineering. 2019;163:585–97.

[399] Han Q, Gu Y, Huang J, Wang L, Low KWQ, Feng Q, et al. Selective laser melting of Hastelloy X nanocomposite: Effects of TiC reinforcement on crack elimination and strength improvement. Composites Part B-Engineering. 2020:202.

[400] Yang S, Han Q, Yin Y, Gao J, Zhang Z, Gu Y, et al. Effects of micrometer-sized TiB2 on crack mitigation, mechanical and electrochemical performance of a Ni-based alloy fabricated by selective laser melting. Opt Laser Technol 2021;142.

[401] Zhang B, Bi G, Wang P, Bai J, Chew Y, Nai MS. Microstructure and mechanical properties of Inconel 625/nano-TiB2 composite fabricated by LAAM. Mater Des 2016;111:70–9.

[402] Wang P, Zhang B, Tan CC, Raghavan S, Lim Y-F, Sun C-N, et al. Microstructural characteristics and mechanical properties of carbon nanotube reinforced Inconel 625 parts fabricated by selective laser melting. Mater Des 2016;112:290–9.

[403] Chen Z, Wei P, Zhang S, Lu B, Zhang L, Yang X, et al. Graphene reinforced nickel-based superalloy composites fabricated by additive manufacturing. Materials Science and Engineering a-Structural Materials Properties Microstructure and Processing. 2020;769.

[404] Kong D, Dong C, Ni X, Zhang L, Man C, Yao J, et al. High-throughput fabrication of nickel-based alloys with different Nb contents via a dual-feed additive manufacturing system: Effect of Nb content on microstructural and mechanical properties. J Alloy Compd 2019;785:826–37.

[405] Abramov OV. High-intensity ultrasonics: theory and industrial applications. CRC Press 2019.

[406] Wang H, Hu Y, Ning F, Cong W. Ultrasonic vibration-assisted laser engineered net shaping of Inconel 718 parts: Effects of ultrasonic frequency on microstructural and mechanical properties. J Mater Process Technol 2020;276.

[407] Frederick CL, Plotkowski A, Kirka MM, Haines M, Staub A, Schwalbach EJ, et al. Geometry-Induced Spatial Variation of Microstructure Evolution During Selective Electron Beam Melting of Rene-N5. Metallurgical and Materials Transactions a-Physical Metallurgy and Materials Science. 2018;49A:5080–96.

[408] Qiu Z, Wu B, Zhu H, Wang Z, Hellier A, Ma Y, et al. Microstructure and mechanical properties of wire arc additively manufactured Hastelloy C276 alloy. Mater Des 2020;195.

[409] Song H, McGaughy T, Sadek A, Zhang W. Effect of structural support on microstructure of nickel base superalloy fabricated by laser-powder bed fusion additive manufacturing. Addit Manuf 2019;26:30–40.

[410] Tang YT, Panwisawas C, Ghoussoub JN, Gong Y, Clark JWG, Nemeth AAN, et al. Alloys-by-design: Application to new superalloys for additive manufacturing. Acta Mater 2021;202:417–36.

[411] Jena A, Atabay SE, Gontcharov A, Lowden P, Brochu M. Laser powder bed fusion of a new high gamma prime Ni-based superalloy with improved weldability. Mater Des 2021;208.

[412] Harrison NJ, Todd I, Mumtaz K. Reduction of micro-cracking in nickel superalloys processed by Selective Laser Melting: A fundamental alloy design approach. Acta Mater 2015;94:59–68.

[413] Vilaro T, Colin C, Bartout JD, Naze L, Sennour M. Microstructural and mechanical approaches of the selective laser melting process applied to a nickel-base superalloy. Materials Science and Engineering a-Structural Materials Properties Microstructure and Processing. 2012;534:446–51.

[414] Raza MM, Lo Y-L. Experimental investigation into microstructure, mechanical properties, and cracking mechanism of IN713LC processed by laser powder bed fusion. Materials Science and Engineering a-Structural Materials Properties Microstructure and Processing. 2021;819.

[415] Zhang X, Chai Z, Chen H, Xu J, Xu L, Lu H, et al. A novel method to prevent cracking in directed energy deposition of Inconel 738 by in-situ doping Inconel 718. Mater Des 2021;197.

[416] Lee YS, Kirka MM, Kim S, Sridharan N, Okello A, Dehoff RR, et al. Asymmetric Cracking in Mar-M247 Alloy Builds During Electron Beam Powder Bed Fusion Additive Manufacturing. Metallurgical and Materials Transactions a-Physical Metallurgy and Materials Science. 2018;49A:5065–79.

[417] Kalentics N, Sohrabi N, Tabasi HG, Griffiths S, Jhabvala J, Leinenbach C, et al. Healing cracks in selective laser melting by 3D laser shock peening. Addit Manuf 2019;30.

[418] Catchpole-Smith S, Aboulkhair N, Parry L, Tuck C, Ashcroft IA, Clare A. Fractal scan strategies for selective laser melting of ʻunweldable' nickel superalloys. Addit Manuf 2017;15:113–22.

[419] Kontis P, Chauvet E, Peng Z, He J, da Silva AK, Raabe D, et al. Atomic-scale grain boundary engineering to overcome hot-cracking in additively-manufactured superalloys. Acta Mater 2019;177:209–21.

[420] Seidel A, Finaske T, Straubel A, Wendrock H, Maiwald T, Riede M, et al. Additive Manufacturing of Powdery Ni-Based Superalloys Mar-M-247 and CM 247 LC in Hybrid Laser Metal Deposition. Metallurgical and Materials Transactions a-Physical Metallurgy and Materials Science. 2018;49A:3812–30.

[421] Moussaoui K, Rubio W, Mousseigne M, Sultan T, Rezai F. Effects of Selective Laser Melting additive manufacturing parameters of Inconel 718 on porosity, microstructure and mechanical properties. Materials Science and Engineering a-Structural Materials Properties Microstructure and Processing. 2018;735: 182–90.

[422] McNeil JL, Sisco K, Frederick C, Massey M, Carver K, List III F, et al. In-SituMonitoring for Defect Identification in Nickel Alloy Complex Geometries Fabricated by L-PBF Additive Manufacturing. Metallurgical and Materials Transactions a-Physical Metallurgy and Materials Science. 2020;51:6528–45.

[423] Kappes B, Moorthy S, Drake D, Geerlings H, Stebner A. Machine Learning to Optimize Additive Manufacturing Parameters for Laser Powder Bed Fusion of Inconel 718. 9th International Symposium on Superalloy 718 and Derivatives - Energy, Aerospace, and Industrial Applications. Champion, PA2000. p. 595-610.

[424] Snell R, Tammas-Williams S, Chechik L, Lyle A, Hernandez-Nava E, Boig C, et al. Methods for Rapid Pore Classification in Metal Additive Manufacturing. JOM 2020;72:101–9.

[425] Huynh T, Mehta A, Graydon K, Woo J, Park S, Hyer H, et al. Microstructural Development in Inconel 718 Nickel-Based Superalloy Additively Manufactured by Laser Powder Bed Fusion. Metallography, Microstructure, and Analysis. 2022;11:88–107.

[426] Gaumann M, Bezencon C, Canalis P, Kurz W. Single-crystal laser deposition of superalloys: Processing-microstructure maps. Acta Mater 2001;49:1051–62.

[427] Zhang J, Wang L, Wang D, Xie G, Lu Y, Shen J, et al. Recent Progress in Research and Development of Nickel-Based Single Crystal Superalloys. Acta Metall Sin 2019;55:1077–94.

[428] Gotterbarm MR, Rausch AM, Körner C. Fabrication of single crystals through a μ-helix grain selection process during electron beam metal additive manufacturing. Metals. 2020;10:313.

[429] Knapp GL, Raghavan N, Plotkowski A, DebRoy T. Experiments and simulations on solidification microstructure for Inconel 718 in powder bed fusion electron beam additive manufacturing. Addit Manuf 2019;25:511–21.

[430] Mukherjee T, Wei HL, De A, DebRoy T. Heat and fluid flow in additive manufacturing-Part I: Modeling of powder bed fusion. Comput Mater Sci 2018;150: 304–13.

[431] Mukherjee T, Wei HL, De A, DebRoy T. Heat and fluid flow in additive manufacturing - Part II: Powder bed fusion of stainless steel, and titanium, nickel and aluminum base alloys. Comput Mater Sci 2018;150:369–80.

[432] Acharya R, Bansal R, Gambone JJ, Das S. A Coupled Thermal, Fluid Flow, and Solidification Model for the Processing of Single-Crystal Alloy CMSX-4 Through Scanning Laser Epitaxy for Turbine Engine Hot-Section Component Repair (Part I). Metallurgical and Materials Transactions B-Process Metallurgy and Materials Processing Science. 2014;45:2247–61.

[433] Acharya R, Bansal R, Gambone JJ, Das S. A microstructure evolution model for the processing of single-crystal alloy CMSX-4 through scanning laser epitaxy for turbine engine hot-section component repair (Part II). Metall Mater Trans B 2014;45:2279–90.

[434] Basak A, Acharya R, Das S. Additive Manufacturing of Single-Crystal Superalloy CMSX-4 Through Scanning Laser Epitaxy: Computational Modeling, Experimental Process Development, and Process Parameter Optimization. Metallurgical and Materials Transactions a-Physical Metallurgy and Materials Science. 2016;47A:3845–59.

[435] Liang Y-J, Cheng X, Li J, Wang H-M. Microstructural control during laser additive manufacturing of single-crystal nickel-base superalloys: New processing-microstructure maps involving powder feeding. Mater Des 2017;130:197–207.

[436] Buerger D, Parsa AB, Ramsperger M, Koerner C, Eggeler G. Creep properties of single crystal Ni-base superalloys (SX): A comparison between conventionally cast and additive manufactured CMSX-4 materials. Materials Science and Engineering a-Structural Materials Properties Microstructure and Processing. 2019; 762.

[437] Meid C, Dennstedt A, Ramsperger M, Pistor J, Ruttert B, Lopez-Galilea I, et al. Effect of heat treatment on the high temperature fatigue life of single crystalline nickel base superalloy additively manufactured by means of selective electron beam melting. Scr Mater 2019;168:124–8.

[438] Pistor J, Körner C. Formation of topologically closed packed phases within CMSX-4 single crystals produced by additive manufacturing. Materials Letters: X. 2019;1:100003.

[439] Ramsperger M, Roncery LM, Lopez-Galilea I, Singer RF, Theisen W, Koerner C. Solution Heat Treatment of the Single Crystal Nickel-Base Superalloy CMSX-4 Fabricated by Selective Electron Beam Melting. Adv Eng Mater 2015;17:1486–93.

[440] Körner C, Ramsperger M, Meid C, Bürger D, Wollgramm P, Bartsch M, et al. Microstructure and mechanical properties of CMSX-4 single crystals prepared by additive manufacturing. Metall Mater Trans A 2018;49:3781–92.

[441] Liang Y-J, Li J, Li A, Cheng X, Wang S, Wang H-M. Experimental optimization of laser additive manufacturing process of single-crystal nickel-base superalloys by a statistical experiment design method. J Alloy Compd 2017;697:174–81.

[442] Wei HL, Elmer JW, DebRoy T. Origin of grain orientation during solidification of an aluminum alloy. Acta Mater 2016;115:123–31.

[443] Wei HL, Elmer JW, DebRoy T. Crystal growth during keyhole mode laser welding. Acta Mater 2017;133:10–20.

[444] Basak A, Acharya R, Das S. Epitaxial deposition of nickel-based superalloy Rene 142 through scanning laser epitaxy (SLE). Addit Manuf 2018;22:665–71.

[445] Zhou Z, Huang L, Shang Y, Li Y, Jiang L, Lei Q. Causes analysis on cracks in nickel-based single crystal superalloy fabricated by laser powder deposition additive manufacturing. Mater Des 2018;160:1238–49.

[446] Anderson TD, DuPont JN, DebRoy T. Origin of stray grain formation in single-crystal superalloy weld pools from heat transfer and fluid flow modeling. Acta Mater 2010;58:1441–54.

[447] Anderson T, DuPont J, DebRoy T. Stray grain formation in welds of single-crystal Ni-base superalloy CMSX-4. Metall Mater Trans A 2010;41:181–93.

[448] Wang Z, Stoica AD, Ma D, Beese AM. Diffraction and single-crystal elastic constants of Inconel 625 at room and elevated temperatures determined by neutron diffraction. Materials Science and Engineering a-Structural Materials Properties Microstructure and Processing. 2016;674:406–12.

[449] Ahmed T, Rack HJ. Phase transformations during cooling in alpha+beta titanium alloys. Materials Science and Engineering a-Structural Materials Properties Microstructure and Processing. 1998;243:206–11.

[450] Szost BA, Terzi S, Martina F, Boisselier D, Prytuliak A, Pining T, et al. A comparative study of additive manufacturing techniques: Residual stress and microstructural analysis of CLAD and WAAM printed Ti-6Al-4V components. Mater Des 2016;89:559–67.

[451] Zhai YW, Lados DA, Brown EJ, Vigilante GN. Understanding the microstructure and mechanical properties of Ti-6Al-4V and Inconel 718 alloys manufactured by Laser Engineered Net Shaping. Addit Manuf 2019;27:334–44.

[452] Carroll BE, Palmer TA, Beese AM. Anisotropic tensile behavior of Ti-6Al-4V components fabricated with directed energy deposition additive manufacturing. Acta Mater 2015;87:309–20.

[453] Wang T, Zhu YY, Zhang SQ, Tang HB, Wang HM. Grain morphology evolution behavior of titanium alloy components during laser melting deposition additive manufacturing. J Alloy Compd 2015;632:505–13.

[454] Waryoba DR, Keist JS, Ranger C, Palmer TA. Microtexture in additively manufactured Ti-6Al-4V fabricated using directed energy deposition. Materials Science and Engineering a-Structural Materials Properties Microstructure and Processing. 2018;734:149–63.

[455] Easton MA, StJohn DH. A model of grain refinement incorporating alloy constitution and potency of heterogeneous nuclean particles. Acta Mater 2001;49: 1867–78.

[456] Bermingham MJ, McDonald SD, Dargusch MS, StJohn DH. Grain-refinement mechanisms in titanium alloys. J Mater Res 2008;23:97–104.

[457] StJohn DH, Qian M, Easton MA, Cao P. The Interdependence Theory: The relationship between grain formation and nuclean selection. Acta Mater 2011;59: 4907–21.

[458] StJohn DH, Prasad A, Easton MA, Qian M. The Contribution of Constitutional Supercooling to Nucleation and Grain Formation. Metallurgical and Materials Transactions a-Physical Metallurgy and Materials Science. 2015;46A:4868–85.

[459] Elmer JW, Aziz M, Tanner LE, Smith PM, Wall M. Formation of bands of ultrafine beryllium particles during rapid solidification of Al- Be alloys: Modeling and direct observations. Acta Metall Mater 1994;42:1065–80.

[460] Zhu J, Kamiya A, Yamada T, Shi W, Naganuma K. Influence of boron addition on microstructure and mechanical properties of dental cast titanium alloys. Materials Science and Engineering a-Structural Materials Properties Microstructure and Processing. 2003;339:53–62.

[461] Tamirisakandala S, Bhat RB, Tiley JS, Miracle DB. Grain refinement of cast titanium alloys via trace boron addition. Scr Mater 2005;53:1421–6.

[462] Bermingham MJ, Kent D, Zhan H, St John DH, Dargusch MS. Controlling the microstructure and properties of wire arc additive manufactured Ti-6Al-4V with trace boron additions. Acta Mater 2015;91:289–303.

[463] Bermingham MJ, McDonald SD, Dargusch MS. Effect of trace lanthanum hexaboride and boron additions on microstructure, tensile properties and anisotropy of Ti-6Al-4V produced by additive manufacturing. Materials Science and Engineering a-Structural Materials Properties Microstructure and Processing. 2018; 719:1–11.

[464] Huber F, Papke T, Scheitler C, Hanrieder L, Merklein M, Schmidt M. In Situ Formation of a Metastable beta-Ti Alloy by Laser Powder Bed Fusion (L-PBF) of Vanadium and Iron Modified Ti-6Al-4V. Metals. 2018;8:9.

[465] Zhu YY, Tang HB, Li Z, Xu C, He B. Solidification behavior and grain morphology of laser additive manufacturing titanium alloys. J Alloy Compd 2019;777: 712–6.

[466] Tedman-Jones SN, McDonald SD, Bermingham MJ, StJohn DH, Dargusch MS. A new approach to nuclei identification and grain refinement in titanium alloys. J Alloy Compd 2019;794:268–84.

[467] Zhang DY, Qiu D, Gibson MA, Zheng YF, Fraser HL, StJohn DH, et al. Additive manufacturing of ultrafine-grained high-strength titanium alloys. Nature 2019; 576:91 -+.

[468] Wang J, Lin X, Wang M, Li JQ, Wang C, Huang WD. Effects of subtransus heat treatments on microstructure features and mechanical properties of wire and arc additive manufactured Ti-6Al-4V alloy. Materials Science and Engineering a-Structural Materials Properties Microstructure and Processing. 2020;776:14.

[469] Murr LE, Gaytan SM, Ramirez DA, Martinez E, Hernandez J, Amato KN, et al. Metal Fabrication by Additive Manufacturing Using Laser and Electron Beam Melting Technologies. J Mater Sci Technol 2012;28:1–14.

[470] Lin JJ, Lv YH, Liu YX, Xu BS, Sun Z, Li ZG, et al. Microstructural evolution and mechanical properties of Ti-6Al-4V wall deposited by pulsed plasma arc additive manufacturing. Mater Des 2016;102:30–40.

[471] Kistler NA, Corbin DJ, Nassar AR, Reutzel EW, Beese AM. Effect of processing conditions on the microstructure, porosity, and mechanical properties of Ti-6Al-4V repair fabricated by directed energy deposition. J Mater Process Technol 2019;264:172–81.

[472] Yang ZW, Liu Q, Wang Y, Ma ZQ, Liu YC. Fabrication of multi-element alloys by twin wire arc additive manufacturing combined with in-situ alloying. Materials Research Letters. 2020;8:477–82.

[473] Zhu YY, Tian XJ, Li J, Wang HM. Microstructure evolution and layer bands of laser melting deposition Ti-6.5Al-3.5Mo-1.5Zr-0.3Si titanium alloy. J Alloy Compd 2014;616:468–74.

[474] Zou ZY, Simonelli M, Katrib J, Dimitrakis G, Hague R. Refinement of the grain structure of additive manufactured titanium alloys via epitaxial recrystallization enabled by rapid heat treatment. Scr Mater 2020;180:66–70.

[475] Zou ZY, Simonelli M, Katrib J, Dimitrakis G, Hague R. Microstructure and tensile properties of additive manufactured Ti-6Al-4V with refined prior-? grain structure obtained by rapid heat treatment. Materials Science and Engineering a-Structural Materials Properties Microstructure and Processing. 2021;814:11.

[476] Bermingham MJ, Thomson-Larkins J, St John DH, Dargusch MS. Sensitivity of Ti-6Al-4V components to oxidation during out of chamber Wire plus Arc Additive Manufacturing. J Mater Process Technol 2018;258:29–37.

[477] Snow Z, Nassar AR, Reutzel EW. Invited Review Article: Review of the formation and impact of flaws in powder bed fusion additive manufacturing. Addit Manuf 2020;36:15.

[478] Chen YH, Clark SJ, Sinclair L, Leung CLA, Marussi S, Connolley T, et al. Synchrotron X-ray imaging of directed energy deposition additive manufacturing of titanium alloy Ti-6242. Addit Manuf 2021;41:9.

[479] Bustillos J, Kim J, Moridi A. Exploiting lack of fusion defects for microstructural engineering in additive manufacturing. Addit Manuf 2021;48:9.

[480] du Plessis A. Effects of process parameters on porosity in laser powder bed fusion revealed by X-ray tomography. Addit Manuf 2019;30:9.

[481] Haijun G, Nadimpalli VK, Rafi K, Starr T, Stucker B. Micro-CT Evaluation of Defects in Ti-6Al-4V Parts Fabricated by Metal Additive Manufacturing. Technologies (Switzerland) 2019;7: 44 (12 pp.)-44 (12:pp.).

[482] du Plessis A, Macdonald E. Hot isostatic pressing in metal additive manufacturing: X-ray tomography reveals details of pore closure. Addit Manuf 2020;34:12.

[483] Caterina I, Alex LCL, Yunhui C, Shaoliang G, C. AR, Jedsada L, et al. Oxidation induced mechanisms during directed energy deposition additive manufactured titanium alloy builds. Additive Manufacturing Letters. 2021;1.

[484] Klassen A, Scharowsky T, Korner C. Evaporation model for beam based additive manufacturing using free surface lattice Boltzmann methods. J Phys D-Appl Phys 2014;47:12.

[485] Juechter V, Scharowsky T, Singer RF, Korner C. Processing window and evaporation phenomena for Ti-6Al-4V produced by selective electron beam melting. Acta Mater 2014;76:252–8.

[486] Cotton JD, Briggs RD, Boyer RR, Tamirisakandala S, Russo P, Shchetnikov N, et al. State of the Art in Beta Titanium Alloys for Airframe Applications. JOM 2015;67:1281–303.

[487] Rack HJ, Qazi JI. Titanium alloys for biomedical applications. Mater Sci Eng C-Biomimetic Supramol Syst. 2006;26:1269–77.

[488] Hao YL, Li SJ, Yang R. Biomedical titanium alloys and their additive manufacturing. Rare Met 2016;35:661–71.

[489] Zheng YF, Williams REA, Sosa JM, Wang YZ, Banerjee R, Fraser HL. The role of the omega phase on the non-classical precipitation of the alpha phase in metastable beta-titanium alloys. Scr Mater 2016;111:81–4.

[490] Carlton HD, Klein KD, Elmer JW. Evolution of Microstructure and mechanical properties of selective laser melted Ti-5Al-5V-5Mo-3Cr after heat treatments. Sci Technol Weld Join 2019;24:465–73.

[491] Carlton HD, Klein KD, Elmer JW. unpublished research. 2019.

[492] Hernandez J, Li SJ, Martinez E, Murr LE, Pan XM, Amato KN, et al. Microstructures and Hardness Properties for beta-Phase Ti-24Nb-4Zr-7.9Sn Alloy Fabricated by Electron Beam Melting. J Mater Sci Technol 2013;29:1011–7.

[493] Li YJ, Li XP, Zhang LC, Sercombe TB. Processing and properties of topologically optimised biomedical Ti-24Nb-4Zr-8Sn scaffolds manufactured by selective laser melting. Materials Science and Engineering a-Structural Materials Properties Microstructure and Processing. 2015;642:268–78.

[494] Wei J, Sun HJ, Zhang DC, Gong LJ, Lin JG, Wen C. Influence of Heat Treatments on Microstructure and Mechanical Properties of Ti-26Nb Alloy Elaborated In Situ by Laser Additive Manufacturing with Ti and Nb Mixed Powder. Materials. 2019;12:13.

[495] Raghunandan U, S. KP, Sokkalingam R, Neera S, Akash A, Kang S, et al. Selective laser melting of high-strength, low-modulus Ti–35Nb–7Zr–5Ta alloy. Materialia. 2020;14.

[496] Bermingham MJ, Kent D, Pace B, Cairney JM, Dargusch MS. High strength heat-treatable beta-titanium alloy for additive manufacturing. Materials Science and Engineering a-Structural Materials Properties Microstructure and Processing. 2020;791:7.

[497] Lima DD, Mantri SA, Mikler CV, Contieri R, Yannetta CJ, Campo KN, et al. Laser additive processing of a functionally graded internal fracture fixation plate. Mater Des 2017;130:8–15.

[498] Bakhshivash S, Asgari H, Russo P, Dibia CF, Ansari M, Gerlich AP, et al. Printability and microstructural evolution of Ti-5553 alloy fabricated by modulated laser powder bed fusion. Int J Adv Manuf Technol 2019;103:4399–409.

[499] Marvel CJ, Sabol JC, Pasang T, Watanabe M, Misiolek WZ. Improving the Mechanical Properties of the Fusion Zone in Electron-Beam Welded Ti-5Al-5Mo-5V-3Cr Alloys. Metallurgical and Materials Transactions a-Physical Metallurgy and Materials Science. 2017;48A:1921–30.

[500] Alloys H-SAPM. Properties and selection: nonferrous alloys and special-purpose materials. 1990.

[501] Olson D.L., Siewert T.A., Liu S., Edwards G.R. Welding, brazing, and soldering. ASM Int. 1993;6:254.

[502] Tiberto D, Klotz UE, Held F, Wolf G. Additive manufacturing of copper alloys: influence of process parameters and alloying elements. Mater Sci Technol 2019; 35:969–77.

[503] Tran TQ, Chinnappan A, Lee JKY, Nguyen Huu L, Tran LT, Wang G, et al. 3D Printing of Highly Pure Copper. Metals. 2019:9.

[504] Silbernagel C, Gargalis L, Ashcroft I, Hague R, Galea M, Dickens P. Electrical resistivity of pure copper processed by medium-powered laser powder bed fusion additive manufacturing for use in electromagnetic applications. Addit Manuf 2019:29.

[505] Ramirez DA, Murr LE, Martinez E, Hernandez DH, Martinez JL, Machado BI, et al. Novel precipitate-microstructural architecture developed in the fabrication of solid copper components by additive manufacturing using electron beam melting. Acta Mater 2011;59:4088–99.

[506] Lodes MA, Guschlbauer R, Koerner C. Process development for the manufacturing of 99.94% pure copper via selective electron beam melting. Mater Lett 2015; 143:298–301.

[507] Milewski J. Additive Manufacturing of Metals: From Fundamental Technology to Rocket Nozzles, Medical Implants. and Custom Jewelry Springer International Publishing AG; 2017.

[508] Mao Z, Zhang DZ, Jiang J, Fu G, Zhang P. Processing optimisation, mechanical properties and microstructural evolution during selective laser melting of Cu-15Sn high-tin bronze. Materials Science and Engineering a-Structural Materials Properties Microstructure and Processing. 2018;721:125–34.

[509] Mao Z, Zhang DZ, Wei P, Zhang K. Manufacturing Feasibility and Forming Properties of Cu-4Sn in Selective Laser Melting. Materials. 2017:10.

[510] Murray T, Thomas S, Wu Y, Neil W, Hutchinson C. Selective laser melting of nickel aluminium bronze. Addit Manuf 2020:33.

[511] Popovich A, Sufiiarov V, Polozov I, Borisov E, Masaylo D, Orlov A. Microstructure and mechanical properties of additive manufactured copper alloy. Mater Lett 2016;179:38–41.

[512] Scudino S, Unterdoerfer C, Prashanth KG, Attar H, Ellendt N, Uhlenwinkel V, et al. Additive manufacturing of Cu-10Sn bronze. Mater Lett 2015;156:202–4.

[513] Zhang G, Chen C, Wang X, Wang P, Zhang X, Gan X, et al. Additive manufacturing of fine-structured copper alloy by selective laser melting of pre-alloyed Cu-15Ni-8Sn powder. Int J Adv Manuf Technol 2018;96:4223–30.

[514] Koerner C. Additive manufacturing of metallic components by selective electron beam melting - a review. Int Mater Rev 2016;61:361–77.

[515] Khoroshko ES, Filippov AV, Shamarin NN, Tarasov SY. Anisotropy of the Mechanical Properties of the Aluminum Bronze Obtained by the Electron Beam Additive Manufacturing. International Conference on Physical Mesomechanics - Materials with Multilevel Hierarchical Structure and Intelligent Manufacturing Technology. Tomsk, RUSSIA2020.

[516] Wolf T, Fu Z, Koerner C. Selective electron beam melting of an aluminum bronze: Microstructure and mechanical properties. Mater Lett 2019;238:241–4.

[517] Baby J, Amirthalingam M. Microstructural development during wire arc additive manufacturing of copper-based components. Welding in the World. 2020;64: 395–405.

[518] Chen W, Chen Y, Zhang T, Wen T, Feng X, Yin L. Effects of Location on the Microstructure and Mechanical Properties of Cu-8Al-2Ni-2Fe-2Mn Alloy Produced Through Wire Arc Additive Manufacturing. J Mater Eng Perform 2020;29:4733–44.

[519] Chen W, Chen Y, Zhang T, Wen T, Yin Z, Feng X. Effect of Ultrasonic Vibration and Interpass Temperature on Microstructure and Mechanical Properties of Cu-8Al-2Ni-2Fe-2Mn Alloy Fabricated by Wire Arc Additive Manufacturing. Metals. 2020:10.

[520] Dharmendra C, Hadadzadeh A, Amirkhiz BS, Ram GDJ, Mohammadi M. Microstructural evolution and mechanical behavior of nickel aluminum bronze Cu-9Al-4Fe-4Ni-1Mn fabricated through wire-arc additive manufacturing. Addit Manuf 2019:30.

[521] Ding D, Pan Z, van Duin S, Li H, Shen C. Fabricating Superior NiAl Bronze Components through Wire Arc Additive Manufacturing. Materials. 2016:9.

[522] Dong B, Pan Z, Shen C, Ma Y, Li H. Fabrication of Copper-Rich Cu-Al Alloy Using the Wire-Arc Additive Manufacturing Process. Metallurgical and Materials Transactions B-Process Metallurgy and Materials Processing Science. 2017;48:3143–51.

[523] Queguineur A, Marolleau J, Lavergne A, Ruckert G. Evaluation of tandem controlled short-circuit GMAW for improved deposition in additive manufacture of large Nickel Aluminium Bronze naval components. Welding in the World. 2020;64:1389–95.

[524] Shakil SI, Dharmendra C, Amirkhiz BS, Verma D, Mohammadi M, Haghshenas M. Micromechanical characterization of wire-arc additive manufactured and cast nickel aluminum bronze: Ambient and intermediate temperatures. Materials Science and Engineering a-Structural Materials Properties Microstructure and Processing. 2020:792.

[525] Shen C, Mu G, Hua X, Li F, Luo D, Ji X, et al. Influences of postproduction heat treatments on the material anisotropy of nickel-aluminum bronze fabricated using wire-arc additive manufacturing process. Int J Adv Manuf Technol 2019;103:3199–209.

[526] Onuike B, Heer B, Bandyopadhyay A. Additive manufacturing of Inconel 718-Copper alloy bimetallic structure using laser engineered net shaping (LENS (TM)). Addit Manuf 2018;21:133–40.

[527] Shen C, Pan Z, Ding D, Yuan L, Nie N, Wang Y, et al. The influence of post-production heat treatment on the multi-directional properties of nickel-aluminum bronze alloy fabricated using wire-arc additive manufacturing process. Addit Manuf 2018;23:411–21.

[528] Elmer JW, Gibbs G. Unpublished research. 2020.

[529] Osipovich KS, Astafurova EG, Chumaevskii AV, Kalashnikov KN, Astafurov SV, Maier GG, et al. Gradient transition zone structure in "steel-copper" sample produced by double wire-feed electron beam additive manufacturing. J Mater Sci 2020;55:9258–72.

[530] Kaplan A, Yildiz AK. The effects of production methods on the microstructures and mechanical properties of an aluminum bronze. Mater Lett 2003;57: 4402–11.

[531] Chen J, Yang Y, Song C, Zhang M, Wu S, Wang D. Interfacial microstructure and mechanical. properties of 316L /CuSn10 multi-material bimetallic structure fabricated by selective laser melting. Materials Science and Engineering a-Structural Materials Properties Microstructure and Processing. 2019;752:75–85.

[532] Yang J, Hawkins L, Song M, He L, Bachhav M, Pan Q, et al. Compositionally graded specimen made by laser additive manufacturing as a high-throughput method to study radiation damages and irradiation-assisted stress corrosion cracking. J Nucl Mater 2022;560.

[533] Teh WH, Chaudhary V, Chen S, Lim SH, Wei F, Lee JY, et al. High throughput multi-property evaluation of additively manufactured Co-Fe-Ni materials libraries. Addit Manuf 2022;58:102983.

[534] Nie J, Wei L, Li D-l, Zhao L, Jiang Y, Li Q. High-throughput characterization of microstructure and corrosion behavior of additively manufactured SS316L-SS431 graded material. Addit Manuf 2020;35:101295.

[535] Wei C, Li L. Recent progress and scientific challenges in multi-material additive manufacturing via laser-based powder bed fusion. Virtual and Physical Prototyping. 2021;16:347–71.

[536] Zhang C, Chen F, Huang Z, Jia M, Chen G, Ye Y, et al. Additive manufacturing of functionally graded materials: A review. Mater Sci Eng A 2019;764:138209.

[537] Reichardt A, Shapiro AA, Otis R, Dillon RP, Borgonia JP, McEnerney BW, et al. Advances in additive manufacturing of metal-based functionally graded materials. Int Mater Rev 2021;66:1–29.

[538] Hasanov S, Alkunte S, Rajeshirke M, Gupta A, Huseynov O, Fidan I, et al. Review on additive manufacturing of multi-material parts: progress and challenges. Journal of Manufacturing and Materials Processing. 2021;6:4.

[539] Wimler D, Kasznar K, Musi M, Breuning C, Markl M, Keckes J, et al. How electron beam melting tailors the Al-sensitive microstructure and mechanical response of a novel process-adapted γ-TiAl based alloy. Mater Des 2021;212:110187.

[540] Zhou J, Li H, Yu Y, Firouzian K, Qian Y, Lin F. Characterization of interfacial transition zone of functionally graded materials with graded composition from a single material in electron beam powder bed fusion. J Alloy Compd 2020;832:154774.

[541] Jamieson CD, Nassar AR. Additive manufacturing of in-situ gas-alloyed functionally-graded titanium. J Mater Process Technol 2022;307:117692.

[542] Wei W, Wu W, Fan S, Duan X. In-situ laser additive manufacturing of Ti6Al4V matrix composites by gas–liquid reaction in dilute nitrogen gas atmospheres. Mater Des 2021;202:109578.

[543] Brentrup G, DuPont J. Fabrication and characterization of graded transition joints for welding dissimilar alloys. Weld J. 2013;92:72s–s79.

[544] Kelly J, Elmer J, Ryerson F, Lee J, Haslam J. Directed energy deposition additive manufacturing of functionally graded Al-W composites. Addit Manuf 2021;39: 101845.

[545] Fu Z, Ye J, Franke M, Körner C. A novel approach for powder bed-based additive manufacturing of compositionally graded composites. Addit Manuf 2022:: 102916.

[546] Wei C, Li L, Zhang X, Chueh Y-H. 3D printing of multiple metallic materials via modified selective laser melting. CIRP Ann 2018;67:245–8.

[547] Walker J, Middendorf JR, Lesko CC, Gockel J. Multi-material laser powder bed fusion additive manufacturing in 3-dimensions. Manufacturing Letters. 2022; 31:74–7.

[548] Lesko C, Walker J, Middendorf J, Gockel J. Functionally Graded Titanium-Tantalum in the Horizontal Direction Using Laser Powder Bed Fusion Additive Manufacturing. JOM 2021;73:2878–84.

[549] Dharmendra C, Shakerin S, Ram GDJ, Mohammadi M. Wire-arc additive manufacturing of nickel aluminum bronze/stainless steel hybrid parts – Interfacial characterization, prospects, and problems. Materialia. 2020;13:100834.

[550] Kou S. Welding Metallurgy. second edition ed: Wiley-Interscience; 2002.

[551] Zhang Y, Bandyopadhyay A. Direct fabrication of bimetallic Ti6Al4V+ Al12Si structures via additive manufacturing. Addit Manuf 2019;29:100783.

[552] Welding ASM. Brazing and Soldering. ASM International; 1993.

[553] Onuike B, Bandyopadhyay A. Additive manufacturing of Inconel 718-Ti6Al4V bimetallic structures. Addit Manuf 2018;22:844–51.

[554] Shang C, Wang C, Xu G, Li C, You J. Laser additive manufacturing of TA15 - Inconel 718 bimetallic structure via Nb/Cu multi-interlayer. Vacuum 2019;169: 108888.

[555] DuPont J. Microstructural evolution and high temperature failure of ferritic to austenitic dissimilar welds. Int Mater Rev 2012;57:208–34.

[556] Zuback J, Palmer T, DebRoy T. Additive manufacturing of functionally graded transition joints between ferritic and austenitic alloys. J Alloy Compd 2019;770: 995–1003.

[557] Sander G, Tan J, Balan P, Gharbi O, Feenstra D, Singer L, et al. Corrosion of additively manufactured alloys: a review. Corrosion 2018;74:1318–50.

[558] Cabrini M, Lorenzi S, Pastore T, Pellegrini S, Ambrosio EP, Calignano F, et al. Effect of heat treatment on corrosion resistance of DMLS AlSi10Mg alloy. Electrochim Acta 2016;206:346–55.

[559] Zeng C, Zhang B, Ettefagh AH, Wen H, Yao H, Meng W, et al. Mechanical, thermal, and corrosion properties of Cu-10Sn alloy prepared by laser-powder-bed-fusion additive manufacturing. Addit Manuf 2020;35:101411.

[560] Li J, Lin X, Tan H, Zhu G, Liu Y, Chan K, et al. Electrochemical dissolution behavior of Ti6Al4V alloy: Effect of microstructure and processing method. J Mater Process Technol 2022;117646.

[561] Kong D, Dong C, Ni X, Zhang L, Man C, Zhu G, et al. Effect of TiC content on the mechanical and corrosion properties of Inconel 718 alloy fabricated by a high-throughput dual-feed laser metal deposition system. J Alloy Compd 2019;803:637–48.

[562] Liu L, Zhuang Z, Liu F, Zhu M. Additive manufacturing of steel-bronze bimetal by shaped metal deposition: interface characteristics and tensile properties. Int J Adv Manuf Technol 2013;69:2131–7.

[563] Pan T, Zhang X, Yamazaki T, Sutton A, Cui W, Li L, et al. Characteristics of Inconel 625-copper bimetallic structure fabricated by directed energy deposition. Int J Adv Manuf Technol 2020;109:1261–74.

[564] Tan C, Zhou K, Ma W, Min L. Interfacial characteristic and mechanical performance of maraging steel-copper functional bimetal produced by selective laser melting based hybrid manufacture. Mater Des 2018;155:77–85.

[565] Articek U, Milfelner M, Anzel I. Synthesis of functionally graded material H13/Cu by LENS technology. Adv Prod Eng Manage 2013;8:169–76.

[566] Elmer JW, Haslam JJ, Unpublished KJP. Research 2019.

[567] Chen Q, Jin Z. The Fe-Cu system: A thermodynamic evaluation. Metall Mater Trans A 1995;26:417–26.

[568] Sarkar S, Srivastava C, Chattopadhyay K. Development of a new class of high strength copper alloy using immiscibility route in Cu-Fe-Si system: Evolution of hierarchical multi-scale microstructure. Mater Sci Eng A 2018;723:38–47.

[569] Park J, Kang JH, Oh CS. Phase-field simulations and microstructural analysis of epitaxial growth during rapid solidification of additively manufactured AlSi10Mg alloy. Mater Des 2020;195.

[570] Nabavizadeha SA, Eshraghib M, Felicellia SD. Three-dimensional phase field modeling of columnar to equiaxed transition in directional solidification of Inconel 718 alloy. J Cryst Growth 2020;549.

[571] Yang M, Wang L, Yan WT. Phase-field modeling of grain evolutions in additive manufacturing from nucleation, growth, to coarsening. npj Comput Mater 2021: 7.

[572] Rolchigo M, Stump B, Belak J, Plotkowski A. Sparse thermal data for cellular automata modeling of grain structure in additive manufacturing. Model Simul Mater Sci Eng 2020;28.

[573] Mohebbi MS, Ploshikhin V. Implementation of nucleation in cellular automaton simulation of microstructural evolution during additive manufacturing of Al alloys. Addit Manuf 2020:36.

[574] Liu S, Shin YC. Integrated 2D cellular automata-phase field modeling of solidification and microstructure evolution during additive manufacturing of Ti6Al4V. Comput Mater Sci 2020:192.

[575] Ao X, Xia H, Liu J, He Q. Simulations of microstructure coupling with moving molten pool by selective laser melting using a cellular automaton. Mater Des 2020;185.

[576] Zhang Y, Zhang J. Modeling of solidification microstructure evolution in laser powder bed fusion fabricated 316L stainless steel using combined computational fluid dynamics and cellular automata. Addit Manuf 2019;28:750–65.

[577] Rolchigo MR, LeSar R. Application of alloy solidification theory to cellular automata modeling of near-rapid constrained solidification. Comput Mater Sci 2019; 163:148–61.

[578] Lian YP, Gan ZT, Yu C, Kats D, Liu WK, Wagner GJ. A cellular automaton finite volume method for microstructure evolution during additive manufacturing. Mater Des 2019;169.

[579] Koepf JA, Soldner D, Ramsperger M, Mergheim J, Markl M, Koerner C. Numerical microstructure prediction by a coupled finite element cellular automaton model for selective electron beam melting. Comput Mater Sci 2019;162:148–55.

[580] Yang J, Yu H, Yang H, Li F, Wang Z, Zeng X. Prediction of microstructure in selective laser melted Ti-6Al-4V alloy by cellular automaton. J Alloy Compd 2018; 748:281–90.

[581] Pineau A, Guillemot G, Tourret D, Karma A, Gandin CA. Growth competition between columnar dendritic grains - Cellular automaton versus phase field modeling. Acta Mater 2018;155:286–301.

[582] Li X, Tan W. Numerical investigation of effects of nucleation mechanisms on grain structure in metal additive manufacturing. Comput Mater Sci 2018;153: 159–69.

[583] Zakirov A, Belousov S, Bogdanova M, Korneev B, Stepanov A, Perepelkina A, et al. Predictive modeling of laser and electron beam powder bed fusion additive manufacturing of metals at the mesoscale. Addit Manuf 2020;35.

[584] Sunny S, Yu H, Mathews R, Malik A, Li W. Improved grain structure prediction in metal additive manufacturing using a Dynamic Kinetic Monte Carlo framework. Addit Manuf 2021;37.

[585] Rodgers TM, Moser D, Abdeljawad F, Jackson ODU, Carroll JD, Jared BH, et al. Simulation of powder bed metal additive manufacturing microstructures with coupled finite difference-Monte Carlo method. 2021;41:101953.

[586] Tan JHK, Sing SL, Yeong WY. Microstructure modelling for metallic additive manufacturing: a review. Virtual and Physical Prototyping. 2020;15:87–105.

[587] Sun W, Shan F, Zong N, Dong H, Jing T. A simulation and experiment study on phase transformations of Ti-6Al-4V in wire laser additive manufacturing. Mater Des 2021;207.

[588] Lu X, Li MV, Yang H. Simulation of precipitates evolution driven by non-isothermal cyclic thermal history during wire and arc additive manufacturing of IN718 superalloy. J Manuf Process 2021;65:258–70.

[589] Khomenko MD, Makoana NW, Mirzade FK, Pityana S. Coupled heat transfer, fluid flow and solidification kinetics for laser additive manufacturing applications. J Manuf Process 2021;67:611–8.

[590] Shi R, Khairallah S, Heo TW, Rolchigo M, McKeown JT, Matthews MJ. Integrated Simulation Framework for Additively Manufactured Ti-6Al-4V: Melt Pool Dynamics, Microstructure, Solid-State Phase Transformation, and Microelastic Response. JOM 2019;71:3640–55.

[591] Kotadia H, Gibbons G, Das A, Howes PJAM. A review of Laser Powder Bed Fusion Additive Manufacturing of aluminium alloys: Microstructure and properties. 2021;46:102155.

[592] Wei HL, Cao Y, Liao WH, Liu TT. Mechanisms on inter-track void formation and phase transformation during laser Powder Bed Fusion of Ti-6Al-4V. Addit Manuf 2020:34.

[593] Wei HL, Liu FQ, Liao WH, Liu TT. Prediction of spatiotemporal variations of deposit profiles and inter-track voids during laser directed energy deposition. Addit Manuf 2020:34.

[594] Bayat M, Mohanty S, Hattel JH. Multiphysics modelling of lack-of-fusion voids formation and evolution in IN718 made by multi-track/multi-layer L-PBF. Int J Heat Mass Transf 2019;139:95–114.

[595] Khairallah S.A., Sun T. Simonds B.J. Onset of periodic oscillations as a precursor of a transition to pore-generating turbulence in laser melting. *Additive Manufacturing Letters* 2021;1.

[596] Bayat M, Thanki A, Mohanty S, Witvrouw A, Yang S, Thorborg J, et al. Keyhole-induced porosities in Laser-based Powder Bed Fusion (L-PBF) of Ti6Al4V: High-fidelity modelling and experimental validation. Addit Manuf 2019:30.

[597] Khairallah SA, Martin AA, Lee JRI, Guss G, Calta NP, Hammons JA, et al. Controlling interdependent meso-nanosecond dynamics and defect generation in metal 3D printing. Science 2020;368:660–+..

[598] Kouraytem N, Chiang PJ, Jiang RB, Kantzos C, Pauza J, Cunningham R, et al. Solidification crack propagation and morphology dependence on processing parameters in AA6061 from ultra-high-speed x-ray visualization. Addit Manuf 2021;42.

[599] Hu Z, Nie X, Qi Y, Zhang H, Zhu H. Cracking criterion for high strength Al-Cu alloys fabricated by selective laser melting. Addit Manuf 2021;37.

[600] Kou MS. A criterion for cracking during solidification. 2015;88:366–74.

[601] Montero Sistiaga ML, Mertens R, Vrancken B, Xiebin W, Van Hooreweder B, Kruth JP, et al. Changing the alloy composition of Al7075 for better processability by selective laser melting. J Mater Process Technol 2016;238:437–45.

[602] Martin JH, Yahata B, Mayer J, Mone R, Stonkevitch E, Miller J, et al. Grain refinement mechanisms in additively manufactured nano-functionalized aluminum. Acta Mater 2020;200:1022–37.

[603] Li R, Wang M, Li Z, Cao P, Yuan T, Zhu H. Developing a high-strength Al-Mg-Si-Sc-Zr alloy for selective laser melting: Crack-inhibiting and multiple strengthening mechanisms. Acta Mater 2020;193:83–98.

[604] Klassen A, Forster VE, Juechter V, Koerner C. Numerical simulation of multi-component evaporation during selective electron beam melting of TiAl. J Mater Process Technol 2017;247:280–8.

[605] Mukherjee T, DebRoy T. Printability of 316 stainless steel. Sci Technol Weld Join 2019;24:412–9.

[606] Liu J, Wen P. Metal vaporization and its influence during laser powder bed fusion process. Materials & Design 2022;215:110505.

[607] Jordan MI, Mitchell TM. Machine learning: Trends, perspectives, and prospects. Science 2015;349:255–60.

[608] LeCun Y, Bengio Y. Hinton G. Deep learning. 2015;521:436–44.

[609] Chowdhury A, Kautz E, Yener B, Lewis D. Image driven machine learning methods for microstructure recognition. Comput Mater Sci 2016;123:176–87.

[610] Popova E, Rodgers TM, Gong X, Cecen A, Madison JD, Kalidindi SR. Process-Structure Linkages Using a Data Science Approach: Application to Simulated Additive Manufacturing Data. Integrating Materials and Manufacturing Innovation. 2017;6:54–68.

[611] Collins PC, Haden CV, Ghamarian I, Hayes BJ, Ales T, Penso G, et al. Progress Toward an Integration of Process-Structure-Property-Performance Models for "Three-Dimensional (3-D) Printing" of Titanium Alloys. JOM 2014;66:1299–309.

[612] Nomoto S, Segawa M, Wakameda H, Koyama T, Yamanaka A. Non-equilibrium phase field model using thermodynamics data estimated by machine learning. The Conference on Computational Engineering ans Science. 2018.

[613] Li J, Sage M, Zhou X, Brochu M, Zhao YF. Machine Learning for Competitive Grain Growth Behavior in Additive Manufacturing Ti6Al4V. MATEC Web Conf (France): EDP Sciences; 2020. p. 03004.

[614] Miyazaki S, Kusano M, Bulgarevich DS, Kishimoto S, Yumoto A, Watanabe M. Image Segmentation and Analysis for Microstructure and Property Evaluations on Ti-6Al-4V Fabricated by Selective Laser Melting. Mater Trans 2019;60:561–8.

[615] Gan Z, Li H, Wolff SJ, Bennett JL, Hyatt G, Wagner GJ, et al. Data-Driven Microstructure and Microhardness Design in Additive Manufacturing Using a Self-Organizing Map. Engineering 2019;5:730–5.

[616] Han Y, Griffiths RJ, Yu HZ, Zhu Y. Quantitative microstructure analysis for solid-state metal additive manufacturing via deep learning. J Mater Res 2020;35:1936–48.

[617] Mukherjee T, Manvatkar V, De A, DebRoy T. Dimensionless numbers in additive manufacturing. J Appl Phys 2017;121.

[618] Cao S, Gu D. Laser metal deposition additive manufacturing of TiC/Inconel 625 nanocomposites: Relation of densification, microstructures and performance. J Mater Res 2015;30:3616–28.

[619] Pfaff A, Jaecklein M, Hoschke K, Wickert M. Designed Materials by Additive Manufacturing-Impact of Exposure Strategies and Parameters on Material Characteristics of AlSi10Mg Processed by Laser Beam Melting. Metals. 2018;8.

[620] Hrabe N, Quinn T. Effects of processing on microstructure and mechanical properties of a titanium alloy (Ti-6Al-4V) fabricated using electron beam melting (EBM), part 1: Distance from build plate and part size. Materials Science and Engineering a-Structural Materials Properties Microstructure and Processing. 2013;573:264–70.

[621] Hrabe N, Quinn T. Effects of processing on microstructure and mechanical properties of a titanium alloy (Ti-6Al-4V) fabricated using electron beam melting (EBM), Part 2: Energy input, orientation, and location. Materials Science and Engineering a-Structural Materials Properties Microstructure and Processing. 2013;573:271–7.

[622] Nassar AR, Reutzel EW. Additive Manufacturing of Ti-6Al-4V Using a Pulsed Laser Beam. Metallurgical and Materials Transactions a-Physical Metallurgy and Materials Science. 2015;46A:2781–9.

[623] Nassar AR, Keist JS, Reutzel EW, Spurgeon TJ. Intra-layer closed-loop control of build plan during directed energy additive manufacturing of Ti-6Al-4V. Addit Manuf 2015;6:39–52.

[624] Sun W, Shan F, Zong N, Dong H, Jing T, et al. Simulation of solidified β grain for Ti–6Al–4V during wire laser additive manufacturing by three-dimensional cellular automaton method 2021;29:065006.

[625] Luo YW, Zhang B, Li CP, Chen GF, Zhang GP. Detecting void-induced scatter of fatigue life of selective laser melting-fabricated inconel 718 using miniature specimens. Mater Res Express 2019;6.

[626] Gong X, Yabansu YC, Collins PC, Kalidindi SR. Evaluation of Ti-Mn Alloys for Additive Manufacturing Using High-Throughput Experimental Assays and Gaussian Process Regression. Materials. 2020;13.

[627] Tang J, Geng X, Li D, Shi Y, Tong J, Xiao H, et al. Machine learning-based microstructure prediction during laser sintering of alumina. Sci Rep 2021;11.

[628] Qi H, Azer M, Ritter A. Studies of Standard Heat Treatment Effects on Microstructure and Mechanical Properties of Laser Net Shape Manufactured INCONEL 718. Metallurgical and Materials Transactions a-Physical Metallurgy and Materials Science. 2009;40A:2410–22.

[629] Liu F, Lin X, Leng H, Cao J, Liu Q, Huang C, et al. Microstructural changes in a laser solid forming Inconel 718 superalloy thin wall in the deposition direction. Opt Laser Technol 2013;45:330–5.

[630] Parimi LL, Ravi GA, Clark D, Attallah MM. Microstructural and texture development in direct laser fabricated IN718. Mater Charact 2014;89:102–11.

[631] Zhong C, Gasser A, Kittel J, Fu J, Ding Y, Poprawe R. Microstructures and tensile properties of Inconel 718 formed by high deposition-rate laser metal deposition. J Laser Appl 2016;28.

[632] Khanzadeh M, Chowdhury S, Marufuzzaman M, Tschopp MA, Bian L. Porosity prediction: Supervised-learning of thermal history for direct laser deposition. J Manuf Syst 2018;47:69–82.

[633] Scime L, Beuth J. A multi-scale convolutional neural network for autonomous anomaly detection and classification in a laser powder bed fusion additive manufacturing process. Addit Manuf 2018;24:273–86.

[634] Scime L, Beuth J. Anomaly detection and classification in a laser powder bed additive manufacturing process using a trained computer vision algorithm. Addit Manuf 2018;19:114–26.

[635] Mosallanejad MH, Niroumand B, Aversa A, Saboori A. In-situ alloying in laser-based additive manufacturing processes: A critical review. J Alloy Compd 2021;872:159567.

[636] Sing S, Huang S, Goh G, Goh G, Tey C, Tan J, et al. Emerging metallic systems for additive manufacturing: In-situ alloying and multi-metal processing in laser powder bed fusion. Prog Mater Sci 2021;119:100795.

[637] Zhai W, Zhou W, Nai SML. Grain refinement of 316L stainless steel through in-situ alloying with Ti in additive manufacturing. Mater Sci Eng A 2022;840: 142912.

[638] Mosallanejad MH, Niroumand B, Ghibaudo C, Biamino S, Salmi A, Fino P, et al. In-situ alloying of a fine grained fully equiaxed Ti-based alloy via Electron Beam Powder Bed Fusion Additive Manufacturing process. Addit Manuf 2022;102878.

[639] Katz-Demyanetz A, Koptyug A, Popov VV. In-situ Alloying as a Novel Methodology in Additive Manufacturing. 2020 IEEE 10th International Conference Nanomaterials: Applications & Properties (NAP): IEEE; 2020. p. 02SAMA5-1-SAMA5-4.

[640] Kumar S, Kishor B. Ultrasound added additive manufacturing for metals and composites: process and control. Additive and subtractive manufacturing of composites: Springer; 2021. p. 53–72.

[641] Nigmetzyanov RI, Sundukov SK, Fatyukhin DS, Grib VV, Kartsov SK. Additive Manufacturing with Ultrasound. Russ Eng Res 2017;37:1070–3.

[642] Yuan D, Shao S, Guo C, Jiang F, Wang J. Grain refining of Ti-6Al-4V alloy fabricated by laser and wire additive manufacturing assisted with ultrasonic vibration. Ultrason Sonochem 2021;73:105472.

[643] Yuan D, Sun X, Sun L, Zhang Z, Guo C, Wang J. Improvement of the grain structure and mechanical properties of austenitic stainless steel fabricated by laser and wire additive manufacturing assisted with ultrasonic vibration. Mater Sci Eng A 2021;813:141177.

[644] Todaro C, Easton M, Qiu D, Zhang D, Bermingham M, Lui E, et al. Grain structure control during metal 3D printing by high-intensity ultrasound. Nat Commun 2020;11:1–9.

[645] Chen Y, Xu M, Zhang T, Xie J, Wei K, Wang S, et al. Grain refinement and mechanical properties improvement of Inconel 625 alloy fabricated by ultrasonic-assisted wire and arc additive manufacturing. J Alloy Compd 2022;910:164957.

[646] Li C, Sun S, Liu C, Lu Q, Ma P, Wang Y. Microstructure and mechanical properties of TiC/AlSi10Mg alloy fabricated by laser additive manufacturing under high-frequency micro-vibration. J Alloy Compd 2019;794:236–46.

[647] Manogharan G, Yelamanchi B, Aman R, Mahbooba Z. Experimental study of disruption of columnar grains during rapid solidification in additive manufacturing. JOM 2016;68:842–9.

[648] Wang Y, Shi J. Texture control of Inconel 718 superalloy in laser additive manufacturing by an external magnetic field. J Mater Sci 2019;54:9809–23.

[649] Wang Y, Chen X, Shen Q, Su C, Zhang Y, Jayalakshmi S, et al. Effect of magnetic Field on the microstructure and mechanical properties of inconel 625 superalloy fabricated by wire arc additive manufacturing. J Manuf Process 2021;64:10–9.

[650] Zhou X, Zhang H, Wang G, Liang L, Fu Y, Bai X, et al. Numerical simulation and experimental investigation of arc based additive manufacturing assisted with external longitudinal static magnetic field. 2014 International Solid Freeform Fabrication Symposium: University of Texas at Austin; 2015.

[651] Zhao R, Chen C, Shuai S, Hu T, Fautrelle Y, Liao H, et al. Enhanced mechanical properties of Ti6Al4V alloy fabricated by laser additive manufacturing under static magnetic field. Materials Research Letters. 2022;10:530–8.

[652] Lee JE, Park SJ, Son Y, Park K, Park S-H. Mechanical reinforcement of additive-manufactured constructs using in situ auxiliary heating process. Addit Manuf 2021;43:101995.

[653] Sang Y-X, Xiao M-Z, Zhang Z-J, Fu Q-Y. Effect of auxiliary heating process on low power pulsed laser wire feeding deposition. Mater Des 2022;218:110666.

[654] Farshidianfar MH, Khajepour A, Gerlich A. Real-time control of microstructure in laser additive manufacturing. Int J Adv Manuf Technol 2016;82:1173–86.

[655] Zhang G, Lu X, Li J, Chen J, Lin X, Wang M, et al. In-situ grain structure control in directed energy deposition of Ti6Al4V. Addit Manuf 2022;55:102865.

[656] Farshidianfar MH, Khodabakhshi F, Khajepour A, Gerlich AP. Closed-loop control of microstructure and mechanical properties in additive manufacturing by directed energy deposition. Mater Sci Eng A 2021;803:140483.

[657] Renken V, Lübbert L, Blom H, von Freyberg A, Fischer A. Model assisted closed-loop control strategy for selective laser melting. Procedia CIRP. 2018;74: 659–63.

[658] Borish M, Post BK, Roschli A, Chesser PC, Love LJ, Gaul KT. Defect identification and mitigation via visual inspection in large-scale additive manufacturing. JOM 2019;71:893–9.

[659] Akhavan J, Manoochehri S. Sensory Data Fusion Using Machine Learning Methods For In-Situ Defect Registration In Additive Manufacturing: A Review. 2022 IEEE International IOT, Electronics and Mechatronics Conference (IEMTRONICS): IEEE; 2022. p. 1-10.

[660] Liu W-W, Tang Z-J, Liu X-Y, Wang H-J, Zhang H-C. A review on in-situ monitoring and adaptive control technology for laser cladding remanufacturing. Procedia Cirp. 2017;61:235–40.

[661] Qin L, Zhao D, Wang W, Yang G. Geometric defects identification and deviation compensation in laser deposition manufacturing. Opt Laser Technol 2022;155: 108374.

[662] Khanzadeh M, Chowdhury S, Tschopp MA, Doude HR, Marufuzzaman M, Bian L. In-situ monitoring of melt pool images for porosity prediction in directed energy deposition processes. IISE Transactions. 2019;51:437–55.

[663] Zhang L, Liao W-H, Liu T-T, Wei H-L, Zhang C-C. In Situ Elimination of Pores During Laser Powder Bed Fusion of Ti–6.5 Al–3.5 Mo–l. 5Zr–0.3 Si Titanium Alloy. Acta Metallurgica Sinica (English Letters) 2022;35:439–52.

[664] Liu L, Ding Q, Zhong Y, Zou J, Wu J, Chiu Y-L, et al. Dislocation network in additive manufactured steel breaks strength-ductility trade-off. Mater Today 2018; 21:354–61.

[665] Bandyopadhyay A, Traxel KD, Lang M, Juhasz M, Eliaz N, Bose S. Alloy design via additive manufacturing: Advantages, challenges, applications and perspectives. Mater Today 2022;52:207–24.

[666] Mukherjee T, Debroy T. A digital twin for rapid qualification of 3D printed metallic components. Appl Mater Today 2019;14:59–65.

[667] Borsato T, Berto F, Ferro P, Carollo C. Effect of in-mould inoculant composition on microstructure and fatigue behaviour of heavy section ductile iron castings. 21st European Conference on Fracture (ECF). Catania, ITALY2016. p. 3150-7.

[668] Whip B, Sheridan L, Gockel J. The effect of primary processing parameters on surface roughness in laser powder bed additive manufacturing. Int J Adv Manuf Technol 2019;103:4411–22.

[669] Mondal B, Gao M, Palmer TA, DebRoy T. Solidification cracking of a nickel alloy during high-power keyhole mode laser welding. J Mater Process Technol 2022;305.

[670] Khairallah SA, Sun T, Simonds BJ. Onset of periodic oscillations as a precursor of a transition to pore-generating turbulence in laser melting. Additive Manufacturing Letters. 2021;1:100002.

Dr. Mukherjee is a Postdoctoral Researcher at the Pennsylvania State University and author of many papers in leading journals including Nature Reviews Materials, Nature Materials, and Progress in Materials Science. He edited a book entitled "The Science and Technology of 3D Printing" (MDPI, 2021) and his textbook on "Theory and Practice of Additive Manufacturing" will be published by Wiley in October 2023 complete with many worked-out examples, visual learning aids in every chapter, and coverage of emerging digital tools. His research interests include additive manufacturing, welding, machine learning, and heat and mass transfer. He served as a Guest Editor for the journals "Computational Materials Science", "Materials", and "Science and Technology of Welding and Joining". He is an Editorial Board Member of the journal "Science and Technology of Welding and Joining" and "Welding Journal".

Dr. Elmer received his ScD in Metallurgy from the Massachusetts Institute of Technology in 1988 and holds BS and MS degrees in Metallurgical Engineering from the Colorado School of Mines. He is employed by Lawrence Livermore National Laboratory (LLNL) where he is a Distinguished Member of the Technical Staff (DMTS) and leader of the Materials Processes Group of the Materials Engineering Division, with over 35 years of experience. Elmer's group is responsible for Materials Joining where he has authored or co-authored more than 170 technical papers on topics relating to additive manufacturing, laser and electron beam processing, vacuum brazing, soldering, diffusion bonding, metallurgical characterization and failure analysis of welds and brazed joints, solidification, and metallurgical phase transformations. He is

Fellow of the ASM International, Fellow and Honorary Member of the American Welding Society, Professional Engineer, and serves on the editorial boards and committees for numerous journals and professional societies.

Dr. Wei is a Professor in the School of Mechanical Engineering at Nanjing University of Science and Technology, China. His research focuses on laser additive manufacturing processes, multi-scale simulation, complex heat transfer and fluid flow, and the solidification behavior of high-performance metallic materials. He is an associate editor of the Elsevier journal "Additive Manufacturing". He is one of the organizing committee members of the Annual International Conference on Research Advances in Additive Manufacturing (RAAM).

Dr. Lienert is Senior LENS Scientist, Optomec, Owner, TJ Lienert Consulting, LLC, and a former President of the American Welding Society (AWS). He was formerly a technical staff member and an R&D engineer at Los Alamos National Laboratory for more than 16 years. He has published many peer-reviewed papers on additive manufacturing, welding, and materials science and several book and handbook chapters. He is a Fellow of the American Welding Society and ASM International.

Dr. Wei Zhang is a Professor of Materials Science and Engineering at The Ohio State University (OSU). Before coming to OSU in 2013, he worked as a Senior Researcher at Oak Ridge National Laboratory from 2008-2012 and as an Engineer Team Leader at Edison Welding Institute from 2004-2008. He was an invited panelist for American Makes Roadmapping from 2020-2022 and for NASA's 2040 Vision for Multi-scale Materials and Structural Modeling from 2017-2018 where he contributed his expertise on physics-based modeling of additive manufacturing. His research at OSU focuses on the modeling of additive manufacturing and welding processes, and light-weight materials and dissimilar metals joining.

Dr. Kou got a Ph.D. in Metallurgy from the Massachusetts Institute of Technology and is a Professor in the Department of Materials Science and Engineering at the University of Wisconsin-Madison (Department Chair in 2000-2004). He authored Welding Metallurgy (3rd edition, 2021, John Wiley) and Transport Phenomena and Materials Processing (1996, John Wiley), the former cited about 5,000 times. Kou is a Fellow of the American Welding Society (AWS) and ASM International. He received Comfort Adams Memorial Lecture Award from AWS, Yoshiaki Arata Award from International Welding Institute, Bruce Chalmers Award from TMS, and Chancellor's Award for Distinguished Teaching from the University of Wisconsin. His technical papers received 16 awards from AWS and TMS.

Dr. DebRoy is a Professor of Materials Science and Engineering at Penn State and the author of two books including a 2023 Wiley textbook on "Theory and Practice of Additive Manufacturing" containing many worked-out examples, five edited books, and over 380 well-cited technical articles. His work has been recognized by over 20 scholastic awards including a Fulbright Distinguished Chair in Brazil from the US State Department, the UK Royal Academy of Engineering's Distinguished Visiting Fellowship at Cambridge University, and Penn State's highest scholastic award, the Faculty Scholar medal. He has served as a Distinguished Visiting Professor at IIT Bombay, Aditya Birla Chair at IISc, Bangalore, Visiting Professor at African University of Science and Technology at Abuja, Nigeria, and Visiting Professor at KTH, Stockholm. He is a Founding Editor of the journal "Science and Technology of Welding and Joining".